2015

Alternative protein conformations: yeast iso-1-cytochrome c and heme crevice dynamics

Levi James McClelland
The University of Montana

ALTERNATIVE PROTEIN CONFORMATIONS: YEAST ISO-1-CYTOCHROME *C* AND HEME CREVICE DYNAMICS

By

LEVI JAMES MCCLELLAND

B.S. Biochemistry, Slippery Rock University, Slippery Rock, PA, 2009

Dissertation

presented in partial fulfillment of the requirements
for the degree of

Doctor of Philosophy
in Biochemistry & Biophysics

The University of Montana
Missoula, MT

December 2015

Approved by:

Dr. J. B. Alexander (Sandy) Ross, Dean of The Graduate School
Graduate School

Dr. Bruce E. Bowler, Chair
Department of Chemistry & Biochemistry

Dr. J. Stephen Lodmell, Committee Member
Division of Biological Sciences

Dr. Edward Rosenberg, Committee Member
Department of Chemistry & Biochemistry

Dr. J. B. Alexander (Sandy) Ross, Committee Member
Department of Chemistry & Biochemistry

Dr. Stephen R. Sprang, Committee Member
Division of Biological Sciences

Abstract

McClelland, Levi J., Ph. D., Fall 2015 Biochemistry & Biophysics

Alternative protein conformations: yeast iso-1-cytochrome *c* and heme crevice dynamics

Chairperson: Bruce E. Bowler

The field of protein biochemistry has been dominated by the dogma that a protein sequence yields a 3-dimensional structure important for a singular function. More modern insights are beginning to demonstrate that proteins are not static structures. Rather, proteins undergo numerous conformational fluctuations yielding an ensemble of conformational populations. Conformational change can result in changed or altered protein function. Small or large energetic barriers existing between conformers regulate the ease with which a protein can sample alternative conformations. In the dissertation work presented here, alternative conformations of yeast iso-1-cytochrome *c* are investigated with particular emphasis on heme crevice loop dynamics. The heme crevice loop, or Ω-loop D, is a highly conserved, dynamic region. Conformational changes in Ω-loop D lead to altered electron transfer and peroxidase activity in cytochrome *c* (Cyt*c*). As Cyt*c* participates in both the electron transport chain and functions as a peroxidase during apoptosis, it is important to understand how this conformational change is regulated. Within Ω-loop D we investigate the effects of a trimethyllysine to alanine mutation and a destabilizing leucine to alanine mutation at residues 72 and 85, respectively, on heme crevice dynamics. Residue 72 plays an important role in regulating access to alternative heme crevice conformers. Of particular interest, residue 72 plays a role in regulating access to a peroxidase capable conformer of Cyt*c*, a function of Cyt*c* during the early stages of apoptosis. We have also solved the structure of the first monomeric Cyt*c* structure in a peroxidase capable conformer, as well as, a dimeric Cyt*c* structure with CYMAL-6 protruding into the interior of the heme cavity, in a manner potentially similar to the Cyt*c*/cardiolipin interaction.

Acknowledgements

I owe a huge debt of gratitude to my advisor, Dr. Bruce Bowler. Your support and understanding have been unwavering on this journey. Thank you for all you have taught me about becoming a scientist. To me, you are the epitome of all that an advisor should be.

Thank you to all of the members of the Bowler Lab past and present, especially Bill, Dustin, Haotian, Harmen, Khurshid, Margaret, Margaret, Matt, Melisa, Michaela, Moses, Sasha, Sean, Shiloh, Travis. I have learned so much from all of you, and appreciate your support and the insight you have provided to me throughout this process. Melisa and Sean, the two of you were invaluable in my training, I could not have asked for more competent, helpful, and patient mentors.

I thank all of my committee members, Dr. Edward Rosenberg, Dr. Steve Lodmell, Dr. Sandy Ross, and Dr. Steve Sprang. Together you have provided invaluable support, insight, and thoughtful discussion along the way, leading to new discoveries, and making possible all that we have accomplished. Furthermore, Dr. Sandy Ross, Dr. Steve Sprang, the Ross Lab, and the Sprang Lab have not only provided the opportunity, but demonstrated the benefits possible through collaboration of ideas and experimentation between lab groups. A special thanks to T.C., crystallographer extraordinaire in the Sprang Lab. Without guidance and assistance from T.C. none of these X-ray crystal structures would have been possible.

I would like to thank all of my friends and family who have supported me throughout the years to make this day possible. Geoff and Harmen, thank you for always being there, your support and friendship means more than you know. My parents, Bud and Rita, thank you for all that you have done for me. Without your love and support I would not have been able to reach my goals. I owe it all to you. Barley, thank you for providing much love and affection, as well as, an escape from reality whenever needed. I especially want to thank my wife, Meghan, thank goodness you understand computers better than me. You have provided the love, support, understanding, and sacrifice to keep me sane along this path, at times at the cost of your own sanity.

Table of Contents

List of Figures

List of Schemes

List of Tables

List of Appendix Tables

Chapter 1 Introduction

In order to understand the role proteins play in cellular processes, it becomes imperative to understand the effects of structure and conformational change on function. Traditionally, a single amino acid sequence has been thought to fold into a single protein structure yielding a set function for that protein (*1*). More recently, conformational flexibility has been identified in proteins (*2*). This conformational flexibility yields an ensemble of conformational states accessed by a protein. Differing conformers can result in different or altered protein function. In this work, alternative protein conformations and regulation of heme crevice dynamics are investigated in yeast iso-1-cytochrome *c*.

Cytochrome *c* (Cyt*c*) is a small, globular hemeprotein that resides within the inner mitochondrial membrane space (Figure 1.1). Originally identified for its participation as an electron shuttle in the electron transport chain (*3*), Cyt*c* is also involved in the initial stages of the intrinsic apoptotic pathway (*4-6*). The porphyrin ring covalently binds to Cyt*c* via two thioether bonds with cysteine residues 14 and 17 (*7*). His18 is the axial heme ligand. In the native Cyt*c* conformer, Met80, part of Ω-loop D which encompasses residues 70-85, is coordinated to the the distal heme site (Figure 1.2). The heme crevice loop, Ω-loop D, is one of the most highly conserved sequence regions of Cyt*c* (*3*). Interestingly, Ω-loop D has also been identified as a region of low stability (*8*). In fact, an increase in pH leads to an ionization event associated with the alkaline conformational transition. During the alkaline conformational transition, rearrangement of Ω-loop D results in loss of Met80-heme ligation (Figure 1.2) (*9, 10*). Lysine residues 73 and 79 replace Met80 as the distal heme ligand in the alkaline conformer.

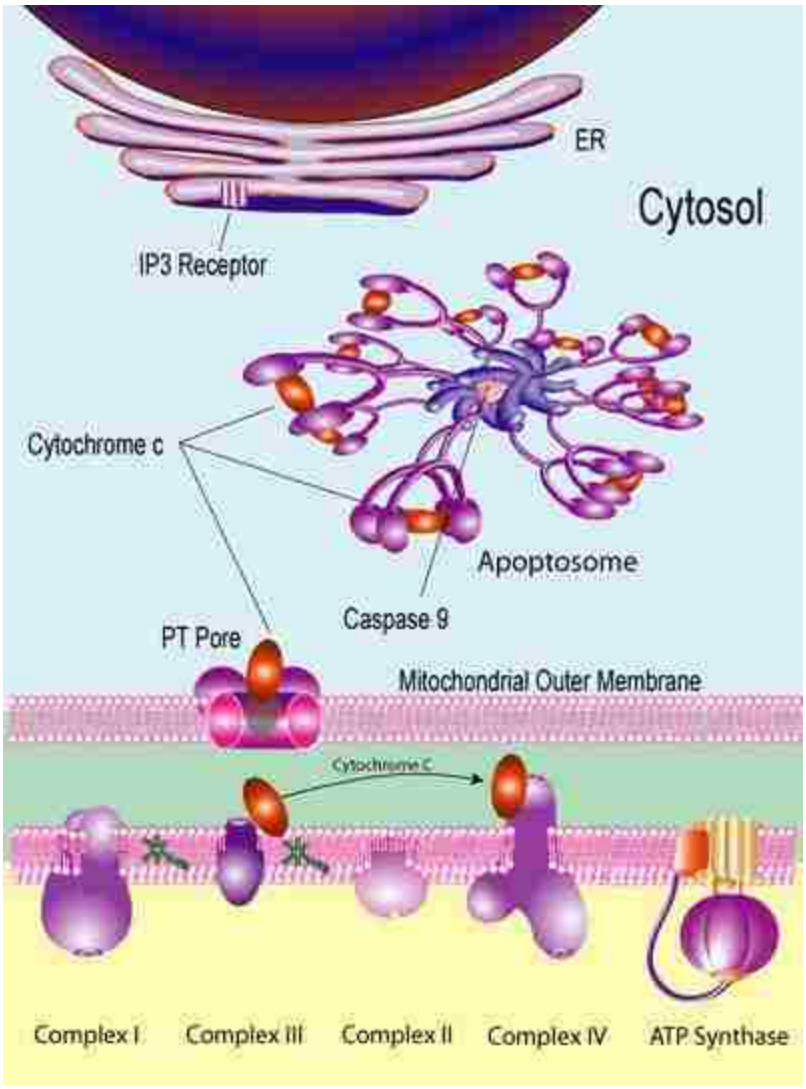

Figure 1.1. Functions of Cyt*c*. Cyt*c* (red sphere) resides in the mitochondrial intermembrane space, where it functions to shuttle electrons between Complex III and Complex IV in the electron transport chain. Cyt*c* is also involved in apoptosis, and upon evacuating the mitochondria participates in formation of the apoptosome. Figure reproduced from ref. (*11*).

Further conformational change occurs during the onset of the intrinsic pathway of apoptosis, where Cyt*c* associates with cardiolipin (CL) (*4-6, 12*). Association with cardiolipin results in a conformational rearrangement of Cyt*c* such that Met80-heme ligation is lost, enabling Cyt*c* to gain peroxidase activity. Cyt*c* oxidizes unsaturated bonds on the acyl chains of CL, leading to Cyt*c* dissociation and compromised membrane integrity. Upon evacuation of the

mitochondria, Cyt*c* associates with Apoptotic protease activating factor 1 (Apaf-1) to form the apoptosome, continuing the apoptotic pathway. As the heme group is important in both electron transport as well as the apoptotic peroxidase role of Cyt*c*, a greater understanding of regulation and the dynamics of the heme crevice is crucial.

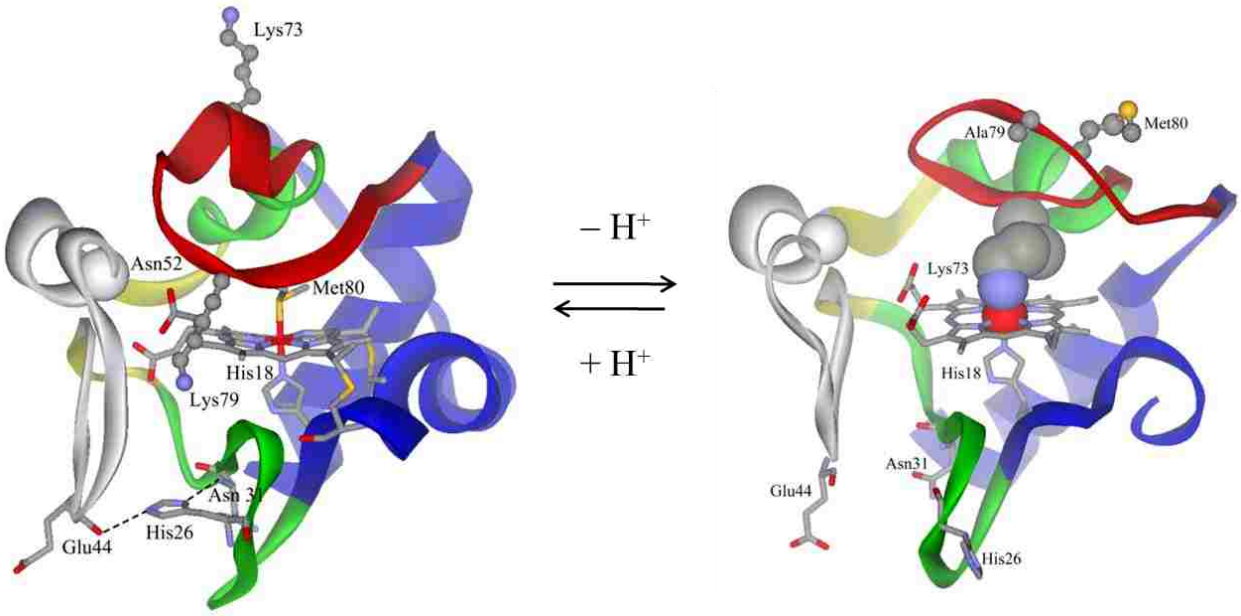

Figure 1.2. The alkaline conformational transition. Met80 is the heme ligand in the native conformer (left, PDB code 2YCC, (*7*)). Following a deprotonation event, the Met80 ligand can be replaced by Lys73 (right, PDB code 1LMS, (*13*)). Heme is shown in grey sticks. Ω-loop D, residues 70-85 is shown as a red ribbon.

This work encompasses the dynamics and regulation of conformational change with particular emphasis on the heme crevice loop. Further the first monomeric structure capable of peroxidase activity is identified and described. We also present the first atomic resolution structure of Cyt*c* with a detergent bound inside a cavity providing heme access to a hydrocarbon chain, potentially mimicking the Cyt*c*/CL interaction.

During the alkaline conformational transition either Lys73 or Lys79, from Ω-loop D, replace the native Met80-heme ligand (Figure 1.2) (*9, 10*). In order to distinguish which residue

binds the heme, one or the other of these lysines can be replaced by a histidine residue (*14-21*). The mechanism for formation of the alkaline conformer appears to proceed differently for the His73-mediated (*21*) and His79-heme alkaline transitions (*16*). Replacement of trimethyllysine (tmK) at position 72 with an alanine leads to increased dynamics in a K79H variant of yeast iso-1-Cyt*c* (*18, 19*). Therefore, it would appear that residue 72 may have an important role in modulation of the heme crevice dynamics required to achieve peroxidase activity. The goal of Chapter 2 is to ask the question whether residue 72 plays a generic role in modulating heme crevice dynamics, or whether residue 72 regulates only dynamics of specific pathways in the heme crevice by investigating the effect of a tmK72A mutation on the dynamics of a K73H yeast iso-1-Cyt*c* variant. As formation of the His73-heme and His79-heme alkaline conformers proceeds via differing mechanisms, the hypothesis that the tmK72A mutation will not increase dynamic motion in a K73H variant seems likely.

Proteins fold into the most energetically favorable state, typically known as the native state. A very stable native state requires large energy barriers to be overcome in order to be capable of undergoing a conformational change. Conversely, a protein conformer with low stability has smaller barriers separating conformational states. As enzyme activity is thought to relate to structure, the "stability-function" hypothesis relates protein stability to protein function (*22*). Psychrophiles take advantage of the "stability-function" hypothesis by reducing stability to gain conformational flexibility for enzymatic activity, in order to compensate for the reduced temperatures they operate at (*23-25*). Mutation of H26N disrupts a hydrogen bond in yeast iso-1-Cyt*c* causing a 2-fold decrease in global stability (Figure 1.2) (*15, 26*). Accompanying this decrease in stability is an increase in heme crevice dynamics (*14*). Replacement of Leu85 with an alanine in yeast iso-1-Cyt*c* is also known to cause a 2-fold decrease in stability (*27*). With

Leu85 residing at the edge of the dynamic heme crevice loop, the hypothesis in Chapter 3 is that the destabilizing Leu85Ala mutation will also cause an increase in Cyt*c* heme crevice dynamics, as seen in psychrophiles and other destabilized variants.

In recent years, Cyt*c* has been of interest for the role it plays in the intrinsic pathway of cellular apoptosis (*4-6*). Cyt*c* interacts with CL on the inner mitochondrial membrane. Upon binding to CL, a conformational change occurs in Cyt*c* where the Met80-heme ligand is lost, enabling Cyt*c* to function as a peroxidase (*12*). It is of particular interest to understand the conformational changes that occur as Cyt*c* converts from an electron shuttle in energy production to a peroxidase capable of initiating cell death. As recent work has shown that residue 72 is important in modulating heme crevice dynamics that may be relevant to peroxidase activity (*18, 19*), here the hypothesis that residue 72 is an important regulator of heme crevice dynamics in accessing a peroxidase capable conformer is investigated. This hypothesis is tested with dynamics, functional, and structural measurements on the tmK72A iso-1 Cyt*c* variant in Chapter 4.

For many years, Cyt*c* has been known to form dimeric structures following acid (*28*) or ethanol (*29*) treatment. More recently, an X-ray crystal structure of an equine Cyt*c* C-terminal domain swapped dimer has been identified (*30*). Intriguingly, Ω-loop D acts as the linker region of the domain swapped dimer resulting in the loss of Met80-heme ligation, providing a peroxidase capable platform. In fact, dimeric Cyt*c* is known to interact with membranes (*31*). The Cyt*c* dimer also demonstrates an increase in peroxidase activity compared to monomeric Cyt*c* (*32*). Other studies have demonstrated that upon interaction with CL membranes monomeric Cyt*c* adopts an extended conformer (*33, 34*), much like the subunits of the Cyt*c* dimer X-ray crystal structure (*30*). This would suggest the hypothesis that dimeric Cyt*c* could be

important for understanding the interaction of Cyt*c* with CL leading to peroxidase activity. Based upon this hypothesis, in Chapter 5 structural studies on tmK72A iso-1-Cyt*c* in the presence of detergents are described. The hypothesis that detergents stabilize the Cyt*c* dimer is also tested via kinetic studies in the absence of detergent.

Chapter 2 The Response of Ω-Loop D Dynamics to Truncation of Trimethyllysine 72 of Yeast Iso-1-cytochrome *c* Depends on the Nature of Loop Deformation[1]

2.1 Introduction

Tier 0 dynamics, which involves interconverison between conformers separated by a thermal barrier, is particularly important in protein function, often controlling access to functionally active conformers (*35*). A detailed understanding of the structural factors that control tier 0 dynamics and thus the function of proteins is essential. Cytochrome *c* (Cyt*c*) has long been a protein of interest due to both its function in electron transport (*3*) and its role in apoptosis (*5*). Of particular interest with regard to these functions are the heme crevice dynamics, which can be studied with the alkaline conformational transition of Cyt*c* (*36*). The alkaline conformational transition is an example of tier 0 dynamics because the barrier between the native and alkaline states is significantly larger than ambient thermal energy (*35*, *37*).

Here, we use yeast iso-1-cytochrome *c* (iso-1-Cyt*c*) as a vehicle to probe the structural factors controlling protein dynamics. Residues 70-85 of iso-1-Cyt*c* comprise the heme crevice loop, Ω-loop D (Figure 2.1), which lies across one face of the heme. These residues are highly conserved across Cyt*c* from different species (*3*, *38*). Met80 is bound to the sixth coordination

[1] Work presented in Chapter 2 has been published previously: McClelland et al. *J. Biol. Inorg. Chem.* (2015) 20:805-819.

site of the heme in the native iso-1-Cyt*c* conformer (*7*). During the tier 0 alkaline conformational transition of the ferric state of Cyt*c*, the Met80-heme ligand is replaced by lysine residues within Ω-loop D. These conformational changes are of particular biological interest because replacement of Met80-heme ligation with Lys-heme ligation can modulate electron transfer properties, possibly optimizing electron flow in the electron transport chain (*13, 14, 36, 39-41*). The Met80 ligand must also leave the 6th coordination site of the heme in order for peroxidase activity to occur in the beginning stages of apoptosis (*5*). Apoptosis can be induced in yeast, causing release of Cyt*c* from the mitochondria. However, the proteins needed to form an apoptosome in the cytoplasm and induce the caspase cascade, which leads to cell death in higher

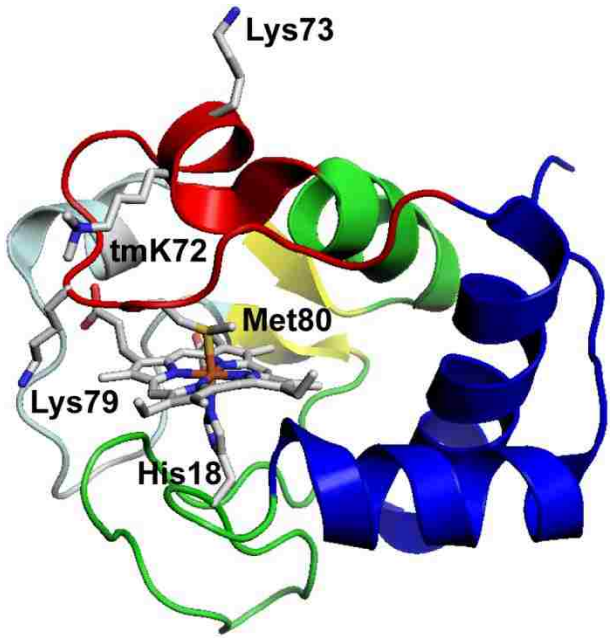

Figure 2.1. Structure of iso-1-Cyt*c* (pdb code: 2YCC, (*7*)). The loop shown in red is Ω-loop D and provides Met80 as a heme ligand in the native state. Lysines 73 and 79 provide the alkaline state ligands for wild type iso-1-Cyt*c*. Lysine 72 is trimethylated, tmK72, when iso-1-Cyt*c* is expressed in its native host yeast. tmK72 can be seen to lie across the surface of the heme crevice loop, Ω-loop D. The cooperative substructures of Cyt*c*, as defined by Englander and coworkers (*42-44*), from least to most stable are color-coded: pale cyan, red, yellow, green and blue.

eukaryotes, are missing (*45*). Given the high degree of conservation of Ω-loop D in Cyt*c* (13 of 16 residues are conserved from yeast to mammals, (*3, 38*)), studies on the dynamics of this loop in iso-1-Cyt*c* provide a relevant model for heme crevice dynamics as it relates to peroxidase activity early in apoptosis, prior to release of cytochrome *c* from the mitochondria.

An increase in pH triggers ionization events leading to replacement of the native state Met80-heme ligand by either Lys73 or Lys79 in the alkaline conformational transition (*9, 10*). The alkaline conformational transition of wild-type iso-1-Cyt*c* expressed from yeast (yWT) is a monophasic conformational transition with either Lys73 or Lys79 replacing Met80 with similar, but not identical, kinetics and thermodynamics (*9, 46*). Variants with a Lys73 to histidine mutation exhibit a biphasic alkaline transition where His73-heme ligation occurs near neutral pH, followed by Lys79-heme ligation above pH 8 (*14, 15, 17, 47*). Not only does incorporating His into Ω-loop D enable the distinction between residues replacing Met80, but additionally the shift in the apparent pK_a, pK_{app}, of the alkaline transition allows the conformational change to be monitored more effectively because it can be done near neutral pH (*16, 47*). Thus, characterization of the dynamics of His-heme conformers allows for thorough investigation of the effect of point mutations on Cyt*c* dynamics as it relates to function.

In yWT iso-1-Cyt*c*, the lysine at residue 72 undergoes posttranslational modification to trimethyllysine (tmK). During expression from *Escherichia coli* Lys72 is not trimethylated. Lack of trimethylation allows Lys72 to become a heme ligand in the alkaline conformational transition (*48*). In order to prevent Lys72-heme ligation during the alkaline conformational transition, residue 72 can be mutated to alanine (*48*). Analysis of the native conformer of yeast iso-1-Cyt*c* (pdb code: 2YCC), shows that loss of a lysine residue at position 72 also results in a loss of contacts between residue 72 and residues Thr78, Met80 and Ala81 on the opposite side of

Ω-loop D (Figure 2.1) (*7*). We have recently reported the crystal structure of tmK72A iso-1-Cyt*c*, which indicates that reducing the steric size of the residue at position 72 favors formation of an alternate conformer with hydroxide replacing Met80 as the heme ligand near pH 9 (*49*). Also, we have previously reported increased heme crevice dynamics for the His79-heme alkaline conformational transition for a K79H variant with a tmK72A mutation compared to yWT/K79H iso-1-Cyt*c* which contains tmK72 (*18, 19*). For horse Cyt*c*, spin-labeling of Lys72 demonstrates that this residue is relatively immobile suggesting that the residue at this position may be important for modulating the dynamics of Ω-loop D in Cyt*c* across a broad range of species (*50*). Furthermore, the tmK72A mutation leads to enhanced peroxidase activity for iso-1-Cyt*c* (*49*). Thus, the residue at position 72 may modulate the dynamics of Ω-loop D necessary for peroxidase activity.

Both residues 73 and 79 belong to Ω-loop D, which is the second least stable of five cooperative substructures (see Figure 2.1), which have been identified in Cyt*c* using native state H/D exchange methods (*42-44*). Although both residues 73 and 79 belong to the same cooperative substructure of Cyt*c*, it is unclear whether dynamics mediated by deformation of a cooperative substructure from two different points in the substructure will be affected in the same way by a point mutation. Greater understanding of the dynamics of cooperative substructures is important for understanding how tier 0 dynamics affect protein function, in general. In the case of Cyt*c*, the effect of the tmK72A mutation on Ω-loop D mediated from position 73 versus 79 could provide greater insight into the nature of the dynamics required for peroxidase function at the onset of apoptosis. Previous work has shown that the mechanisms of the His79-mediated alkaline transition and the His73-mediated alkaline transition differ (*14-21*). Additionally, denaturant *m*-values, which correlate to the surface area exposed by partial or full

unfolding of a protein (*44, 51, 52*), are smaller for formation of the His79-heme alkaline conformer than for the His73-heme alkaline conformer indicating less structural rearrangement during formation of the His79-heme conformer than for the His73-heme conformer (*16, 17, 47, 53*). Similarly, the enthalpies of the alkaline transition mediated by Lys73 versus Lys79, also differ significantly (*9*). These differences between both the kinetic and thermodynamic properties of alkaline transitions of Cyt*c* mediated by two different sequence positions along the Ω-loop D substructure, suggest that the effects of the tmK72A mutation on the dynamics of a K73H variant of iso-1-Cyt*c* could differ from those of a K79H variant.

In order to investigate the effect of the tmK72A mutation on the dynamics of the His73-mediated versus His79-mediated alkaline transition, we have characterized the thermodynamic and kinetic properties of the His73-mediated alkaline conformational of tmK72A/K73H iso-1-Cyt*c* allowing comparison with previous work on K73H variants of iso-1-Cyt*c*. The data show that the His73-mediated alkaline transition is less favorable in the presence of the tmK72A mutation and that the dynamics of return to the native state from the His73-heme alkaline conformer are increased. This result contrasts markedly with the increase in stability of the His79-heme alkaline conformer relative to the native state of iso-1-Cyt*c* and the increase in the dynamics of formation of the His79-heme alkaline conformer upon introduction of the tmK72A mutation (*18, 19*).

2.2 Experimental Procedures

2.2.1 Preparation of iso-1-Cyt*c* variants.

Two variants of iso-1-Cyt*c* were used in this work: WT*, which contains C102S and K72A mutations and WT*/K73H, which adds the K73H mutation to the WT* background. The C102S mutation prevents disulfide dimerization during physical studies. The K72A mutation is

commonly used in *Escherichia coli*-expressed iso-1-Cyt*c* to prevent Lys72, which is trimethylated in its native host, *Saccharomyces cerevisiae*, from acting as an alkaline state ligand (*48*). Both proteins were expressed from the pRbs_BTR1 vector (*54*), which is a derivative of the pBTR1 vector (*48, 55*) with an optimized ribosomal binding site (*56*). This vector co-expresses the iso-1-Cyt*c* (*CYC1*) and the heme lyase (*CYC3*) genes from *S. cerevisiae*, so that heme insertion occurs efficiently in the cytoplasm of *E. coli*. The pRbs_BTR1 vector was originally prepared carrying the TM variant (H26N, H33N, H39Q, C102S) of iso-1-Cyt*c* (*54*). Conversion to the WT* variant was accomplished in four steps. A K72A mutation was first introduced into this vector using the unique restriction site elimination method (*57*) with single-stranded pRbs_BTR1 DNA as template. The K72A oligonucleotide and the selection primer $EcoRV^{-}AatII^{+}$ (see Table A1, eliminates a unique EcoRV site and creates a unique AatII site in pRbs_BTR1) were used to introduce the K72A mutation. The remaining mutations were introduced using double-stranded pRbs_ BTR1 DNA as template and the PCR-based QuikChange protocol (Agilent Technologies). The wild type histidines of iso-1-Cyt*c* were re-introduced into the *CYC1* gene in the order His26, His39 and His33 using the primer pairs, N26H and N26H-r, Q39H and Q39H-r, and N33H and N33H-r (Table A1), respectively. The pRbs_BTR1 vector containing the WT* variant was used as the template to prepare the WT*/K73H variant with the QuikChange protocol and the primer pair K73H and K73H-r (Table A1). Each mutation to the *CYC1* gene was confirmed using dideoxy sequencing of the entire coding region of the gene. All sequencing was carried out at the Murdock DNA Sequencing Facility at the University of Montana.

2.2.2 Protein expression and purification.

Protein was expressed in BL21(DE3) *E. coli* cells from the pRbs_BTR1 vector carrying either WT* or WT*/K73H iso-1-Cyt*c*, as described previously (*18, 54*). Protein was purified as previously reported (*18, 58, 59*). Briefly, after breaking the cells with a French Pressure Cell (SLM Aminco), the lysate was cleared by centrifugation. Contaminants were precipitated by adjusting the lysate to 50% ammonium sulfate. After centrifugation, the supernatant was dialyzed against 12.5 mM sodium phosphate buffer, pH 7.2, 1 mM EDTA, 2 mM β-mercaptoethanol (β-ME). Iso-1-Cyt*c* was batch absorbed to CM-Sepharose Fast Flow resin equilibrated with 50 mM sodium phosphate buffer, pH 7.2, 1 mM EDTA and 2 mM β-ME, then protein was eluted with a linear gradient of 0-0.8 M NaCl in 50 mM sodium phosphate buffer, pH 7.2, 1 mM EDTA and 2 mM β-ME. Aliquots of about 2 mg/mL protein were flash frozen in liquid nitrogen and stored at -80 °C. Thawed aliquots were purified by cation-exchange HPLC using an Agilent Technologies 1200 series HPLC with a BioRad UNO S6 Column (catalog no. 720-0023). After collection of the iso-1-Cyt*c* peak, samples were concentrated by ultrafiltration before oxidation with $K_3[Fe(CN)_6]$. A G25 Sephadex column was used to separate the oxidized protein from the oxidizing agent.

The molecular weight of the WT* and WT*/K73H variants were measured to be 12,592.9 ± 0.1 g/mol (expected, 12,595.1 g/mol) and 12,603.3 ± 0.7 g/mol (expected, 12,604.1 g/mol) using a Bruker microflex MALDI-ToF mass spectrometer. Protein Calibration Standard I (Bruker Part No. 206355) was used to calibrate the mass spectrometer with an enhanced cubic calibration routine.

2.2.3 Global stability measurements by guanidine hydrochloride denaturation.

Stability measurements by guanidine hydrochloride (GdnHCl) denaturation at 25 °C and pH 7.5 in 20 mM Tris and 40 mM NaCl buffer were monitored, as previously described (*17*), using an Applied Photophysics Chirascan circular dichroism (CD) spectrometer coupled to a Hamilton MICROLAB 500 Titrator. The free energy of unfolding in the absence of denaturant, $\Delta G_u°'(H_2O)$, and the *m*-value were extracted from nonlinear least squares fits (SigmaPlot v. 7.0) of the data employing a two-state model assuming a linear free energy relationship (*60*), as previously described (*26*). In these fits, the native state baseline was assumed to be independent of GdnHCl concentration (*26*). Parameters are the average and standard deviation of a minimum of three independent trials.

2.2.4 pH titrations to measure the alkaline conformational transition of iso-1-Cyt*c* variants.

pH titrations were carried out at 22 ± 1 °C to monitor the alkaline conformational transition of each variant. Titrations were followed at 695 nm, as previously reported (*61*), in 100 mM NaCl using a Beckman Coulter DU 800 UV/Vis spectrophotometer. 600 µL of a 2x stock solution containing 400 µM oxidized protein in 200 mM NaCl was prepared. 400 µL of the 2x stock solution was combined with 400 µL of MilliQ water and the solution was mixed with a 1000 µL pipetman. pH was adjusted by adding equal volumes of the 2x stock solution and either NaOH or HCl solutions of appropriate concentration and measured with a Denver Instrument UB-10 pH/mV meter using an Accumet semimicro calomel pH probe (Fischer Scientific Cat. No. 13-620-293). Baseline corrections were made by subtracting the absorbance at 750 nm, A_{750}, from the absorbance at 695 nm, A_{695}, yielding $A_{695corr}$. Corrected molar extinction coefficients, $\varepsilon_{695corr}$, were then calculated from $A_{695corr}$ using concentration evaluated from

absorbance at 570 nm and 580 nm near pH 5 (*16*) and the known molar extinction coefficients for these wavelengths (*62*).

The monophasic $\varepsilon_{695corr}$ versus pH data from the WT* iso-1-Cyt*c* variant were fit to Eq. 2.1,

(2.1)

$$\varepsilon_{695\mathrm{corr}} = \frac{\varepsilon_{\mathrm{N}} + \varepsilon_{\mathrm{alk}} * 10^{n[pK_{\mathrm{app}} - \mathrm{pH}]}}{1 + 10^{n[pK_{\mathrm{app}} - \mathrm{pH}]}}$$

using nonlinear least squares methods (SigmaPlot v. 7.0). Eq. 2.1 is a modified form of the Henderson-Hasselbalch equation, which allows the numbers of protons, *n*, linked to the conformational change to be evaluated from the fit (*47*). In Eq. 2.1, ε_N is the corrected extinction coefficient of the native state Met80-heme conformer at 695 nm, ε_{alk} is the corrected extinction coefficient of either the Lys73- or Lys79-heme bound alkaline state conformer at 695 nm, and pK_{app} is the apparent acid dissociation constant for the alkaline conformational transition.

The biphasic $\varepsilon_{695corr}$ versus pH data from the WT*/K73H variant were fit to a model (Eq. 2.2) which includes the ionization triggers for formation of both the His73-heme and Lys79-heme

(2.2)

$$\varepsilon_{695\mathrm{corr}} = \frac{\left\{\varepsilon_{\mathrm{N}} + \varepsilon_{\mathrm{alk}} * \left(\frac{10^{[-\mathrm{p}K_{\mathrm{C1}}(\mathrm{His})]}}{1 + 10^{[\mathrm{p}K_{\mathrm{a}}(\mathrm{His}) - \mathrm{pH}]}} + \frac{10^{[-\mathrm{p}K_{\mathrm{C2}}(\mathrm{Lys})]}}{1 + 10^{[\mathrm{p}K_{a}(\mathrm{Lys}) - \mathrm{pH}]}}\right)\right\}}{\left\{1 + \left(\frac{10^{[-\mathrm{p}K_{\mathrm{C1}}(\mathrm{His})]}}{1 + 10^{[\mathrm{p}K_{\mathrm{a}}(\mathrm{His}) - \mathrm{pH}]}} + \frac{10^{[-\mathrm{p}K_{\mathrm{C2}}(\mathrm{Lys})]}}{1 + 10^{[\mathrm{pK_{a}}(\mathrm{Lys}) - \mathrm{pH}]}}\right)\right\}}$$

conformers (*47*). In Eq. 2.2, pK_a(His) and pK_a(Lys) are the acid dissociation constants for the ionizing trigger groups corresponding to population of the His73-heme and Lys79-heme conformers, respectively. pK_{C1}(His) and pK_{C2}(Lys) are the equilibrium constants corresponding to replacement of the Met80-heme ligand by the fully deprotonated His73 and Lys79 ligands, respectively. pK_a(Lys) was set to 10.8 as previously determined for the conformational change

to the Lys79-heme alkaline state conformer (*9*). Reported parameters from fits to Eqs. 2.1 and 2.2 are the average and standard deviation of a minimum of three independent trials.

2.2.5 pH jump stopped-flow kinetic experiments.

All stopped-flow mixing experiments were carried out at 25 °C using an Applied Photophysics SX20 stopped-flow spectrometer, as previously reported (*16*). Both long (50 – 350 s) and short (1 s) time scale data acquisitions were monitored at 406 nm, collecting 5000 points logarithmically for each. Upward pH jump mixing experiments began with 20 μM protein in 0.1 M NaCl at pH 5 followed by 1:1 mixing with 20 mM buffer in 0.1 M NaCl to achieve the desired pH. Upward pH jump experiments were carried out in steps of 0.25 pH units over the pH range of 6 – 10 for WT*/K73H. Downward pH jump experiments were executed in the same way but began at pH 8.05 and ended at pH values ranging from 5.0 – 6.5 in steps of 0.25 pH units. Buffers used were as follows: acetic acid (pH 5-5.25), MES (pH 5.5-6.5), NaH_2PO_4 (pH 6.75-7.5), Tris (pH 7.75-8.75), and H_3BO_3 (pH 9-10). In all cases the effluent was collected and the actual pH after mixing was determined with a Denver Instrument UB-10 pH/mV meter using an Accumet semimicro calomel pH probe. A minimum of 5 and 8 trials were collected for long and short time scale data acquisitions, respectively, for each pH jump experiment.

2.2.6 Heme reduction by hexaammineruthenium(II) chloride followed by stopped-flow.

Conformationally-gated electron transfer (gated ET) experiments were performed by following reduction of oxidized WT*/K73H Cyt*c* at 550 nm, a wavelength that is very sensitive to the redox state of Cyt*c*, with an Applied Photophysics SX20 stopped-flow spectrometer using previously established methods (*14, 16, 20, 63*). The reducing reagent, hexaammineruthenium(II) chloride (a_6Ru^{2+}), was prepared by reduction of hexaammineruthenium(III) chloride (Strem Chemicals) with zinc (*64*). IR spectra confirmed

formation of a_6Ru^{2+} (*65*) and the product was stored under argon at -20 °C. Immediately before use, a_6Ru^{2+} was dissolved under an argon atmosphere in argon-purged 100 mM NaCl and 10 mM buffer: acetic acid (pH 5), MES (pH 6), NaH_2PO_4 (pH 7), Tris (pH 8), and H_3BO_3 (pH 9). The concentration of a_6Ru^{2+} was determined spectrophotometrically using a Beckman Coulter DU 800 UV/Vis Spectrophotometer with extinction coefficients at 390 nm of 35 $M^{-1}cm^{-1}$ (*66*) and at 400 nm of 30 $M^{-1}cm^{-1}$ (*67*). Absorbance at 550 nm was used to correct for variation in background absorbance. The concentration of a_6Ru^{2+} was evaluated immediately prior to and following stopped-flow mixing. The average and standard deviation of these two measurements is reported as the a_6Ru^{2+} concentration. At the lowest a_6Ru^{2+} concentration, absorbance at 275 nm was also used to evaluate concentration using ε_{275} of 632 $M^{-1}cm^{-1}$, which is the average of the reported extinction coefficients of 624 $M^{-1}cm^{-1}$ (*67*) and 640 $M^{-1}cm^{-1}$ (*66*). Iso-1-Cyt*c* solutions were also prepared in argon-purged buffers. Gas tight syringes were used to transfer iso-1-Cyt*c* and a_6Ru^{2+} solutions to the stopped-flow and UV-Vis instruments. Argon-purged 10 mM buffer in 100 mM NaCl was used to flush the stopped-flow unit prior to use. Heme reduction was followed at 25 °C via 1:1 stopped-flow mixing. Final protein concentration after mixing was 5 μM and a_6Ru^{2+} concentrations were approximately 0.6, 1.25, 2.5, 5, and 10 mM.

Kinetic traces were collected logarithmically with 5000 data points for time periods of 1 to 300 seconds. Data were fit to the appropriate exponential equation using SigmaPlot (version 7.0). For pH 7 and above, a quadruple exponential function was used to fit the data as two slow phases are present under these conditions. Below pH 7, these slow phases are absent and the data are best fit to a two exponential function. To accurately capture the slow phases, data were collected on a 150 to 300 second timescale for pH 7, 8 and 9. As the slower phases were absent

at pH 5 and 6, long timescale runs were not necessary and data were collected on a 1 to 5 second time scale.

At pH 6-9, one second data sets were also collected using drive pressure holds to reduce recoil noise from the drive syringe, which otherwise can cause artifacts on a timescale similar to the two faster phases. To help constrain the upper baseline of the pH 7 to 9 short timescale data sets, the data were fit to a triple exponential equation and the slow phase rate constant was set equal to $k_{obs,4}$ from the longer timescale fits. $k_{obs,4}$ was used over $k_{obs,3}$ because the associated amplitude was much larger for $k_{obs,4}$ than for $k_{obs,3}$. Typically, 5 and 8 trials were collected for long and short time scale data acquisitions, respectively, for each gated ET experiment.

2.3Results

2.3.1 Global stability of *E. coli*-expressed iso-1-Cyt*c* variants.

The global stabilities of the WT* and WT*/K73H iso-1-Cyt*c* variants were determined by GdnHCl denaturation at 25 °C monitored by CD spectroscopy. Denaturation curves of WT* and

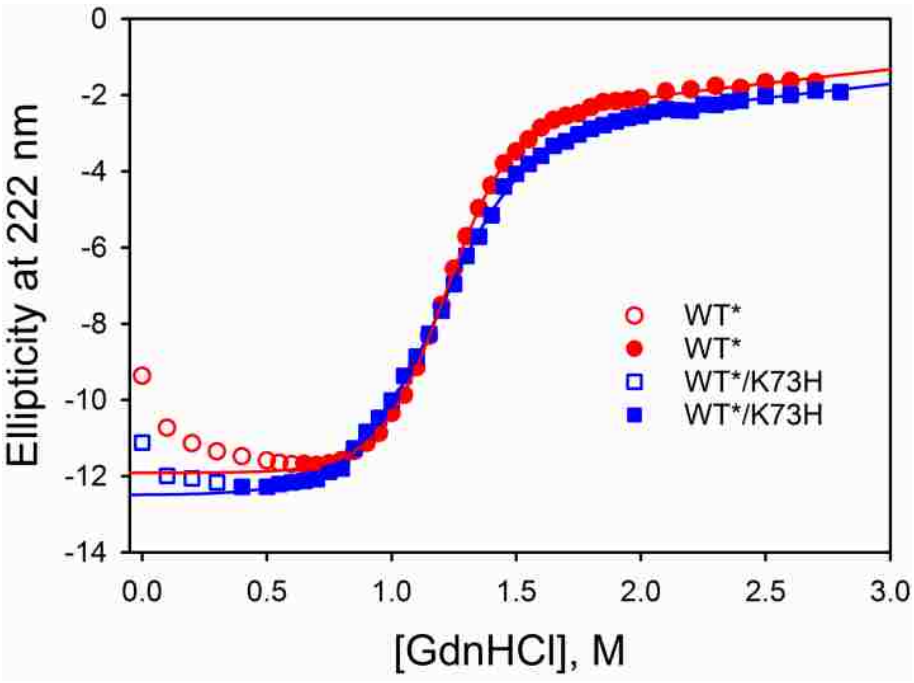

Figure 2.2. GdnHCl denaturation curves for WT* (red circles) and WT*/K73H (blue squares) iso-1-Cyt*c*. Unfolding was monitored at 222 nm as GdnHCl was titrated into iso-1-Cyt*c* buffered with 40 mM NaCl, 20 mM Tris buffer, pH 7.5 at 25 °C. Data in open symbols were not included in the fit to a two-state model (solid curves), described in the Experimental Procedures.

WT*/K73H variants in Figure 2.2 show that the midpoint GdnHCl concentration for unfolding, C_m, is similar for both variants. The unfolding transition of WT*/K73H is also broader than that of WT* (Figure 2.2). The K73H mutation causes a decrease of about 1 kcal mol^{-1} M^{-1} in the *m*-value (rate of change of ΔG_u with respect to GdnHCl concentration), as seen in Table 2.1. Previously we have demonstrated that GdnHCl unfolding of K73H variants progresses from a partially unfolded His73-heme conformer at pH 7.5, which is responsible for the decreased *m*-value (*17, 47, 53*). In the case of WT*/K73H, the free energy of unfolding in the absence of denaturant, $\Delta G_u°´(H_2O)$, is about 25% lower than that of WT* iso-1-Cyt*c* (Table 2.1). Comparison with the yeast expressed variants, yWT and yWT/K73H, show that the effect of the tmK72A mutation on global stability is modest (*53, 68*) (Table 2.1).

Table 2.1. Thermodynamic parameters for iso-1-Cyt*c* variants obtained by GdnHCl denaturation monitored by CD at 25 °C and pH 7.5.[a]

Variant	$\Delta G_u^{o'}(H_2O)$ (kcal mol^{-1})	*m*-value (kcal mol^{-1}M^{-1})	C_m (M)
WT*	5.31 ± 0.08	4.39 ± 0.09	1.21 ± 0.01
yWT[b]	5.77 ± 0.40	5.11 ± 0.36	1.13 ± 0.02
WT*/K73H	4.09 ± 0.11	3.49 ± 0.12	1.17 ± 0.01
yWT/K73H[c]	4.32 ± 0.12	3.59 ± 0.01	1.20 ± 0.03

[a] Parameters are the average and standard deviation of a minimum of three trials. [b] Parameters are from ref. (*68*). [c]Parameters are from ref. (*53*).

2.3.2 Alkaline conformational transition of WT* and WT*/K73H variants of iso-1-Cyt*c*.

Local unfolding of iso-1-Cyt*c* variants at alkaline pH was monitored at 695 nm, an absorbance band which reports on the presence of the native Met80-heme ligand (*3*, *69*, *70*). WT* iso-1-Cyt*c* has a monophasic alkaline conformational transition (Figure 2.3). The pK_{app} for WT* was found to be 8.66 ± 0.01, comparable to the value previously reported for yWT of 8.6 ± 0.1 with either a C102T or a C102S mutation (*9*, *47*). The number of protons, *n*, involved in the conformational change, as determined from a fit of the data to Eq. 2.1 (Experimental Procedures), is near 1 (1.15 ± 0.02) for WT* iso-1-Cyt*c*, as expected.

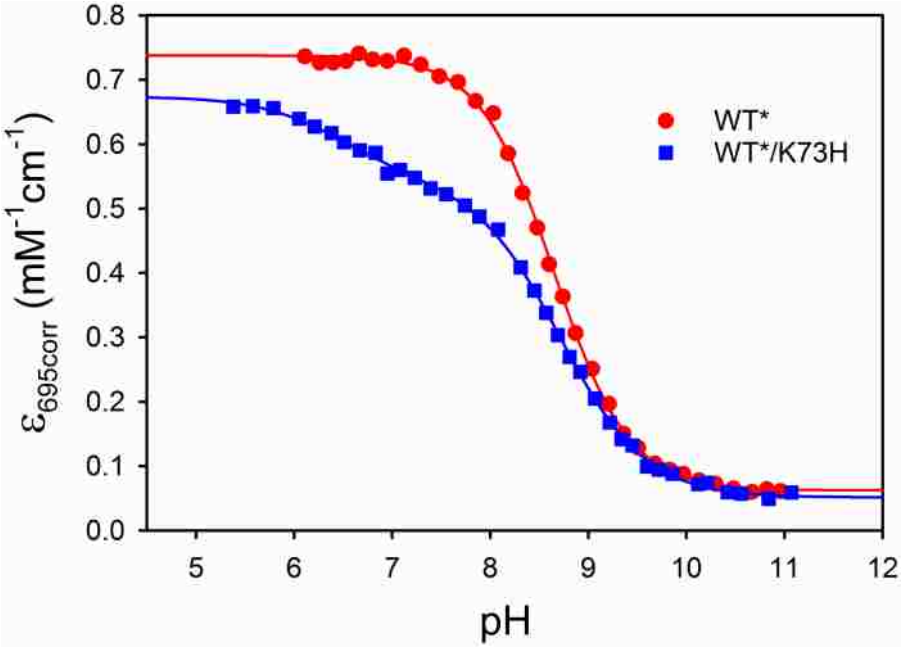

Figure 2.3. $\varepsilon_{695corr}$ vs pH data for WT* (red circles) and WT*/K73H (blue squares) iso-1-Cyt*c*, which monitor the alkaline conformational transition of iso-1-Cyt*c*. WT* iso-1-Cyt*c* displays a monophasic transition (solid red curve is a fit to Eq. 2.1 in Experimental Procedures) and WT*/K73H shows a biphasic transition (solid blue curve is a fit to Eq. 2.2 in Experimental Procedures). Data were acquired in 100 mM NaCl at 22 ± 1 °C.

WT*/K73H iso-1-Cyt*c* has a biphasic alkaline conformational transition (Figure 2.3). Between pH 6 and 8 a His73-heme ligated conformer populates followed by a Lys79-heme ligated state between pH 8 and 10. Thus, the K73H mutation allows the conformational changes mediated by the residues at positions 73 and 79 to be distinguished readily. WT*/K73H pH titration data were fit using Eq. 2.2 (Experimental Procedures). Within error, the pK_a(His) values, which are consistent with the ionization of His73, are similar for both WT*/K73H and yWT/K73H (see Table 2.2). The conformational equilibrium constant for the alkaline conformational transition mediated by His73, pK_{C1}(His), is more positive for WT*/K73H than for yWT/K73H (*47*), indicating that the alkaline conformer is less favored when tmK72 is replaced by Ala (Table 2.2).

Table 2.2. Thermodynamic parameters for the alkaline transition of iso-1-Cyt*c* variants obtained by pH titrations at 695 nm.[a]

Variant	pK_{C1}(His)	pK_{C2}(Lys)	pK_a(His)
WT*/K73H	0.67 ± 0.05	-2.04 ± 0.13	6.72 ± 0.10
yWT/K73H[b]	0.28 ± 0.01	-2.18 ± 0.11	6.60 ± 0.06
WT*/K79H[c]	-1.04 ± 0.04	-2.8 ± 0.2	6.35 ± 0.04
	(-1.06 ± 0.05)[d]		
yWT/K79H[e]	-0.99 ± 0.07	-3.25 ± 0.24	6.62 ± 0.08
	(-0.91 ± 0.03)[d]		

[a] Parameters are the average and standard deviation of a minimum of three trials. [b] Parameters are from ref. (*47*). [c]Parameters are from ref. (*19*). To fit equilibrium pH titration data more reliably, amplitude data from gated ET experiments were used to estimate the extinction coefficient of the native conformer . [d]Amplitude data from gated ET experiments at pH 7.5 were used to estimate pK_{C1}(His) (*19*). [e]The extinction coefficient at 695 nm for fully native yWT/K79H was estimated using amplitudes from gated ET data reported in ref. (*19*) for yWT/K79H and used to refit equilibrium pH titration data for the yWT/K79H variant from ref. (*16*)

2.3.3 Dynamics of the His73-mediated alkaline transition by pH jump methods**.**

In order to elucidate the kinetics of the alkaline transition of the WT*/K73H iso-1-Cyt*c* variant, stopped-flow pH jump methods were employed. Both upward and downward pH jumps were monitored at 406 nm to follow heme-ligand changes produced from Ω-loop D rearrangement. The kinetic data are consistent with three kinetic phases below pH 8 (Tables A2-A6 and Figure 2.4). Above approximately pH 8, a fourth kinetic phase becomes evident (Table A3 and Figure 2.4).

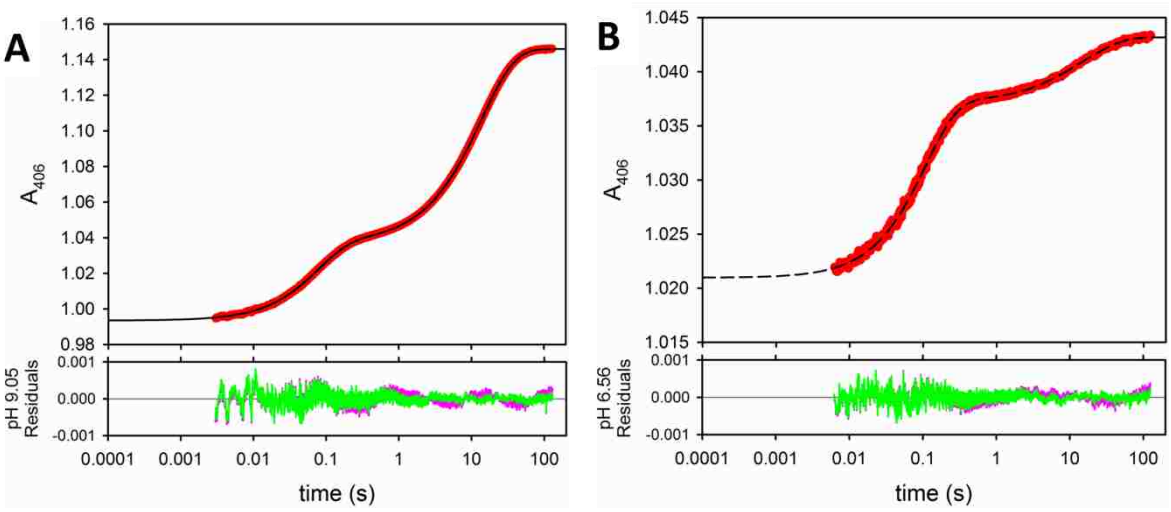

Figure 2.4. Representative fits to raw data from upward pH jump experiments at a low pH where only three phases are present as well as at higher pH where four phases are present. (A) Upward pH jump data at pH 9.05 data (red circles) shows a fit to a quadruple exponential curve (solid black line). Residuals below the graph are for a fit to triple (pink) and quadruple (green) exponential equations, demonstrating less deviation from zero for the quadruple exponential fit. (B) Upward pH jump data at pH 6.56 (red circles) showing a fit to a triple exponential equation (dashed curve). Residuals below the graph are for a fit to a double (pink) versus a triple (green) exponential equation, demonstrating less deviation from zero for the triple exponential fit.

The fast kinetic phase (Figure 2.4, observed rate constant, $k_{obs,1}$) occurs on a 100 millisecond timescale. The amplitude of the fast phase increases from pH 6 to pH 8, as expected for the His73-heme alkaline conformer based on thermodynamic data, which shows (see Figure 2.3) that equilibrium population of the His73-heme alkaline conformer occurs over this pH range. We also see an increase in amplitude from pH 9 to pH 10 (Table A2).

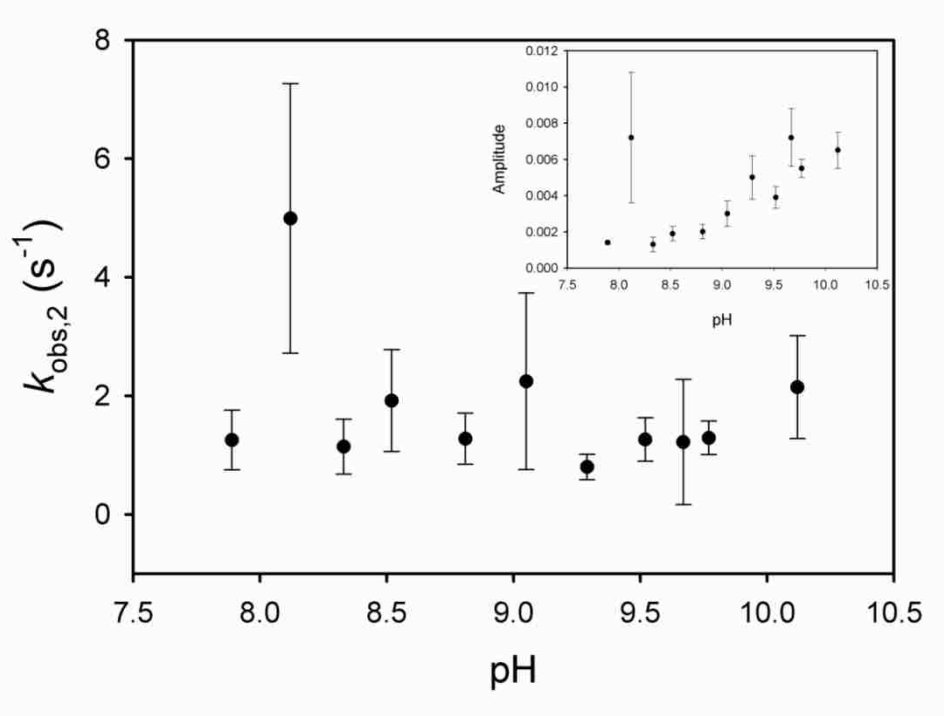

Figure 2.5. Plot of $k_{obs,2}$ vs pH, the intermediate phase, of the alkaline conformational transition of WT*/K73H iso-1-Cyt*c*. Solid circles represent data from upward pH jumps experiments. The inset is a plot of the corresponding amplitudes vs pH using the same symbols as for $k_{obs,2}$ data. Data were collected at 25 °C in 10 mM buffer, 0.1 M NaCl.

Near pH 8 and above, an intermediate 1 s time scale phase is observed (Figure 2.5, observed rate constant, $k_{obs,2}$). Within error, $k_{obs,2}$ is invariant with pH. Although the amplitude is low, an increase in amplitude between pH 8 and 10 is evident. A similar low amplitude intermediate phase from stopped-flow pH jump experiments that only populates above pH 7.3 has previously been reported for a K79H variant carrying the tmK72A mutation (*18*). Stopped-flow conformationally-gated electron transfer (gated ET) experiments on two iso-1-Cyt*c* variants expressed from yeast (i.e., tmK72), AcH73 (this variant has H26N, H33N and H39Q and K73H mutations as well as two mutations near the N-terminus which lead to N-terminal acetylation in vivo (*14*)) and K73H/K79A (*20*), exhibit the presence of an intermediate phase from pH 5 to 9 with low amplitude and observed rate constants of a comparable magnitude to values reported

here for $k_{obs,2}$. This phase has previously been attributed to a conformational change involving an acid state below pH 7, or a high-spin species above pH 7 (*14, 18, 20*).

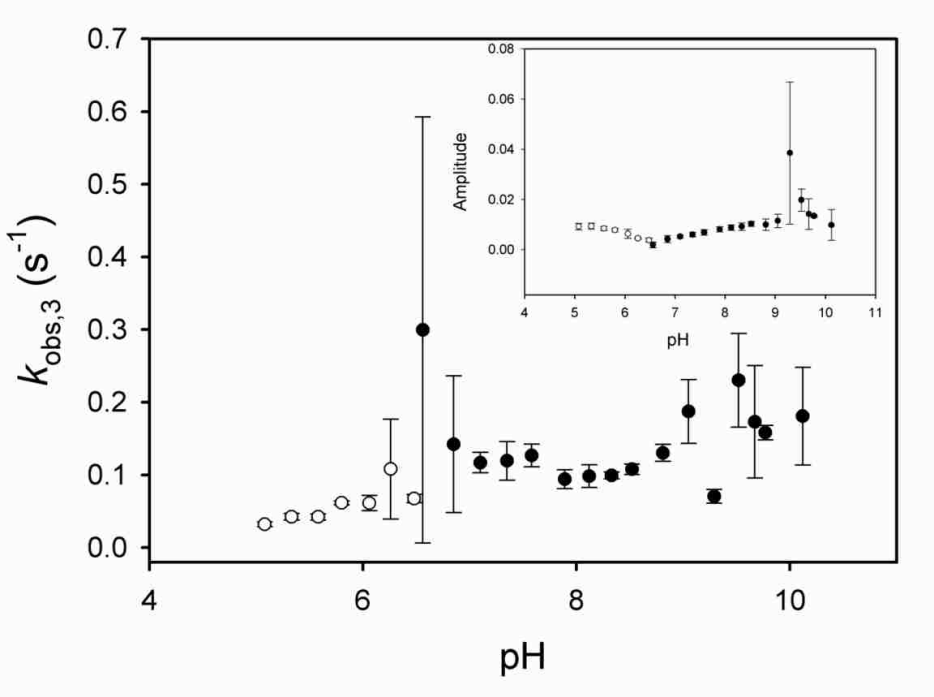

Figure 2.6. Plot of $k_{obs,3}$ vs pH, a slow phase, of the alkaline conformational transition of WT*/K73H iso-1-Cyt*c*. Solid and open circles represent data from upward and downward pH jump experiments, respectively. The inset is a plot of the corresponding amplitude vs pH using the same symbols as for $k_{obs,3}$ data. Data were collected at 25 ^{o}C in 10 mM buffer, 0.1 M NaCl.

Two slow phases, on a 10 – 100 s timescale are observed. Based on previous work on K73H variants of iso-1-Cyt*c*, these phases likely correspond to formation of a Lys79-heme ligated conformer as well as isomerization of proline in the His73-heme alkaline conformer (*20, 21, 61*). The observed rate constant for the first slow phase, $k_{obs,3}$ (Figure 2.6), ranges from 0.1 to 0.2 s^{-1}, consistent with the rate of proline isomerization reported for yeast-expressed K73H/K79A iso-1-Cyt*c* (i.e., tmK72) in the same pH regime (*20, 61*). The amplitude of this phase shows a modest increase from pH 6 to 8, consistent with the slow phase associated with proline isomerization linked to the His73-heme alkaline transition observed with K73H/K79A iso-1-Cyt*c* (*61*).

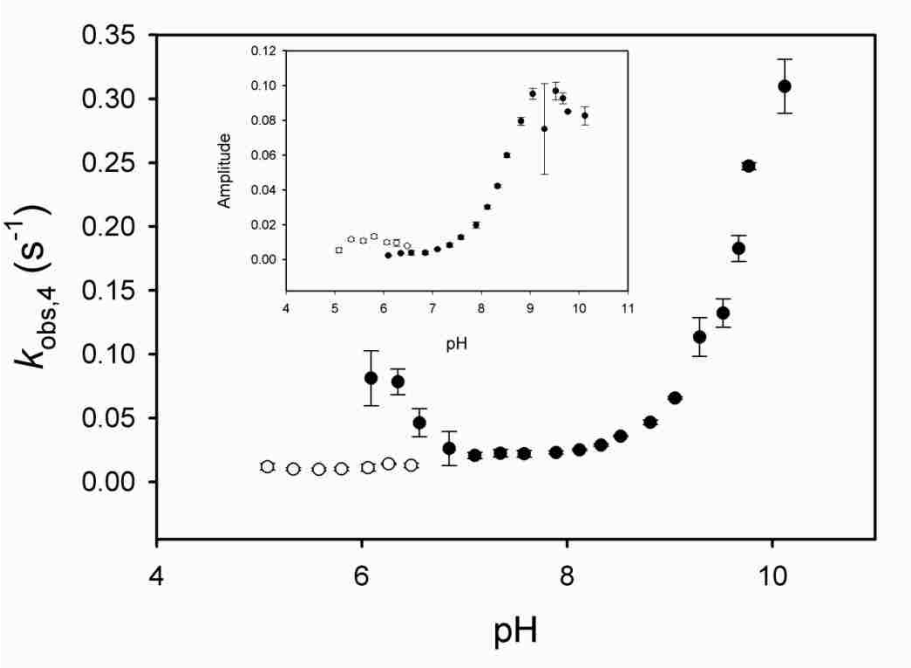

Figure 2.7. Plot of $k_{obs,4}$ vs pH, a slow phase, of the alkaline conformational transition of WT*/K73H iso-1-Cyt*c*. Solid and open circles represent data from upward and downward pH jump experiments, respectively. The inset is a plot of the corresponding amplitudes vs pH using the same symbols as for $k_{obs,4}$ data. Data were collected at 25 ^{o}C in 10 mM buffer, 0.1 M NaCl.

The slowest kinetic phase (Figure 2.7) yields an observed rate constant, $k_{obs,4}$, near 0.03 s^{-1} from pH 5 to 8. Above pH 8, $k_{obs,4}$ begins to increase. Corresponding amplitude data for this slow phase also begins to increase near pH 8. The increase in amplitude and observed rate constant for this phase is consistent with thermodynamic data which show that the Lys79-heme ligated conformer populates from pH 8 to 10 (Figure 2.3).

2.3.4 Direct measurement of microscopic rate constants for the alkaline transition by gated ET.

Gated ET methods were used to directly measure the microscopic rate constants corresponding to Ω-loop D opening and replacement of the native Met80-heme ligand with either histidine or lysine. As previously described (*14, 15, 19, 20, 36, 63, 71*), oxidized protein

with the Met80-heme ligand will undergo direct reduction by hexammineruthenium(II), a_6Ru^{2+} (Scheme 2.1), whereas the

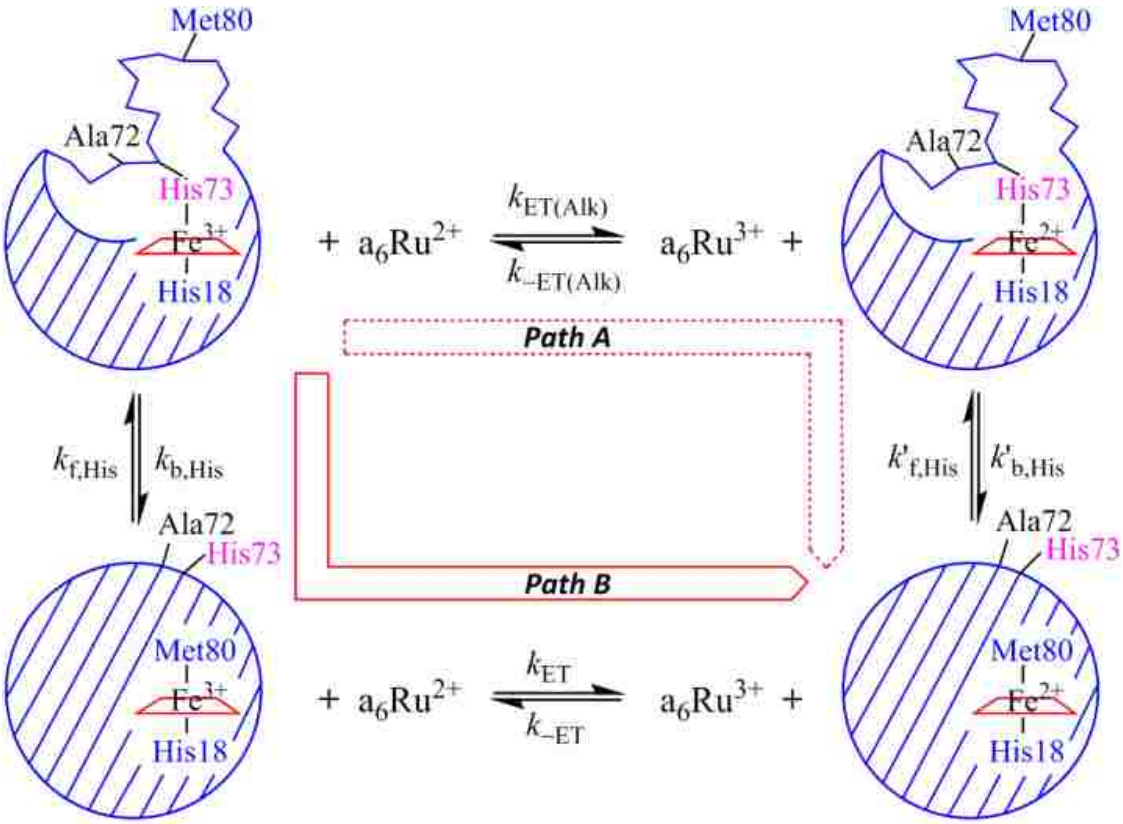

Scheme 2.1. Gated ET square scheme for the WT*/K73H iso-1-Cyt*c* variant showing paths A and B.

His73-heme alkaline conformer is unable to undergo reduction due to a lower reduction potential (*72*). Thus, a conformational change must occur to achieve the native Met80-heme ligated conformer before reduction can occur (Path B in Scheme 2.1). If the conformational change occurs on a much slower timescale than direct ET, a conformational ET gate exists.

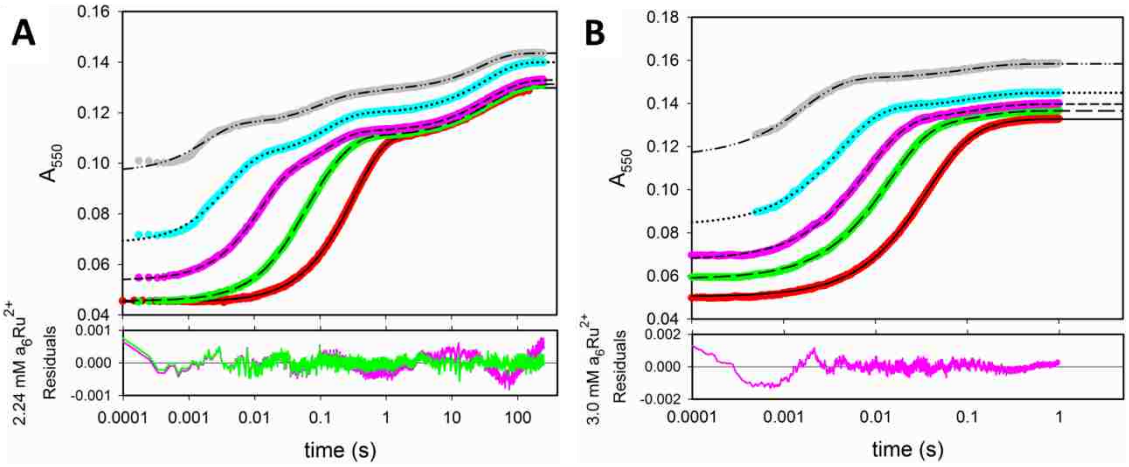

Figure 2.8. Representative data for conformationally-gated electron transfer experiments at high and low pH values. (A) Quadruple exponential fits are shown to the electron transfer data at pH 8, where both fast and slow phases are present. Hexaammineruthenium(II) chloride concentrations were as follows: 0.4 mM a_6Ru^{2+} (red circles, fit to solid line), 1.03 mM a_6Ru^{2+} (green circles, fit to long dashed line), 2.24 mM a_6Ru^{2+} (pink circles, fit to short dashed line), 5.97 mM a_6Ru^{2+} (cyan circles, fit to dotted line), 12.04 mM a_6Ru^{2+} (gray circles, fit to dash-dot-dot-dashed line). Below the graph, residuals from fits to triple (pink) and quadruple (green) exponential equations for the 2.24 mM a_6Ru^{2+} trace demonstrate the appropriateness of the quadruple exponential equation. (B) Double exponential fits are shown to the electron transfer data at pH 6 with pressure holds, where slow phases are absent in the data. Hexaammineruthenium(II) chloride concentrations were as follows: 0.74 mM a_6Ru^{2+} (red circles, fit to solid line), 1.6 mM a_6Ru^{2+} (green circles, fit to long dashed line), 3.0 mM a_6Ru^{2+} (pink circles, fit to short dashed line), 5.8 mM a_6Ru^{2+} (cyan circles, fit to dotted line), 12.8 mM a_6Ru^{2+} (gray circles, fit to dash-dot-dot-dashed line). Below the graph is the residual for a double (pink) exponential fit to the 3.0 mM a_6Ru^{2+} trace.

Short time scale data acquisitions at pH 5 and 6 were fit to a two-exponential equation (Figure 2.8). These fits are consistent with equilibrium population of both the native Met80-heme ligated conformer and the His73-heme ligated alkaline conformer at these pH values, as illustrated in Scheme 2.1. Above pH 7, a quadruple exponential equation was needed to fit the data (Figure 2.8) indicating the presence of additional conformers with alternate heme ligands at equilibrium in solution that must convert to the native Met80-heme conformer before being reduced by a_6Ru^{2+}. Amplitude and rate constant data for each phase are given in Tables A7-A10. To distinguish them from the observed rate constants from pH jump experiments, we designate

the observed rate constants from the gated ET experiments, k_{gET1}, $_{k}gET2$, k_{gET3}, and k_{gET4}, from fastest to slowest kinetic phase, and the associated amplitudes as, A_{gET1}, A_{gET2}, A_{gET3} and A_{gET4}. Amplitude data from gated ET experiments are plotted against pH in Figure 2.9. When $k_{ET}[a_6Ru^{2+}]$ is

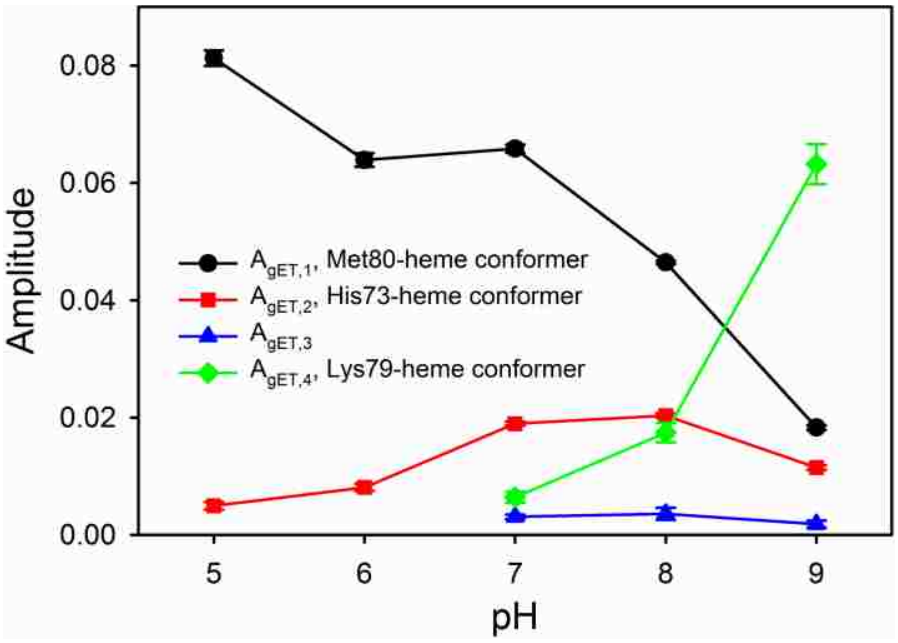

Figure 2.9. Amplitude data vs pH from gated ET experiments on WT*/K73H iso-1-Cyt*c*. Amplitude values correspond to the change in absorbance at 550 nm. Concentrations of a_6Ru^{2+} for $A_{gET,1}$ (black circles and line) and $A_{gET,2}$ (red squares and line) for pH 5, 6, 7, 8 and 9 were 2.8, 3.0, 3.7, 3.9 and 2.8 mM, respectively. $A_{gET,1}$ and $A_{gET,2}$ are both from short (1 to 5 s) data acquisitions, Concentrations of a_6Ru^{2+} for $A_{gET,3}$ (blue triangles and line) and $A_{gET,4}$ (green diamonds and line) for pH 7, 8 and 9 were 1.9, 2.24 and 1.78 mM, respectively. $A_{gET,3}$ and $A_{gET,4}$ are both from long timescale (150 to 300 s) data acquisitions. Error bars are the standard deviation of the average.

much greater than $k_{f,His73}$ (see Scheme 2.1, or $k_{f,L}$'s, rate constants for formation of conformers with other ligands, L, replacing Met80), individual amplitudes are directly proportional to the population of a given iso-1-Cyt*c* conformer present at each pH because reduction is fast compared to the rate of the conformational change that returns the alternatively ligated conformer to the native state. Values of amplitudes from reduction of WT*/K73H iso-1-Cyt*c*

with a_6Ru^{2+} concentrations between 2 and 4 mM were optimal for this purpose. At higher a_6Ru^{2+} concentration, the direct electron transfer rates are fast enough relative to the dead time of our stopped-flow instrument that the associated amplitude may be underestimated (see Figure 2.8). Conversely, at lower a_6Ru^{2+} concentrations, $k_{ET}[a_6Ru^{2+}]$ begins to approach $k_{f,His73}$, such that Met80-ligated WT*/K73H can convert to the His73-heme bound conformer before it is reduced, leading to an apparent increase in the amplitude resulting from the His73-heme alkaline conformer (see Table A8).

In Figure 2.9, $A_{gET,1}$ shows a decrease in magnitude as pH increases. $A_{gET,1}$ decreases slowly from pH 5 to 7 and then more rapidly above pH 7. This behavior mimics the loss of absorbance at 695 nm due to Fe^{3+}-Met80 ligation as pH is increased in the equilibrium pH titration data in Figure 2.3. Thus, the fastest kinetic phase is assigned to WT*/K73H in the native conformer with Met80-heme ligation. $A_{gET,2}$ initially increases as pH is increased above pH 5, maximally populates near pH 7-8, and then decreases. This behavior is consistent with the His73-heme conformer, which should increase in population as pH is increased reaching a maximum when His73 is fully deprotonated near pH 7.5. $A_{gET,3}$ remains relatively invariant from pH 7-9. There is some uncertainty regarding the species corresponding to $A_{gET,3}$, but it may correspond to iso-1-Cyt*c* with a high spin heme as has been observed with other K73H variants of iso-1-Cyt*c* (*14*, *18*, *20*). The equilibrium population of this species is clearly small (Figure 2.9), so, absorbance features near 650 nm, typical of a high spin heme, are not evident in equilibrium pH titration data (not shown). $A_{gET,4}$, grows from a minor phase at pH 7 to the largest amplitude at pH 9. The increase in $A_{gET,4}$ as $A_{gET,1}$ and $A_{gET,2}$ decrease is consistent with the behavior expected for the Lys79-heme conformer. Lys79 is expected to displace both Met80 and His73 as the heme ligand

at high pH. The pH dependence of amplitude data from gated ET experiments observed here is similar to that previously reported for AcH73 iso-1-Cyt*c* (*14*).

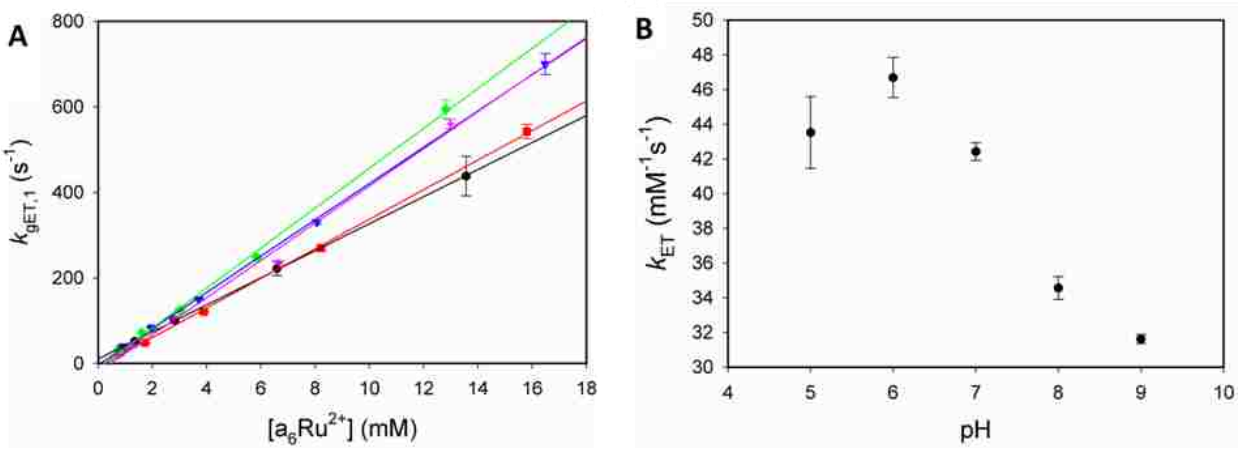

Figure 2.10. Direct ET of WT*/K73H iso-1-Cyt*c*. (A) Plots of $k_{gET,1}$ versus a_6Ru^{2+} concentration (data from Table A7) from gated ET experiments fit to Eq 2.5. Data points at each pH are represented as follows: pH 5, pink crosshairs; pH 6, green diamonds; pH 7, blue inverted triangles; pH 8, red squares; pH 9, black circles. Fits to Eq 2.5 are plotted as solid lines in the same color as the corresponding data points. (B) Plot of k_{ET} derived from fits in part A versus pH.

The magnitude of the rate constant for the fastest phase of the gated ET experiment, $k_{gET,1}$, is strongly dependent on the concentration of a_6Ru^{2+} consistent with direct ET with bimolecular rate constant, k_{ET} (Scheme 2.1), to the native state of WT*/K73H iso-1-Cyt*c* (Table A7 and Figure 2.10). The other rate constants from the gated ET experiments show little dependence on the concentration of a_6Ru^{2+} (Figure 2.11 and Tables A8 to A10). Thus, these rate constants reflect reduction of WT*/K73H iso-1-Cyt*c* gated by a conformational change.

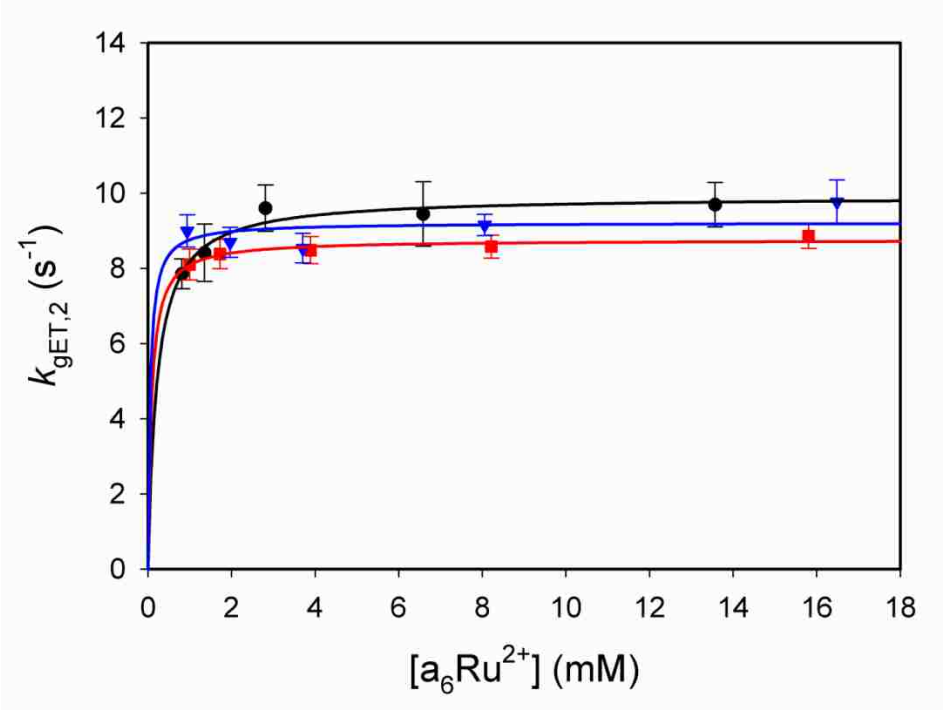

Figure 2.11. Plots of $k_{gET,2}$ versus a_6Ru^{2+} concentration for WT*/K73H iso-1-Cyt*c* from stopped-flow gated ET experiments fit to Eq. 2.6. Data points at each pH are represented as follows: pH 7, blue inverted triangles; pH 8, red squares; pH 9, black circles. Fits to Eq. 2.6 for data at pH 7, 8 and 9 are plotted with solid lines of the same color as the respective data points.

2.4Discussion

2.4.1 Effects of the tmK72A mutation on the global and local stability of yeast iso-1-Cyt*c*.

The crystal structure of yeast iso-1-Cyt*c* shows that tmK72 lies across Ω-loop D, potentially sterically hindering opening of the heme crevice (Figures 2.1 and 2.14, below). Previously, we have shown that for variants of iso-1-Cyt*c* carrying a K79H mutation, similar stability parameters are obtained from GdnHCl denaturation regardless of whether trimethyllysine or alanine is present at residue 72 (*18*). Here, within error, we also report only a modest effect of the tmK72A mutation on the stability of a K73H variant of iso-1-Cyt*c* (Table 2.1). Similarly, the tmK72A mutation does not affect the global stability of iso-1-Cyt*c* (yWT versus WT* in Table 2.1)

Global unfolding experiments were performed at pH 7.5 where WT*/K73H partially populates the His73-heme conformer as is apparent from Figures 2.3 and 2.9. The decrease in the denaturant *m*-value of WT*/K73H iso-1-Cyt*c* relative to WT* iso-1-Cyt*c* (see Table 2.1) is consistent with global unfolding monitored by CD occurring primarily from the partially unfolded His73-heme alkaline conformer as for other K73H variants of iso-1-Cyt*c* (*15, 53, 61*).

pH titration studies demonstrate that pK_{app} is similar for WT* iso-1-Cyt*c* and yWT iso-1-Cyt*c* indicating that the tmK72A mutation has little effect on the Lys-mediated alkaline conformational transition. When the K73H mutation is introduced, within error pK_{C2}(Lys), which corresponds to the Lys79-mediated alkaline transition, is also unaffected by the tmK72A mutation (Table 2.2). However, pK_{C1}(His), which corresponds to the His73-mediated alkaline transition is about twice the positive magnitude for WT*/K73H compared to yWT/K73H (Table 2.2). Thus, the tmK72A mutation destabilizes the His73-heme alkaline conformer relative to the native conformer ($\Delta\Delta G$ of 0.53 ± 0.09 kcal/mol). By contrast, data in Table 2.2 for previously reported K79H variants of iso-1-Cyt*c*, show that tmK72A mutation has little effect on the stability of the His79-heme alkaline conformer relative to the native conformer (*18*). Interestingly, the tmK72A mutation makes pK_{C2}(Lys) for the Lys73-heme alkaline conformer less favorable relative to the native conformer ($\Delta\Delta G$ of 0.45 ± 0.31 kcal/mol) for K79H variants. Thus, the tmK72A mutation appears to have less effect on the stability of alkaline conformers relative to the native state when the alkaline state ligand is from position 79, whereas it appears to destabilize the alkaline conformer relative to the native conformer by about 0.5 kcal/mol when the ligand is from position 73. Thus, the Ω-loop D substructure (red in Figure 2.1) clearly responds differently to the tmK72A mutation when deformed from position 73 versus position 79.

Histone binding proteins interact with trimethyllysine residues on histone tails using aromatic cage motifs, which are rich in aromatic residues (Tyr, Phe, Trp) and methionine (*73, 74*). Trimethyllysine binding is stabilized by π-cation interactions. In the NMR structure of the Lys73-heme alkaline conformer (*13*), Met80 and Tyr67 are proximal to the side chain of position 72 providing a potential aromatic cage-like motif to bind tmK72 that could stabilize alkaline conformers with His/Lys73-heme ligation (see Figure 2.14 below).

2.4.2 The tmK72A mutation affects the dynamics of the His73-mediated alkaline transition at both low and high pH.

Figure 2.12 compares the pH dependence of $k_{obs,1}$ from pH jump experiments for the His73-heme alkaline conformational transition of WT*/K73H to previously reported data for yWT/K73H (*21*). Below pH 6, $k_{obs,1}$ remains constant for WT*/K73H whereas it increases for yWT/K73H (*21*). Between pH 6 and 8, $k_{obs,1}$ is identical for the two variants. From pH 8 to 10, $k_{obs,1}$ initially increases more slowly with increasing pH for WT*/K73H compared to yWT/K73H. Thus, except for near neutral pH the tmK72A mutation significantly affects $k_{obs,1}$. This behavior contrasts sharply with the effect of the tmK72A mutation on the dynamics of the His79-heme alkaline transition. In this case, the change in dynamics caused by the mutation is more pronounced near neutral pH and less pronounced near pH 5 and 10 (*18, 19*). The mechanism of the alkaline transition is different when mediated by His73 than when mediated by His79. In general, three ionizable groups are required to fit kinetic data for the His73-mediated alkaline transition (*14, 20, 21, 61*), while only two are required to fit the kinetics of the His79-mediated alkaline transition (*16, 18, 19*). Thus, it is perhaps not surprising that the two alkaline transitions respond differently to the tmK72A mutation.

Normally the His73-mediated alkaline conformational transition is best fit to a model involving three ionizable groups. Since the ionizable group with a pK_a near 5.5 (pK_{H1} in ref. (*21*)) is not evident for WT*/K73H (Figure 2.12) we fit the $k_{obs,1}$ versus pH data to a model involving two ionizable groups (Scheme 2.2) (*16*, *21*).

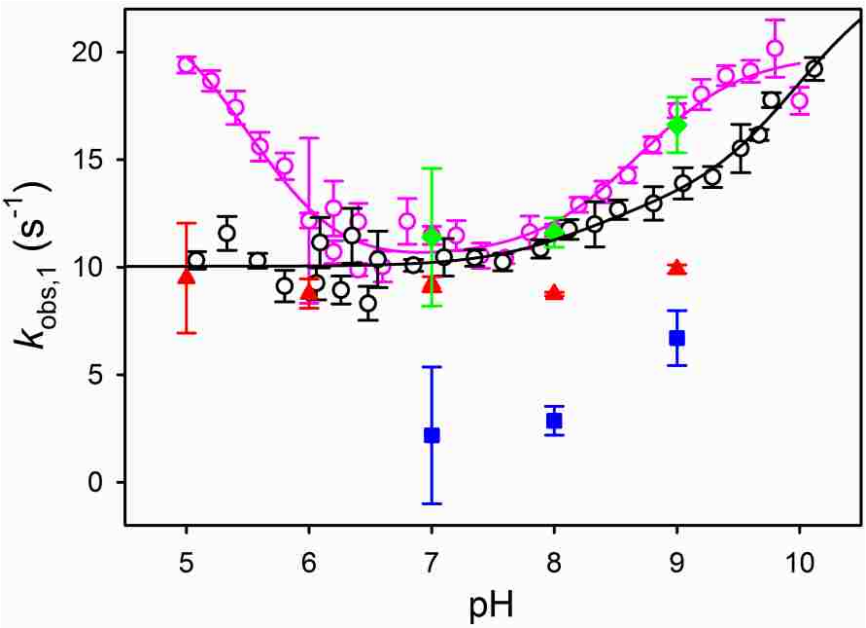

Figure 2.12. Overlay of $k_{obs,1}$ vs pH from pH jump experiments for WT*/K73H (open black circles) and yWT/K73H (open pink circles, data are from ref. (*21*)) iso-1-Cyt*c*. All data were collected at 25 °C in 10 mM buffer containing 0.1 M NaCl. The black solid line is a fit of the WT*/K73H data to Eq. 2.3 from the Discussion and the pink solid line is a fit of the yWT/K73H data to Eq. 2.5 from ref. (*21*). The microscopic rate constants, $k_{b,His}$ (red triangles) and $k_{f,His}$ (blue squares), extracted from gated ET experiments are shown for comparison. $k_{obs,1}$ (green diamonds) determined from gated ET experiments is also shown, where $k_{obs,1}$ is given by the sum of $k_{f,His}$ and $k_{b,His}$.

This model yields Eq. 2.3 for the pH dependence of $k_{obs,1}$.

(2.3)

$$k_{\mathrm{obs},1} = \left(\frac{K_{\mathrm{HL}}}{K_{\mathrm{HL}} + [\mathrm{H}^+]}\right) * \left(\frac{k_{\mathrm{f1,His}} * [\mathrm{H}^+] + k_{\mathrm{f2,His}} * K_{H2}}{K_{\mathrm{H2}} + [\mathrm{H}^+]}\right) + \left(\frac{k_{\mathrm{b1,His}} * [\mathrm{H}^+] + k_{\mathrm{b2,His}} * K_{\mathrm{H2}}}{K_{\mathrm{H2}} + [\mathrm{H}^+]}\right)$$

In Eq. 2.3, the methionine-heme to histidine-heme ligand conformational switch corresponds to forward rate constant, $k_{f1,His}$, near neutral pH and the reverse rate constant for the conformational

switch is $k_{b1,His}$. K_{HL} (or pK_{HL}) is the ionization constant for the ligand (His73 in this case) which replaces Met80. As a result of the second ionization event (K_{H2} or pK_{H2}), the rate constants change to $k_{f2,His}$ and $k_{b2,His}$. In this model, $k_{b1,His}$ is equal to $k_{obs,1}$ at low pH where the native conformer is fully populated. $k_{b2,His}$ cannot be determined directly from the $k_{obs,1}$ versus pH data. From amplitude data, we can estimate the K_{C1}(His) at pH values above pK_{H2}, $K_{C1}(His)_{Hi}$, to be 0.94 (see Chapter 2.4.3). With this value for $K_{C1}(His)_{Hi}$ as a constraint, $k_{f2,His}$ and $k_{b2,His}$ can be obtained from the fit of Eq. 2.3 to the $k_{obs,1}$ versus pH data for WT*/K73H iso-1-Cyt*c* in Figure 2.12A. The parameters from the fit of the $k_{obs,1}$ versus pH data for WT*/K73H in Figure 2.12A are summarized in Table 2.3. Compared to yWT/K73H the forward rate constant, $k_{f1,His}$, is similar but, $k_{b1,His}$ is larger for WT*/K73H, consistent with the destabilizing effect of the tmK72A mutation on the His73-heme alkaline conformer observed in our thermodynamic data (Table 2.2).

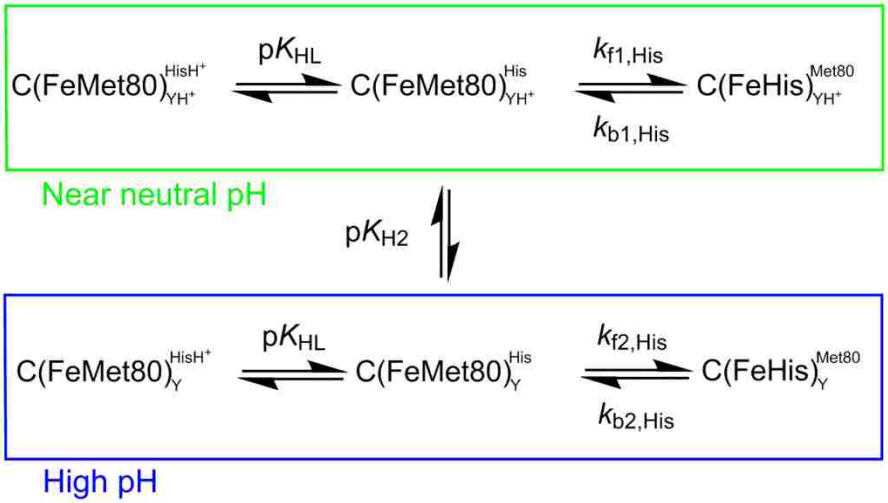

Scheme 2.2. Kinetic scheme for the His73-mediated alkaline transition involving two ionizations used for the derivation of Eqs. 3 and 4 (*16*, *21*). The YH^+/Y ionization in the scheme corresponds to pK_{H2}.

The behavior of the K73H variants is quite opposite of that of the K79H variants. $k_{b1,His}$ is unaffected by the tmK72A mutation with the K79H variants whereas $k_{f1,His}$ increases by 1.5- to

2.5-fold (*18, 19*). It is also noteworthy that following the second ionization event for K79H variants, the magnitude of $k_{obs,1}$ decreases (*16, 18, 19*), opposite of what occurs with K73H variants (*14, 20, 21, 61*).

Table 2.3. Rate and ionization constants for the His73-mediated alkaline transition of K73H variants of iso-1-Cyt*c* at 25 °C in 10 mM buffer, 0.1 M NaCl.[a]

Parameter	Variant	
	WT*/K73H	yWT/K73H[a]
$k_{f1,His}$	3 ± 2	3.5 ± 0.2
$k_{b1,His}$	10.0 ± 0.2	7.0 ± 0.4
$k_{f2,His}$	12 ± 3	6.6 ± 0.2
$k_{b2,His}$	13 ± 9	13.2 ± 0.4
pK_{HL}	8.2 ± 0.6 (6.8 ± 0.1)[b]	6.4 ± 0.5
pK_{H2}	10.0 ± 0.6 (9.9 ± 0.2)[b]	8.7 ± 0.2

[a]Parameters are from ref. (*21*). [b]Values in brackets are from fits of the two ionization mechanism to amplitude versus pH data.

The pK_{HL} from fitting the $k_{obs,1}$ versus pH data for WT*/K73H iso-1-Cyt*c* in Figure 2.12A has a higher value than the pK_a(His) of about 6.7, reported in Table 2.2 from pH titration data. The amplitude versus pH data for the His73-heme alkaline transition shows two phases (Figure 2.13). Thus, we can also fit the amplitude versus pH data to obtain values for pK_{HL} and pK_{H2} using Eq. 2.4 (*16, 21*), which describes the behavior of the amplitude of the His73-heme alkaline transition

(2.4)

$$\text{Amplitude} = C_{\text{T}} * \left\{ \frac{\left(\frac{K_{\text{HL}}}{K_{\text{HL}} + [H^+]}\right)}{\left(\frac{K_{\text{HL}}}{K_{\text{HL}} + [\text{H}^+]}\right) + \left(\frac{k_{\text{b1,His}} * [\text{H}^+] + k_{\text{b2,His}} * K_{\text{H2}}}{k_{\text{f1,His}} * [\text{H}^+] + k_{\text{f2,His}} * K_{\text{H2}}}\right)} \right\}$$

expected for the two ionization mechanism (Scheme 2.2). In Eq. 2.4, C_{T} is the amplitude if the conformational transition goes to completion. In fitting the data, the microscopic rate constants ($k_{\text{f1,His}}$, $k_{\text{b1,His}}$, $k_{\text{f2,His}}$ and $k_{\text{b2,His}}$) from the fit of the $k_{\text{obs,1}}$ versus pH data in Figure 2.12 (Table 2.3) were used as constants in Eq. 2.4. The fit of the data yields a value for pK_{HL} of 6.8 ± 0.1 which is in good agreement with the pK_{a}(His) obtained from thermodynamic data (Table 2.2). This value for

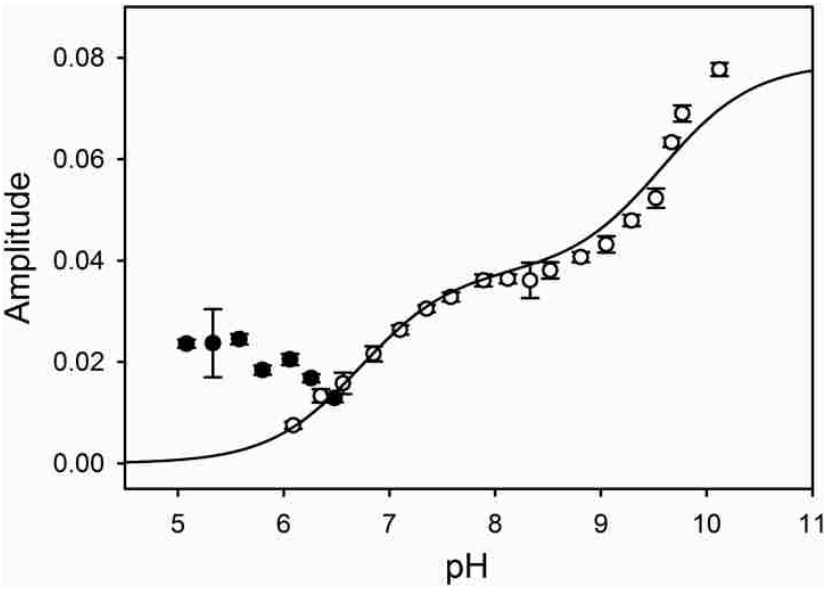

Figure 2.13. Amplitude versus pH for the fast phase ($k_{\text{obs,1}}$) from pH jump stopped-flow experiments. Amplitudes correspond to the change in absorbance at 406 nm. Upward (open circles) pH jump amplitudes are fit to Eq. 2.4 in the Discussion, derived from the kinetic scheme in Scheme 2.2 (*16, 21*)**. The fit yields C_{T} equal to 0.164 ± 0.009. Downward pH jump amplitudes (filled black circles) are not used in the fit. Error bars on data points are the standard deviation of the average.**

pK_{HL} is likely more reliable than the one obtained from the $k_{\text{obs,1}}$ versus pH data, given the size of errors bars and the scatter in the $k_{\text{obs,1}}$ data below pH 7. Within error the value for pK_{H2} did not

change whether fitting $k_{obs,1}$ or amplitude versus pH data (Table 2.3). It is possible that a third ionization event may occur at a lower pH, however, within the error of the reported data points we are unable to reliably detect this ionization, which is clearly present for yWT/K73H iso-1-Cyt*c* (Figure 2.12). pK_{HL} is similar for both WT*/K73H and yWT/K73H (*21*). However, pK_{H2} increases by about 1 unit for WT*/K73H compared to yWT/K73H (Table 2.3). By contrast, the tmK72A mutation does not affect pK_{H2} for the His79-heme alkaline transition. We previously speculated that the outer heme propionate (also referred to as heme propionate-7 and heme propionate D), which is believed to have a pK_a greater than 9 (*3*, *75*, *76*), could be responsible for the pK_{H2} ionization (*16*). If our earlier speculation is correct, the tmK72A mutation increases the pK_a of the outer heme propionate in the context of the K73H mutation, but not in the context of the K79H mutation (*18*). In summary, our kinetic data also show that the effect of the tmK72A mutation depends on whether Ω-loop D is deformed from position 73 or 79.

2.4.3 Obtaining $K_{C1}(His)_{Hi}$ for the His73-heme alkaline transition of WT*/K73H.

To fit the pH dependence of $k_{obs,1}$ in Figure 2.12 it was necessary to estimate the change in K_{C1}(His) for the His73-heme alkaline transition that occurs above pH 8 based on the amplitude data in Figure 2.13. The amplitude for population of the His73-heme conformer increases by a factor of ~ 2.1 from pH 8 to pH 10 (A_1 in Table A2). We can use this increase to estimate the increase in $K_{C1}(His)_{Hi}$ (= $k_{f2,His}/k_{b2,His}$) relative to $K_{C1}(His)_{Lo}$ (= $k_{f1,His}/k_{b1,His}$) after the ionization corresponding to pK_{H2} (Scheme 2.2). The change in magnitude of A_1 by ~2.1-fold was determined from A_1 near pH 8 and pH 10 (Table A2).

Given that: K_{C1}(His) = [His73-heme]/[Met80-heme]

and f_{His} = [His73-heme]/([His73-heme] + [Met80-heme]) = K_{C1}(His)/1+ K_{C1}(His)

We can write: $f_{His,Hi} = 2.1 \times f_{His,Lo}$

Therefore: $$\frac{K_{C1}(His)_{Hi}}{1+K_{C1}(His)_{Hi}} = 2.1 \times \frac{K_{C1}(His)_{Lo}}{1+K_{C1}(His)_{Lo}}$$

$$K_{C1}(His)_{Hi} + K_{C1}(His)_{Hi} \times K_{C1}(His)_{Lo} = 2.1(K_{C1}(His)_{Lo} + K_{C1}(His)_{Hi} \times K_{C1}(His)_{Lo})$$

$$K_{C1}(His)_{Hi} - 1.1 \times K_{C1}(His)_{Hi} \times K_{C1}(His)_{Lo}) = 2.1 \times K_{C1}(His)_{Lo}$$

$$K_{C1}(His)_{Hi} = \frac{2.1 \times K_{C1}(His)_{Lo}}{1 - 1.1 \times K_{C1}(His)_{Lo}}$$

If we use $K_{C1}(His)_{Lo} = k_{f1,His}/k_{b1,His} = 3\ s^{-1}/10\ s^{-1} = 0.3$ (Table 2.3) these values are insensitive to the ratio used to constrain k_{f2} and k_{b2}.

We obtain: $$K_{C1}(His)_{Hi} = \frac{2.1 \times 0.3}{1 - 1.1 \times 0.3} = 0.94$$

Therefore, $k_{f2,His}/k_{b2,His} = 0.94$. $k_{b2,His} = k_{f2,His}/0.94$ was used in fitting eq 3 to the $k_{obs,1}$ versus pH data for WT*/K73H in Figure 2.12 yielding the parameters in Table 2.3.

2.4.4 Determining forward and reverse rate constants of the alkaline conformational transition**.**

The individual rate constants from the gated ET experiments were plotted against a_6Ru^{2+} concentration. $k_{gET,1}$, which corresponds to bimolecular ET from a_6Ru^{2+} to the native state, shows a linear dependence on a_6Ru^{2+} concentration (Figure 2.10) as expected for a bimolecular reaction under pseudo-first-order conditions (see Scheme 2.1). Fitting the $k_{gET,1}$ versus a_6Ru^{2+} concentration data to Eq. 2.5, yields the bimolecular rate constant k_{ET} as the slope. In Eq. 2.5, k_{uni}

(2.5)

$$k_{gET,1} = k_{ET} * [a_6Ru^{2+}] + k_{uni}$$

represents a summation of all unimolecular rate constants ($k_{f,His}$, see Scheme 2.1, and $k_{f,L}$'s for species corresponding to $A_{gET,3}$ and $A_{gET,4}$, see Figure 2.9) that lead to the disappearance of the

native conformer. The k_{ET} values as a function of pH are listed in Table 2.4 and plotted in Figure 2.10. k_{ET} values decrease with increasing pH. A similar pH dependence for k_{ET} is observed for the AcH73 variant of iso-1-Cyt*c* (*14*), as well as, for a yWT/K73H/K79A variant of iso-1-Cyt*c* (*20*) both of which contain the native tmK72 residue. This observation suggests that the mechanism of direct ET is similar, regardless of whether Ω-loop D is sterically hindered by tmK72 or sterics have been relieved by the tmK72A mutation.

By contrast, k_{ET} for reduction of WT*/K79H increases as pH increases (*19*). The relative

Table 2.4. Rate constants obtained from reduction of oxidized WT*/K73H by hexaammineruthenium(II) chloride at 25 ˚C in 10 mM buffer, 0.1 M NaCl.[a]

pH	k_{ET} (mM^{-1}, s^{-1})[b]	$k_{b,His}$ (s^{-1})[c]	$k_{f,His}$ (s^{-1})[d]
5	44 ± 2	9 ± 2	-
6	47 ± 1	8.8 ± 0.7	-
7	42.4 ± 0.5	9.2 ± 0.4	2 ± 3
8	34.6 ± 0.7	8.76 ± 0.08	2.8 ± 0.7
9	31.6 ± 0.2	9.9 ± 0.2	7 ± 1

[a] Errors are standard errors reported by SigmaPlot unless otherwise noted. [b] k_{ET} is obtained from fits to Eq. 2.5, as described in the text. The intercepts, k_{uni}, of the fits to Eq. 2.5 were close to zero within error. [c] At pH 5 and 6, $k_{b,His73}$ is taken as the average value of $k_{gET,2}$ across all concentrations of a_6Ru^{2+}. Error is the standard deviation of the average. At pH 7 to 9, $k_{b,His}$ is from fits to Eq. 2.6, as described in the text. [d] From fits to Eq. 2.6, as described in the text.

proximity of His73 versus His79 to the heme may account for these differences. At higher pH, deprotonation of His79, which is close to the heme edge (see Figure 2.1), will make it easier for a_6Ru^{2+} to form a precursor complex (*77*), which has a_6Ru^{2+} close to the heme of iso-1-Cyt*c*. Thus, the observed increase in k_{ET} as pH increases is reasonable. His73 is located above Met80 far removed from the heme edge (see Figure 2.1). Deprotonation of His 73 would thus increase the probability that a_6Ru^{2+} would form a precursor complex with Cyt*c* at a greater distance from

the heme edge. At this location, ET is expected be less favorable, leading to the observed drop in k_{ET} at higher pH.

At all pH values, the magnitude of $k_{gET,2}$, which corresponds to reduction of the His73-heme conformer, is independent of a_6Ru^{2+} concentration at high concentrations of a_6Ru^{2+}. Evidently at high a_6Ru^{2+} concentration, $k_{ET}[a_6Ru^{2+}]$ is much greater than $k_{f,His}$, such that the rate of reduction is controlled by the unimolecular conformational change back to the native state (i.e., $k_{gET,2}$ is approximately equal to $k_{b,His}$, see Eq. 2.6 and Scheme 2.1). At pH 8 and 9, there is some decrease in $k_{gET,2}$ at the lowest concentrations of a_6Ru^{2+}. Thus, it is possible to fit the dependence of $k_{gET,2}$ on a_6Ru^{2+} concentration to the full form of Eq. 2.6, which is derived assuming a steady-state approximation (*78-80*), so that both rate constants, $k_{b,His}$ and $k_{f,His}$, associated with the

(2.6)

$$k_{gET,2} = \frac{\left(k_{b,His} k_{ET}[a_6Ru^{2+}]\right)}{\left(k_{f,His} + k_{ET}[a_6Ru^{2+}]\right)}$$

conformational transition can be obtained (Figure 2.11). At pH 7 and below, no clear decrease in $k_{gET,2}$ is observed at the lowest a_6Ru^{2+} concentrations. The data at pH 7 were fit to Eq. 2.6, to obtain $k_{b,His}$. The fit also provides $k_{f,His}$, but the error in its magnitude is large (Table 2.4) and at best it provides an upper limit for $k_{f,His}$ at pH 7. At pH 5 and 6, the errors in the magnitudes of $k_{gET,2}$ are larger, so, we have used the average of $k_{gET,2}$ at all concentrations of a_6Ru^{2+} as an estimate for the magnitude of $k_{b,His}$. All values of $k_{f,His}$ and $k_{b,His}$ obtained from gated ET experiments are reported in Table 2.4.

In Figure 2.12, the microscopic rate constants, $k_{f,His}$ and $k_{b,His}$, obtained from the gated ET experiments along with their sum, which should be equal to $k_{obs,1}$ obtained from pH jump experiments, are plotted against $k_{obs,1}$ for the His73-heme alkaline transition obtained from pH jump experiments. Across the pH regime studied, values for $k_{b,His}$ are invariant within error for

WT*/K73H, except at pH 9 where $k_{b,His}$ appears to increase by about 10% (Table 2.4). For yWT/K73H and other variants with K73H mutations, an ionizable group with a pK_a near 5.5 is observed (see Figure 2.12 and refs. (*14, 20*)). If there is an ionization affecting the His73-heme alkaline transition in this pH regime, its effect on the magnitude of $k_{b,His}$ is within the error of our measurements. As the pH is increased, the rate constant associated with opening of the heme crevice and replacing the methionine-heme ligand with histidine, $k_{f,His}$, increases. Below pH 7, $k_{f,His}$ is too small to evaluate. At pH 5 and 6, $k_{b,His}$ is within error of the magnitude of $k_{obs,1}$ from pH jump experiments (Figure 2.12), indicating that $k_{f,His}$ is close to zero. At pH 7 and above, the sum of $k_{f,His}$ and $k_{b,His}$ matches $k_{obs,1}$ from pH jump experiments reasonably well (Figure 2.12). At pH 8, where the His73-heme alkaline conformer is maximally populated (Figure 2.9), the ratio of $k_{f,His}$ to $k_{b,His}$ should be close to K_{C1}(His) obtained from equilibrium measurements. At pH 8, K_{C1}(His) (obtained as $k_{f,His}$ divided by $k_{b,His}$) equals 0.32 ± 0.08, which is close to K_{C1}(His) of 0.21 ± 0.02 from equilibrium data for WT*/K73H (derived from pK_{C1}(His) in Table 2.2). At pH 9, $k_{f,His}$ and $k_{b,His}$ yield 0.7 ± 0.1 for K_{C1}(His). This value approaches our estimate of the increase from K_{C1}(His) near 0.21 to $K_{C1}(His)_{Hi}$ of about 0.94 due to the ionization of the group with pK_{H2} of 10 (Figure 2.13 and Table 2.3). Interestingly, the pK_{H2} ionization also increases the stability of the His73-heme conformer relative to the native conformer for the AcH73 variant of iso-1-Cyt*c* (*20*).

2.4.5 Effect of the tmK72A mutation on the free energy landscape of K73H variants of iso-1-Cyt*c*.

Figure 2.14 shows the effect of the tmK72A mutation on the free energy landscape of the His73-mediated alkaline transition of iso-1-Cyt*c* using thermodynamic and kinetic data presented here for WT*/K73H and reported previously for yWT/K73H (*21*, *47*). In Figure 2.14, we have

assumed that the tmK72A mutation does not affect the stability of the native state. This choice is partially dictated by the small decrease in the stability of the His73-heme conformer based on GdnHCl unfolding data in Table 2.1 (given that global unfolding of K73H variants proceeds primarily from the His73-heme conformer, ref. (*47*)), which is similar in magnitude to the effect of the tmK72A mutation on the relative stability of the native conformer versus the His73-heme alkaline conformer (Table 2.2). As discussed above, the NMR structure of the Lys73-heme alkaline conformer suggests that tmK72 could interact with an aromatic cage-like motif (*73, 74*), derived from Tyr67 and Met80 in the Lys/His73-heme alkaline conformer (*13, 18*). Truncation of tmK72 to an Ala would eliminate this interaction (*13*) (see Figure 2.14, lower right), supporting the contention that the increase in the positive magnitude of pK_{C1}(His) (less favorable equilibrium) results primarily from a destabilization of the His73-heme conformer with little effect on the free energy of the native state (Figure 2.14). The lesser effect of the tmK72A mutation on the transition state (TS, see Figure 2.14) would be consistent with partial formation of the aromatic cage-like motif in the TS.

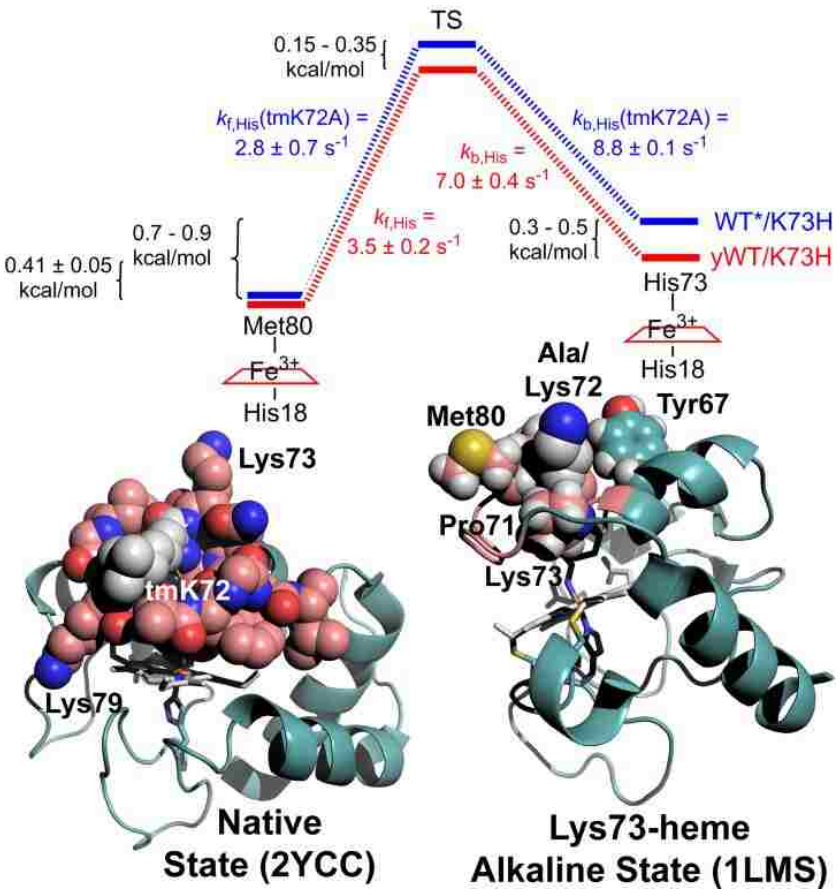

Figure 2.14. Effect of the tmK72A mutation on the free energy landscape of the His73-heme mediated alkaline conformational transition of iso-1-Cyt*c*. yWT/K73H has tmK72 and WT*/K73H carries the tmK72A mutation. The range given for the relative stabilities of the native conformer and His73-heme alkaline conformer for WT*/K73H is based on kinetic (0.7 kcal/mol; using $k_{f,His}$ and $k_{b,His}$ at pH 8 in Table 2.4 to obtained K_{C1}(His)) and thermodynamic data (0.9 kcal/mol, using pK_{C1}(His) in Table 2.2). The range in the magnitude of K_{C1}(His) produces a similar range for the relative stabilities of the His73-heme alkaline conformers of WT*/K73H and yWT/K73H. The change in the height of the barrier is calculated using the Eyring equation, yielding a decrease in the barrier for return to the native conformer by about 0.15 kcal/mol with the tmK72A mutation ($k_{b,His}$ increases from 7 to 8.8 s^{-1}). The range in the ΔG of the TS for WT*/K73H versus yWT/K73H results from the range in the ΔG of the His73-heme conformers of WT*/K73H and yWT/K73H. Lower left: structure of native iso-1-Cytc (pdb code: 2YCC with Ω-loop D colored salmon shown as a space-filling model. Lower right: structure of the Lys73-heme alkaline conformer (pdb code: 1LMS) with Ω-loop D colored salmon. Met80, Tyr67, Pro71 and Ala/Lys72 are shown as space filling models. Ala72 in this structure has been converted to Lys using the mutate function of PyMol (added carbons are shown in gray).

Assigning effects of mutations to one ground state or another is always uncertain. The global stability of the yWT/K73H is sensitive to how the global unfolding data are fit and could be somewhat lower than for the WT*/K73H variant (*81*). Also, the overlap between partial unfolding to the His73-heme alkaline conformer by GdnHCl and global unfolding is likely greater for the WT*/K73H variant than for the yWT/K73H variant because the His73-heme alkaline conformer is destabilized by the tmK72A mutation (Table 2.2). Thus, the estimation of the free energy of the His73-heme alkaline conformer for WT*/K73H iso-1-Cyt*c* versus yWT/K73H iso-1-Cyt*c* has some uncertainty. The discussion here is supported by structural data for the Lys73-heme alkaline conformer (Figure 2.14, lower right) (*13*). However, the factors affecting the stabilities of the two ground states as a result of the tmK72A mutation may be more complex. What is clear is that tmK72A mutation decreases the barrier from the His73-heme alkaline conformer to the TS and may cause a slight increase in the barrier from the native conformer to the TS (although the errors in $k_{f,His}$ for WT*/K73H and yWT/K73H are overlapping, see Figure 2.14).

Thus, the tmK72A mutation has very different effects on the free energy landscape of Ω-loop D with respect to formation of a His73-heme versus a His79-heme alkaline conformer. For the His79-heme alkaline transition, the tmK72A mutation decreases the barrier from the native conformer to the TS allowing faster formation of the His79-heme alkaline conformer (*18, 19*). For the His73-heme alkaline transition, the tmK72A mutation decreases the barrier from the His73-heme alkaline conformer to the TS speeding formation of the native conformer. This observation has interesting general implications for the effects of mutations on the tier 0 dynamics of protein substructures involved in function. In particular, our results show that the dynamic accessibility of different higher energy states of a protein substructure can be affected

differently by mutation, which could change the partitioning between different functions or modulate the specificity of a function. In the case of iso-1-Cyt*c*, peroxidase activity is enhanced by the tmK72A mutation (*49*), suggesting that the tier 0 dynamics required to access the higher energy state of Ω-loop D that mediates peroxidase activity may be similar to the tier 0 dynamics required to access the His79-heme alkaline conformer but not those to access His73-heme alkaline conformer. Given the high conservation of Ω-loop D between yeast and mammals, it is possible that the residue at position 72 has similar effects on the tier 0 dynamics required for peroxidase activity early in apoptosis for mammalian Cyt*c*.

2.5 Conclusion

2.5.1 Effect of tmK72A on the alkaline conformational transition.

The primary observation of the present work is that the effect of the tmK72A mutation on the His73-heme alkaline transition is entirely opposite from that observed for the His79-heme alkaline transition. Near neutral pH, this mutation destabilizes the His73-heme alkaline conformer relative to the native conformer, whereas it destabilizes the native conformer relative to the His79-heme alkaline conformer. This mutation also enhances the rate of formation of the His79-heme alkaline conformer near neutral pH while enhancing the rate of formation of the native conformer from the His73-heme alkaline conformer. Therefore, the effect of the tmK72A mutation on the dynamics of Ω-loop D clearly depends of the nature of the deformation of this substructure. Peroxidase activity assays on yWT versus WT* iso-1-Cyt*c* show that k_{cat} is 2-fold larger near pH 8 for WT* iso-1-Cyt*c*, which carries the tmK72A mutation (*49*). Given the high degree of conservation of Ω-loop D from yeast to mammals, and the current results on the effect of the tmK72A mutation on the dynamics of the His73-heme alkaline transition, our previous peroxidase activity results suggest that the dynamics of heme crevice opening required for

peroxidase activity early in apoptosis may be similar to the dynamics of Ω-loop D which lead to formation of the His79-heme alkaline conformer.

Chapter 3 Lower Protein Stability Does Not Necessarily Increase Local Dynamics

3.1 Introduction

Proteins have long been thought to have evolved resulting in a sequence bias or propensity favoring a particular folding pathway ultimately resulting in a stable protein structure (*1, 82*). The stability associated with this protein structure, or native conformer, can be represented as the lowest energy minima at the bottom of the folding funnel (*83*). Although there may be a favored, natively folded state, energy landscapes at the bottom of the folding funnel can have alternative pathways leading to local energy minima of various stabilities separated by energetic barriers from the native conformer (*35*). Native conformers with high stability typically lie in the bottom of a deep energy funnel and have large energy barriers between conformational states. Proteins with shallow energy landscapes containing low energy barriers between multiple conformers typically have a less stable native conformer as multiple conformational states exist close in energy to one another. As overall decreased global stability leads to compressed energy wells in the folding funnel, conformational promiscuity can increase as the energy barriers between conformers are lowered. The "stability-function" hypothesis suggests a relationship between stability and activity (*22*). As flexibility is often required for enzymatic activity, stability may be sacrificed, conversely, increasing stability may decrease flexibility and, therefore, activity.

There exists an inverse correlation between protein flexibility and protein stability, where proteins with greater stability demonstrate decreased flexibility (*84*). One such example of proteins with altered stabilities affecting dynamic motion is the case of extremophiles. Psychrophilic proteins have decreased stability compared to their thermophilic counterparts (*23,*

24). This decreased stability arises from the need to compensate for decreased catalytic activities imposed by the harsh environmental conditions psychrophiles inhabit (*25*). There exists a "conformational-motion" temperature or lower temperature limit below which only small protein motions can occur (*84*). To overcome this temperature barrier, psychrophiles can increase their flexibility affecting a reduction in thermostability ultimately conferring catalytic activity at the low temperature of the environment (*25*).

Increased flexibility from decreased stability is not necessarily unique to extremophiles alone. In fact, deletion of the C-terminal helix in yeast phosphoglycerate kinase yields a 5 kcal/mol loss in stability and an increase in flexibility (*85*). Temperature denaturation experiments show replacement of a conserved proline with glycine or alanine, via site directed mutagenesis, unfolds *Bacillus thuringiensis* δ-endotoxins at lower temperatures (*86*). Lower stability is suggested to be conveyed via increased helix mobility.

In previous work we have demonstrated increased protein dynamics in a destabilized variant of yeast iso-1-cytochrome *c* (*14, 15*). Disruption of the hydrogen bond between His26 and Glu44 via a His26Asn mutation can decrease the global stability of cytochrome *c* (Cyt*c*) to as much as half its value in the absence of this mutation (*15, 26*). The decreased stability caused by the mutation of His26Asn also brings about a 2 fold increase in the observed rate constants for interconversion between the native and alkaline conformers (*14*). This behavior has been compared to the behavior of psychrophilic enzymes and has been suggested to demonstrate relaxed barriers between conformers at the bottom of low stability folding funnels (*15*).

Cytochrome *c* (Cyt*c*) Ω-loop D is a highly conserved sequence consisting of residues 70-85 that lies over the heme crevice. This flexible heme crevice loop contains the native state heme ligand Met80. Concurrent with increasing pH, an alkaline conformer of Cyt*c* forms

resulting in a rearrangement of the heme crevice loop (*13, 87*). Deprotonation of the lysines within Ω-loop D enables replacement of the native heme ligand, Met80, with either lysine 73 or 79 (*9, 10*). To decrease the pH at which the alkaline transition occurs we have previously replaced either lysine 73 or 79 with a histidine (*14, 15, 18, 19, 21, 53, 61, 88*). Decreasing the pH of the alkaline transition through lysine mutation to histidine also enables differentiation between the residue 73- and 79-mediated alkaline transition pathways (*18, 88*).

Leucine 85 is a highly conserved residue residing near the edge of Ω-loop D (*3*). Making up part of the hydrophobic interior of the heme crevice, Leu85 has been proposed to be of structural importance (*27, 89, 90*). Data from a crystal structure of yeast iso-1-Cyt*c* with a Leu85Ala substitution demonstrates that replacement of leucine with a smaller less hydrophobic amino acid results in formation of a larger hydrophobic cavity (*91, 92*). This free volume causes small shifts in the side chains of Leu9 and Leu94. A significant reorientation of Arg13 leads to a loss of hydrogen bonding between the side chain of Arg113 and the carbonyl of Gly84 and a new interaction between the Arg13 and Asp90 side chains (Figure 3.1). Although these side chains undergo rearrangement in the space no longer occupied by Leu85, there is minimal perturbation to the backbone of the protein structure. Even so, the Leu85Ala mutation has been shown to cause a two-fold decrease in global stability from calorimetric studies (*27*). Yet, the Leu85Ala mutation does not significantly affect the reduction potential of the heme (*93*).

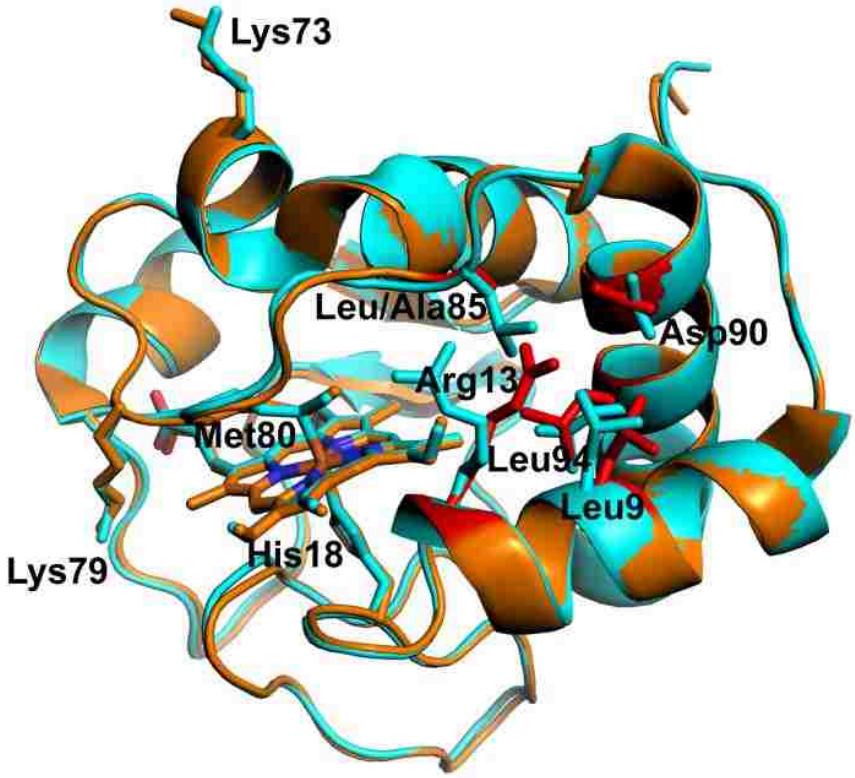

Figure 3.1. Overlay of structures of yeast iso-1-Cyt*c* wild-type (cyan) (PDB 2YCC) and L85A variant (orange) (PDB 1CHI). Residues (Leu9, Arg13, Ala85, Asp90, and Leu94) of the L85A variant demonstrating altered conformations are shown as red sticks versus cyan sticks for wild type iso-1-Cyt*c*. Residues His18, Lys73, Lys79, and Met80 are also shown as sticks.

Using stopped-flow experimental techniques we characterize the kinetics of Ω-Loop D during the alkaline conformational transition for the Leu85Ala iso-1-Cyt*c* variant. Rather than increasing protein dynamics as previously seen in extremophiles (see above), the destabilizing Leu85Ala mutation has little effect above pH 7 and in fact demonstrates decreased dynamic motion below pH 7.

3.2 Experimental Procedures

3.2.1 Protein expression.

L85A and L85A-r mutagenesis primers (Invitrogen) (Table B1) were used to add the L85A mutation via PCR-based mutagenesis to the WT* and WT*/K73H variants (*88*) in the

pRbs_BTR1 expression vector (*54*). WT*/L85A and WT*/K73H/L85A yeast iso-1-Cyt*c* variants were expressed in BL21(DE3) *Escherichia coli* cells using the pRbs_BTR1 vector (*54*). WT* denotes two background mutations: K72A, which eliminates the Lys72-heme ligand in the alkaline state (*48*), and C102S, which prevents disulfide dimerization. Sequencing to confirm the L85A mutations was performed by the Murdock DNA Sequencing Facility.

Purification was carried out as previously reported (*18, 19, 58, 59*). Briefly, cells were broken using a French Pressure Cell (SLM Aminco) and the lysate was cleared via centrifugation. Following 50% ammonium sulfate saturation, precipitates were again cleared via centrifugation and the supernatant was dialyzed against 12.5 mM sodium phosphate, pH 7.2, 1 mM EDTA, 2 mM β-mercaptoethanol (β-ME). Protein was then batch absorbed to CM-Sepharose Fast Flow resin pre-equilibrated to 50 mM sodium phosphate buffer, pH 7.2, 1 mM EDTA, 2 mM β-ME and then eluted with a linear gradient of 0-0.8 M NaCl in 50 mM sodium phosphate buffer, pH 7.2, 1 mM EDTA, 2 mM β-ME. Aliquots of ~2 mg/mL were flash frozen in liquid nitrogen and stored at -80 °C and thawed for cation-exchange HPLC purification with an Agilent Technologies 1200 series HPLC and a Biorad UNO S6 Column (catalog no. 720-0023). Protein samples were concentrated by ultrafiltration, oxidized with $K_3[Fe(CN)_6]$, followed by separation of oxidized Cyt*c* from the oxidizing agent on a G25 Sephadex column.

Mass spectra were acquired with a Bruker microflex MALDI-ToF mass spectrometer. Calibration was performed in cubic enhanced mode with Protein Calibration Standard I (Bruker part no. 206355). WT*/L85A and WT*/K73H/L85A were found to be 12552 ± 1 g mol^{-1} (predicted: 12552.05 g mol^{-1}) and 12560.7 ± 0.3 g mol^{-1} (predicted: 12561.02 g mol^{-1}), respectively.

3.2.2 Guanidine hydrochloride denaturation global stability measurements.

Global stability measurements were performed using guanidine hydrochloride (GdnHCl) as a denaturant. Measurements were performed on an Applied Photophysics Chirascan circular dichroism (CD) spectrometer coupled to a Hamilton MICROLAB 500 Titrator at 25 °C, as previously discussed (*17*). Protein was adjusted to 4 µM in 20 mM Tris, pH 7.5, 40 mM NaCl. Data collection was performed at 222 and 250 nm. Baseline corrections were accomplished by subtracting the ellipticity at 250 nm from the ellipticity at 222 nm ($\theta_{222corr} = \theta_{222} - \theta_{250}$). Using nonlinear least squares fits applied to a two-state model, assuming a linear free energy relationship and a native state baseline that is independent of GdnHCl concentration, the free energy of unfolding in the absence of denaturant, $\Delta G_u°'(H_2O)$, and the *m*-value were extracted, as previously outlined (*68*). Parameters are the average and standard deviation of a minimum of three independent trials.

3.2.3 Determination of the alkaline conformational transition by pH titration.

A Beckman Coulter DU800 spectrophotometer was used for pH titrations monitored at 695 nm and 22 ± 1 °C to measure the alkaline conformational transition, as previously described (*61*). A 600 µL 2X stock solution of 400 µM oxidized protein in 200 mM NaCl was prepared. 1:1 mixing with a 1000 µL pipetman of 2X stock and MilliQ water was performed to achieve a 1X solution of 200 µM oxidized protein in 100 mM NaCl. pH titrations were carried out by adding equal volumes of either NaOH or HCl solutions of appropriate concentration and the 2X stock to maintain a 200 µM protein concentration throughout the titration. pH was measured with a Denver Instrument UB-10 pH/mV meter using an Accumet semimicro calomel pH probe (Fischer Scientific Cat. No. 13-620-293). Absorbance at 750 nm was subtracted from absorbance at 695 nm to correct for baseline drift ($A_{695corr} = A_{695} - A_{750}$). From the corrected

absorbance, the corrected molar extinction coefficient, $\varepsilon_{695corr}$, was determined, using concentrations determined from the absorbance at 570 and 580 nm near pH 5 (*16*) and the molar extinction coefficients 5.2 mM^{-1} cm^{-1} and 3.5 mM^{-1} cm^{-1}, respectively (*62*).

Data for the WT*/L85A variants were fit to a modified form of the Henderson-Hasselbalch equation, Eq 3.1.

(3.1)

$$\varepsilon_{695\mathrm{corr}} = \frac{\varepsilon_{\mathrm{N}} + \varepsilon_{\mathrm{alk}} * 10^{n[pK_{\mathrm{app}} - \mathrm{pH}]}}{1 + 10^{n[pK_{\mathrm{app}} - \mathrm{pH}]}}$$

In equation 3.1, ε_N is the native state Met80-heme bound ligand extinction coefficient at 695 nm and ε_{alk} is the alkaline bound heme ligand, either Lys73 or Lys79, extinction coefficient at 695 nm.

Data for the WT*/K73H/L85A variant were fit to a model involving two ionizable ligands corresponding to His73 and Lys79 as given by Eq. 3.2. Equation 3.2 accounts for formation of both the His73-heme and Lys79-heme alkaline states (*47*).

(3.2)

$$\varepsilon_{695\mathrm{corr}} = \frac{\varepsilon_{\mathrm{N}} + \varepsilon_{\mathrm{alk}} * \left(\frac{10^{[-\mathrm{p}K_{\mathrm{C1}}(\mathrm{His})]}}{1+10^{[\mathrm{p}K_{\mathrm{a}}(\mathrm{His}) - \mathrm{p}H]}} + \frac{10^{[-\mathrm{p}K_{\mathrm{C2}}(\mathrm{Lys})]}}{1+10^{[\mathrm{p}K_{\mathrm{a}}(\mathrm{Lys}) - pH]}} \right)}{1 + \left(\frac{10^{[-\mathrm{p}K_{\mathrm{C1}}(\mathrm{His})]}}{1+10^{[\mathrm{p}K_{\mathrm{a}}(\mathrm{His}) - \mathrm{p}H]}} + \frac{10^{[-\mathrm{p}K_{\mathrm{C2}}(\mathrm{Lys})]}}{1+10^{[\mathrm{p}K_{\mathrm{a}}(\mathrm{Lys}) - pH]}} \right)}$$

The acid dissociation constants for the ionization triggers are pK_a(His) and pK_a(Lys), respectively. As previously, pK_a(Lys) was constrained to 10.8 (*9*). The molar extinction coefficient ε_{alk} was constrained to equal ε_N – 0.53 mM^{-1} cm^{-1}, as determined from WT*/K73H iso-1-Cyt*c* pH titration data, where WT*/K73H appears to be fully native at low pH (*14*). Equilibrium constants for the replacement of Met80 by deprotonated His73- and Lys79-heme ligands are pK_{C1}(His) and pK_{C2}(Lys), respectively.

3.2.4 pH Jump stopped-flow kinetics.

As previously reported (*16*), pH jump stopped-flow experiments were executed using an Applied Photophysics SX20 stopped-flow spectrometer at 25 °C. 5000 data point plots were collected on a logarithmic time scale monitoring at 406 nm. Short, 1 s, timescale trials were collected with pressure hold to reduce drive syringe artifacts for the K73H/L85A variant. Long, 50-350 s, timescale trials were employed to capture the entire alkaline conformational transition. Both upward and downward pH jumps were collected in increments of 0.25 pH units. Initial sample conditions for upward pH jumps were 20 µM Cyt*c* in 0.1 M NaCl (pH 5), which was mixed in a 1:1 ratio with 20 mM buffer in 0.1 M NaCl of the desired pH (pH 6-10). Downward pH jumps were carried out in a similar manner beginning at pH 7.5 and jumping to the pH regime 5-6.5 for the K73H/L85A variant. For the L85A variant, downward pH jumps were performed from both pH 8.5 and 9.5 jumping to pH 5-6.5. Effluent was collected and the final pH was measured with a Denver Instrument UB-10 pH/mV meter using an Accumet semimicro calomel pH probe. Buffers were as follows: acetic acid (pH 5-5.25), MES (pH 5.5-6.5), NaH_2PO_4 (pH 6.75-7.5), Tris (pH 7.75-8.75), and H_3BO_3 (pH 9-10). A minimum of 5 trials were collected at each pH. Data were fit to the appropriate exponential function with SigmaPlot v. 7.0 (*21*).

3.2.5 Stopped-flow electron transfer kinetics.

Gated electron transfer experiments were carried out monitoring reduction of oxidized Cyt*c* at 550 nm on an Applied Photophysics SX20 stopped-flow spectrophotometer at 25 °C, as described previously (*19*). Bis(2,2′,2″-terpyridine)cobalt(II) hexafluorophosphate, $Co(terpy)_2^{2+}$, synthesized as previously (*19, 94*), was the reducing reagent for oxidized Cyt*c*. A 10 mM $Co(terpy)_2^{2+}$ stock solution was prepared in Ar-degassed 10 mM buffer and 0.1 M NaCl. From

the stock 1, 2, 4, 6, 8 and 10 mM $Co(terpy)_2^{2+}$ solutions were prepared in degassed 10 mM buffer and 0.1 M NaCl and the actual concentration was determined by absorbance measurements at 505 nm, $\varepsilon = 1404\ M^{-1}\ cm^{-1}$ (*94*). 10 µM oxidized Cyt*c* in 10 mM buffer and 0.1 M NaCl was mixed 1:1 with 1, 2 and 4 mM $Co(terpy)_2^{2+}$ using a 10 mm path length yielded final concentrations of 5 µM Cyt*c* and 0.5, 1, and 2 mM $Co(terpy)_2^{2+}$. 1:1 mixing with 50 µM Cyt*c* and 6, 8 and 10 mM $Co(terpy)_2^{2+}$ using a 2 mm path length yielded final concentrations of 25 µM Cyt*c* and 3, 4 and 5 mM $Co(terpy)_2^{2+}$. 10 mM buffers were as follows: acetic acid (pH 5), MES (pH 5.5-6.5), NaH_2PO_4 (pH 7). At each pH and $Co(terpy)_2^{2+}$ concentration a minimum of 8 short timescale, 5 s, trials were collected using pressure holds and a minimum of 5 long timescale, 100-400 s, trials were collected. Data were fit to the appropriate exponential function using SigmaPlot v. 7.0.

3.2.6 Numerical fitting of gated ET data with Pro-Kineticist software.

Pro-Kineticist software (Applied Photophysics) was used to numerically integrate the kinetics equations for gated ET to fit the kinetic traces at lower concentrations of $Co(terpy)_2^{2+}$ where the direct electron transfer and gated ET phases of the reduction of WT*K73H/L85A are poorly separated and the steady state approximation used to fit gated ET data breaks down. Full details of the fitting procedure are outlined in Chapter 3.4.5.

3.3 Results

3.3.1 Global stability of iso-1-Cyt*c* variants.

Circular dichroism spectroscopy was employed to measure the global stability of variants containing the destabilizing WT*/L85A mutation with respect to WT* iso-1-cytochrome *c* (iso-1-Cyt*c*: WT* has K72A and C102S background mutations) by GdnHCl denaturation at 25 °C and pH 7.5. As seen from the denaturation curves of Figure 3.2, the L85A variant is

considerably less stable than WT* iso-1-Cyt*c*. Fits of the data in Figure 3.2 to a two-state model assuming a linear free energy relationship between the free energy of unfolding, ΔG_u, and GdnHCl concentration show that the free energy of unfolding in the absence of denaturant, $\Delta G_u°´(H_2O)$, for the WT*/L85A variant decreases to approximately half that of WT* iso-1-Cyt*c* (Table 3.1). $\Delta G_u°´(H_2O)$ for WT*/L85A is similar to the stability for the yWT/L85A variant reported from calorimetric studies (yWT denotes iso-1-Cyt*c* expressed from *Saccharomyces cerevisiae* with a trimethylated lysine at residue 72) (*27*). Similarly, the unfolding midpoint, C_m, for WT*/L85A iso-1-Cyt*c* is approximately half that of WT* iso-1-Cyt*c*, consistent with the two-fold decrease in stability between WT* iso-1-Cyt*c* and the L85A variant. Combining the destabilizing L85A mutation with the K73H mutation also decreases $\Delta G_u°´(H_2O)$ and C_m. The *m*-value (rate of change of ΔG_u with respect to GdnHCl concentration) is similar for both the L85A variant and WT* iso-1-Cyt*c*, whereas addition of the K73H mutation causes a drop of about 1 kcal mol^{-1} M^{-1} in the *m*-value. Our previous work on K73H variants has shown that the decrease in the *m*-value arises from GdnHCl unfolding proceeding from a partially unfolded His73-heme conformer at pH 7.5 (*47, 53*).

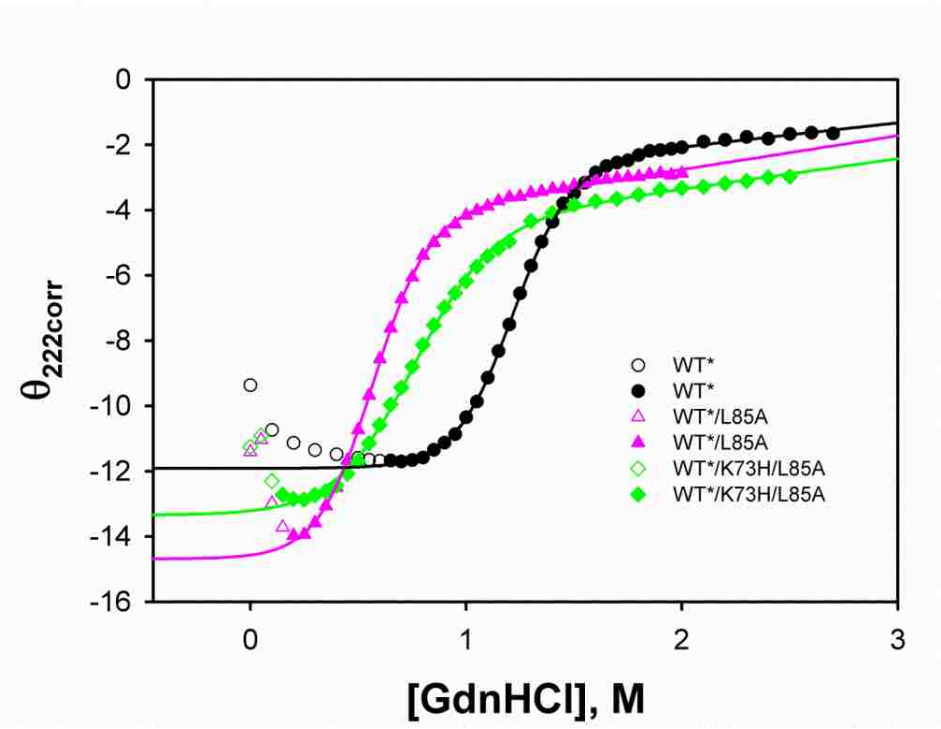

Figure 3.2. Plots of $\theta_{222corr}$ vs GdnHCl concentration showing global unfolding of the WT* (black circles), WT*/L85A (pink triangles), and WT*/K73H/L85A (green diamonds) variants of yeast iso-1-Cyt*c* at 25 °C. Filled data points were used in the fit to a two-state model (solid curves). Unfilled data points were not included in the fit.

Table 3.1. Thermodynamic parameters for the iso-1-Cyt*c* variants obtained by GdnHCl denaturation monitored by circular dichroism at 25 °C and pH 7.5.[a]

Variant	$\Delta G_u^o(H_2O)$ **(kcal/mol)**	*m*-value **(kcal mol^{-1}M^{-1})**	C_m **(M)**
WT*[b]	5.31 ± 0.08	4.39 ± 0.09	1.21 ± 0.01
yWT/L85A[c]	2.7 ± 0.2	-	-
WT*/L85A	2.66 ± 0.05	4.74 ± 0.08	0.56 ± 0.01
WT*/K73H/L85A	2.36 ± 0.09	3.36 ± 0.13	0.70 ± 0.03

[a]Parameters are the average and standard deviation of a minimum of three trials. [b]Parameters are from ref. (*88*). [c]Parameters are from ref. (*27*). yWT/L85A carries a C102T rather than a C102S mutation.

3.3.2 Alkaline conformational transition of iso-1-Cyt*c* variants.

Heme ligation, monitored as a function of pH at 695 nm, provides an excellent method to investigate the local unfolding thermodynamics of the alkaline conformational transition. The

absorbance band at 695 nm corresponding to the Met80-heme (native) ligated conformation readily identifies pH-induced conformational transitions as heme ligation changes with pH (*3, 69, 70*). Figure 3.3 compares pH titrations for WT* iso-1-Cyt*c* and the WT*/L85A and WT*/K73H/L85A variants. Both WT* iso-1-Cyt*c* and the WT*/L85A variant exhibit a monophasic alkaline transition, where increasing pH leads to the transition from native Met80-heme ligation to an alkaline conformational state in which Lys-heme ligation becomes favored. The fits of the data for WT* iso-1-Cyt*c* and the WT*/L85A variant Eq. 3.1 (Experimental Procedures), which allows evaluation of the number of protons, *n*, linked to the conformational change show that *n* is approximately equal to 1 (Table 3.2) consistent with a one proton process, as expected for the alkaline transition (*3, 47*). The apparent acid dissociation constant for the alkaline transition, pK_{app}, of 8.66 for WT* iso-1-Cyt*c* is similar to the pK_{app} previously reported for yWT (Table 3.2) (*9, 81, 90*). The destabilizing mutation, L85A, shifts the equilibrium of the alkaline transition by 0.82 units when compared to WT* iso-1-Cyt*c*, similar to that previously reported for the yWT/L85A variant (*90*) (see Table 3.2).

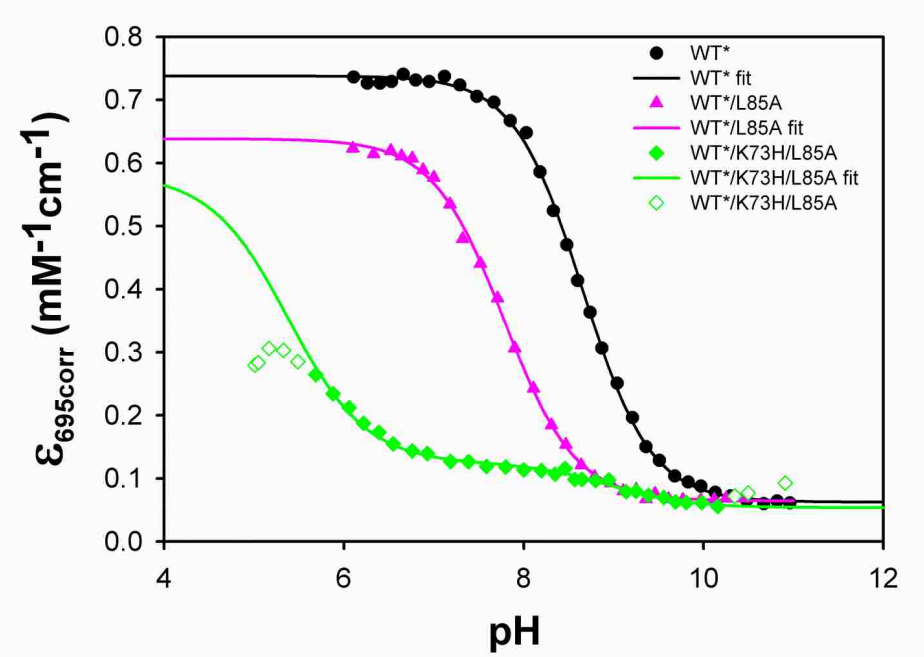

Figure 3.3. Millimolar extinction coefficients, $\varepsilon_{695corr}$ vs pH for WT* (black circles), WT*/L85A (pink triangles), and WT*/K73H/L85A (green diamonds) variants of yeast iso-1-Cyt*c* in 100 mM NaCl at 22 °C monitoring formation of the alkaline conformer. The monophasic transitions of WT* (solid black curve) and WT*/L85A (solid pink curve) are fit to Eq. 3.1 and the biphasic transition of WT*/K73H/L85A (solid green curve) is fit to Eq. 3.2 from Experimental Procedures. Data points shown as open green diamonds were not used in the fit.

Table 3.2. Thermodynamic parameters for the alkaline transition of iso-1-Cyt*c* variants obtained by pH titrations at 695 nm.[a]

Variant	pK_a	*n*-value
WT*[b]	8.66 ± 0.01	1.15 ± 0.02
yWT[c]	8.6 ± 0.1	-
WT*/L85A	7.84 ± 0.06	1.15 ± 0.09
yWT/L85A[c]	7.7 ± 0.1	-

[a]Parameters are the average and standard deviation of a minimum of three trials. [b]Parameters are from ref. (*88*). [c]Parameters are from ref. (*90*), fits assume *n* = 1. yWT/L85A carries a C102T rather than a C102S mutation

Inclusion of the K73H mutation results in biphasic behavior for the alkaline conformational transition requiring Eq. 3.2 (Experimental Procedures) to fit the data. The equilibrium constants for the His73-heme and Lys79-heme alkaline conformers are pK_{C1}(His) = -

0.84 ± 0.02 and pK_{C2}(Lys) = -2.8 ± 0.2, respectively. Population of a His73-heme ligand bound conformation occurs between pH 6 and 7.5 where His73 is expected to ionize. The fit to Eq. 3.2 (Experimental Procedures) yields pK_a(His) = 6.23 ± 0.08 consistent with ionization of His73. A Lys79-heme ligated population arises at a more alkaline pH (Figure 3.3). His73-heme ligation shifts the beginning of the alkaline transition to a more neutral pH because of the lower pK_a of histidine relative to lysine. For the WT*/K73H/L85A variant almost complete loss of Met80 has occurred by pH 7.5 (Figure 3.3). In fact, for K73H/L85A iso-1-Cyt*c*, the native state never fully populates prior to the onset of acid unfolding (Figure 3.3).

3.3.3 Kinetics of the alkaline conformational transition of WT*/L85A iso-1-Cyt*c*.

Populations of different iso-1-Cyt*c* conformers can be determined from the above thermodynamic studies. But to determine the actual rates of interconversion between conformations, kinetic studies utilizing stopped-flow pH jump techniques are used. Measured observed rate constants (k_{obs}) for conversion from the native (Met80-heme) to the alkaline conformers (His-heme, Lys-heme) are obtained from pH jump data. An example of fitted raw data is provided in Figure 3.4A.

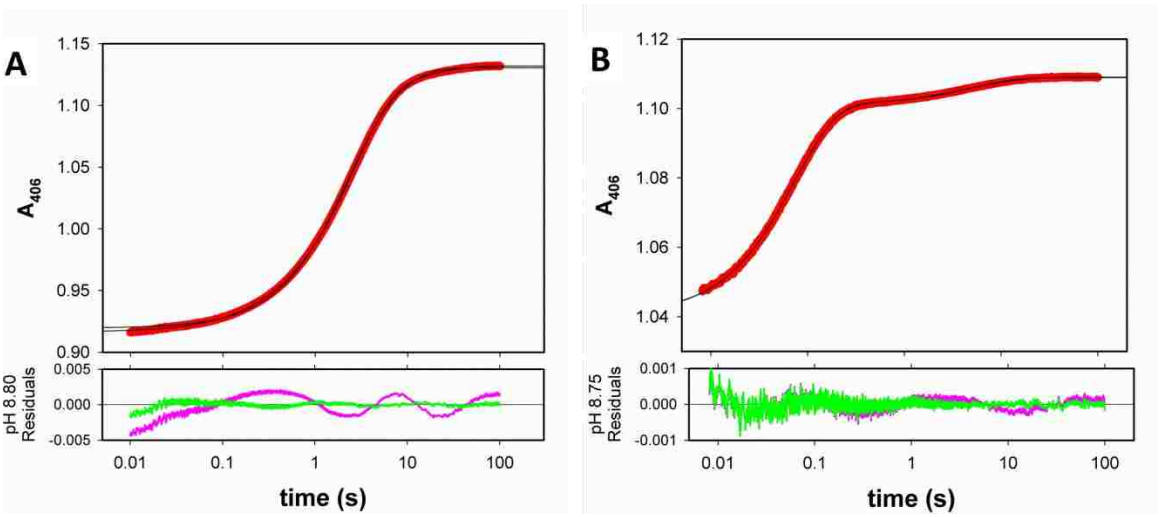

Figure 3.4. Representative fits to raw data from upward pH jump experiments demonstrating appropriateness of fits to a triple exponential equation versus fits to a double exponential equation for (A) WT*/L85A iso-1-Cyt*c* at pH 8.80 and (B) WT*/K73H/L85A iso-1-Cyt*c* at pH 8.75. Residuals are shown below each graph for both double (pink) and triple (green) exponential fits.

Three kinetic phases corresponding to a fast phase ($k_{obs,1,A85}$), and two slower phases ($k_{obs,2,A85}$ and $k_{obs,3,A85}$) are observed for the WT*/L85A variant (Figures 3.4 and 3.5 and Tables B2-B4).

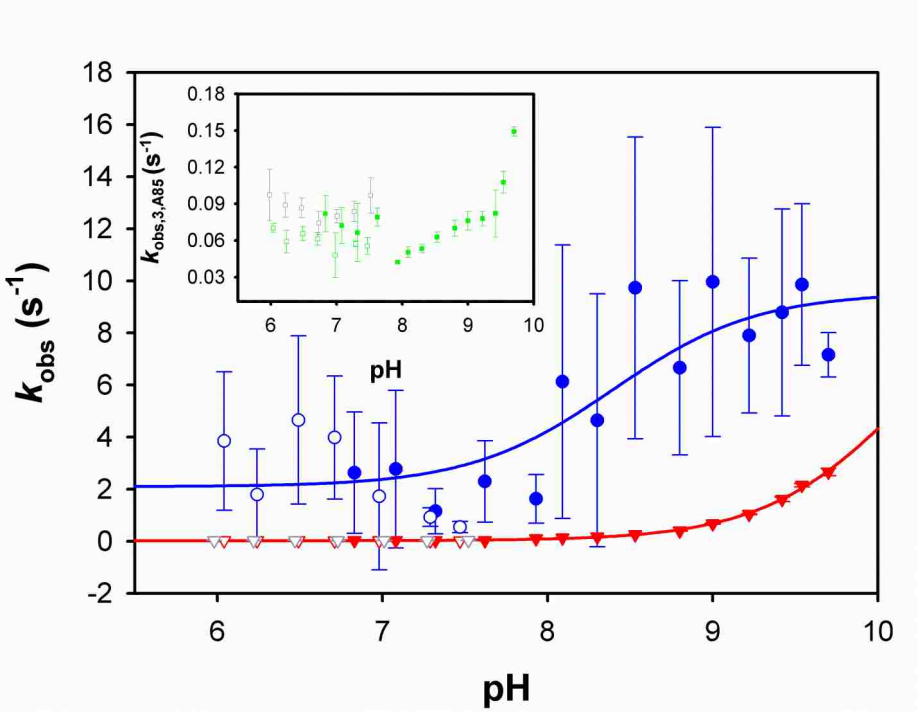

Figure 3.5. WT*/L85A iso-1-Cyt*c* plots comparing k_{obs} vs pH for the three kinetic phases observed for the alkaline conformational transition. Data from the fast phase ($k_{obs,1,A85}$) are shown as circles. One slow phase, $k_{obs,2,A85}$, is shown as inverted triangles. The other slow phase $k_{obs,3,A85}$, is shown as squares (inset). Filled data points are from upward pH jumps. Unfilled data points are from downward pH jumps from pH 8.5. Gray unfilled data points are for downward jumps from pH 9.5. All data points were used in the fits of $k_{obs,1,A85}$ and $k_{obs,2,A85}$ to Eq. 3.3. Data points are the average and standard deviation of a minimum of five trials.

The fast phase rate constant, $k_{obs,1,A85}$, of the WT*/L85A Cyt*c* variant cannot be obtained with high precision. Values near 2 s^{-1} begin increasing above pH 8 and approach 10 s^{-1}. The amplitude for the fast phase, $A_{1,A85}$, of the WT*/L85A variant is small at low pH but shows an increase beginning near pH 8. The relatively low amplitude of this phase may be the cause of the uncertainty observed in rate constants, particularly below pH 9.

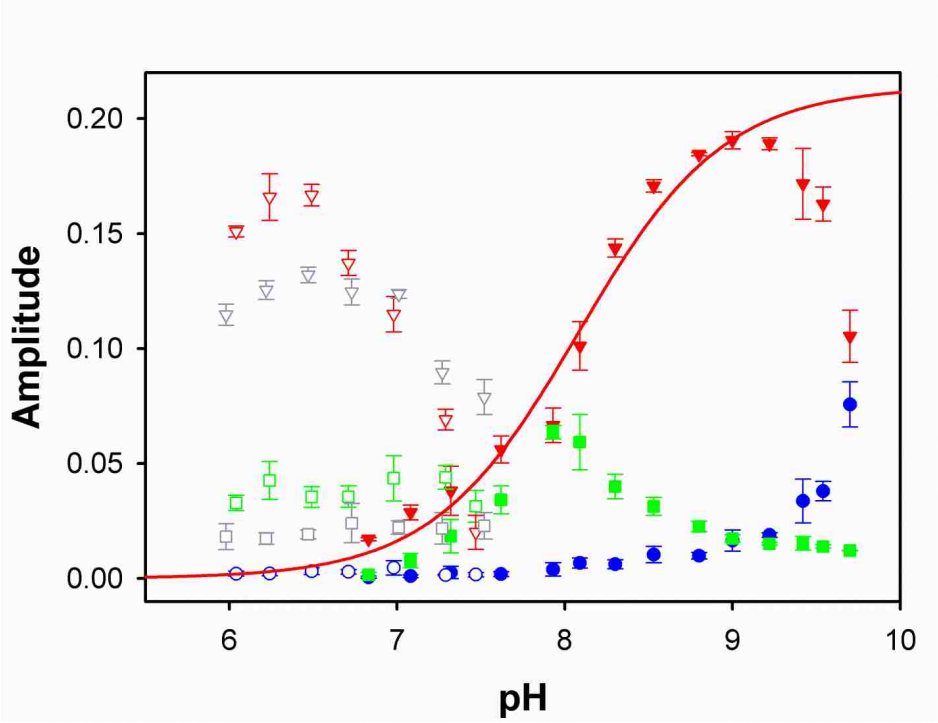

Figure 3.6. WT*/L85A iso-1-Cyt*c* plots comparing amplitudes vs pH for the three kinetic phases observed for the alkaline conformational transition. Circles correspond to fast phase amplitude, $A_{1,A85}$, inverted triangles to the amplitude for one slow phase, $A_{2,A85}$, and squares to the other slow phase amplitude, $A_{3,A85}$. Filled data points are from upward pH jumps. Unfilled data points are from downward pH jumps from either pH 8.5 or pH 9.5 (gray). $A_{2,A85}$ upward pH jump data from pH 6.83-9.22 are fit to Eq. 3.4 (red curve). Data points are the average and standard deviation of a minimum of five trials.

The rate constant for one of the two slow phases, $k_{obs,2,A85}$, remains relatively constant below pH 8, with values near 0.02 s^{-1} (Table B2). Above pH 8, $k_{obs,2,A85}$ increases to 1 s^{-1} as pH approaches 10. The amplitude for this phase, $A_{2,A85}$, displays the largest growth as pH increases. $A_{2,A85}$ increases from about 0.03 at pH 7 to 0.2 near pH 9, but begins to decrease above pH 9.

The rate constant for the other slow phase, $k_{obs,3,A85}$, is larger than $k_{obs,2,A85}$ at low pH (~0.06 s^{-1}, see Table B2). A slight dip in $k_{obs,3,A85}$ occurs near pH 8 followed by an increase as pH approaches 10. The amplitude for this phase, $A_{3,A85}$, initially increases reaching a maximum near pH 8 and then decreases (Figure 3.6).

In order to obtain accurate rate constants in the lower pH regime, downward pH jump experiments were carried out beginning at either pH 8.5 or pH 9.5, jumping to pH 5-6.5 in both cases. Downward pH jumps from pH 8.5 were fit to a tri-exponential equation. Only two phases could be resolved for downward jumps from pH 9.5. Observed rate constants for the two phases present in downward pH jumps from pH 9.5 correspond with $k_{obs,2,A85}$ and $k_{obs,3,A85}$ observed in upward pH jumps. The magnitudes of the amplitudes for downward pH jumps from either pH 8.5 or 9.5 are consistent with amplitude data for the corresponding upward pH jump kinetic phases (Figure 3.5).

3.3.4 Kinetics of the alkaline conformational transition of WT*/K73H/L85A iso-1-Cyt*c*.

Similarly for the WT*/K73H/L85A variant, three kinetic phases, a fast phase, and two slower phases, are present for the alkaline conformational transition. Representative kinetic traces are provided in Figure 3.4B. Observed rate constants and corresponding amplitude values are shown in Figures 3.7 and 3.8 and are collected in Tables B5-6.

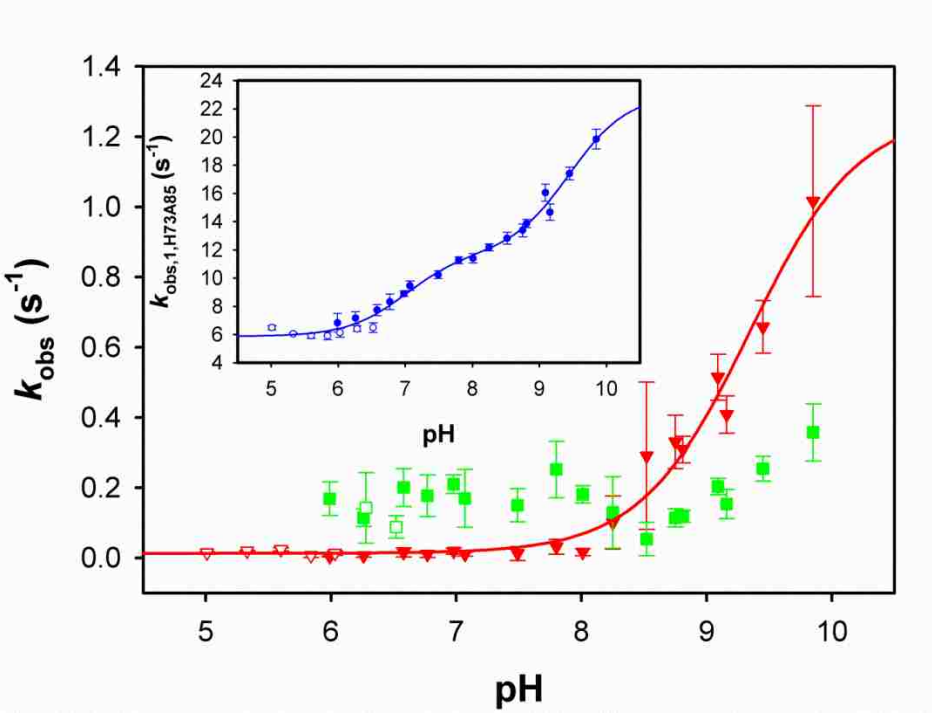

Figure 3.7. WT*/K73H/L85A iso-1-Cyt*c* plots comparing k_{obs} vs pH for the three kinetic phases of the alkaline conformational transition. Data for one slow phase, $k_{obs,2,H73A85}$, are shown as inverted triangles. Data for the other slow phase, $k_{obs,3,H73A85}$, are shown as squares. Fast phase data, $k_{obs,1,H73A85}$, (inset) are shown as circles. Filled data points are from upwards pH jumps and unfilled data points are from downward pH jumps from pH 7.5. Upward and downward data were included in the fits (solid curves) of $k_{obs,1,H73A85}$ and $k_{obs,2,H73A85}$ versus pH data to Eq. 3.5 and Eq 3.3, respectively. Data points are the average and standard deviation of a minimum of five trials.

For the WT*/K73H/L85A variant, the fast kinetic phase rate constant ($k_{obs,1,H73A85}$, inset to Figure 3.7) initially increases from pH 6-8, then continues to increase again above pH 9. $A_{1,H73A85}$ is considerably larger than $A_{2,H73A85}$ and $A_{3,H73A85}$ at all pH values. $A_{1,H73A85}$ increases levelling out near pH 7-9 and begins dropping off above pH 9.

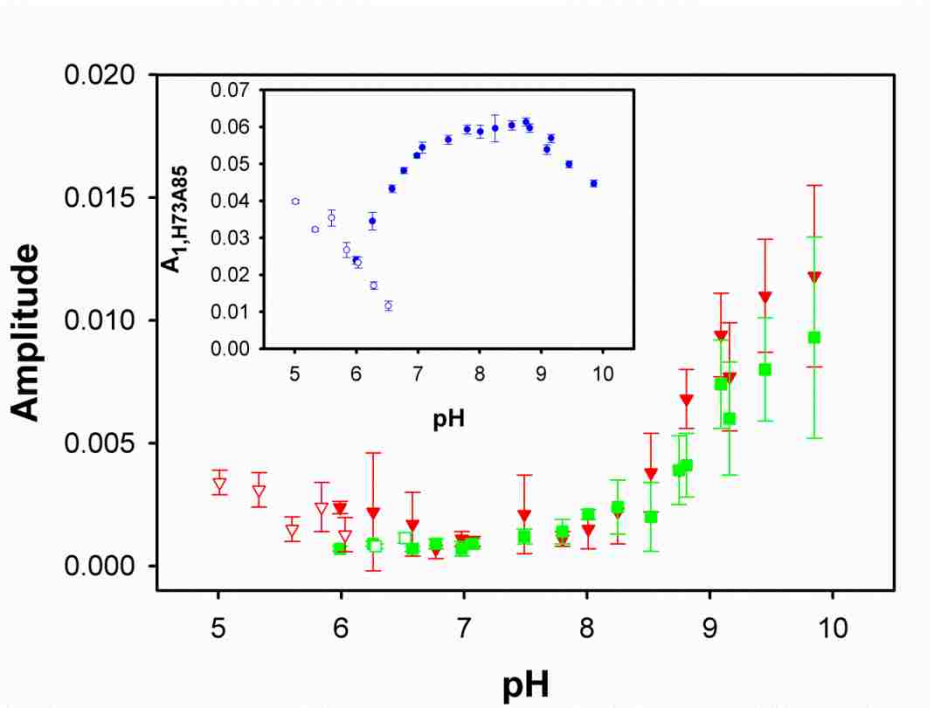

Figure 3.8. WT*/K73H/L85A iso-1-Cyt*c* plots comparing amplitudes vs pH for the three kinetic phases of the alkaline conformational transition. Inverted triangles correspond to one slow phase amplitude, $A_{2,H73A85}$, and squares to the other slow phase amplitude, $A_{3,H73A85}$. Circles (inset) correspond to the fast phase amplitude, $A_{1,H73A85}$. Filled data points are from upwards pH jumps and unfilled data points are from downward pH jumps from pH 7.5. Data points are the average and standard deviation of a minimum of five trials.

The rate constant for one of the two slow phases, $k_{obs,2,H73A85}$, is relatively invariant below pH 8. From pH 8 to 10 $k_{obs,2,H73A85}$ increases by almost two orders of magnitude. An increase in the amplitude for this phase, $A_{2,H73A85}$, also begins near pH 8. This increase in $A_{2,H73A85}$ at higher pH coincides with the decrease in $A_{1,H73A85}$. This behavior mirrors that of $k_{obs,2,A85}$.

The other slow phase rate constant, $k_{obs,3,H73A85}$, remains relatively invariant near 0.17 s^{-1}, although a small increase may be evident approaching pH 10. In the WT*/K73H/L85A variant $A_{3,H73A85}$ values demonstrate similar behavior and magnitude to $A_{2,H73A85}$.

In the case of downward pH jumps, fits to bi-exponential equations were found to be appropriate. The faster of these two phases demonstrates amplitude magnitudes consistent with

$A_{1,H73A85}$ for upward pH jumps. Due to the similarities in $A_{2,H73A85}$ and $A_{3,H73A85}$ the second phase could not be assigned from amplitude data alone. However, the rate constants from pH 5-6 are consistent with $k_{obs,2,H73A85}$ from upward jumps. From pH 6-6.5 for downward pH jumps, the rate constant correlates better with the upward pH jump rate constant $k_{obs,3,H73A85}$. Relatively small amplitude values may be responsible for the difficulty in resolving each of these phases individually.

3.3.5 Conformationally-gated electron transfer experiments.

In order to directly measure the forward and backward microscopic rate constants associated with the alkaline conformational transition of the WT*/K73H/L85A variant, conformationally-gated electron transfer (gated ET) techniques were applied. Direct electron transfer from $Co(terpy)_2^{2+}$ reduces oxidized Cyt*c* in the native Met80-heme ligand conformer (*14, 15, 19, 63*). Non-native conformers, such as the His73-heme or Lys79-heme alkaline conformers, which have lower reduction potentials and cannot be reduced directly (*9, 39, 72*), first must undergo a conformational rearrangement to the native Met80-ligand before reduction by $Co(terpy)_2^{2+}$ can be observed. The slower timescale of conformational rearrangement relative to direct reduction of the native protein yields gated ET.

Data collected on a long, 100-400 s, timescale were fit to a triple or quadruple exponential equation (Figure 3.9A). Due to drive syringe artifacts on a similar timescale, the fastest phase becomes less reliable when determined from these data. Therefore, short, 5 s, timescale data, collected using pressure holds, were used to minimize drive syringe artifacts and more accurately measure the fastest phase. Bi-exponential fits were found to be most appropriate for the short timescale data (Figure 3.9B). Observed rate constants and corresponding amplitude values can be found in Tables B7 and B8.

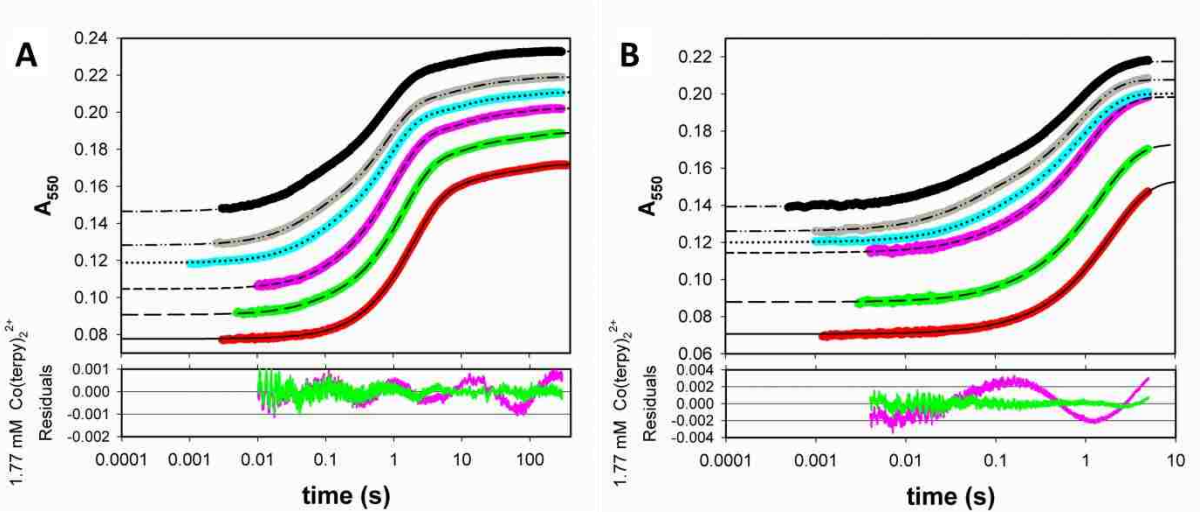

Figure 3.9. Representative fits to raw data for conformationally-gated electron transfer experiments for (A) long, 300-350 s, runs and (B) short, 5 s, runs with pressure holds of the WT*/K73H/L85A iso-1-Cyt*c* variant at pH 6. Bis(2,2',2"-terpyridine)cobalt(II) hexafluorophosphate concentrations were as follows: 0.50 mM $Co(terpy)_2^{2+}$ (red circles, fit to solid line), 0.87 mM $Co(terpy)_2^{2+}$ (green circles, fit to long dashed line), 1.77 mM $Co(terpy)_2^{2+}$ (pink circles, fit to short dashed line), 2.92 mM $Co(terpy)_2^{2+}$ (cyan circles, fit to dotted line), 4.22 mM $Co(terpy)_2^{2+}$ (gray circles, fit to dash-dot-dot-dashed line), and 5.11 mM $Co(terpy)_2^{2+}$ (black circles, fit to dash-dot-dashed line). Below graph A are the residuals of a triple (pink) and quadruple (green) exponential fit for 1.77 mM $Co(terpy)_2^{2+}$. Below graph B are the residuals of a single (pink) and double (green) exponential fit for 1.77 mM $Co(terpy)_2^{2+}$. These residuals demonstrate that a double and quadruple exponential fits are appropriate for the short and long runs, respectively. For clarity between individual traces in both A and B, A_{550} has been offset by subtracting the following absorbance values: 0.3, 0.46, 0.85, 0.28, 0.4, and 0.43 at 0.50, 0.87, 1.77, 2.92, 4.22, and 5.11 mM $Co(terpy)_2^{2+}$, respectively.

For gated ET experiments, when the concentration of $Co(terpy)_2^{2+}$ is high, direct electron transfer is fast compared to conformational rearrangements. Therefore, comparison of the amplitudes associated with each of the four phases provides the relative population of the conformations of iso-1-Cyt*c* present in solution at each pH (Figure 3.10). The amplitude of the fastest phase, $Amp_{1,ET}$ (black circles, Figure 3.10), decreases with an increase in pH, as expected for the native Met80-heme conformer undergoing direct electron transfer. The amplitude of the second phase, $Amp_{2,ET}$ (red squares, Figure 3.10), contributes a significant proportion of the amplitude throughout the pH regime investigated consistent with the His73-heme alkaline

conformer. Two slow phases show minor contributions. $Amp_{3,ET}$ (blue triangles, Figure 8) undergoes a slight increase in amplitude near pH 6 and decreases approaching pH 7. This increase mirrors the His73-heme phase, suggestive of proline isomerization associated with the His73-heme conformer, where $Amp_{2,ET}$ corresponds to the His73-heme *trans*-Pro phase and $Amp_{3,ET}$ is the His73-heme *cis*-Pro conformer (*14*, *21*). As expected for a Lys79-heme conformer in this pH regime, $Amp_{4,ET}$ (green diamonds, Figure 3.10) remains relatively invariant.

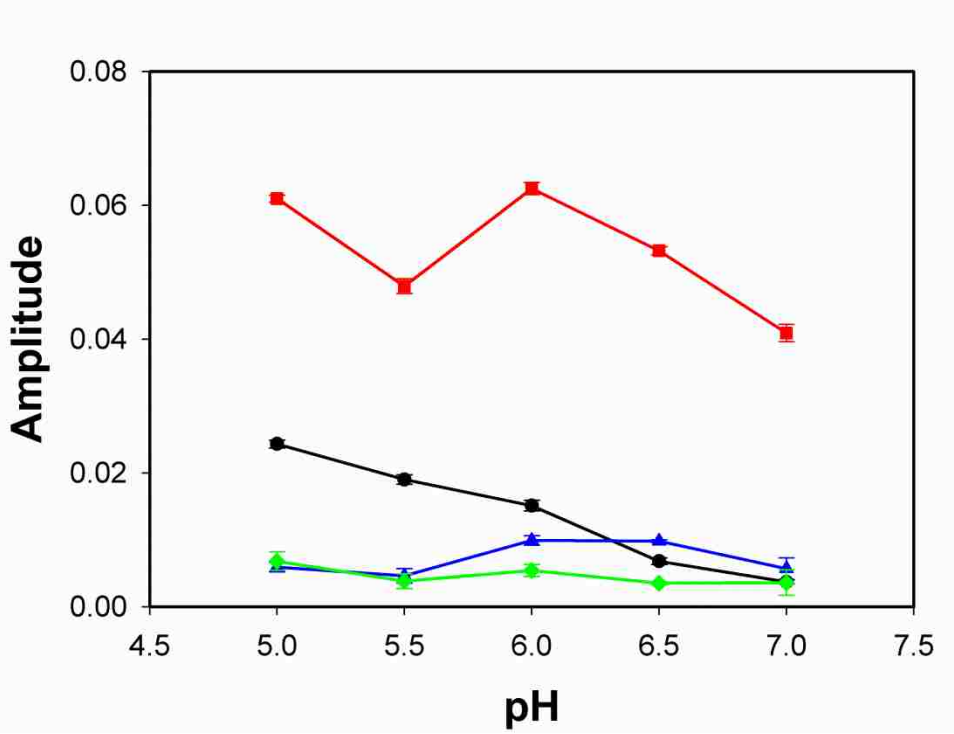

Figure 3.10. Amplitude data vs pH, corresponding to change in absorbance at 550 nm, from gated ET experiments for WT*/K73H/L85A iso-1-Cyt*c*. $Co(terpy)_2^{2+}$ concentrations for $Amp_{1,ET}$ (black circles and line), $Amp_{2,ET}$ (red squares and line), $Amp_{3,ET}$ (blue triangles and line), and $Amp_{4,ET}$ (green diamonds and line) at pH 5, 5.5, 6, 6.5, and 7 were 3.26, 3.17, 2.92, 3.05, and 3.19 mM, respectively. $Amp_{1,ET}$ data points are from 5 s experiments carried out with pressure holds. $Amp_{2,ET}$, $Amp_{3,ET}$, and $Amp_{4,ET}$ are from 100-400 s timescale data acquisitions. Error bars are the standard deviation of the average.

3.4 Discussion

3.4.1 Thermodynamic effects of L85A on yeast iso-1-Cyt*c*.

This work investigates a variant of iso-1-Cyt*c* destabilized by a Leu85Ala mutation residing near the edge of the heme crevice loop. Replacement of Leu85 with alanine leads to a decrease in global stability by a factor of two (Table 3.1), as expected from previous work performed on yWT/L85A (*27*). Addition of the K73H mutation to this destabilized WT*/L85A Cyt*c* variant contributes only modestly to the global stability (Table 3.1), providing a platform to investigate the effects of a destabilizing mutation located near the edge of Ω-loop D on heme crevice dynamics. Monitoring the alkaline transition as a function of pH demonstrates a biphasic transition for the WT*/K73H/L85A variant, providing the ability to distinguish between the dynamics of the residue 73-mediated and the residue 79-mediated alkaline conformational transition (Figure 3.3). As noted previously (*90*), the L85A mutation causes a loss of stability in the heme crevice loop, enabling access to the alkaline transition at a more neutral pH (Table 3.2). Compared to WT*/K73H, where pK_{C1}(His) = 0.67 ± 0.05 (*88*), the WT*/K73H/L85A variant demonstrates a negative magnitude for pK_{C1}(His) (-0.84 ± 0.02). Therefore, the L85A mutation stabilizes the His73-mediated alkaline state relative to the native state ($\Delta\Delta G$ = -2.04 ± 0.09). Interestingly, this $\Delta\Delta G$ is similar to the change in global stability during unfolding experiments (Table 3.1). Lower global stability caused by destabilization of a low stability region, such as Ω-loop D, is consistent with previously identified behavior in the foldon units of equine Cyt*c* (*8*). The effect of the L85A mutation on global and local stability supports the finding that Ω-loop D may represent a region of unfolding early in the unfolding pathway of Cyt*c* (*95*).

3.4.2 Effect of the L85A mutation on the kinetics of the alkaline transition.

Wild-type cytochrome *c* has previously been described to access the alkaline conformer via a two state transition (*96*). In this standard model, a conformational rearrangement occurs as Lys replaces the Met80-heme ligand following a rapid deprotonation equilibrium, represented as K_H or pK_H. From equation 3.3, with increasing pH the observed rate constant k_{obs} is expected to increase.

(3.3)

$$k_{obs} = k_b + k_f\left(\frac{1}{1 + 10^{pK_H - pH}}\right)$$

The forward rate constant, k_f, corresponds to opening of the heme crevice loop as the Met80-heme ligand is lost and k_b, represents the return to the native conformer from the alkaline state.

pH titration data clearly shows the monophasic behavior of a two state transition for the WT*/L85A iso-1-Cyt*c* variant as either Lys73 or Lys79 become ligated to the heme (Figure 3.3). Interestingly, three phases are observed during pH jump stopped-flow experiments. The rate constants for the fastest phase, $k_{obs,1,A85}$, have large error bars. We can fit $k_{obs,1,A85}$ versus pH to Eq. 3.3. Parameters from the fit of $k_{obs,1,A85}$ are: pK_H = 8.4 ± 0.3, k_b = 2.1 ± 0.6, and k_f = 7 ± 1. Application of the fit associated with a single pH ionization should be viewed with some skepticism due to the large error bars on $k_{obs,1,A85}$. However, formation of an intermediate state during the alkaline transition with a loss of the Met80-heme ligand and a midpoint of formation near pH 8.8, prior to formation of Lys-heme conformers has previously been demonstrated in horse cytochrome *c* (*97*). Further, another intermediate between native and alkaline conformers where Met80 is still associated with the heme has been described in horse Cyt*c* with a pK_a of 8.5 (*98*). This similarity in pK_a values may suggest that the $k_{obs,2,A85}$ phase is an intermediate transiently populating along the pathway to access the alkaline conformer. In downward pH

jump experiments, this phase is observed when jumping downward from pH 8.5 but not from pH 9.5, indicating that the intermediate associated with this phase is only transiently populated at higher pH.

As expected from the standard two state transition model for the Lys-heme alkaline conformer, with increasing pH $k_{obs,2,A85}$ increases as the Met80-heme ligand is replaced with Lys from either residue 73 or 79 (Figure 3.5). An increase in amplitude above pH 7 (Figure 3.6) is consistent with Lys-heme ligation from thermodynamic data (Figure 3.3). Parameters for the fit of $k_{obs,2,A85}$ versus pH to equation 3 are: pK_H = 10.18 ± 0.06, k_b = 0.018 ± 0.007, and k_f = 11 ± 1. This pK_H value is similar to the value previously published for a Lys73Ala variant of yeast iso-1-Cyt*c* (10.8 ± 0.1) where Lys79 is the heme ligand in the alkaline conformer (*9*). Furthermore, the k_b value from the fit of $k_{obs,2,A85}$ is in good agreement with that from the Lys73Ala (0.016 ± 0.001) (*9*). The value for k_f obtained from the fit does not match that for the K73A as well. However, values for k_f are more poorly determined because of the lack of a well-defined upper constraint on the fit.

Amplitude versus pH data for $A_{2,A85}$ (Figure 3.6) were also fit to the standard kinetic model for the alkaline conformational transition using Eq. 3.4 (*18*, *96*).

(3.4)

$$\Delta A = \Delta A_t \left(\frac{1}{1 + \frac{k_b}{k_f}(1 + 10^{pK_H - pH})} \right)$$

The total amplitude of the alkaline transition is represented by ΔA_t. In the fit to $Amp_{2,A85}$ versus pH data k_b and k_f were set equal to the values determined from the fit of $k_{obs,2,A85}$ versus pH by Eq. 3.3. $A_{2,A85}$ versus pH fit to eq. 4 yields values for ΔA_t and pK_H of 0.214 ± 0.009 and 10.87 ± 0.06, respectively. This value for pK_H is similar to that calculated from the observed rate

constants for a Lys79-heme ligated alkaline conformer and again is consistent with data for the K73A variant of iso-1-Cyt*c* (*9*), consistent with assignment of this kinetic phase to formation of the Lys79-heme alkaline conformer.

The final phase for the L85A variant, $k_{obs,3,A85}$ and $A_{3,A85}$, may be due to Lys73 as an alkaline state heme ligand. As pH increases this phase initially populates reaching a maximum near pH 8. Above this pH, Lys73 is outcompeted by Lys79. This decreased population of this phase above pH 8 may be related to the ionization event near 8.4 observed for $k_{obs,1,A85}$. $k_{obs,3,A85}$ does show an increase above pH 9. However, this increase is insufficient to allow Lys73 to compete with Lys79 for heme binding in the alkaline state.

3.4.3 Kinetics of the alkaline transition of WT*/K73H/L85A variant.

Replacement of Lys73 with histidine leads to a more complicated pathway for accessing the alkaline state. Previous work on variants with histidine replacing a lysine has demonstrated multiple ionization events linked to the alkaline conformational transition (*14, 16, 18-21, 63, 88*). The pH dependence of $k_{obs,1,H73A85}$ in Figure 3.7 inset was fit to equation 3.5, which assumes that two ionizable groups, His73-H^+ and a second ionizable group termed Y-H^+, affect this rate constant as outlined in Scheme 3.1 (*16, 21*).

(3.5)

$$k_{obs} = \left(\frac{K_{HL}}{K_{HL} + [H^+]}\right)\left(\frac{k_{f1}[H^+] + k_{f2}K_{H2}}{K_{H2} + [H^+]}\right) + \left(\frac{k_{b1}[H^+] + k_{b2}K_{H2}}{K_{H2} + [H^+]}\right)$$

The parameters from the fit are reported in Table 3.3. K_{HL}, or pK_{HL}, is the ionization constant of the His73 ligand replacing the Met80-bound heme, which occurs near neutral pH. The pK_{HL} obtained from the fit is consistent with ionization of His73. The forward rate constant, k_{f1}, of the conformational change from a Met80-heme to a His73-heme bound conformer and the reverse rate constant, k_{b1}, are found to be equal to one another. pK_{H2} obtained from the fit is consistent

with values obtained for this ionization with other variants of iso-1-Cyt*c* carrying a K73H mutation.

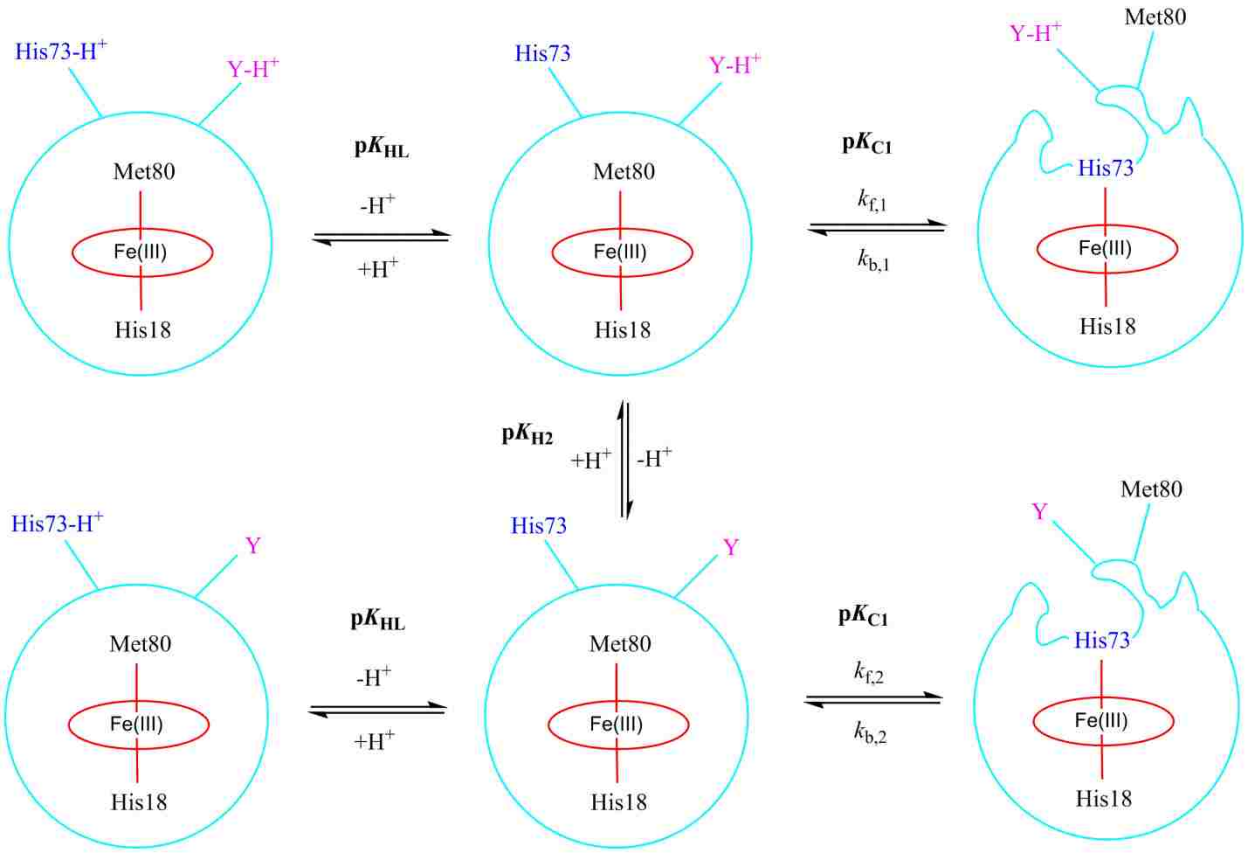

Scheme 3.1. Representation of kinetic equilibria as a function of pH during the alkaline conformational transition for the WT*/K73H/L85A variant. Y-H$^+$ represents a second ionizable group within the protein.

Table 3.3. Rate and ionization constants of the WT*/K73H/L85A His73-heme alkaline transition at 25 °C.[a]

Parameter	WT*/K73H/L85A
k_{f1} (s^{-1})	5.9 ± 0.4
k_{b1} (s^{-1})	5.9 ± 0.2
k_{f2} (s^{-1})	11.6 ± 0.9
k_{b2} (s^{-1})[b]	12 ± 1
pK_{HL}	7.0 ± 0.1
pK_{H2}	9.4 ± 0.1

[a]Errors are standard errors reported by SigmaPlot. [b]For the second ionization, k_{b2} has been constrained to equal $k_{f2}*k_{b1}/k_{f1}$.

One of the slower kinetic phases of the WT*/K73H/L85A variant demonstrates behavior suggestive of Lys-heme ligation. $k_{obs,2,H73A85}$ and its associated amplitude both increase above pH 8. Parameters for the fit of $k_{obs,2,H73A85}$ versus pH to equation 3.3 (see Figure 3.7) are: pK_H = 9.34 ± 0.08, k_b = 0.01 ± 0.01, and k_f = 1.26 ± 0.10. Although, the error is more significant, k_b for this phase of the WT*/K73H/L85A Cyt*c* variant is similar to the aforementioned value for a Lys79-heme alkaline conformer. This further supports the assignment of a Lys79-heme conformer to $k_{obs,2,A85}$. Interestingly, replacement of Lys73 with histidine appears to lower the pK_H of the lysine alkaline conformer.

Increased amplitude is observed at elevated pH for the third phase of the WT*/K73H/L85A variant, suggestive of an additional poorly defined alkaline conformer partially populating. Mutation of Leu85, a highly conserved residue on the edge of the heme-crevice loop may enable heme ligation from residues near Ω-loop D, such as Lys86 or Lys87. Additional mutagenesis would be required to identify specific ligand contributions.

Interestingly, comparison of thermodynamic and kinetic data for the His73-heme alkaline transition yields a lack of coincidence. From the fit of $k_{obs,1,H73A85}$ versus pH to equation 3.5 (Table 3.5), k_{f1} and k_{b1} are equal to one another predicting a 1:1 equilibrium ratio (K_{C1}(His) = 1). However, from analysis of equilibrium data, K_{C1}(His) = 6.9. Clearly, the currently employed kinetic model is unable to accurately determine the forward and reverse rate constants. This lack of coincidence between kinetic and thermodynamic measurements suggests that there may be further ionization events which affect the kinetics of the His73-heme alkaline transition of WT*/K73H/L85A iso-1-Cyt*c*. In order to more directly measure these rate constants, gated ET methods were employed.

Table 3.4. Kinetic parameters from gated ET data for $k_{obs,1,ET}$ and $k_{obs,2,ET}$ for the WT*/K73H/L85A iso-1-Cyt*c* variant.[a]

pH	k_{ET} (mM^{-1} s^{-1})[b]	k_{uni} (s^{-1})[b]	$k_{b,His}$ (s^{-1})[c]	$k_{f,His}$ (s^{-1})[c] ($k_{f,His,PK}$ (s^{-1})[d])
5	3.9 ± 0.2	2.8 ± 0.7	2.6 ± 0.1	4.3 ± 0.7 (4.8 ± 0.8)
5.5	4.0 ± 0.7	3 ± 2	2.6 ± 0.3	7 ± 2 (9 ± 2)
6	3.2 ± 0.2	5.4 ± 0.8	1.62 ± 0.02	3.3 ± 0.1 (4.0 ± 0.2)
6.5	3.0 ± 0.6	8 ± 2	1.27 ± 0.04	5.7 ± 0.5 (8.0 ± 0.7)
7	3.1 ± 0.3	8 ± 1	1.2 ± 0.1	8 ± 2 (12 ± 3)

[a]Errors are standard errors reported by SigmaPlot. [b]From fits to equation 3.6. [c]From fits to equation 3.7. [d]From fits of $k_{obs,2,ET}$ to equation 3.7 using $k_{ET,PK}$ from Table 3.5.

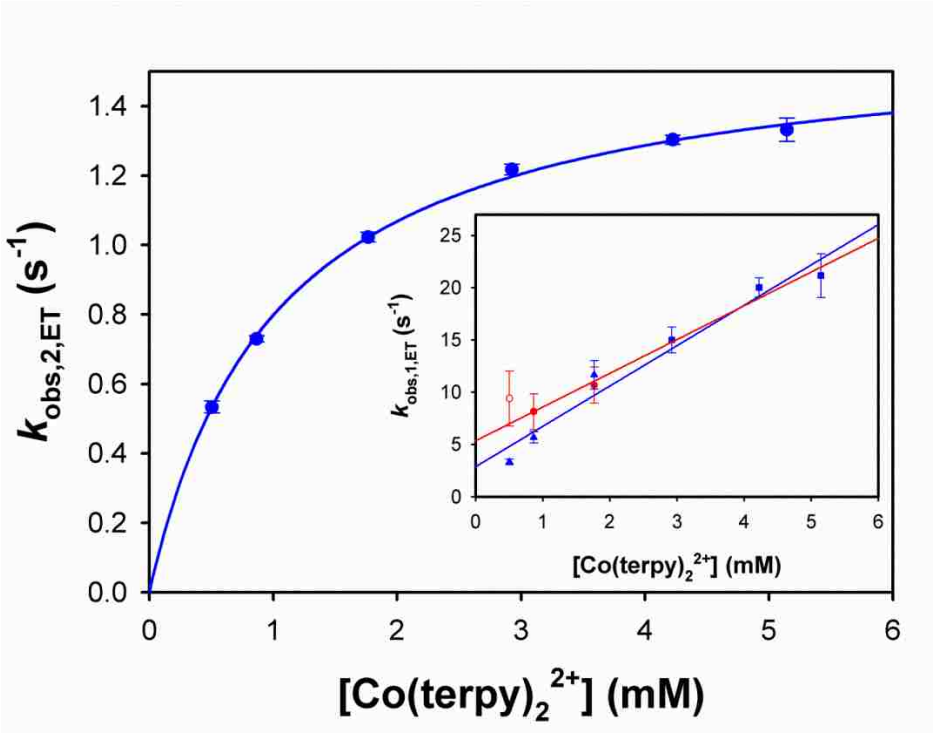

Figure 3.11. Plot of $k_{obs,2,ET}$ vs [Co(terpy)$_2^{2+}$] at pH 6 fit to Eq. 3.7 (solid curve) where k_{ET} values were set to equal $k_{ET,PK}$ from Table 3.5. Inset: Plot of $k_{obs,1,ET}$ vs [Co(terpy)$_2^{2+}$] at pH 6. Data for $k_{obs.1.ET}$ values determined from fits of raw data in SigmaPlot (red and blue circles) are fit to Eq. 3.5 (red curve). The unfilled data point at 0.5 mM Co(terpy)$_2^{2+}$ was not included in the fit. Low Co(terpy)$_2^{2+}$ concentration $k_{obs,1,ET,PK}$ values determined from Pro-Kineticist (blue triangles) and high Co(terpy)$_2^{2+}$ concentration $k_{obs,1,ET}$ values determined from SigmaPlot (blue circles) were fit to Eq. 3.6 (blue curve). Data for both plots are the average and standard deviation of a minimum of five trials.

3.4.4 Analysis of conformationally-gated ET experiments.

Electron transfer rate data, $k_{obs1,ET}$, which corresponds to $Amp_{1,ET}$, is associated with direct reduction of Cyt*c* by bis(2,2′,2″-terpyridine)cobalt(II) hexafluorophosphate, $Co(terpy)_2^{2+}$ (Figure 3.10). A plot of $k_{obs1,ET}$ versus $[Co(terpy)_2^{2+}]$ is linear (Figure 3.11, inset). Scheme 3.2 outlines the square scheme mechanism used to analyze gated ET data (*14*, *15, 19, 20, 36, 63, 71, 88*). For iso-1-Cyt*c* in the native state, $Co(terpy)_2^{2+}$ reduces the protein in a bimolecular reaction with rate constant k_{ET} according to the rate law in Eq. 3.6.

(3.6)

$$k_{\mathrm{obs,1,ET}} = k_{\mathrm{ET}} * [\mathrm{Co(terpy)_2^{2+}}] + k_{\mathrm{uni}}$$

In equation 3.6, all unimolecular rate constants leading to disappearance of the native Met80-heme conformer are represented by k_{uni} ($k_{f,His}$ in Scheme 3.2, for example). Equation 3.6 also assumes that the back electron transfer is negligible (k_{-ET}). Thus, k_{ET} can be determined by fitting plots of $k_{obs,1,ET}$ versus $[Co(terpy)_2^{2+}]$ to Eq. 3.6. At the lowest $Co(terpy)_2^{2+}$ concentration (~0.5 mM), $k_{ob,s1,ET}$ increased rather than continuing to decrease at most pH values (Figure 3.11, inset and Table B7). The low amplitude of this phase at ~0.5 mM $Co(terpy)_2^{2+}$ and the overlap of the two fastest phases under these conditions makes it difficult to accurately determine $k_{obs,1,ET}$. Thus, the ~ 0.5 mM $Co(terpy)_2^{2+}$ data points were left out of fits at pH 5-6.5. As pH increased from 5-7, k_{ET} was found to decrease from 4 to 3 s^{-1} (Figure 3.12). Parameters from the fits of $k_{obs,1,ET}$ versus $[Co(terpy)_2^{2+}]$ are listed in Table 3.4. Following the trend observed for other K73H variants (*14, 20, 88*), k_{ET} values decrease with increasing pH.

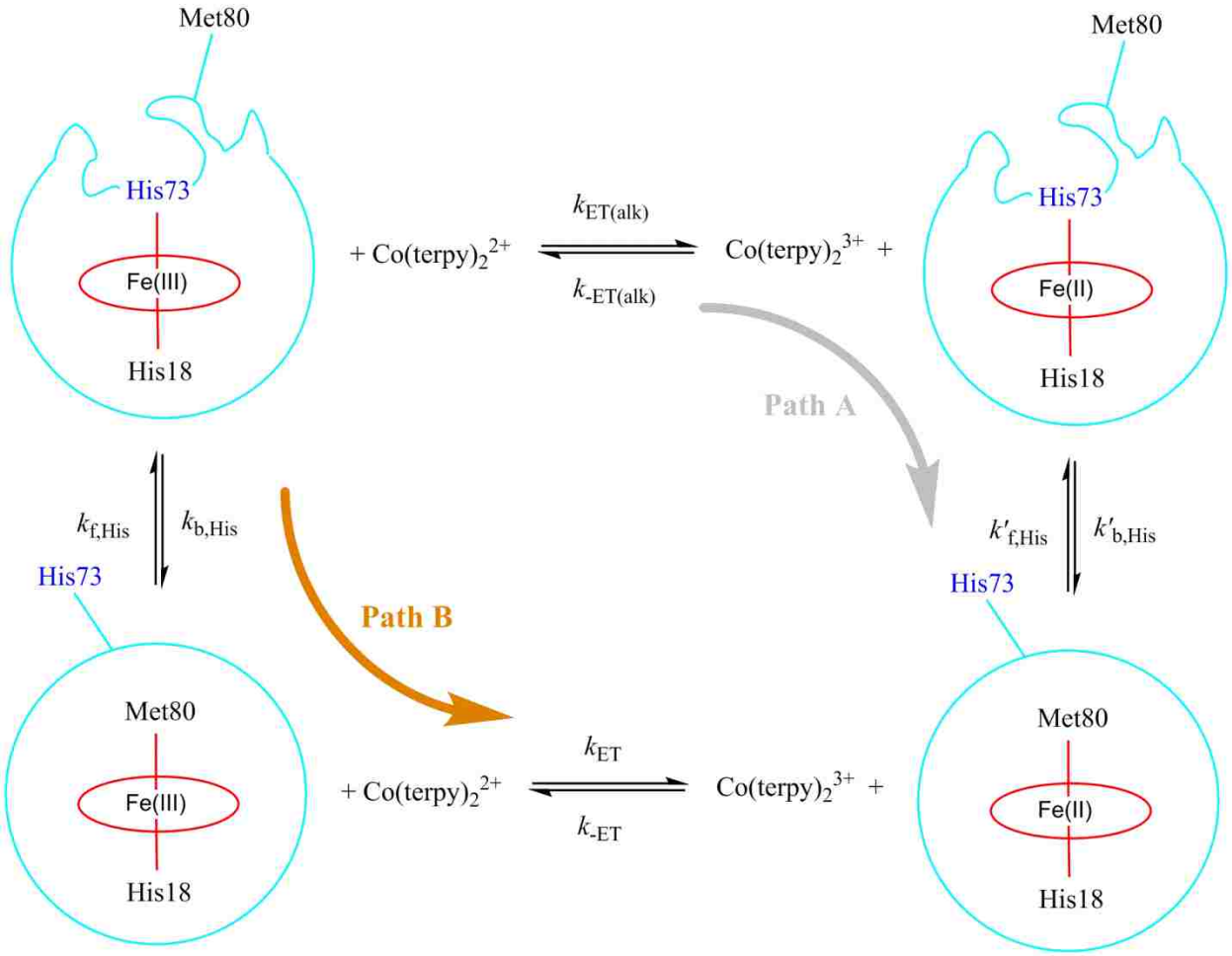

Scheme 3.2. Gated ET square scheme for the WT*/K73H/L85A iso-1-Cyt*c* variant showing Paths A and B.

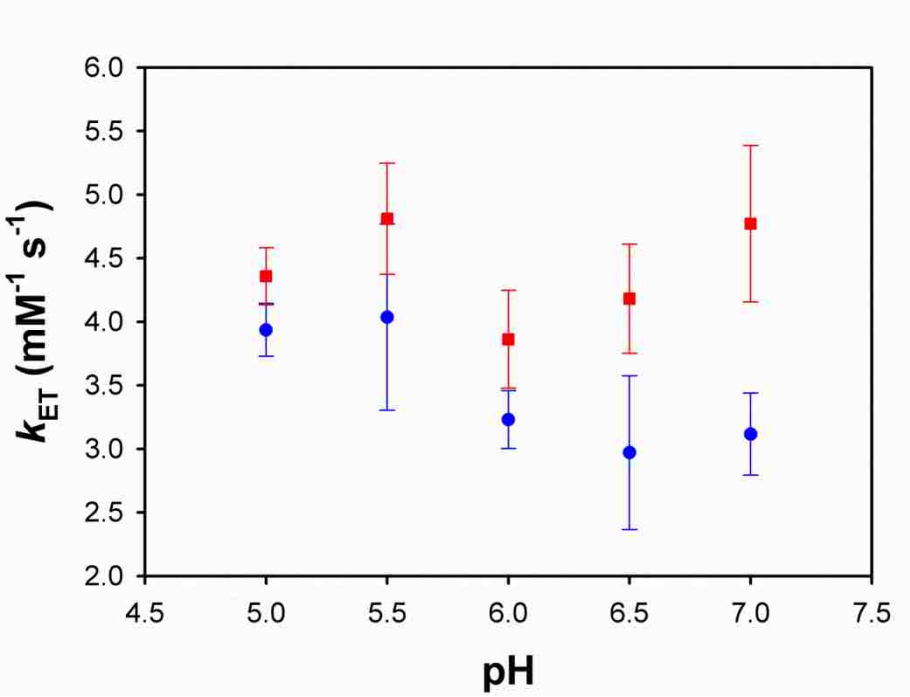

Figure 3.12. Comparison of k_{ET} and $k_{ET,PK}$ values vs pH determined from fits in Figure 3.9 inset and Tables 3.4 and 3.5. Error bars are the standard error of the slopes reported from fits of $k_{obs,1,ET}$ data. Blue circles correspond to k_{ET} values determined from fits of Eq 3.6 to the Co(terpy)$_2^{2+}$ concentration dependence of $k_{obs,1,ET}$ obtained using exponential fits to gated ET data in SigmaPlot. Red squares correspond to $k_{ET,PK}$ values (Table 3.5) from $k_{obs,1,ET}$ versus Co(terpy)$_2^{2+}$ concentration where $k_{obs,1,ET}$ at 0.5, 1, and 2 mM Co(terpy)$_2^{2+}$ corresponds to $k_{obs,ET,PK}$ in Table B10 determined from numerical fits in Pro-Kineticist.

Previous work has demonstrated that iso-1-Cyt*c* in an alkaline conformer must proceed through a conformational gate, returning to Met80-heme ligation, before undergoing reduction of the heme, as represented by Path B (*14*, *15*, *19*, *63*) in Scheme 3.2. Use of the steady-state approximation leads to Eq. 3.7 for reduction of the His73-heme alkaline conformer by Co(terpy)$_2^{2+}$ (*78-80*).

(3.7)

$$k_{\mathrm{obs,2,ET}} = \frac{k_{\mathrm{b,His}} k_{\mathrm{ET}} [\mathrm{Co(terpy)_2^{2+}}]}{k_{\mathrm{ET}} [\mathrm{Co(terpy)_2^{2+}}] + k_{\mathrm{f,His}}}$$

Based on amplitude data (Figure 3.10), $k_{obs,2,ET}$ corresponds to reduction of the His73-heme alkaline conformer by $Co(terpy)_2^{2+}$. A plot of $k_{obs,2,ET}$ versus $[Co(terpy)_2^{2+}]$ shows the hyperbolic shape expected from Eq. 3.7. The solid curve in Figure 3.9 shows a fit of $k_{obs,2,ET}$ versus $[Co(terpy)_2^{2+}]$ at pH 6 to Eq. 3.7 using k_{ET} obtained from the $k_{obs,1,ET}$ data (Figure 3.9, inset). The microscopic rate constants, $k_{f,His}$ and $k_{b,His}$, respectively, for the transition between Met80-heme and His73-heme ligated conformers from the fits of $k_{obs,2,ET}$ versus $[Co(terpy)_2^{2+}]$ at all pH values are provided in Table 3.4.

3.4.5 Numerical fitting of conformationally-gated ET experiments.

In order to address the possible breakdown of the steady state approximation used to derive Eq. 3.7 at low $Co(terpy)_2^{2+}$ concentration, and problems with the overlap of phases corresponding to $k_{obs,1,ET}$ and $k_{obs,2,ET}$ at low $Co(terpy)_2^{2+}$ concentration, which lead to apparent increases in $k_{obs,1,ET}$ at low $Co(terpy)_2^{2+}$ concentration (Figure 3.11, inset), we also fit stopped-flow gated ET traces using the numerical fitting program Pro-Kineticist. In Pro-Kineticist, data are directly fit to the reaction model shown in Scheme 3.3 using numerical integration accounting for concentration profiles of each substate in the reaction mechanism.

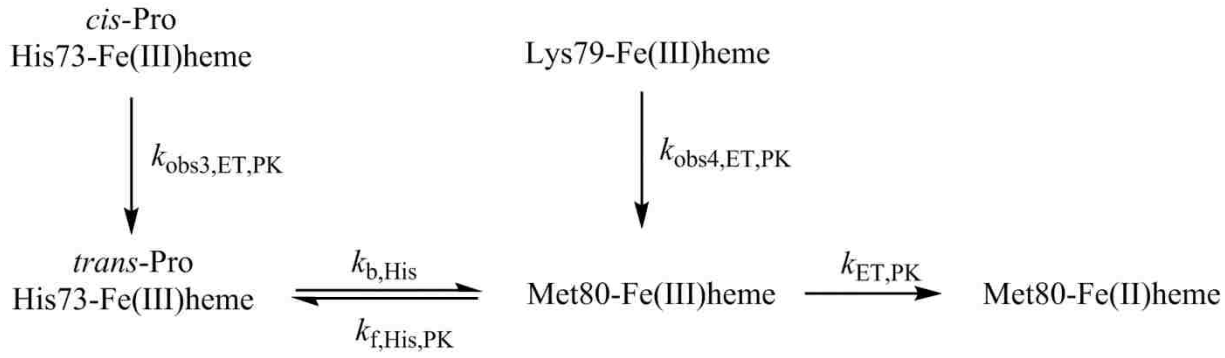

Scheme 3.3. Kinetic mechanism utilized for numerical fits in Pro-Kineticist.

For numerical integration, the initial concentrations of all protein conformers must be provided. These concentrations were calculated from amplitude data as determined from fits to

kinetic traces of gated ET data with exponential functions in SigmaPlot (see Experimental Procedures). Total amplitude, corresponding to the total change in absorbance at 550 nm, at each $Co(terpy)_2^{2+}$ concentration was calculated and the Cyt*c* concentration was determined using the difference between reduced and oxidized molar extinction coefficients ($\Delta\varepsilon_{550}$ = 19000 M^{-1} cm^{-1}). Fractional amplitude values for each protein conformer determined from fits of exponential curves in SigmaPlot at 5 mM $Co(terpy)_2^{2+}$, where the steady state approximation holds true, were used to determine the concentration of each protein conformer in the reaction mechanism (Scheme 3.3) present at each $Co(terpy)_2^{2+}$ concentration (Table B9). The reaction model in Scheme 3.3 was entered into the Pro-Kineticist program. Protein in the *cis*-Pro His73-Fe(III)heme conformer isomerizes to the *trans*-Pro His73-Fe(III)heme form before following Path B (Scheme 3.2) and undergoing reduction by $Co(terpy)_2^{2+}$. The Lys79-Fe(III)heme alkaline conformer also returns to the native Met80-heme conformer before undergoing reduction. At pH 5 and pH 5.5 a simpler model was used, where the Lys79-Fe(III)heme conformer was removed from the reaction scheme as this conformer does not have a significant population in this pH regime (see Table B9). The cis-Pro His73-heme, Lys79-heme, and Met80-heme conformers were constrained to have the known molar extinction coefficient for the oxidized form of the protein (ε = 9000 M^{-1} cm^{-1}). The extinction coefficients of the oxidized His73-heme conformer and of the reduced native state of the protein were not constrained.

To account for $Co(terpy)_2^{2+}$ absorbance, stopped-flow electron transfer trials were background corrected for numerical fitting in Pro-Kineticist by subtracting the absorbance associated with $Co(terpy)_2^{2+}$ from the total absorbance at 550 nm. Absorbance of $Co(terpy)_2^{2+}$ for long timescale trials was determined by subtracting the calculated reduced (FeII) iso-1-Cyt*c* absorbance contribution from the average total absorbance at the end of the reaction. Reduced

Cyt*c* absorbance contributions were calculated from the starting Cyt*c* concentrations (Table B9) with the reduced molar extinction coefficient ($\varepsilon = 28000\ M^{-1}\ cm^{-1}$). As short timescale trials have not achieved the fully populated reduced amplitude, the oxidized, Fe(III), Cyt*c* absorbance contribution was subtracted from the starting absorbance of traces to determine the background absorbance due to $Co(terpy)_2^{2+}$. Oxidized Cyt*c* absorbance contributions were calculated using the oxidized molar extinction coefficient and starting Cyt concentrations (Table B9).

As $k_{b,His}$ can accurately be determined from plots of $k_{obs,2,ET}$ versus $Co(terpy)_2^{2+}$ concentration, $k_{b,His}$ values from Table 3.4 were locked in Pro-Kineticist. All other rate constants were not constrained during numerical fitting. To more accurately account for the total amplitude in short timescale numerical fits, the slower proline isomerization and Lys79-heme conformer transitions were set to equal the average rate constants from long timescale numerical fits. Due to difficulty in numerically fitting pH 7 long timescale electron transfer data at 0.5 mM $Co(terpy)_2^{2+}$, the slow phase proline isomerization and Lys79-heme rate constants could not be directly measured. In order to account for the total amplitude during numerical fitting of pH 7 0.5 mM $Co(terpy)_2^{2+}$ short timescale data, rates for these slow phases were set equal to the average of 1 mM and 2 mM $Co(terpy)_2^{2+}$ long timescale data. The observed rate constant corresponding to electron transfer and the forward rate constant associated with formation of the His73-heme conformer from the native state, $k_{obs,ET,PK}$ and $k_{f,His,PKnum}$ respectively, were determined from numerical fits to the short timescale kinetic traces. In order to distinguish between data values determined using SigmaPlot versus Pro-Kineticist, rate and amplitude labels determined using Pro-Kineticist include a 'PK' subscript.

Rate constants for accessing the His73-heme conformer from the native state, $k_{f,His,PK,num}$ and for bimolecular electron transfer, $k_{obs,ET,PK}$, determined from numerical fits at 0.5, 1 and 2

mM $Co(terpy)_2^{2+}$ were averaged at each pH and are reported in Table 3.5. All rate constants obtained from numerical fitting with Pro-Kineticist may be found in Table B10. Values of $k_{obs,ET,PK}$ were plotted with 3, 4, and 5 mM $Co(terpy)_2^{2+}$ $k_{obs,1,ET}$ values and fit to Eq. 3.6 (Figure 3.11, inset). Rate constants from these fits at all pH values are summarized in Table 3.5. The intercept of these fits, corresponding to the sum of all unimolecular rate constants leading to loss of the Met80-heme conformer, $k_{uni,PK}$ in Table 3.5, demonstrate small rate constants suggesting minimal contribution, from these processes. Bimolecular rate constants of electron transfer determined using rate constants from numerical fits in Pro-Kineticist, $k_{ET,PK}$, demonstrate little change within error throughout the pH range 5 to 7 (Figure 3.12).

Table 3.5. Kinetic parameters for gated ET experiments on WT*/K73H/L85A iso-1-Cyt*c **based on numerical fitting with Pro-Kineticist software.

pH	$k_{ET,PK}$ (mM^{-1} s^{-1})[a]	$k_{uni,PK}$ (s^{-1})[a]	$k_{f,His,PK,num}$ (s^{-1})[b]
5	4.4 ± 0.2	1.2 ± 0.7	4.6 ± 0.6
5.5	4.8 ± 0.4	0.01 ± 1	6.0 ± 0.9
6	3.9 ± 0.4	3 ± 1	5.6 ± 0.6
6.5	4.2 ± 0.4	2 ± 1	10 ± 3
7	4.8 ± 0.6	1 ± 2	12 ± 2

[a]From fits to equation 3.5 as shown in Figure 3.11, inset. [b]Average and standard deviation from fits in Pro-Kineticist at each pH.

Using the corrected direct electron transfer value, $k_{ET,PK}$, $k_{obs,2,ET}$ versus $[Co(terpy)_2^{2+}]$ data were fit to equation 3.7 to re-evaluate forward microscopic rate constant, $k_{f,His,PK}$ (Table 3.4). There is a small increase in $k_{f,\ His,PK}$ relative to $k_{f,His}$ values in Table 3.4 due to the increase in $k_{ET,PK}$ relative to k_{ET}. Within error, $k_{f,His,PK}$ values are approximately equal to the forward rate constant determined directly from numerical fits, $k_{f,His,PK,num}$, in Table 3.5 except at pH 5.5.

3.4.6 Comparison of pH jump and conformationally-gated ET stopped-flow data.

The values of the forward and backward microscopic rate constants should sum to the observed rate constant from pH jump stopped-flow experiments. To compare the values obtained between pH jump and electron transfer stopped-flow experiments, $k_{b,His}$, $k_{f,His,PK,num}$, $k_{obs,1,gET} = k_{b,His} + k_{f,His,PK,num}$, and $k_{obs,1,H73A85}$ are plotted versus pH in Figure 3.13. We use $k_{f,His,PK,num}$ because unlike fitting $k_{obs,2,ET}$ versus [$Co(terpy)_2^{2+}$] data to Eq. 3.7, its evaluation should be insensitive to the breakdown in the steady-state approximation at low $Co(terpy)_2^{2+}$ concentration. Although, $k_{b,His}$ is well defined, there is clearly more difficulty in measuring the forwards microscopic rate constant for formation of the His73-heme alkaline conformer. The error bars for both $k_{f,His,PK,num}$ and $k_{obs,1,gET}$ are large. Given the difficulty in accurately determining $k_{f,His,PK,num}$ the agreement between gated ET and pH jump stopped-flow data is reasonable.

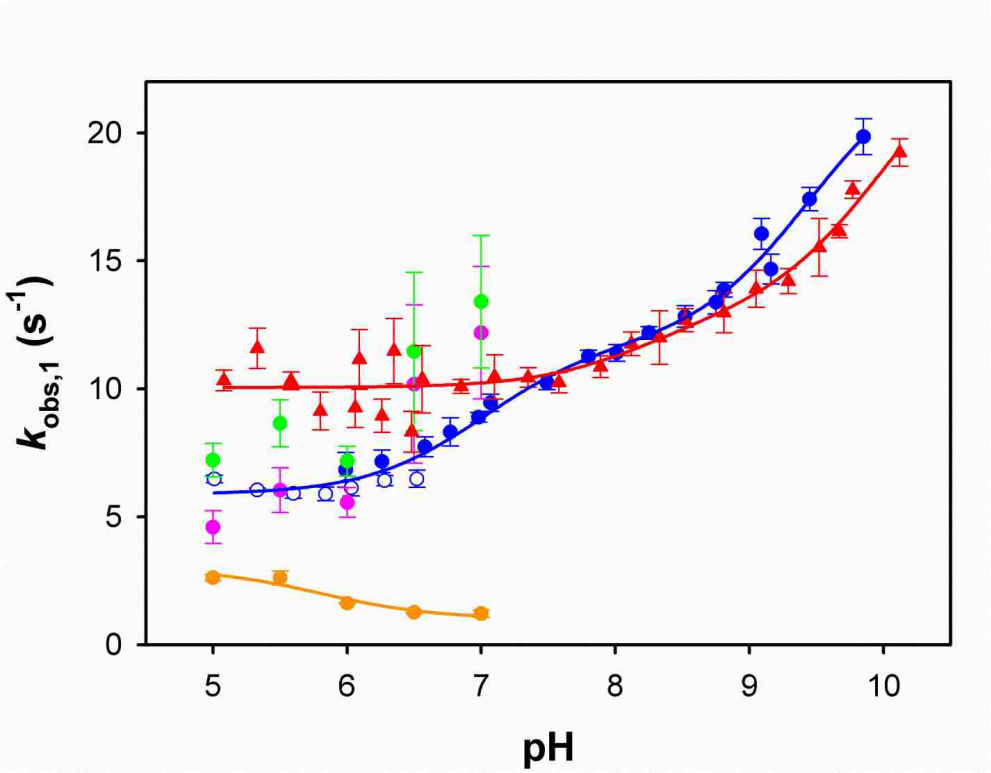

Figure 3.13. Plot comparing the observed rate constants for the His73-heme phase of the alkaline transition of WT*/K73H/L85A iso-1-Cyt*c*, $k_{obs,1,H73A85}$ (blue circles) and WT*/K73H iso-1-Cyt*c*, $k_{obs,1,WT*/K73H}$ (*88*), from pH jump experiments. The forward, $k_{f,His,PK,num}$ (pink circles), and backward, $k_{b,His}$ (orange circles), rate constants for the His73-heme alkaline transition from gated ET experiments on WT*/K73H/L85A iso-1-Cyt*c* are also shown. The sum of $k_{f,His,PK,num}$ and $k_{b,His}$ equal $k_{obs,1,gET}$ (green circles) is also plotted versus pH. $k_{obs,1,H73A85}$ versus pH data are fit to Eq 3.5 (blue curve). The $k_{b,His}$ versus pH data are fit to Eq. 3.8 (orange curve).

In Figure 3.7, we fit the $k_{obs,1,H73A85}$ versus pH data to a model involving only two ionization events (Eq. 3.5) because only two ionization events are evident in the data. Due to the disagreement between thermodynamic and kinetic values for K_{C1}(His) it is possible that a third ionization event affects the His73-mediated alkaline transition for WT*/K73H/L85A iso-1-Cyt*c*. It is evident that $k_{b,His}$ in Table 3.4 decreases with pH. For other K73H variants of iso-1-Cyt*c*, a low pH ionization affects only $k_{b,His}$, and the acid dissociation constant for this ionization, pK_{H1},can be determined by fitting $k_{b,His}$ versus pH below pH 7 to Eq. 3.8 (*14*).

(3.8)

$$k_{\mathrm{b}} = \frac{k_{\mathrm{b1}}[\mathrm{H^+}] + k_{\mathrm{b2}}K_{\mathrm{H1}}}{K_{\mathrm{H1}} + [\mathrm{H^+}]}$$

The fit to Eq. 3.8 yields: k_{b1} = 3.0 ± 0.4 s^{-1}, k_{b2} = 1.0 ± 0.3 s^{-1}, and pK_{H1} = 5.8 ± 0.4. This third ionization constant is similar to previously identified ionization events (5.6-6.2) in K73H, K73H/K79A, and H26N/K73H yeast iso-1-Cyt*c* variants (*14, 20, 21*).

3.5 Conclusion

3.5.1 Effect of the destabilizing L85A mutation on yeast iso-1-Cyt*c* dynamics.

Figure 3.13 also compares the observed rate constants of the WT*/K73H/L85A Cyt*c* variant to the WT*/K73H variant (*88*). Contrary to the expectation that dynamics around the heme crevice would be faster for the less stable WT*/K73H/L85A variant, as previously seen in the destabilized H26N/K73H variant (*14*), the rate constants were similar to yWT/K73H above pH 7. In fact, below pH 7 the dynamics are even slower in the presence of the destabilizing L85A mutation. Thus, although the global stability has been dramatically reduced, the dynamics of the alkaline conformational transition are not increased. This result suggests that local dynamics are not necessarily linked to global stability. Recent work on the kinetics of psychrophilic enzymes indicates that changes in the heat capacity of the ground state of the enzyme relative to the transition state for catalysis strongly affect the temperature dependence of enzyme activity (*99*). Similar effects could explain the apparently slower kinetics for formation of the His73-heme alkaline conformer in the destabilized WT*/K73H/L85A variant described here. Future work will address this possibility.

Chapter 4 Structure of a Mitochondrial Cytochrome *c* Conformer Competent for Peroxidase Activity[2]

4.1 Introduction

Mitochondrial cytochrome *c* (Cyt*c*) plays a pivotal role in energy storage in living organisms providing a critical link between complex III and complex IV of the electron transport chain (*100*). More recently, the role of Cyt*c* as an initiator of the intrinsic pathway of apoptosis has been elucidated (*4*). Release of Cyt*c* from mitochondria into the cytoplasm is a conserved step in apoptosis from yeast up through mammals (*45*). However, subsequent assembly with Apaf-1 to form the apoptosome is unique to metazoan animals (*101, 102*). Mitochondrial cytochromes *c* contain a *c*-type heme with axial His18 and Met80 ligands (*103*). However, when Cyt*c* binds to the inner mitochondrial membrane lipid, cardiolipin (CL), Met80 ligation is lost (*12, 104*). In this state, Cyt*c* catalyzes CL peroxidation, which provides an early signal for initiation of apoptosis (*12*).

Despite advances in our understanding of the role of Cyt*c* in apoptosis, our knowledge of the structural factors that facilitate the peroxidase activity of Cyt*c* remains rudimentary. In the structure of a domain-swapped dimer of horse Cyt*c*, Met80 is replaced by water as a heme ligand (*30*), causing a 4-fold increase in peroxidase activity relative to monomeric Cyt*c* (*32*). However, evidence for dimerization of Cyt*c* on CL vesicles is lacking. Fluorescence methods provide evidence for an equilibrium between compact and extended conformers on the surface of CL vesicles (*34, 105, 106*), with the extended conformer linked to higher peroxidase activity (*34*). However, other studies suggest that compact conformers of Cyt*c* are also competent for peroxidase activity (*107*).

[2] Work presented in Chapter 4 has been published previously: McClelland et al. *PNAS* (2014) 111, no 18:6648-6653.

The heme crevice loop of Cyt*c* (residues 70 to 85) is the most highly conserved segment of the primary structure of Cyt*c* (*3, 38*). This surface loop contains the Met80 heme ligand and is likely important for both electron transfer function in electron transport and peroxidase activity in apoptosis. Our knowledge of the sequence constraints operating in the heme crevice loop that modulate the dynamics necessary for peroxidase activity remains sparse. We have shown recently that the dynamics of the heme crevice loop are enhanced when lysine 72 of yeast iso-1-cytochrome *c* (iso-1-Cyt*c*) is mutated to alanine (*18, 19*). When synthesized in its native host (*Saccharomyces cerevisiae*), but not in a heterologous *Escherichia coli* expression system, lysine 72 of iso-1-Cyt*c* is trimethylated (tmK72) (*48*). Structural studies on yeast-expressed iso-1-Cyt*c* (hereafter yWT iso-1-Cyt*c*) show that tmK72 lies across the surface of the heme crevice loop (*7*). Here, we show by high-resolution X-ray crystallography that mutation of lysine 72 to alanine produces a variant of iso-1-Cyt*c* (hereafter WT* iso-1-Cyt*c*) that permits ejection of Met80 from the heme-binding pocket and its replacement by water (Figure 4.1). An extensive buried water channel results, a feature required for substrate access to the heme active site (*107, 108*) and for proton transport away from the active site during catalysis. As anticipated from the crystal structure, we show that mutation of residue 72 to alanine (WT* iso-1-Cyt*c* variant) enhances peroxidase activity of iso-1-Cyt*c* near physiological pH.

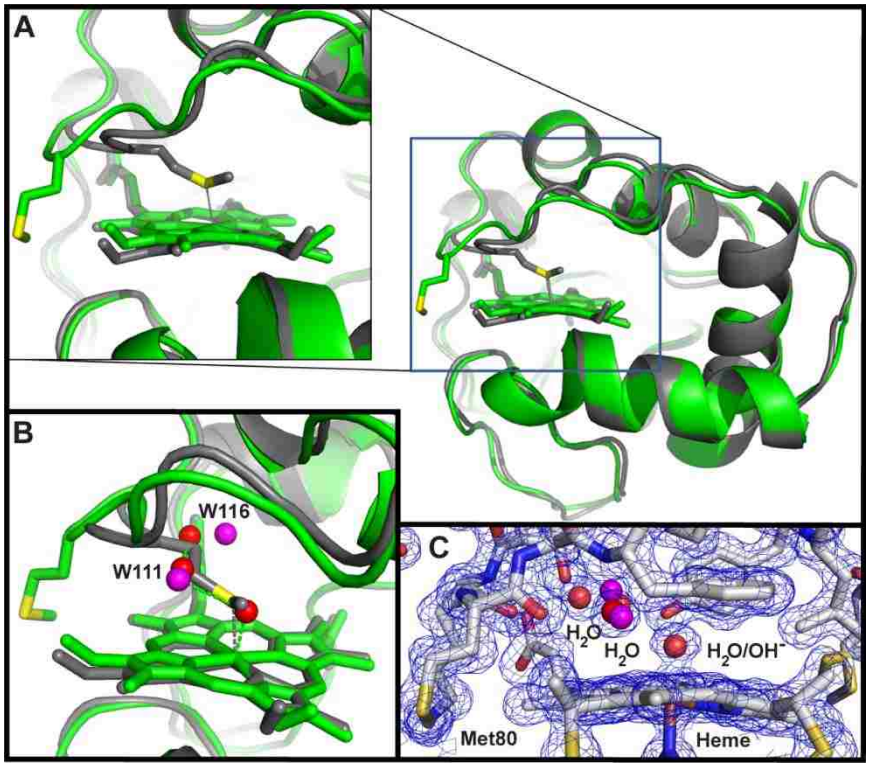

Figure 4.1. Comparison of WT* iso-1-Cyt*c* and yWT iso-1-Cyt*c* overall structures. (A**) Alignment of WT* iso-1-Cyt*c* (green, chain A of pdb code: 4MU8) with yWT iso-1-Cyt*c* (gray, pdb code: 2YCC, carries a C102T mutation). The heme and Met80 are shown as stick models. A close-up of the heme and Met80 is shown on the left. (**B**) Close-up of the heme crevice showing waters (red spheres) in WT* iso-1-Cyt*c* in the space occupied by Met80 in yWT iso-1-Cyt*c*. Low occupancy positions observed for two of the waters are shown in purple. (**C**) Heme crevice close-up showing the $2|F_o|-|F_c|$ electron density map contoured at 1.2σ (blue mesh) with the model used to fit the data.**

4.2 Experimental Procedures

4.2.1 Protein expression and purification.

Saccharomyces cerevisiae GM-3C-2 cells (*109*) were used to express yWT iso-1-Cyt*c*. Cells transformed with the pRS425/CYC1 shuttle vector (*110*) carrying the iso-1-cytochrome *c* gene, *CYC1*, with the C102S mutation were grown on YPG media as described previously (*16*). Autolysis with ethyl acetate was used to extract yWT iso-1-Cyt*c* from GM-3C-2 cells (*58, 59*). yWT has trimethyllysine at residue 72 and contains a C102S mutation to prevent intermolecular disulfide dimerization (*111*).

WT* iso-1-Cyt*c* was expressed in BL21(DE3) *E. coli* cells using the pRbs_BTR1 vector (*54*), as described previously (*18*). WT* iso-1-Cyt*c* contains two background mutations: K72A, which eliminates Lys72-heme ligation in the alkaline state (*48*) and C102S, which prevents intermolecular disulfide dimerization.

Both variants were purified as previously outlined (*18, 58, 59*). Briefly, after centrifugation to clear the lysate, a 50% ammonium sulfate solution was used to precipitate contaminating proteins. After centrifugation to remove the precipitant, the supernatant was dialyzed against 12.5 mM sodium phosphate buffer, pH 7.2, 1 mM EDTA, 2 mM β-mercaptoethanol (β-ME). Following batch adsorption of the dialyzed protein to CM-Sepharose Fast Flow resin previously equilibrated with 50 mM sodium phosphate buffer, pH 7.2, 1 mM EDTA and 2 mM β-ME, a linear gradient of 0-0.8 M NaCl in 50 mM sodium phosphate buffer, pH 7.2, 1 mM EDTA and 2 mM β-ME was used for protein elution. Eluted iso-1-Cyt*c* was concentrated and flash frozen in 1.5 mL aliquots of ~2 mg/mL for storage at -80 °C.

Protein was thawed from -80 °C and reduced with sodium dithionite prior to purification by cation-exchange chromatography using an Agilent Technologies 1200 series HPLC with a BioRad UNO S6 Column (catalog no. 720-0023) (*18*). Protein samples were concentrated by ultrafiltration after collection from the HPLC and oxidized with $K_3[Fe(CN)_6]$. Oxidized protein for peroxidase assay experiments was loaded on a G25 Sephadex column pre-equilibrated with 50 mM potassium phosphate buffer of the appropriate pH.

4.2.2 Crystallization, structure determination and refinement.

Initial screening was performed with oxidized WT* iso-1-Cyt*c* at concentrations ranging from 2-8 mg/mL in both 0.35 M sodium chloride and 75% ammonium sulfate using reservoir solutions of 75-98% ammonium sulfate and 0.1 M sodium phosphate, pH 5.4-8.9 (*112*), but no

crystallization was observed. Typically, oxidized mitochondrial Cyt*c* crystallizes between pH 6 and 7 under these conditions (*7, 112*). Crystallization conditions were then screened with several commercial crystallization screening kits. Initial hits were found using the JCSG Core Suite. Further optimization of the crystallization conditions was performed with additive screening and several grid screenings, which varied the concentration of ammonium sulfate and the pH.

Crystals of oxidized Cyt*c* were obtained by vapor diffusion from sitting drops containing 1:1 (vol/vol) protein solution of 6 mg/ml in 75% aqueous ammonium sulfate to a reservoir solution of 90% ammonium sulfate, 0.1 M Tris-HCl (pH 8.8), and 4% tert-butanol at 20 °C within 1-2 weeks. Crystals were harvested in a cryoprotectant consisting of 80% ammonium sulfate, 0.1 M Tris-HCl (pH 8.8), and 10% (V/V) glycerol. The cryoprotected crystals were mounted in 0.2-0.3 mm nylon loops and stored in liquid nitrogen.

Diffraction data were collected at the Stanford Synchrotron Radiation Lightsource SSRL-SMB-MC 11-1 beamline by the oscillation method (0.3 °/frame, 10 s/frame). The incident beam wavelength was 0.978 Å. The images were processed using HKL2000 (*113*). The structure was determined by molecular replacement using PHASER as implemented in the PHENIX software suite (*114*) and the atomic coordinates of oxidized tmK72Cyt*c* expressed from *S. cerevisiae* (PDB code: 2YCC) were used as the initial search model (*7*). Atomic positions and thermal parameters were refined using the PHENIX suite. Occupancies of residues exhibiting two alternative conformations were refined. The model was iteratively improved by manual refitting into a likelihood-weighted $2|F_o|-|F_c|$ map using the computer graphics program Coot (*115*) and subsequent refinement cycles with PHENIX to 1.45 Å resolution. The graphics program PyMOL (*116*) was used to visualize the refined structure and produce illustrations. Data collection and

refinement statistics are listed in Table C1. Atomic coordinates and structure factors have been deposited in the Protein Data Bank (www.pdb.org) (*117*) with ID code 4MU8.

Purity of the WT* iso-1-Cyt*c* variant used for crystallization trials was assessed from overloaded SDS-PAGE gels. The mass spectrum of the WT* iso-1-Cyt*c* variant was measured with a Bruker microflex MALDI-ToF mass spectrometer yielding a molecular weight of 12,600.9 Daltons (Expected: 12,595.1 Daltons).

4.2.3 Guaiacol assay of peroxidase activity.

Guaiacol assays were performed at 25 °C with an Applied Photophysics SX20 stopped-flow spectrophotometer and peroxidase activity was monitored as the formation of tetraguaiacol at 470 nm. Temperature was controlled at 25 °C with a Thermo Neslab RTE7 circulating water bath interfaced with the stopped-flow spectrophotometer. Concentration determinations were carried out using a Beckman Coulter DU 800 spectrophotometer. Solutions were prepared in degassed 50 mM potassium phosphate buffers that had been pH adjusted using a Denver Instrument UB-10 pH/mV meter and an Accumet semimicro calomel pH probe (Fischer Scientific Cat. No. 13-620-293). A 0.1 M H_2O_2 solution was prepared from a 30% stock solution and the concentration was determined at 240 nm using the average of reported extinction coefficients of 39.4 M^{-1} cm^{-1} (*118*) and 43.6 M^{-1} cm^{-1} (*119*).

Guaiacol (Sigma) was used to prepare an initial 10 mM stock solution. A 400 μM solution of guaiacol was prepared from the 10 mM stock solution and the concentration was determined at 274 nm with an extinction coefficient of 2150 M^{-1} cm^{-1} (*120*). The concentration of iso-1-Cyt*c* solutions, determined spectrophotometrically (*62*), was adjusted to 4 μM.

The 400 μM guaiacol solution was then mixed with the 4 μM iso-1-Cyt*c* solution and 50 mM potassium phosphate buffer to produce 2X iso-1-Cyt*c*/guaiacol solutions of 2 μM iso-1-Cyt*c*

and 4 to 200 μM guaiacol. This 2X iso-1-Cyt*c*/guaiacol solution was then mixed in a 1:1 ratio with 0.1 M H_2O_2 in the stopped-flow spectrophotometer producing final mixtures of 1 μM Cyt*c*, 2 to 100 μM guaiacol (2, 4, 6, 8, 10, 15, 20, 25, 30, 40, 50, 60, 80 and 100 μM guaiacol) and 50 mM H_2O_2 in 50 mM potassium phosphate buffer at the desired pH. Peroxidase activity was monitored as the formation of tetraguaiacol at 470 nm using the molar absorption coefficient of 26.6 mM^{-1} cm^{-1} (*121, 122*). A minimum of 5 traces was collected at every guaiacol concentration and 3 independent sets of data were collected at each pH (pH 6, 6.5, 7, 7.5 and 8). The rate of the steady-state reaction was determined from the maximum of the first derivative of the tetraguaiacol formation curve, i.e. the linear phase. Rate of change of absorbance at 470 nm was converted to μM guaiacol consumed per second using an absorption coefficient of 26.6 mM^{-1} cm^{-1} for tetraguaiacol (*121, 122*). Michaelis-Menten plots were then used to extract k_{cat} and K_m for guaiacol from the data using SigmaPlot v. 7.0.

4.3 Results and Discussion

4.3.1 Crystallization of WT* Cyt*c*.

The K72A variant of yeast iso-1-Cyt*c*, WT*, was expressed from *E. coli* (*48, 54*). This variant carries an additional C102S mutation to eliminate disulfide dimerization (*111*). Crystals of oxidized (Fe(III)heme) WT* Cyt*c* grown from 90% ammonium sulfate at pH 8.8 diffracted to 1.45 Å. Refinement yielded a structural model with R_{work}/R_{free} = 0.143/0.156 (Table C1). Two molecules of WT* iso-1-Cyt*c* (chains A and B) are contained in the asymmetric unit of the crystal lattice. The RMSD between chains A and B is 0.25 Å. Heme proteins are susceptible to reduction to the Fe(II) state by synchrotron radiation (*123*). Therefore, we cannot eliminate the possibility that some reduction of the WT* iso-1-Cyt*c* heme occurs during data collection. However, treatment of crystals with sodium dithionite leads to crystal cracking, which is not

observed following data collection. Also, since data were collected at 100 K, large structural rearrangements due to heme reduction should be minimal.

4.3.2 Structural consequences of the trimethyllysine-72 to alanine substitution.

The structure of WT* iso-1-Cyt*c* superimposed on that of oxidized yWT iso-1-Cyt*c* crystallized near pH 6.5 (*7*) shows that the two proteins are quite similar (RMSD at C_α positions: 0.64 Å) (Figure 4.1). The key difference is that Met80 has swung out of the heme crevice in WT* iso-1-Cyt*c* (Figure 4.1A). Most previous structures of monomeric mitochondrial cytochromes *c* have Met80 bound to the heme iron (*103*). Exceptions include NMR structures of an alkaline conformer of K79A iso-1-Cyt*c* obtained at pH 10 where Met80 is displaced by Lys73 (*13*) and of horse Cyt*c* and a M80A variant of iso-1-Cyt*c* with exogenous ligands bound in place of Met80 (*124-126*). In WT* iso-1-Cyt*c*, water (W) 113 (probably hydroxide at pH 8.8) is bound to the heme iron in place of Met80. The Fe-O distance of 2.00 Å is similar to that observed in the oxidized (Fe(III)-heme) horse Cyt*c* domain swapped dimer and trimer structures (~2.10 Å, (*30*)), and the 2.01 Å Fe-O distance observed for two *Geobacter sulfurreducens* chemotaxis protein sensor domains (*127*). The presence of H_2O/OH^- as the axial ligand in place of Met80 does not affect the Fe-N bond distance (2.04 Å) of the trans-axial His18 ligand and is similar to that of yWT iso-1-Cyt*c* (Figure 4.2A) and to the Fe-N bond distance of 2.0 to 2.1 Å observed for *c*-type cytochromes with a water bound trans to the histidine of an Fe(III)heme (*30, 127*). The orientation of the plane of the imidazole ring of His18 remains typical of *c*-type cytochromes (*128*) and is indistinguishable from that in yWT iso-1-Cyt*c* (Figure 4.2A). Three more buried water molecules are located on the Met80-proximal side of the heme. Two of these waters sit near positions occupied by the C_β and C_γ atoms of Met80 in the yWT iso-1-Cyt*c* structure (Figure 4.1B) and have well defined electron density (Figure 4.1C).

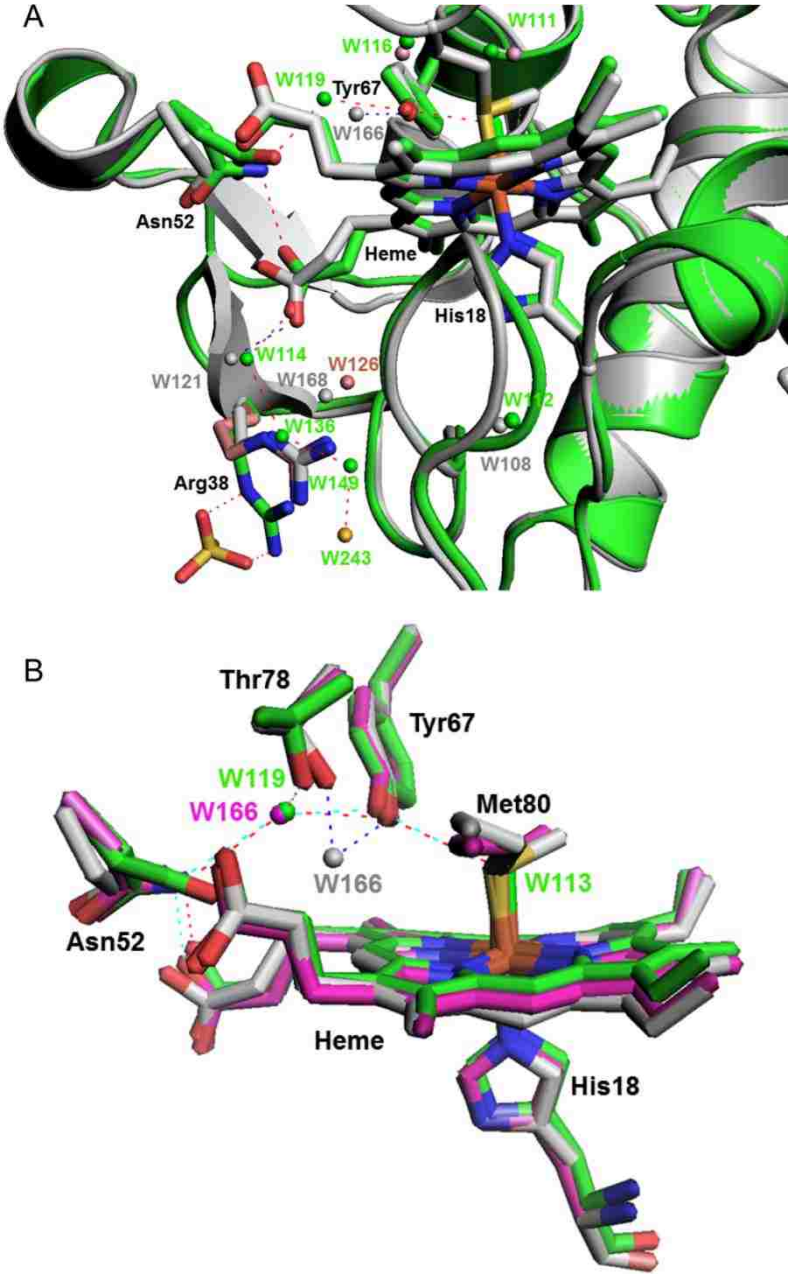

Figure 4.2. Comparison of buried water molecules. (A) Alignment of the structures of oxidized WT* iso-1-Cyt*c* (pdb file: 4MU8) and oxidized yWT iso-1-Cyt*c* (pdb file: 2YCC) showing buried water molecules. Chain A from the WT* iso-1-Cyt*c* structure is shown in green and the yWT iso-1-Cyt*c* structure is shown in gray. Buried water molecules are shown as small spheres in green for chain A of WT* iso-1-Cyt*c* and gray for yWT iso-1-Cyt*c*. The low occupancy positions of W111 and W116 are shown in pink. Waters are labeled using the same color scheme with their numbers from the pdb files. The yellow sphere is the first water in the hydrogen bonded chain that is on the surface of chain A in the WT* iso-1-Cyt*c* structure. The positions of Arg38 and W126 from chain B of yWY iso-1-Cyt*c* are shown in dark salmon. Residues 41 to 51 are not shown to improve the view of the buried waters. Red dashed lines show some of the hydrogen bonds that are

≤3.2 Å connecting the chain of buried waters in the WT* iso-1-Cyt*c* structure: OH^-/H_2O (W113) bonded to Fe(III)---Tyr67OH, 3.18 Å; Tyr67OH---W119, 2.75 Å; W119---AsnNH_2, 3.12 Å; Asn52NH_2---Heme propionate A, 3.21 Å; Heme propionate A---W114, 2.67 Å; W114---W136, 2.90 Å; W136---W149, 2.72 Å; W149---W243, 3.09 Å. Corresponding hydrogen bonds in the yWT iso-1-Cyt*c* structure are shown with blue dashed lines: Tyr67OH---W166, 2.63 Å; Heme propionate A---W121, 2.85 Å. (B) Alignment of heme and surrounding side chains for oxidized WT* iso-1-Cyt*c* (green, pdb file: 4MU8), oxidized yWT iso-1-Cyt*c* (gray, pdb file: 2YCC) and reduced yWT iso-1-Cyt*c* (magenta, pdb file: 1YCC). Hydrogen bonds are shown with dashed lines for oxidized WT* iso-1-Cyt*c* (red), oxidized yWT iso-1-Cyt*c* (blue) and reduced yWT iso-1-Cyt*c* (cyan). The position of W119 (green sphere) corresponds to W166 from reduced yWT iso-1-Cyt*c* (magenta sphere) not oxidized yWT iso-1-Cyt*c* (gray sphere).

4.3.3 Alternate side chain conformers and buried water channels in WT* iso-1-Cyt*c*.

In oxidized yWT iso-1-Cyt*c*, all residues are modeled as single conformers (*7*). However, in WT* iso-1-Cyt*c* several residues occupy two conformations (Table C2). Three of these residues, Asn52, Met64 and Leu85, are fully buried and pack against the heme (Figure 4.3). Thus, invasion of water into the heme crevice when Met80 ligation is lost creates disorder around the heme. Both conformations of Asn52 can hydrogen bond to W119, which is also hydrogen bonded to Tyr67 (Figure 4.2A). Two waters, W111 and W116, near the heme also adopt alternate high (~80%) and low (~20%) occupancy positions displaced from each other by 0.67 Å and 1.45 Å, respectively (Figure 4.1B, Table C2). In their high occupancy positions, these two waters form a hydrogen-bonded chain emanating from the axial H_2O/OH^- heme ligand (Figure 4.4A). In the low occupancy state, W116 breaks this chain and forms alternative hydrogen bonds (Figure 4.4B). Thus, W111 and W116 could act as a transient proton shuttle in general acid/base catalysis during peroxidative turnover catalyzed by the heme of the WT* iso-1-Cyt*c* conformation reported here.

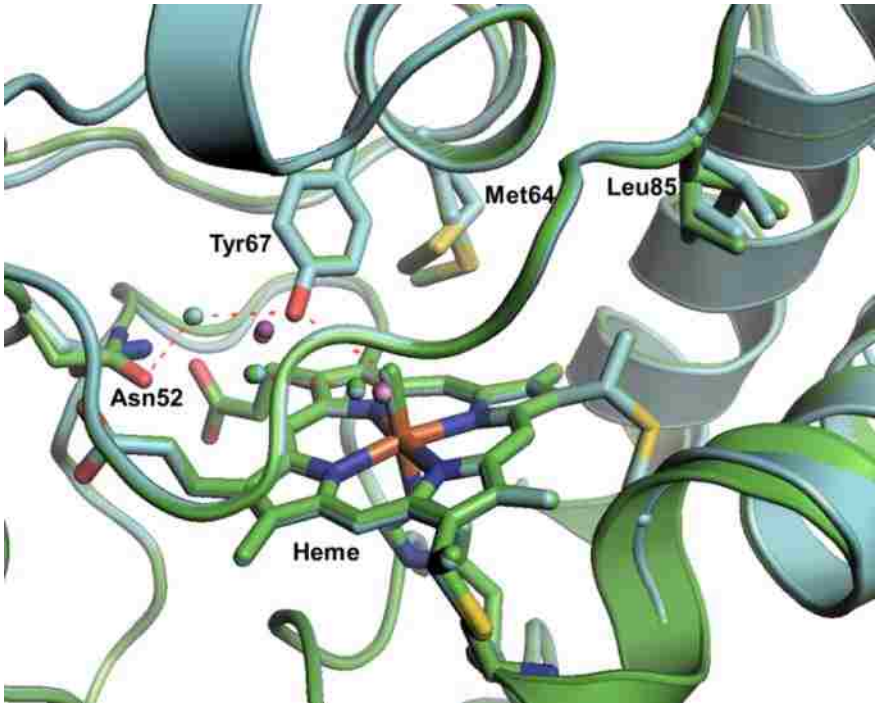

Figure 4.3. Buried side chains with two conformations that are adjacent to the heme of WT* iso-1-Cyt*c*. The two conformations of Asn52, Met64 and Leu85 are shown for both chains A (green) and B (cyan). The heme, Cys14, Cys17 and His18, and Tyr67 are shown as stick models. The buried water molecules in the heme pocket are also shown for both chains A and B as green and cyan spheres, respectively. The low occupancy positions for two of the water molecules are shown in pink (chain A) and purple (chain B). Hydrogen bonds (≤ 3.2 Å) are shown in red between the high occupancy waters and Asn52, Tyr67 and the water/hydroxide bound to the heme iron.

The position of water molecules on the Met80-proximal side of the heme of yWT iso-1-Cyt*c* is sensitive to the redox state of the heme (*7*). In particular, W166 in the native structure of iso-1-Cyt*c* (*7*) is 1.7 Å closer to the iron of the oxidized compared to the reduced heme. In the structure of WT* iso-1-Cyt*c*, the corresponding water, W119, occupies the same position as W166 in reduced yWT iso-1-Cyt*c* (Figure 4.2B). This observation could be taken as evidence for reduction of the heme by synchrotron radiation. However, the water bound to the iron atom of the heme is likely hydroxide at pH 8.8. Therefore, the oxidized form of WT* iso-1-Cyt*c* has a heme with no net charge like the reduced form of yWT iso-1-Cyt*c* (*129*). We conclude that it is

more likely that the position of W119 in WT* iso-1-Cyt*c* reflects a neutral heme rather than reduction of the heme during data collection.

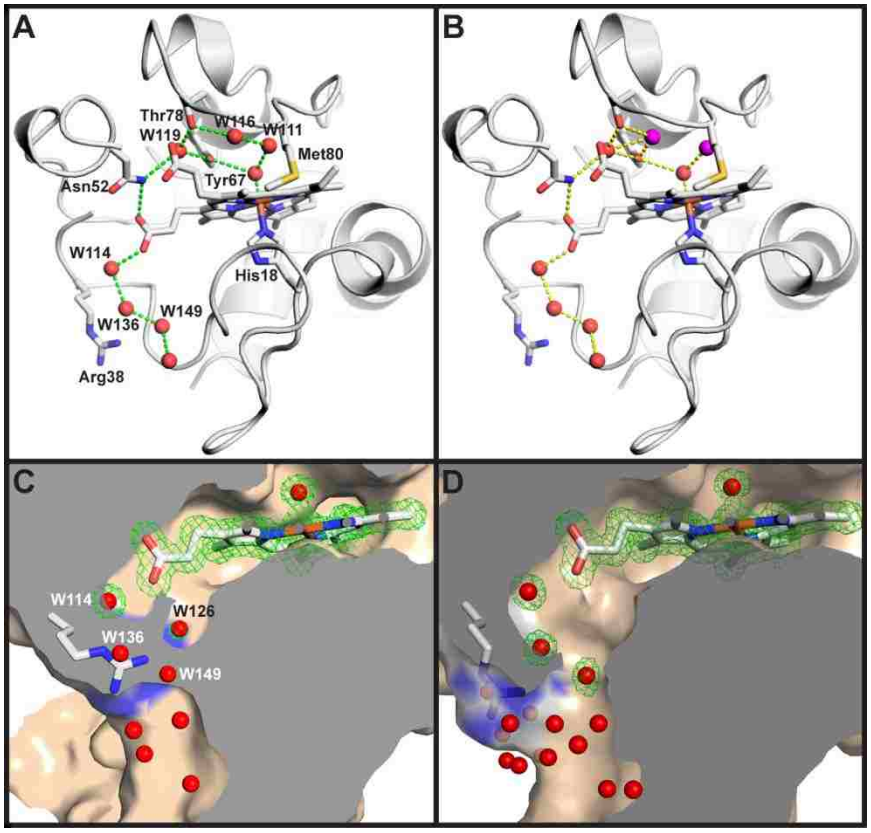

Figure 4.4. Water structure around the heme of WT* iso-1-Cyt*c*. (A) Hydrogen bond network of buried water molecules (red spheres) showing high occupancy positions of W111 and W116 in the context of chain A. (B) Hydrogen bond network of buried water molecules showing low occupancy positions (purple spheres) of W111 and W116. In panels A and B, residues 41 to 50 are removed to enhance the view of the buried water network. The heme and selected side chains are shown as stick models (labeled in panel A). (C) Section through the surface representation of chain B of WT* iso-1-Cyt*c* with Arg38 positioned to close the water channel to the protein surface. (D) Section through the surface representation of chain A of WT* iso-1-Cyt*c* with Arg38 positioned to open the water channel to the protein surface. In panels C and D, the heme and buried water molecules are shown with the $2|F_o|-|F_c|$ electron density (green wire). External water and the partially-occupied waters, W136 and W149, in (*C*) are shown without electron density.

WT* iso-1-Cyt*c* harbors four buried waters on the His18-proximal side of the heme of chain A compared to two for yWT iso-1-Cyt*c* (*103*) (Figure 4.4A and Figure 4.2A). These buried waters, together with those located at positions vacated by the ejected Met80, occupy a channel

that leads from the hydroxide bound heme to the protein surface (Figures 4.4A and 4.4B), permitting them to exchange with bulk water. This water channel is similar to one identified by molecular dynamics (MD) simulations on iso-1-Cyt*c* (*108*). Near the entrance of this channel in chain B of the asymmetric unit, Arg38 assumes multiple states. In an ordered, but partially occupied state (60% occupancy) similar to that observed in yWT iso-1-Cyt*c* (Figure 4.2A) (*7*), the side chain of Arg38 fully blocks the channel opening at the protein surface (Figure 4.4C and Figure 4.5 and Table C2). In chain B, but not in Chain A, a partially occupied water, W126 (48% occupancy), is observed near the position of W168 in yWT iso-1-Cyt*c* within hydrogen bonding distance of Arg38 (Figures 4.4C and 4.2A). In an alternative, fully disordered state, Arg38 in chain B is replaced by W136 and W149, which also have counterparts in chain A (Figures 4.4C and 4.4D). In chain A, Arg38, stabilized by its interaction with a sulfate ion, adopts a single conformation in which the channel is open to bulk solvent (Figures 4.4D and 4.5). In an X-ray structure of iso-1-Cyt*c* with an R38A mutation, a similar water channel with a much larger opening at the protein surface is observed (*130*). Thus, it appears that side chain of Arg38 can act as a conformational switch that gates access of buried waters in WT* iso-1-Cyt*c* to bulk water at the protein surface. By contrast, MD simulations suggested that access to buried water channels is mediated by main chain, not side chain, motions (*108*). This buried water channel (Figures 4.2and 4.4) could afford substrate access to the heme active site and shuttle protons to the surface during Cyt*c*-mediated peroxidation activity. Due to fluctuations in the conformations of Arg38, Asn52 and the positions of buried water molecules, the channel would be expected to flicker between low and high conductivity states. Previous work suggests that Arg38 plays a role in regulating heme redox potential (*131*), thus this conserved residue may play a role in both functions of mitochondrial Cyt*c*.

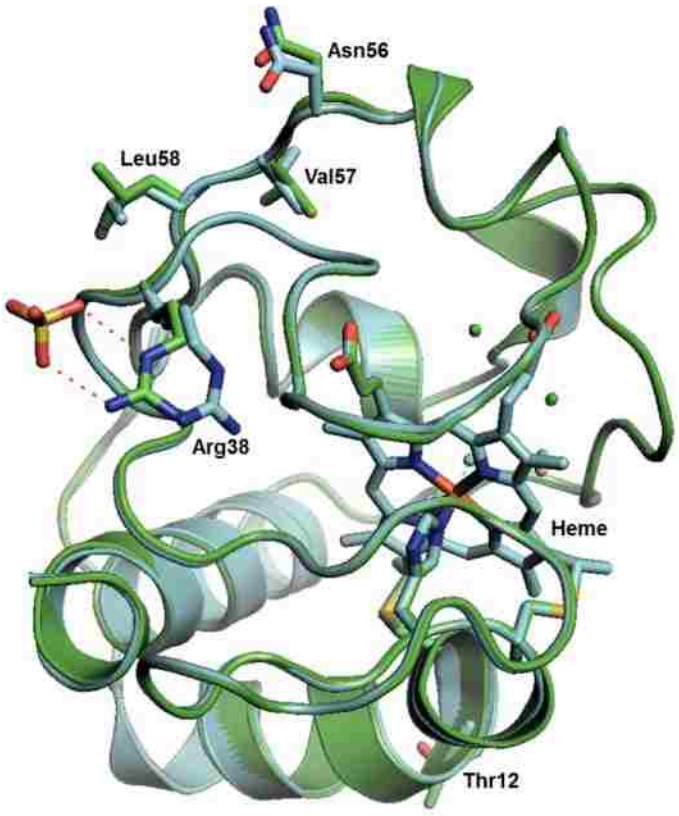

Figure 4.5. Alignment of chains A and B of the WT* iso-1-Cyt*c* structure showing side chains with conformations that differ between the two chains. Chain A is shown in green and chain B is shown in cyan. The heme and Cys14, Cys17 and His18 which attach the heme to the polypeptide are shown as stick models. Water molecules in the heme crevice are shown as small green (chain A) or cyan (chain B) spheres. The low occupancy positions of two of the waters are shown in pink (chain A) or purple (chain B). Residues which populate different rotamers or significantly different positions in chain A versus chain B are labeled and shown as stick models. Arg38 in chain A is fully occupied and hydrogen bonded to a sulfate ion. Arg38 in chain B is only partially occupied (see Table C2). No sulfate is located adjacent to Arg38 in chain B. The change in the position of Arg38 appears to propagate to Asn56, Val57 and Leu58 in the adjacent loop. Thr12 near the C-terminus of the N-terminal helix occupies different rotamers in chains A and B.

Arg38 is also unusual in that it is part of a short segment of yWT iso-1-Cyt*c* that becomes more rigid, rather than less rigid, in the oxidized state versus the reduced state of the protein (*7*). The thermal factors for residues near Arg38 are lower for chain A versus chain B (Figure 4.6) and the pattern of variation of thermal factors near Arg38 is similar to oxidized yWT iso-1-Cyt*c* for chain A and similar to reduced yWT iso-1-Cyt*c* for chain B (*7*). This difference is likely

attributable to the presence of sulfate ion interactions with Arg38 in chain A which are absent in chain B.

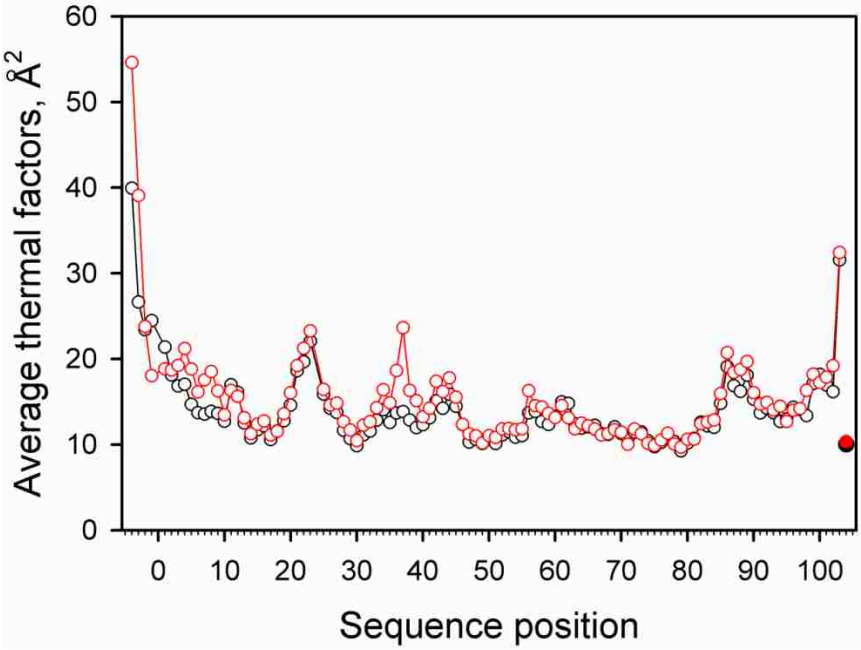

Figure 4.6. Average main chain thermal factors as a function of sequence position for chain A (open black circles) and chain B (open red circles) of WT* iso-1-Cyt*c*. The average thermal factor for the heme cofactor is shown with solid circles for chain A (black) and chain B (red) at sequence position 104.

4.3.4 Structural constraints mediating ejection of Met80 from the heme crevice of iso-1-Cyt*c*.

Relatively small backbone adjustments are sufficient to permit Met80 to swing out of the heme crevice of Cyt*c* (Figures 4.1 and 4.7). Large displacements occur between the WT* iso-1-Cyt*c* and yWT iso-1-Cyt*c* structures at Met80 (C_α RMSD 3.59 Å), Ala81 (C_α RMSD 2.18 Å) and to a lesser extent at Gly83 (C_α RMSD 1.26 Å) in the heme crevice loop (Figures 4.7A and 4.7B). Otherwise, C_α RMSD values for alignment of the two structures are mostly < 1 Å (Figure 4.8). The deviation of the main chain observed here for the heme crevice loop is considerably smaller than when Met80 is expelled from the heme crevice by exogenous ligands such as cyanide (*126*) and imidazole (*125*).

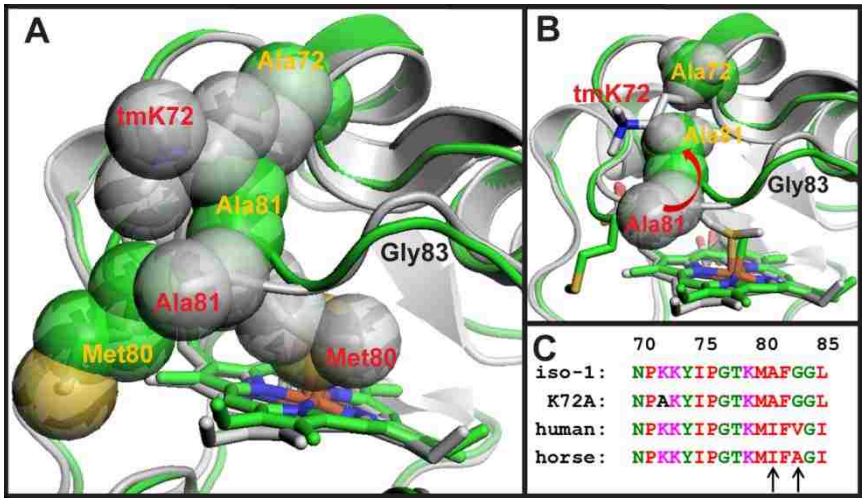

Figure 4.7. Steric stabilization of the native conformer of Cyt*c* by the residue at position 72. (A**) Overlay of the structures of WT* iso-1-Cyt*c* (green, yellow labels) and yWT iso-1-Cyt*c* (gray, red labels) with residues 72, 80 and 81 shown as space filling models. The portion of the backbone corresponding to Gly83 is indicated with a black label. (**B**) Overlay of WT* iso-1-Cyt*c* and yWT iso-1-Cyt*c* showing the movement of Ala81 toward Ala72 when Met80 swings out of the heme crevice. (**C**) Alignment of yeast and mammalian Cyt*c* sequences for the highly conserved heme crevice loop (residues 70-85). Residues 81 and 83 are marked with black arrows.**

Mutation of tmK72→Ala facilitates expulsion of Met80. In yWT iso-1-Cyt*c*, tmK72 sterically blocks movement of Ala81, inhibiting release of Met80 from the heme (Figure 4.7A). In horse Cyt*c*, where Lys72 is not trimethylated, a similar situation exists. Lys72 lies across the heme crevice loop forming hydrogen bonds to the carbonyls of Met80 and Phe82 (*132*). In WT* iso-1-Cyt*c*, Ala81 is free to move toward Ala72 as Met80 swings out of the heme crevice (Figure 4.7B). Our structural data demonstrate that the more than 2-fold increase we observe in the dynamics of the His79-mediated alkaline conformational transition of iso-1-Cyt*c* in the presence of the tmK72→Ala mutation (*18*) results from relaxation of steric constraints in the heme crevice loop.

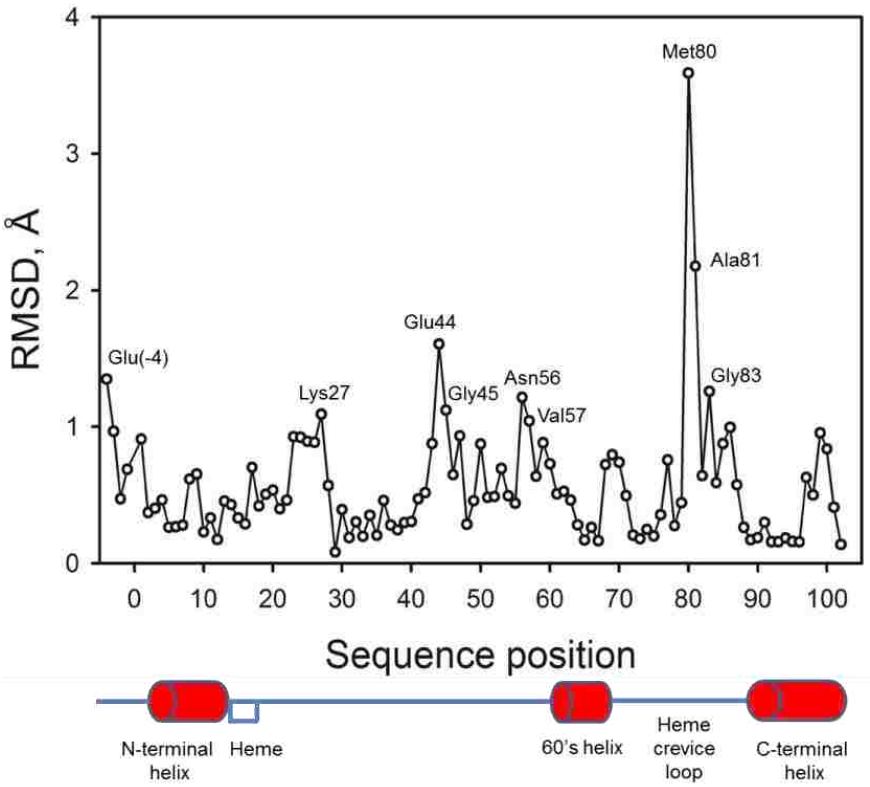

Figure 4.8. C_α RMSD as a function of sequence position for alignment of the structures of chain A of WT* iso-1-Cyt*c* and yWT iso-1-Cyt*c* (pdb file: 2YCC). Structural alignment was done within the graphics program Coot. The secondary structure is diagramed below the sequence position axis. The three long helices are shown as red cylinders. Intervening surface loops are shown with a blue line. The position of covalent heme attachment is also shown. All residues with C_α RMSD > 1 Å are labeled. The surface loop that runs from residues 40 to 57 is adjacent to the heme crevice loop in the structure of Cyt*c*.

The most highly conserved portion of the Cyt*c* sequence is the heme crevice loop. It encompasses both tmK72 and the mobile heme ligand, Met80 (*38*). Within this loop, yeast and mammals differ at positions 81 and 83 (Figure 4.7C), two residues that move significantly when Met80 is displaced from the heme crevice. At both positions, more sterically demanding side chains are present in mammalian Cyt*c* than in its yeast counterpart. Phylogenetic analysis shows that ancestral mitochondrial Cyt*c* has alanine at position 81, as in yeast (*133*). Moving up the phylogenetic tree from yeast to mammals, position 81 first mutates to Val then Ile (*3*, *38*). These

observations suggest that the heme crevice loop in mammals has evolved to more stringently minimize access to Cyt*c* conformers capable of peroxidase activity than in yeast.

4.3.5 Peroxidase activity of yWT iso-1-Cyt*c* versus WT* iso-1-Cyt*c*.

To test the effect of the tmK72→Ala mutation on the peroxidase activity of iso-1-Cyt*c*, we compared the rate of oxidation of guaiacol to tetraguaiacol (*32, 121, 122*) for yWT iso-1-Cyt*c* versus WT* iso-1-Cyt*c* (Figure 4.9). At pH 7.5 (Figure 4.10A), k_{cat} for peroxidase activity is 35% greater for WT* iso-1-Cyt*c* than for yWT iso-1-Cyt*c*. The pH dependence of k_{cat} shows that peroxidase activity is similar at pH 6 and 6.5 for both proteins (Figure 4.10B and Table C3). At these lower pH values, peroxidase activity is expected to be suppressed by the need to deprotonate H_2O_2 (*121, 134, 135*). However, from pH 7 to 8, k_{cat} for WT* iso-1-Cyt*c* increases and remains high while it declines for yWT iso-1-Cyt*c*. The pH dependence of the peroxidase activity of the yeast-expressed iso-1-Cyt*c*, yWT iso-1-Cyt*c*, mirrors that of horse Cyt*c* (*121*), relatively constant below about pH 7 and then decreasing at higher pH. The similarity in the pH dependence of yeast and horse cytochromes *c* likely reflects the similar ordering of substructure stabilities for the two proteins (*43, 44, 54*).

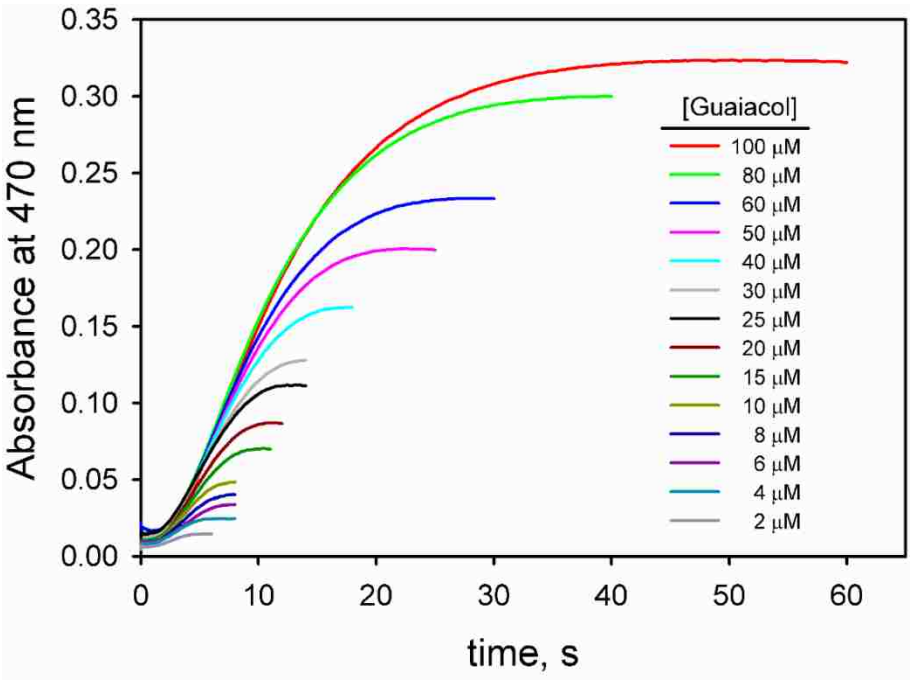

Figure 4.9. Oxidation of guaiacol to tetraguaiacol by WT* iso-1-Cyt*c* at pH 7 and 25 °C monitored at 470 nm. WT* iso-1-Cyt*c* concentration was 1 µM, H_2O_2 concentration was 50 mM. Guaiacol concentrations are indicated on the graph. Stopped-flow mixing was carried out as described in Experimental Procedures.

At pH 8, the tmK72→Ala mutation leads to an enhancement of k_{cat} by two-fold (Figure 4.10B). Furthermore we observe that crystals of WT* iso-1-Cyt*c* crack and dissolve below pH 7, also suggesting that the Cyt*c* conformer observed in the WT* iso-1-Cyt*c* structure is less stable at lower pH. Accordingly, the tmK72→Ala mutation favors a Cyt*c* conformer with higher peroxidase activity above pH 6.5.

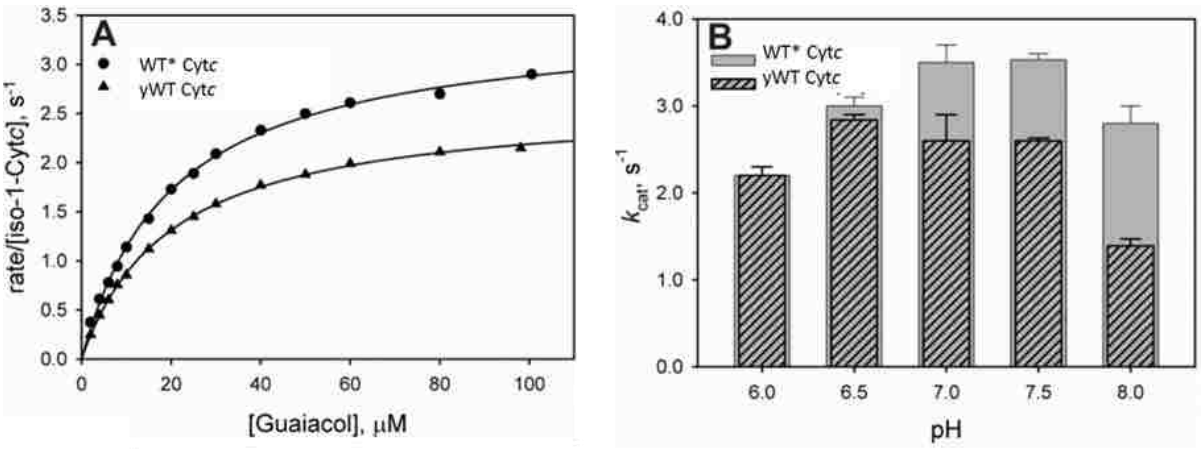

Figure 4.10. Effect of the tmK72→Ala mutation on peroxidase activity of iso-1-Cyt*c*. (A) Michaelis-Menten plots of rate of consumption of guaiacol as a function of guaiacol concentration at 25 °C and pH 7.5 in 50 mM potassium phosphate buffer. Cyt*c* concentration was 1 μM and H_2O_2 concentration was 50 mM. (B) Plot of k_{cat} versus pH for WT* iso-1-Cyt*c* and yWT iso-1-Cyt*c*.

In mitochondria, the fatty acid chains of CL, which are subject to peroxidation, are believed to bind near Asn52 (site C) and lysines 72, 73 and 86 (site A) (*136*, *137*). The channel of waters that fill the void left when Met80 is expelled could readily be displaced by a fatty acid chain entering from either site A or site C. The side chains of Asn52, Met64 and Leu85 also occupy two rotamers indicating conformational plasticity on the Met80-proximal side of the heme that could facilitate binding of CL near the heme iron.

The peroxidase activity enhancement we observe compares well in magnitude to the increase in the dynamics of the His79-mediated alkaline conformational transition resulting from the tmK72→Ala mutation (*18*). Thus, residue 72 in the heme crevice loop significantly impacts the heme crevice dynamics necessary for peroxidase activity. Notably, k_{cat} for the peroxidase activity of horse Cyt*c* at pH 7 (*32*) determined under identical conditions is 20-fold and 27-fold less than for yWT iso-1-Cyt*c* and WT* iso-1-Cyt*c*, respectively (Table C3). The additional steric congestion at positions 81 and 83 (Figure 4.7C), in addition to the hydrogen bond contacts that Lys72 makes with the Met80 and Phe82 carbonyls in mammalian Cyt*c* (*132*), appear to diminish

heme crevice dynamics needed for peroxidase activity for mammalian versus yeast Cyt*c*. We suggest that Cyt*c* in higher organisms has evolved to limit peroxidase activity, leading to stress-induced release of Cyt*c* from mitochondria, thereby imposing a more stringent barrier to the onset of apoptosis.

Chapter 5 Detergent Bound Cytochrome *c* Dimer: a Model for the Cytochrome *c*/Cardiolipin Interaction via an Extended Lipid Anchorage

5.1 Introduction

In recent years, cytochrome *c* (Cyt*c*) has risen to notoriety for the role it plays early in apoptosis (*4-6*). During the initial stages of apoptosis, Cyt*c* associated with the negatively charged phospholipid, cardiolipin (CL), is capable of oxidizing carbons adjacent to unsaturated bonds on the acyl chains of CL in the presence of reactive oxygen species (*12*). In order for Cyt*c* to act as a peroxidase, the Met80-heme ligand must be lost providing an open heme site for catalysis. Having a decreased affinity for oxidized CL, Cyt*c* dissociates from the membrane, exits the mitochondria and binds with Apaf-1 in the cytoplasm to form the apoptosome. In fact, the peroxidase activity of the Cyt*c*/CL complex may contribute to membrane permeabilization (*138*). Although there has been much work and interest in the mechanism of Cyt*c*/CL interaction, an atomic resolution structure of the interaction has been lacking.

A number of anionic phospholipids have been demonstrated to increase peroxidase activity of Cyt*c* (*139, 140*). Interestingly other ligands with hydrophobic chains, including sodium dodecyl sulfate detergent, vitamin E derivatives, and trimethylammonium bromide detergents with various length carbon tails, have been shown to increase peroxidase activity in Cyt*c* (*140-142*). It is possible that the interaction of these molecules with Cyt*c* causes a conformational change in Cyt*c*, stabilizing a peroxidase capable conformer.

Multiple CL binding sites on Cyt*c* have been proposed. The first sites identified were the A- and C-sites (*143, 144*). Electrostatic interactions are responsible for the A-site, involving residues: Lys72, Lys73, Lys86, and Lys87 (*50, 136, 143, 144*). Accommodation of the acyl chain by the hydrophobic cleft of the heme crevice loop has also been proposed (*136, 145*).

Asn52, the C-site, has been proposed to stabilize the Cyt*c*/CL interaction by hydrogen bonding to protonated phosphate (*143, 144*). Intriguingly, the C-site is also near a channel lined with hydrophobic residues that reaches in towards the heme (*144, 146, 147*). Another electrostatic interaction site for Cyt*c*, the L-site, comprised of Lys22, Lys25, His26, Lys27, and His33, residing on the opposite side of the protein as the A-site has been proposed (*148*). These opposing A- and L- binding sites have been implicated in enabling Cyt*c* to bridge lipid membranes, facilitating membrane fusion. One proposed model of CL interaction is the extended lipid anchorage (*144, 147, 149*). In this model, a lipid acyl chain extends from the lipid and incorporates itself into a hydrophobic cavity or channel within a peripheral protein, effectively anchoring the protein to the membrane. Binding sites stabilize the interaction with a phosphate group at the membrane surface, while an acyl chain inserts into Cyt*c*. Rather than merely accommodating a single acyl chain, two acyl chains have also been suggested to protrude into Cyt*c* (*137*).

An alternative to the extended lipid anchorage mechanism, suggests that native Cyt*c* interacts electrostatically with CL in a compact conformer, which then partially unfolds or exists in an extended state after interacting with CL and partially inserts into the membrane (*33, 34*). There is a conformational equilibrium between compact and extended conformers in this peripheral binding mechanism (*106*). Other studies have also suggested altered or partially unfolded protein conformers upon interaction with CL containing liposomes (*150, 151*).

Recently, a crystal structure demonstrating a C-terminal domain swapped dimer of equine Cyt*c* has been reported (*30*). Ω-loop D, residues 70-85, acts as the hinge loop for the domain swap. When Ω-loop D is acting as the hinge loop, Met80-heme ligation is lost leading to an open heme coordination site. As one might expect with an open heme coordination site, the

domain swapped dimer demonstrates enhanced peroxidase activity over the monomeric protein (*32*). Domain swapped oligomeric Cyt*c* has been shown to interact with negatively charged membranes (*31*). Thus, formation of a Cyt*c* domain swapped dimer on a membrane could provide a potential platform for CL oxidation during the initial stages of apoptosis.

Although atomic resolution structural data are relatively recent, Cyt*c* dimer formation has been previously established. Treatment of bovine heart muscle Cyt*c* with acid was first shown to form dimeric protein in 1960 (*28*). Tetrameric, trimeric, and dimeric horse heart Cyt*c* was purified following ethanol treatment a few years later (*29*). More recently, further domain swapped Cyt*c* dimers with varying structures have been solved by X-ray methods for *Hydrogenobacter thermophilus* $Cyt c_{552}$ (*152*), *Aquifex aeolicus* $Cyt c_{555}$ (*153*), and *Pseudomonas aeruginosa* $Cyt c_{551}$ (*154*). Dimeric Cyt*c* was purified following treatment with ethanol in the four crystal structures described above. Similar structures of the horse Cyt*c* dimer have also been solved for dimer isolated after refolding from an acid molten globule state (*155*) or a guanidine hydrochloride denatured state (*156*). Furthermore, addition of sodium dodecyl sulfate detergent to either monomeric or dimeric Cyt*c* has been shown to create an equilibrium between the monomer and the domain swapped dimer species (*30*).

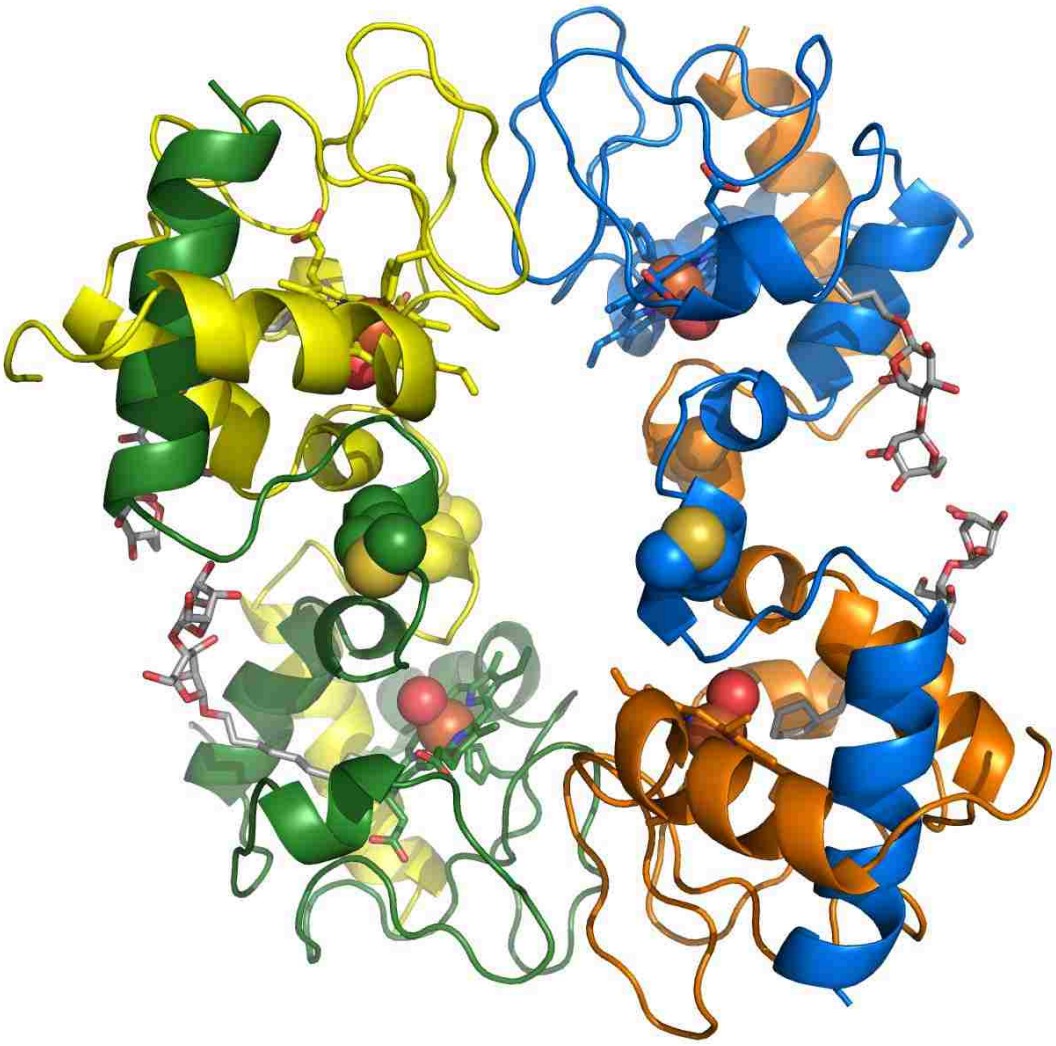

Figure 5.1. Structure of WT* yeast iso-1-Cyt*c* dimer demonstrating both dimers (green/yellow, and blue/orange) in the asymmetric unit (PDB code: 5DC1). The Met80 residue is shown as spheres. A CYMAL-6 (gray sticks) molecule inserts into the heme cavity of each subunit. Water coordinated to the heme is shown as a red sphere and the Fe^{3+} of heme as an orange sphere .

In this work, we attempted to crystallize yeast iso-1-Cyt*c* carrying a K72A mutation in the presence of various detergents. We have solved a C-terminal domain swapped dimer for this variant using CYMAL-6 detergent at a resolution of 2.003 Å (Figure 5.1). Although this structure is similar to that previously reported for the domain swapped equine Cyt*c* dimer (*30*), this new dimer structure exhibits a channel providing access to the heme which accommodates the aliphatic chain of the CYMAL-6 detergent. For the first time, an atomic resolution structure

has been solved, demonstrating how a lipid acyl chain can bind Cyt*c* in a specific pocket that places the acyl chain adjacent to the heme such that heme-mediated peroxidation could occur. Furthermore, the results provide direct evidence for the extended lipid anchorage as a mechanism for the interaction of Cyt*c* and other proteins with lipid bilayers.

5.2 Experimental Procedures

5.2.1 Protein expression and purification.

Expression and purification was performed as previously described (*18, 58, 59, 88*). WT* iso-1-Cyt*c* contains two background mutations, K72A and C102S. K72A prevents K72-heme ligation when expressed in *Escherichia coli*, as K72 is trimethylated, preventing heme ligation, in wild type yeast iso-1-Cyt*c* expressed in *Saccharomyces cerevisiae* (*48*). C102S prevents disulfide dimerization. During cation-exchange HPLC purification a Waters ProteinPak SP 8HR column (part no. WAT035655) was used for preparing protein for screening crystallization conditions and a BioRad UNO S6 column (catalog no. 720-0023) was used for protein preparation in dimer dissociation and absorbance experiments.

5.2.2 Crystallization, structure determination, and refinement.

Oxidized WT* iso-1-Cyt*c* in 75% $(NH_4)_2SO_4$ and 0.1 M Tris (pH 8) with a concentration of ~6mg/ml was used for initial crystallization trials. Purity of protein was confirmed using SDS-PAGE prior to setting up commercial crystallization screening trials. Initial hits were found in the HR2-410 Detergent Screen 1 kit and further optimized with detergent additive screening (Hampton Research) where vapor diffusion hanging drops were mixed 2:2:1 (vol/vol) with protein solution, reservoir solution [90% $(NH_4)_2SO_4$ and 0.1 M Tris-HCl (pH 8)], and detergent. Additional crystallization conditions were performed in grid screening by expanding the pH range and $(NH_4)_2SO_4$ concentration with various detergents in 24-well VDX plates, and

incubated at 20 °C. Large cubic-shaped crystals were obtained in 86% $(NH_4)_2SO_4$, 0.1 M Tris-HCl (pH 7.4) reservoir solution, and 5.6 mM CYMAL-6 with 16 mg/mL of WT* iso-1-Cyt*c* in 75% $(NH_4)_2SO_4$. Prior to X-ray diffraction analysis, crystals were allowed to continue growth for several weeks before being transferred into an 80% $(NH_4)_2SO_4$, 0.1 M Tris-HCl (pH 7.4) cryoprotectant containing 10% (v/v) glycerol and flash-frozen in a liquid nitrogen stream.

Diffraction data were collected at the Stanford Synchrotron Radiation Lightsource SSRL-SMB 14-1 beamline using a MAR325 CCD detector at an incident beam wavelength of 0.9875 Å. Images were indexed, integrated, and scaled using HKL2000 (*113*). The initial phasing map was determined by the molecular replacement method with Phaser, integrated in PHENIX software suite (*114*), using coordinates of residues 1-72 of yeast iso-1-Cyt*c* (PDB code: 2YCC) as a search model. There are 4 molecules per asymmetric unit with pseudo two-fold rotational symmetry. Cyclic model rebuilding with Coot (*115*) and refinement of atomic positions, real space, occupancy, and thermal parameters with PHENIX have improved the model to a final resolution of 2.0 Å. Data collection and refinement statistics are shown in Table D1. Coordinates have been deposited at the Protein Data Bank (www.rcsb.org) under PDB code: 5DC1.

5.2.3 Dimer dissociation kinetics.

About 2.2 mg of purified and oxidized WT* in 50 mM potassium phosphate (pH 7) was precipitated by addition of ethanol to 80% (vol/vol). Samples were incubated on ice for 15 min, centrifuged for 5 min at 4 °C, flash frozen in liquid nitrogen, and then lyophilized overnight. Lyophilized samples were stored at -80 °C. Lyophilized oligomeric iso-1-Cyt*c* preparations were resuspended in 270 µL of 50 mM potassium phosphate (pH 7) at 4 °C for 15 min, mixing

with a pipet every 5 min. Samples were then incubated on ice for 30 minutes, mixing with a pipet every 10 min and centrifuged at 4 °C for 5 min before separation by FPLC.

Following resuspension, oligomeric iso-1-Cyt*c* solutions were purified by size exclusion gel chromatography using an AKTA-FPLC (GE Healthcare, pump P-920 and monitor UPC-900) and a BioRad ENrich SEC-70 column (catalog no. 780-1070) at 4 °C in 50 mM potassium phosphate (pH 7). Iso-1-Cyt*c* dimer peaks were collected and incubated at 30, 25, 20, 15, and 10 °C in either a Thermolyne Type 17600 Dri-Bath (model no. DB17615) with 4 °C ambient temperature or a Julabo F12-ED refrigerated/heating circulator. Approximately 120-150 µL fractions of the dimer solution were analyzed by FPLC to monitor monomer formation from dimer with time. Fraction dimer and monomer, f_{Dimer} and $f_{Monomer}$, from FPLC traces were calculated from peak heights. Baseline for peak height measurements was determined by fitting a straight line to baseline selected before and after the dimer and monomer peaks. Initial dimer concentration was near 50 µM (heme content, i.e. actual dimer conventration is 25 µM), measured after return to monomer. Rate constants for dimer to monomer conversion, k_{DM}, were determined by fitting f_{Dimer} and $f_{Monomer}$ versus time plots to single exponential decay and rise to maximum equations, respectively.

5.2.4 Absorbance spectra.

Ethanol treated WT* iso-1-Cyt*c* was prepared for FPLC as described above. Absorbance spectra of dimer and monomer fractions were monitored on a Beckman Coulter DU800 spectrophotometer at 4 °C. Following initial scans, dimer fractions were incubated at 30 °C for 2 hours and measured again, to monitor return to monomer. To correct for baseline drift, absorbance at 750 nm was subtracted from the absorbance at all other wavelengths ($A_{corr} = A - A_{750}$).

5.2.5 Circular dichroism measurements.

Following ethanol treatment, resuspension in 50 mM potassium phosphate (pH 7), and FPLC purification, secondary structure of dimeric and monomeric iso-1-Cyt*c* was monitored using an Applied Photophysics Chirascan circular dichroism (CD) spectrophotometer with a 0.1 cm pathlength. Initial ellipticity measurements were collected at 4 °C. Dimeric iso-1-Cyt*c* was then incubated at 30 °C for 2 hours and the spectrum was collected again, at 30 °C. Absorbance spectra were then collected on a Beckman Coulter DU800 spectrophotometer. Absorbance spectra were corrected for baseline drift as described above. The corrected molar extinction coefficients, ε_{corr}, were calculated from A_{corr} using concentrations determined from the absorbance at 339, 526.5, and 541.74 nm and the molar extinction coefficients 20.9 mM^{-1} cm^{-1}, 11.0 mM^{-1} cm^{-1}, and 9.9 mM^{-1} cm^{-1}, respectively (*62*). Molar ellipticity, [θ], was calculated from ellipticity using the concentrations determined from absorbance spectra.

5.2.6 Formation of dimer in solution.

A 300 µL sample of 16 mg/mL WT* iso-1-Cyt*c* in 75% $(NH_4)_2SO_4$, 86% $(NH_4)_2SO_4$ in 0.1 M Tris-HCl (pH 7.4), and 5.6 mM CYMAL-6 mixed 2:2:1 (vol/vol) was prepared and incubated at 20 °C to mimic initial crystallization conditions. 15 µL samples were diluted with 100 µL of 50 mM potassium phosphate (pH 7), immediately prior to FPLC size exclusion gel chromatography as described above. FPLC traces were collected immediately after preparation, at one month, and at three and a half months incubation at 20 °C.

5.3 Results

5.3.1 Yeast iso-1-Cyt*c* C-terminal domain swapped dimer.

Here we present a crystal structure of the WT* yeast iso-1-Cyt*c* C-terminal domain swapped dimer at 2 Å resolution formed at pH 7.4 (Figure 5.1). Monomeric WT* iso-1-Cyt*c*

was incubated with $(NH_4)_2SO_4$, Tris, and CYMAL-6 detergent at 20 °C and crystallized as an iso-1-Cyt*c* dimer. There are four molecules, two dimers, residing in each asymmetric unit. Two molecules of CYMAL-6 are bound to each dimer, one incorporating into a channel on each subunit of the dimer. The C-terminal α-helix swings away from each iso-1-Cyt*c* subunit and incorporates itself into the second monomeric unit of the dimer. Although there are only minimal structural changes in a large portion of the dimer relative to monomeric iso-1-Cyt*c* (Figure 5.2), a large relocation of Ω-loop D occurs as Ω-loop D becomes the hinge loop or linker between subunits of the dimer. With Ω-loop D spanning the two subunits, the native Met80-heme ligation is lost. Instead, a water molecule coordinates to the distal heme site. Perturbation of Ω-loop D begins near residue 72. It is interesting to note that there exists a slight shift in the backbone away from the cavity accommodating CYMAL-6 beginning near residue 72, enabling accommodation of the detergent. By Leu85, which lies at the end of Ω-loop D, the domain swapped C-terminus aligns with the monomeric iso-1-Cyt*c* structure once again. Figure 2B demonstrates that there are some significant changes in the region accommodating insertion of the detergent (RMSD approaching 3 Å), beginning near residue 40, which lies at the bottom of the CYMAL-6 cavity.

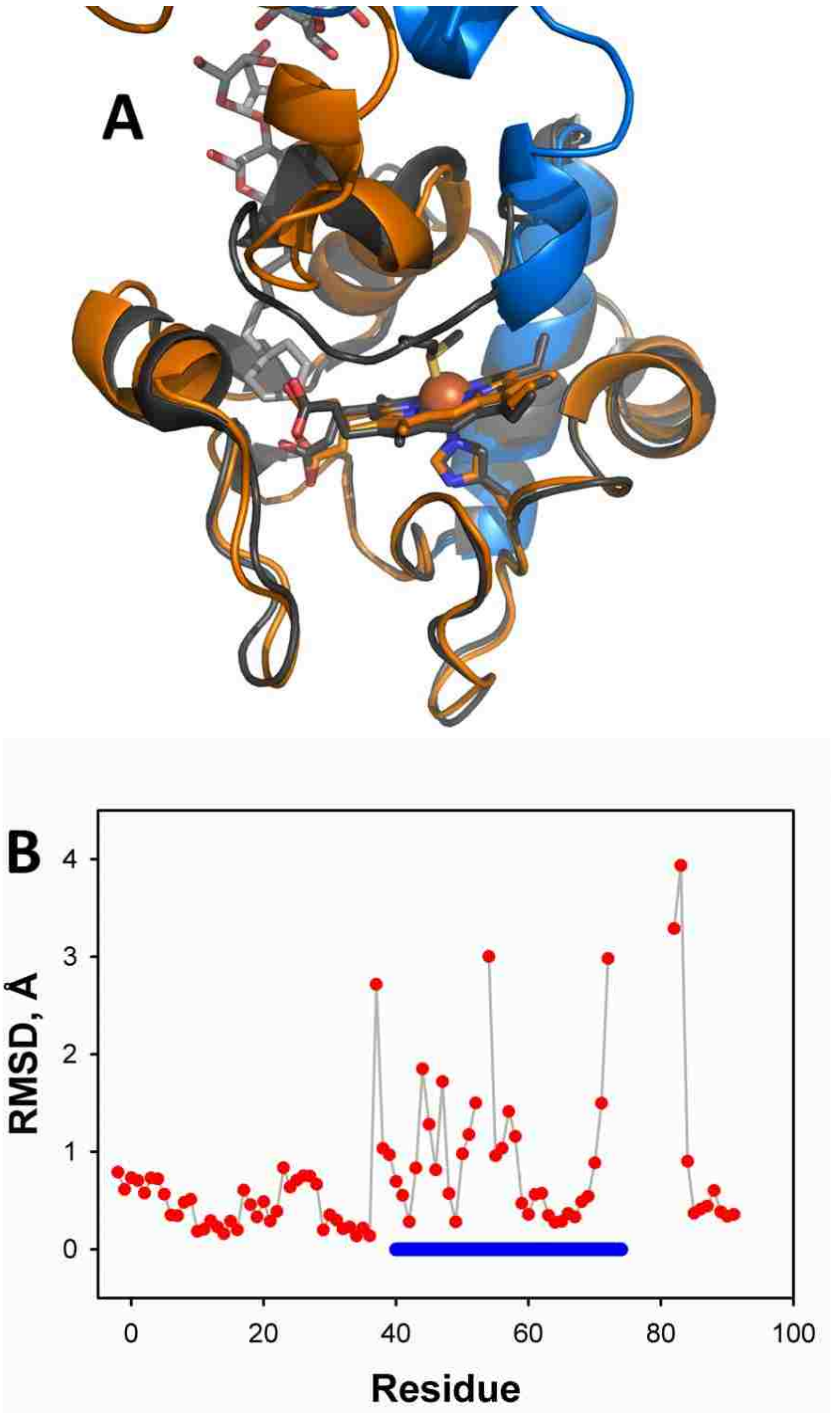

Figure 5.2. Iso-1-Cyt*c* dimer vs monomer. (A) Overlay of yeast iso-1-Cyt*c* dimer (blue/orange, PDB code: 5DC1) with yeast iso-1-Cyt*c* monomer (black, PDB code: 2YCC (*7*)). (B) RMSD as a function of residue number from an alignment of monomeric yeast iso-1-Cyt*c* (PDB code: 2YCC) with WT* iso-1-Cyt*c* dimer chain C (residues -2 to 72) and chain B (residues 82 to 103), performed in the graphics program Coot (*115*). The blue bar represents residues 40-74, the area demonstrating perturbations resulting from CYMAL-6 insertion.

5.3.2 Accommodating a hydrocarbon chain in the heme cavity.

The hydrocarbon chain and cyclohexyl ring of CYMAL-6 inserts into a cavity on each subunit of the dimer, providing access to the heme (Figure 5.3). The cavity resides in the loop between residues 55 and 74, which encompasses the 60's helix. As shown in Figure 5.2, there are only small scale movements within the area surrounding the cavity. The maltose head group of CYMAL-6 remains on the exterior surface near the dimer interface. The electron density of the alkyl chain of CYMAL-6 is well-defined. However, the electron density of the maltose head group is diffuse indicating that its position is fluxional. Nevertheless, the electrostatic surface representation in Figure 5.3, illustrates that these maltose head groups emerge in a positive region or patch on the dimer surface. Interestingly, the area of positive charge in the hinge loop region of the dimer coincides with the residues of the A-site suggested in electrostatically binding CL. At the entrance to the channel, Lys55 and Lys73 protrude outward toward the maltose head groups. Thus, the channel on each subunit of the monomer is capable of accommodating an aliphatic chain, with a positive patch near the exterior capable of electrostatic interactions with a negatively-charged lipid head group. The cutaway image in Figure 5.3C highlights the interior of the cavity with CYMAL-6 protruding down to the heme.

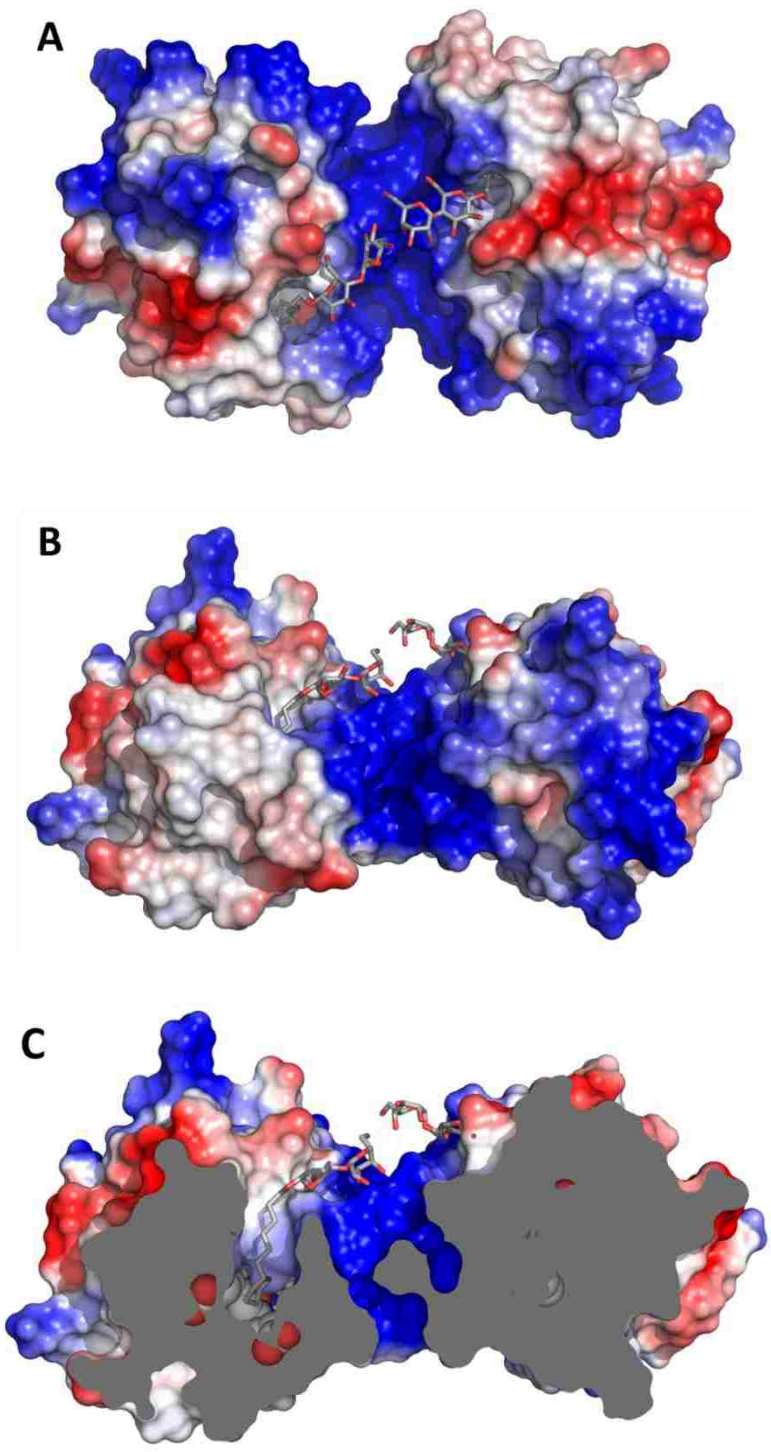

Figure 5.3. Electrostatic potential surface view of WT* iso-1-Cyt*c* dimer, where blue is positive, gray is neutral, and red is negative. (A) View looking downward into the cavity accommodating CYMAL-6 (gray sticks), (B) 45° rotation, and (C) visualization of the cavity using a cutaway view (interior of the protein is shown in gray). Heme is shown as a space-filling models (red spheres protruding through the gray surface are the oxygens of the heme propionate).

Two other channels also appear on each subunit of the dimer. Accessing the heme near the cyclohexyl ring of CYMAL-6, Lys55 and Tyr74 separate the second channel from the cavity occupied by CYMAL-6 (Figure 5.4A). A narrow third channel accesses the interior from the side opposite Ω-loop D linker region (Figure 5.4B).

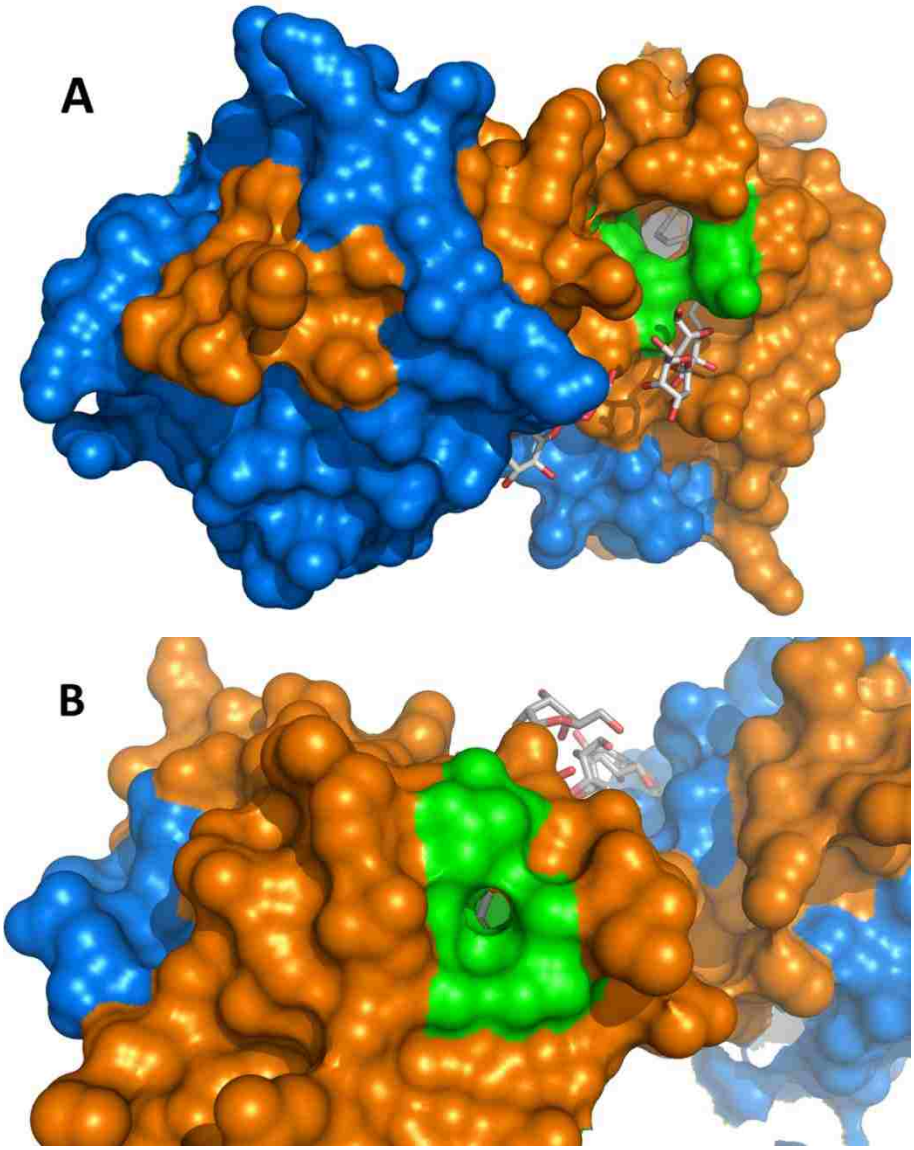

Figure 5.4. Additional channels into iso-1-Cyt*c*. The two iso-1-Cyt*c* subunits are shown in blue and orange. CYMAL-6 is shown in gray sticks. (A) The CYMAL-6 cyclohexane ring can be seen through the second channel accessing the heme cavity, separated from the CYMAL-6 channel by Lys55 and Tyr74 (green surface area). (B) A third channel into the heme, where CYMAL-6 can be seen at the bottom of the channel (Ser39, Gly40, Asn52, Asn56, Tyr67, and Tyr74 are shown in green).

5.3.3 Water in the heme cavity.

There are six water molecules buried within the heme cavity (Figure 5.5). The first of the four waters that create a network from the heme to the occupying detergent coordinates to the heme distal site. These four water molecules spanning from the iron to CYMAL-6 form a hydrogen bonded chain with distances of 2.70-3.05 Å from one another. Of these four water molecules, three are near the hydroxyl group of Tyr67. The water molecule bound to the heme is 3.09 Å from the hydroxyl group of Tyr67, and the next two water molecules are 3.57 and 2.72 Å away from the hydroxyl group of Tyr67. Two other water molecules are located on the proximal side of the heme. Interestingly, these two waters are also conserved in monomeric yeast iso-1-Cyt*c* (*7*).

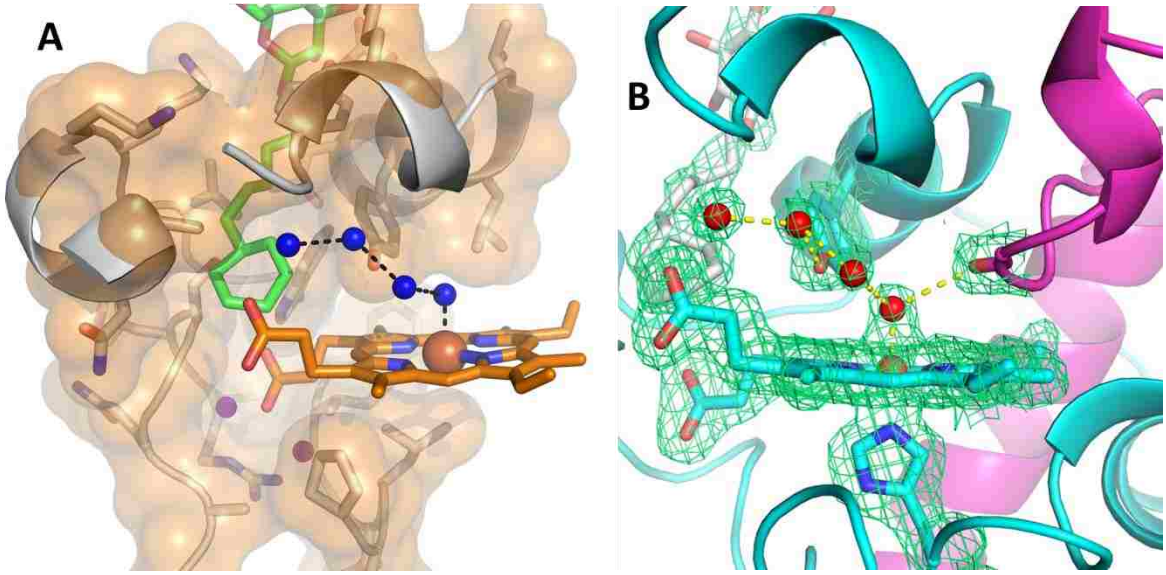

Figure 5.5. Water network in the heme cavity. (A) Zoomed in view demonstrating the water network (blue spheres) between CYMAL-6 (green sticks) and the heme group. Residues 30-44 and 51-74 are shown as gray sticks with a transparent orange surface. Two buried waters on the proximal side of the heme are shown as purple spheres. (B) Electron density (green mesh) for the water network (red spheres), the heme, His18, Tyr67, the carbonyl of Phe82 and CYMAL-6 (gray sticks) in the heme cavity.

5.3.4 Comparison to equine Cyt*c* dimer.

Initial comparison to the equine Cyt*c* dimer, demonstrates a number of similarities. Both structures are C-terminal domain swapped dimers, where Ω-loop D acts as the hinge loop region, and water has become the heme ligand. Four Cyt*c* molecules were also found in the asymmetric unit cell of the equine Cyt*c* dimer (*30*). Upon alignment of the two dimers, the subunits themselves have similar structures (Figure 5.6). The major differences between the two dimers exist in the hinge loop region. Residues 72-85 of Ω-loop D rearrange to form the hinge loop in the yeast iso-1-Cyt*c* dimer. Overlaying equine Cyt*c* dimer (*30*) and monomer (*132*) demonstrates a shorter hinge loop in the equine dimer, made up of only residues 78-83. In fact, the heme centers of the yeast iso-1-Cyt*c* dimer are over 7.5 Å further apart from one another compared to the equine dimer. It is possible that bound CYMAL-6 stabilizes this more extended dimer as the maltose head group interacts with the positive patch at the dimer interface. In light of the work presented here, as well as the structural data from other Cyt*c* dimers (*30, 152-154*), the specific orientation may be less important as Ω-loop D may exist as a relatively flexible hinge loop, allowing each subunit to adopt the most stable conformer relative to its dimeric subunit. Alanine 72 residues from each subunit of the yeast iso-1-Cyt*c* dimer lie in close proximity to one another (Figure 5.6). If the larger native trimethyllysine was present, this extended linker conformer, with residues 72 near one another, would be sterically less favorable.

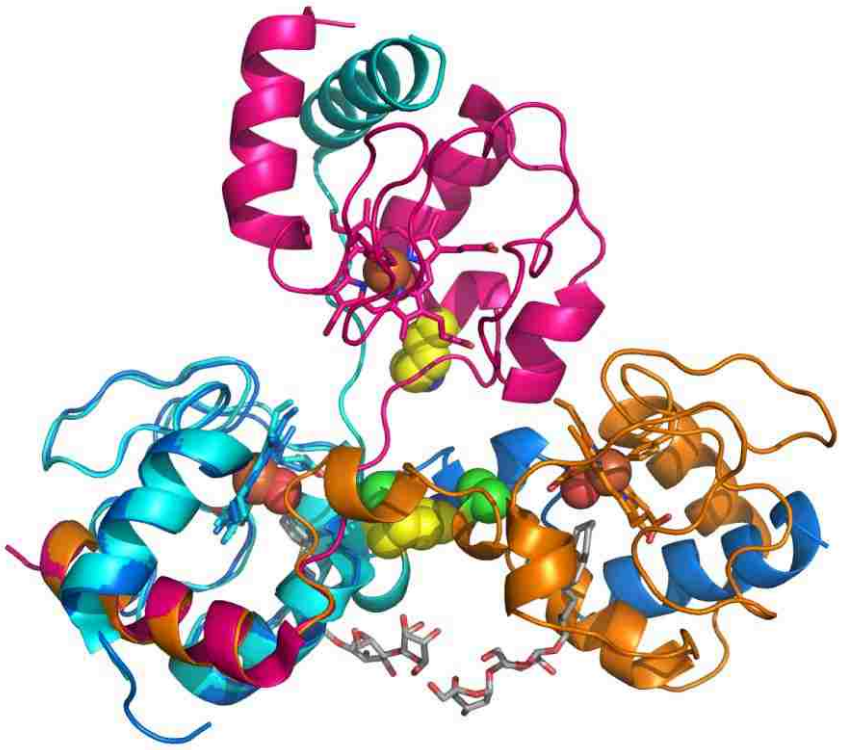

Figure 5.6. Comparison of the yeast iso-1-Cyt*c* (blue/orange, PDB code: 5DC1) and equine Cyt*c* dimers (cyan/magenta, PDB code: 3NBS (*30*)). Blue and cyan subunits are overlaid with one another. Lysine 72 in the equine Cyt*c* dimer and alanine 72 in the yeast dimer are shown as yellow and green spheres, respectively.

5.3.5 Dimer dissociation kinetics.

In order to investigate the physical properties of the iso-1-Cyt*c* dimer in solution, dimeric iso-1-Cyt*c* was isolated from monomer and higher order oligomers following ethanol treatment by FPLC size exclusion gel chromatography (Figure 5.7). Purified dimer was incubated at 30, 25, 20, 15, and 10 °C and over time the return to monomer was monitored by FPLC. A representative elution profile for return of dimer to monomer at 20 °C is shown in Figure 5.7 (bottom elution profile). The fraction dimer and monomer, f_{Dimer} and $f_{Monomer}$, were plotted versus time (Figure 5.8) and fit to single exponential equations to determine the rate constant for dimer dissociation to monomer, k_{DM} (Table 5.1). It is clear that as temperature increases from 10 to 30 °C, the rate of dimer dissociation to monomer becomes much faster.

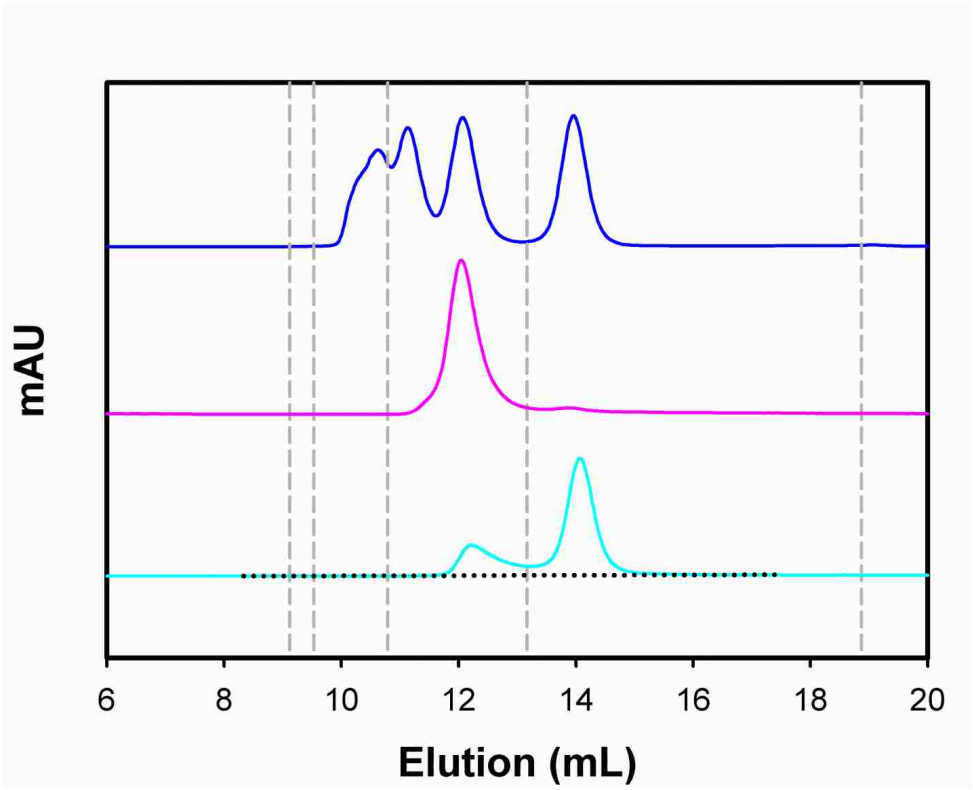

Figure 5.7. Elution curves of WT* iso-1-Cyt*c* followed by FPLC. FPLC trace following resuspension of ethanol treated iso-1-Cyt*c* in 50 mM potassium phosphate (pH 7) (blue curve). FPLC trace of dimer sample immediately following purification (pink curve) and after ~5 hours at 20 °C (cyan curve). The dotted black curve represents baseline for peak height determination for the bottom elution profile. Time zero and 5 hour curves were scaled by a factor of 20 relative to the blue curve showing the initial purification of the dimer. Dashed gray lines correspond to protein standard (BioRad 151-1901) elution times. Standards from left to right: Thyroglobulin (bovine) MW: 670,000, γ-globulin (bovine) MW: 158,000, Ovalbumin (chicken) MW: 44,000, Myoglobin (horse) MW: 17,000, Vitamin B_{12} MW: 1,350.

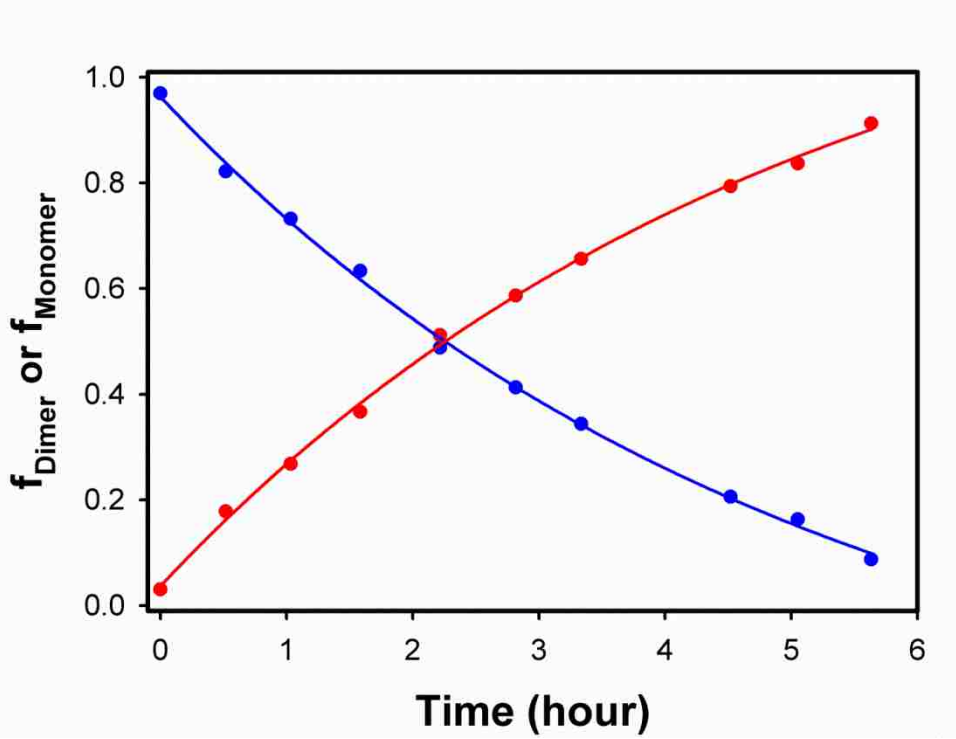

Figure 5.8. Representative fit of data following loss of dimer (blue) and formation of monomer (red) when incubated at 20 °C. Fraction dimer versus time and fraction monomer versus time are fit to single exponential equations.

Table 5.1. Rates of dimer to monomer conversion followed by FPLC at 10 to 30 °C.

Temperature (°C)	k_{DM} (hour^{-1})[a]
30	12 ± 1
25	2.0 ± 0.1
20	0.22 ± 0.02
15	0.03 ± 0.01
10	0.024 ± 0.002

[a]Parameters are the average and standard deviation of a minimum of three independent trials.

5.3.6 Absorbance spectra of yeast Cyt*c* dimer and monomer.

Figure 5.9 shows an overlay of WT* iso-1-Cyt*c* dimer, monomer, and dimer following incubation at 30 °C. Compared to the monomer, the Soret peak has been shown to shift to a shorter wavelength in the horse Cyt*c* dimer (*30*, *157*). Dimeric yeast iso-1-Cyt*c* has a maximal

Soret peak near 407.6 nm, about 2 nm lower than the yeast iso-1-Cyt*c* monomer (409.7 nm) (Figure 5.9B), which is similar to the shift seen between dimeric equine Cyt*c* (406.5 nm) and monomeric equine Cyt*c* (409 nm) (*30, 157*). Although the 695 nm band, corresponding to Met80-heme coordination (*3, 69, 70*), shows a loss of amplitude in the iso-1-Cyt*c* dimer trace, the 695 nm peak has not completely disappeared (Figure 5.9C). Incomplete loss of the 695 nm peak in dimeric Cyt*c* has been previously reported (*30, 157*). Incubation of the dimer sample at 30 °C, led to a return to a monomer spectrum (Figure 5.9).

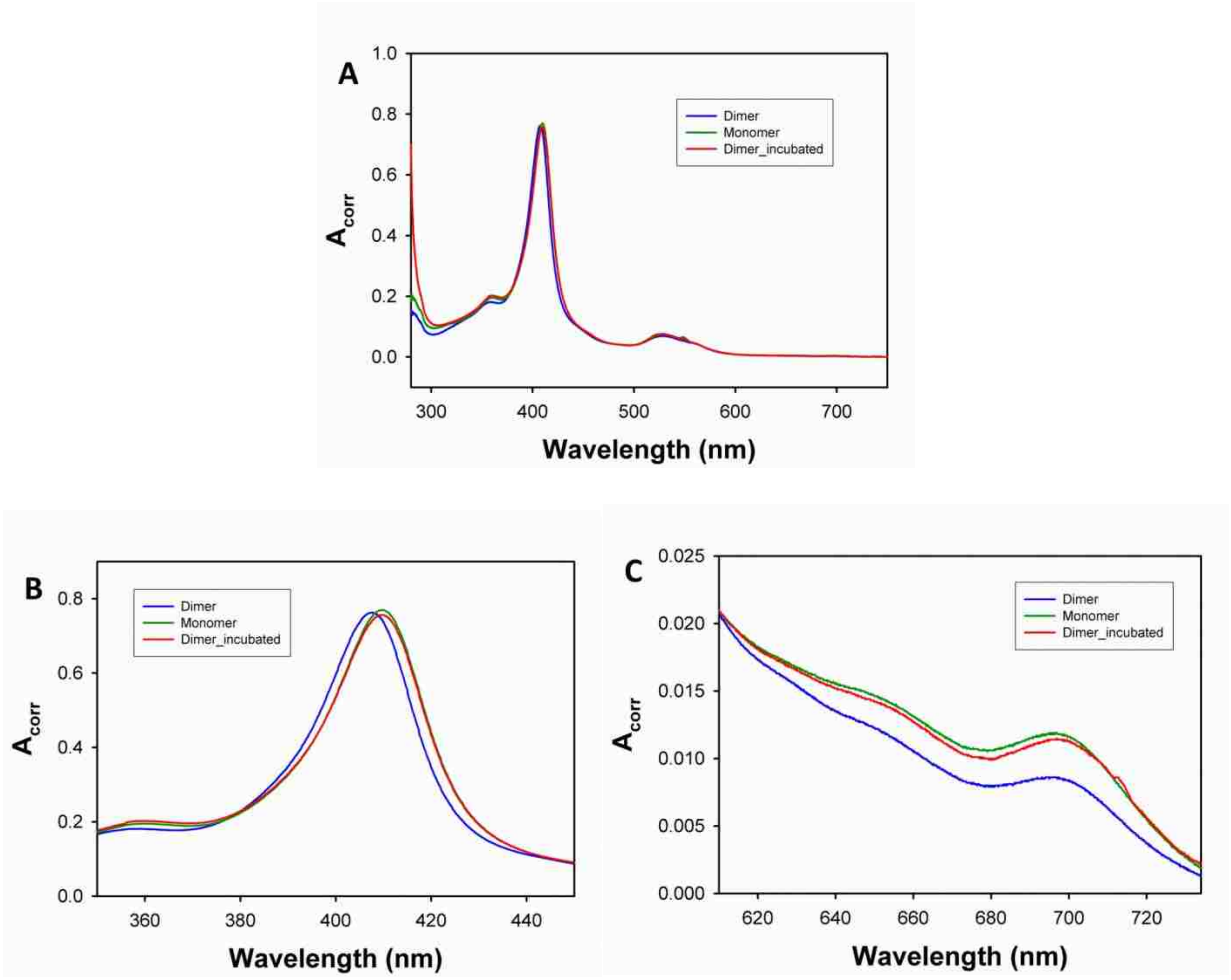

Figure 5.9. Absorption spectra comparing oxidized WT* iso-1-Cyt*c* dimer (blue curve), monomer (green curve), and dimer after incubation at 30 °C (red curve). (A) Full absorbance spectra from 280 - 750 nm. (B) Iso-1-Cyt*c* heme Soret peak, dimer after 30 °C incubation and monomer concentration were about 6.7 µM heme. (C) The 695 nm band, where dimer after 30 °C incubation and monomer concentrations were near 20 µM heme.

5.3.7 Effects of the Cyt*c* dimer on secondary structure.

In order to determine how the secondary structure is affected by formation of dimeric iso-1-Cyt*c*, dimer and monomer were monitored by CD spectroscopy. Immediately following FPLC purification, ellipticity of the dimer and monomer was measured at 4 °C (Figure 5.10A). Dimer was incubated at 30 °C to check the CD spectrum after dimer dissociation to monomer. There is minimal perturbation of secondary structure upon iso-1-Cyt*c* dimer formation. After 30 °C incubation, dimeric and monomeric absorbance spectra were collected and absorbance was converted to molar extinction coefficients. Figure 5.10B demonstrates that following incubation at 30 °C, the Soret peak of the dimeric iso-1-Cyt*c* sample overlays well with the monomeric spectra.

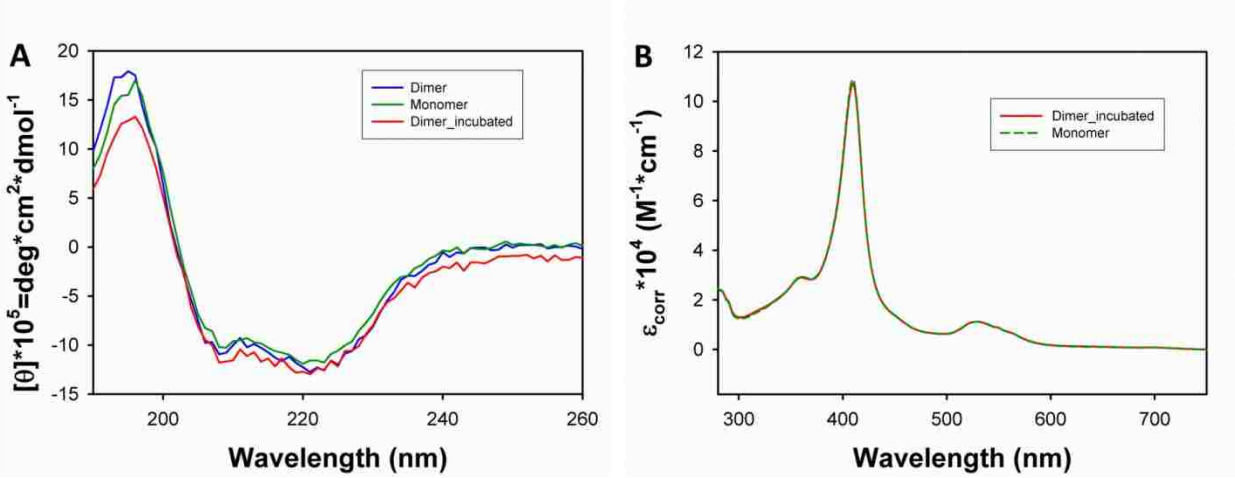

Figure 5.10. CD and absorbance spectra of dimeric and monomeric Cyt*c*. (A) Molar ellipticity of iso-1-Cyt*c* dimer (blue curve) and monomer (green curve) at 4 °C and dimeric iso-1-Cyt*c* after 30 °C incubation (red curve). (B) Molar extinction coefficients of dimeric iso-1-Cyt*c* after 30 °C incubation (red curve) and monomeric iso-1-Cyt*c* (green dashed curve). Absorbance spectra were acquired at room temperature (~22°C). Concentration of dimeric iso-1-Cyt*c* and monomeric iso-1-Cyt*c* was 6.6 µM and 8.7 µM heme, respectively.

5.3.8 Formation of dimer in solution.

Under the conditions described here (Experimental Procedures), monomeric Cyt*c* crystallizes as a domain swapped dimer. In order to see if the iso-1-Cyt*c* dimer forms in solution

under similar conditions, a 300 µL sample of the hanging drop solution was prepared and incubated at 20 °C in an Eppendorf tube. Figure 5.11 shows that initially only monomer was present in the solution. After one month, a small dimer peak appears, and by three and a half months, dimer and trimer peaks are present. Although there is only a small oligomer population, this suggests that under these conditions, there is some equilibrium driving oligomeric iso-1-Cyt*c* formation. The fact that this sample was incubated in an Eppendorf tube and unable to vapor diffuse with a reservoir solution may account for the relatively small oligomeric population formed.

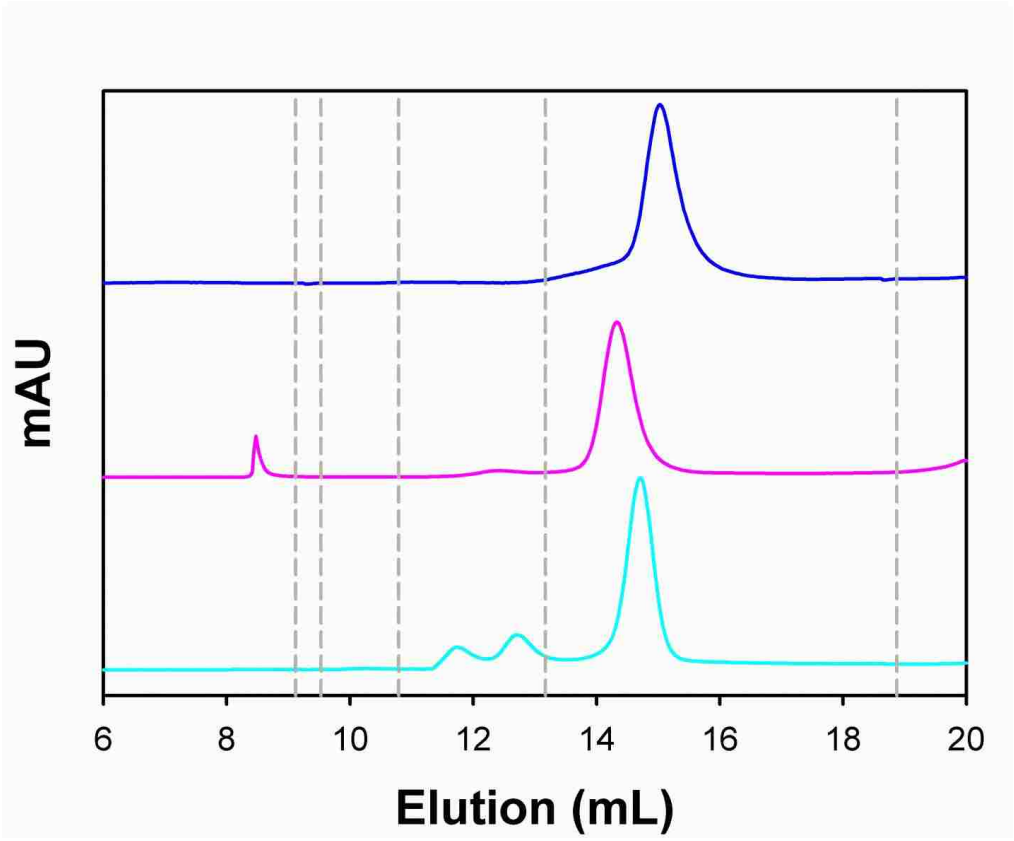

Figure 5.11. Elution curves of WT* iso-1-Cyt*c* followed by FPLC. 16 mg/mL WT* in 75% $(NH_4)_2SO_4$, 86% $(NH_4)_2SO_4$ in 0.1 M Tris-HCl (pH 7.4), and 5.6 mM CYMAL-6 were mixed 2:2:1 (vol/vol) to mimic crystallization conditions. Elution curves were collected immediately after preparation (blue curve), after one month incubation (pink curve), and after three and a half month incubation (cyan curve). Dashed gray lines correspond to protein standards (BioRad 151-1901) described in the caption to Figure 5.7.

5.4 Discussion

5.4.1 Yeast iso-1-Cyt*c* C-terminal domain swapped dimer.

For the first time an atomic resolution structure with detergent insertion into Cyt*c* allowing access to the heme crevice has been solved. The yeast iso-1-Cyt*c* C-terminal domain swapped dimer clearly demonstrates a hydrocarbon chain projecting into an interior channel providing access to an open heme coordination site, as is required for peroxidase activity of the Cyt*c*/CL complex. Displacement of the three waters that run between CYMAL-6 and the heme, could readily allow accommodation of longer hydrocarbon chains.

Previous crystal structures of dimeric Cyt*c* were achieved by purification of dimeric Cyt*c* following ethanol treatment and setting up crystallization trials with dimeric Cyt*c* (*30*, *152-154*). This work is unique in that monomeric iso-1-Cyt*c* was used in hanging drop crystallization trials. Under the conditions presented here, monomeric iso-1-Cyt*c* crystallizes as a dimer.

Residues 55 through 74 make up the loop accommodating the cavity occupied by CYMAL-6. Previously, these residues have been identified as surrounding a hydrophobic channel to the heme (*146*). This channel has previously been suggested to accommodate a CL acyl chain for either the A- or C-sites, where a positive lysine patch and Asn52 are located across the channel entrance from one another (*144*). The CYMAL-6 maltose group associates with a positive patch on the iso-1-Cyt*c* dimer, much as for the proposed A-site. Asn52 does not lie at the tunnel entrance. The fact that Asn52 does not lie at the tunnel entrance may provide support for the model where two acyl chains can bind one Cyt*c* subunit (*137*), where there may be the possibility for an acyl chain interaction at the A-site and at the C-site.

When Cyt*c* functions as a peroxidase, hydrogen peroxide interacting with the heme causes formation of Compound I, which in turn leads to formation of Compound II and a

tyrosine radical (*32, 158, 159*). This tyrosine radical has been proposed to abstract a hydrogen atom from a substrate, creating a carbon radical for peroxidative oxidation. In equine Cyt*c*, the highly conserved Tyr67, with the hydroxyl group located less than 4 Å from the heme moiety, has been proposed to be responsible for radical-driven hydrogen abstraction from CL, during CL oxidation (*158*). Both Tyr 46 and Tyr48 have also been suggested to be involved in peroxidase activity in human Cyt*c* (*160*). In the yeast iso-1-Cyt*c* dimer presented here, the hydroxyl group on Tyr67 lies 3.58 Å from the heme moiety and 3.45 Å from the cyclohexane ring on CYMAL-6 (Figure 5). The close proximity of Tyr67 to CYMAL-6 indicates that its participation in CL oxidation is feasible.

It is interesting to note that previous work on the Cyt*c*/CL interaction has demonstrated that an extended conformer of Cyt*c* forms on the lipid membrane where residues 66-92 appear to have unfolded and interactions between the N- and C-terminals are broken (*34*). Such an extended conformer may provide a platform for dimer formation on a lipid membrane. However, the authors are not aware of any definitive evidence that Cyt*c* dimers form naturally in vivo.

As noted previously, although Met80-heme ligation is lost in the C-terminal domain swapped equine Cyt*c* dimer structure, in solution, the 695 nm band is not completely lost (*30, 157*). Figure 5.9 also demonstrates persistence of the 695 nm band in dimeric iso-1-Cyt*c*. It is possible that the linker region may have enough flexibility to allow Met80-heme ligation in a subpopulation of species. At this point in time we cannot rule out incomplete domain swaps, enabling Met80-heme coordination, also contributing to persistence of the 695 nm band.

5.4.2 Temperature dependence of dimer dissociation.

To better understand the mechanism of dimer dissociation, the k_{DM} data (Table 5.1) were plotted as ln(k_{DM}) versus 1/T. There is clear curvature in this plot, so, rather than using the standard Eyring equation, we fit the data to Eq. 5.1 to account for the effect of the change in the heat capacity on the temperature dependence of $\Delta G^{\ddagger}$ (*99*) (Figure 5.12).

(5.1)

$$\ln(k) = \ln\left(\frac{k_B}{h}\right) - \frac{\left[\Delta H^{\ddagger}_{T_o} + \Delta C^{\ddagger}_p(T - T_o)\right]}{RT} + \frac{\left[\Delta S^{\ddagger}_{T_0} + \Delta C^{\ddagger}_p * \ln(T/T_o)\right]}{R}$$

In Eq. 5.1, T represents temperature in Kelvin, k_B is the Boltzmann's constant, and *h* is Planck's constant. T_o corresponds to the reference temperature, in this case, the lowest temperature in our data set, 283.15 K, was used. $\Delta C^{\ddagger}_p$, $\Delta H^{\ddagger}_{To}$, and $\Delta S^{\ddagger}_{To}$ are the difference in heat capacity, enthalpy, and entropy between the ground state and the transition state, respectively, at T_o. The fit of ln(k_{DM}) versus 1/T to Eq. 5.1 yields: $\Delta C^{\ddagger}_p = 3.0 \pm 0.8$ kcal*mol^{-1}*K^{-1}, $\Delta H^{\ddagger}_{To} = 24 \pm 8$ kcal*mol^{-1}, and $\Delta S^{\ddagger}_{To} = 0.004 \pm 0.03$ kcal*K*mol^{-1}. It is apparent that there are only minimal entropic contributions, but that a large enthalpic barrier exists for spontaneous dissociation of dimer to monomer. There is also a large change in the heat capacity to reach the transition state for dimer dissociation.

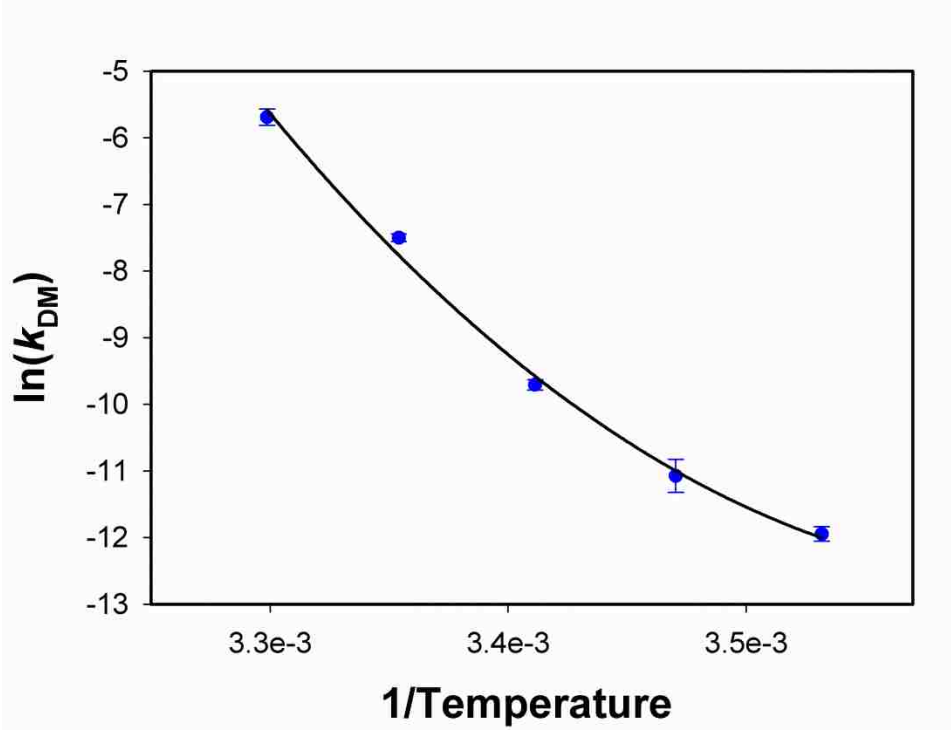

Figure 5.12. Plot of ln(k_{DM}) versus 1/T. Data are fit to Eq. 5.1 (black curve).

From thermal denaturation data the heat capacity increment, ΔC_p, for unfolding of wild-type yeast iso-1-Cyt*c* (containing trimethylated lysine 72) was found to be 1.4 kcal*mol^{-1}*K^{-1} (*161-163*). $\Delta C^{\ddagger}_p$ for dimer dissociation is about twice the ΔC_p for thermal unfolding, suggesting that the Cyt*c* dimer largely unfolds to reach the transition between the dimer and monomer. Cyt*c* folding studies have suggested that the N- and C-terminal helix interaction occurs early in the folding pathway, and that to disrupt the N- and C-terminal interaction requires global unfolding (*8, 164*). As the N- and C-terminal helix interaction must be broken to form the C-terminal domain swapped dimer, following this folding model it would appear that a large unfolding event is required for dimer decay. All methods for efficient preparation of the dimer require refolding from a denatured (*30, 156*) or molten globule state (*155*). Thus, studies on the formation of the dimer are also consistent with the transition state for the monomer-dimer

equilibrium being unfolded Cyt*c*. This observation suggests that the dimer could persist once formed, particularly for the more stable mammalian cytochromes *c*.

5.5 Conclusion

5.5.1 Detergent bound yeast iso-1-Cyt*c* C-terminal domain swapped dimer.

In summary, we have solved a 2.003 Å yeast iso-1-Cyt*c* C-terminal domain swapped dimer crystal structure with CYMAL-6 bound inside a cavity that provides access of the hydrocarbon chain to heme with an open coordination site. This result supports the proposed extended lipid anchorage model of Cyt*c*/CL interaction (*147*). Cyt*c*/CL binding studies indicate that Cyt*c*/membrane interactions are complex (*4-6, 33, 34, 136, 137, 143, 147*). Thus, our results do not rule out other modes of binding that have been proposed (*33, 34, 150*). Although there is no distinct proof of Cyt*c* dimer formation biologically, or that a Cyt*c* dimer is important in Cyt*c*/CL complex formation, this is the first model of a hydrocarbon chain protruding into a cavity providing access to an open heme coordination site. Monomeric Cyt*c* may interact with lipid in a similar manner. Additionally, the Cyt*c* oligomer system may provide a model system for understanding oligomeric protein interactions.

Chapter 6

6.1 **Conclusion**

Cytochrome *c* is a dynamic protein that functions in multiple cellular roles. On one hand Cyt*c* helps produce cellular energy by shuttling electrons in the electron transport chain. Conversely, following a conformational change, Cyt*c* initiates the intrinsic apoptotic pathway resulting in cell death. In order to elucidate the mechanism by which Cyt*c* converts between pathways with such drastic effect upon cellular outcome, it is of key importance to understand how conformational change is regulated in Cyt*c*. Ω-loop D is a highly conserved, yet flexible region of Cyt*c*. Residues from within Ω-loop D are responsible for the distal site heme ligand. Met80 ligates to the heme in the native conformer of Cyt*c*, but peroxidase activity requires a loss of Met80-heme ligation. The focus of the work presented here is to further understand the mechanisms by which the heme crevice loop is regulated and to provide a more accurate depiction of peroxidase capable conformers of Cyt*c*.

In cytochrome *c* the heme crevice is easily modulated by pH, as increasing pH leads to formation of the alkaline conformational transition (*9*). This alkaline conformer has similarities to the peroxidase capable conformer of Cyt*c*, where Ω-loop D undergoes a rearrangement yielding loss of the native Met80-heme ligand. Mutation of residue 72 from lysine to alanine has been shown to both enhance peroxidase activity of Cyt*c* (*49*) and increase heme crevice dynamics for the His79-heme mediated alkaline conformer of a K79H variant (*18, 19*). Not surprisingly, as residue 73 is much farther from the heme and part of a helical turn, formation of the His73-heme and His79-heme mediated alkaline conformers proceed differently. Rather than increasing dynamics of the heme crevice loop, data here, characterizing the thermodynamic and kinetic properties of the His73-heme mediated alkaline conformer, demonstrate a stabilization of

the native conformer for the tmK72A mutation. Therefore, residue 72 does not provide a generic regulatory role for heme crevice dynamics, but rather only regulates heme dynamics corresponding to His79-heme ligation, which appears to behave in a similar manner as the transition to a peroxidase capable conformer. In mammals residue 72 is not trimethylated and in fact interacts with residues in Ω-loop D, possibly further constraining heme crevice loop dynamics. To determine whether residue 72 plays a similar role in regulation of the K79-heme mediated alkaline pathway in mammalian Cyt*c* a K72A/K73A variant could be employed. Experiments need to be carried out to determine whether residue 72 also regulates peroxidase activity for mammalian Cyt*c*.

Work on psychrophilic enzymes (*23*-*25*) and a destabilized variant of iso-1-Cyt*c* (*14*, *15*, *26*) have demonstrated that decreased stability can lead to increased dynamics. In this work, experiments on the yeast iso-1-Cyt*c* destabilizing L85A mutation found that although the global stability is decreased, heme crevice dynamics for the alkaline conformational transition were not enhanced. Thus, in the case of the L85A destabilizing mutation, local dynamics are not linked to global stability. It is possible that the heat capacity change to reach the transition state is altered by the L85A mutation resulting in the decrease in dynamics at the temperature of the kinetic studies on the WT*/K73H/L85A variant (*99*). If this is the case, the studies performed here, may not be at the optimal temperature for the alkaline conformational transition to occur. Future studies, performing kinetic experiments over a broad range of temperatures would enable determination of how temperature might affect the dynamics of the destabilized Cyt*c* alkaline conformational transition for this variant.

During the early stages of apoptosis, Cyt*c* acts as a peroxidase which oxidizes the acyl chain of CL (*12*). In order for Cyt*c* to gain peroxidase function the native Met80-heme ligation

must be lost to provide H_2O_2 heme access. This work presents a 1.45 Å X-ray crystal structure of tmK72A yeast iso-1-Cyt*c* with hydroxide coordinated to the heme and Met80 swung away from the heme. A buried water channel provides peroxide access to the heme cavity. The tmK72A mutation results in enhanced peroxidase activity compared to native tmK72 iso-1-Cyt*c*. As tmK72 lies across Ω-loop D in the native structure, it appears that residue 72 plays an important role in regulating heme crevice dynamics required to gain peroxidase activity. The monomeric Cyt*c*/CL interaction has not yet been identified at atomic resolution. Future work will investigate the incorporation of CL acyl chains or other related ligands into the interior of the heme, to provide close proximity to the heme for oxidation by Cyt*c*. Further, although Lys72 appears to play an important role in regulating heme crevice dynamics associated with peroxidase activity, the effects of a tmK72A mutation in electrostatic interactions with CL remains to be determined.

Dimeric Cyt*c* has been shown to form following acid (*28*) and ethanol (*29*) treatment. The C-terminal domain swapped Cyt*c* dimer presented here forms in the presence of CYMAL-6 detergent. To gain access to the heme, CYMAL-6 binds inside a cavity in each subunit of the dimer. This provides the first atomic resolution structure of a hydrocarbon chain protruding into Cyt*c* in a manner similar to the proposed extended lipid anchorage model for the Cyt*c*/CL interaction (*144, 147, 149*). Ω-loop D acts as a linker region between dimeric subunits, resulting in loss of Met80-heme ligation. With no distal heme ligand, this C-terminal domain swapped dimeric structure of Cyt*c* has the potential to act as a peroxidase in CL oxidation. Although dimeric Cyt*c* has not been shown to form naturally, it is possible that interaction with the mitochondrial membrane may provide a platform for dimer formation in the cell. It will be interesting to see if the monomeric Cyt*c*/CL interaction proceeds through a mechanism similar to

the dimeric extended lipid anchorage model demonstrated here. Further, it remains to be determined what other ligands are capable of forming dimeric crystals from monomeric Cyt*c* and if they use the same channel into the heme cavity. Similar studies should be performed on mammalian Cyt*c* to potentially identify a general binding mechanism for the Cyt*c*/CL interaction. It also remains to be determined how the addition of CYMAL-6 to Cyt*c* in solution may affect peroxidase activity.

Bibliography

1. Anfinsen, C. B. (1973) Principles that govern the folding of protein chains, *Science 181*, 223-230.
2. Dill, K. A., and Chan, H. S. (1997) From Levinthal to pathways to funnels, *Nat. Struct. Biol. 4*, 10-19.
3. Moore, G. R., and Pettigrew, G. W. (1990) *Cytochromes c: Evolutionary, Structural and Physicochemical Aspects*, Springer-Verlag, New York.
4. Ow, Y. P., Green, D. R., Hao, Z., and Mak, T. W. (2008) Cytochrome *c*: functions beyond respiration, *Nat. Rev. Mol. Cell Biol. 9*, 532-542.
5. Kagan, V. E., Bayir, H. A., Belikova, N. A., Kapralov, O., Tyurina, Y. Y., Tyurin, V. A., Jiang, J., Stoyanovsky, D. A., Wipf, P., Kochanek, P. M., Greenberger, J. S., Pitt, B., Shvedova, A. A., and Borisenko, G. (2009) Cytochrome *c*/cardiolipin relations in mitochondria: a kiss of death, *Free Radical Biol. Med. 46*, 1439-1453.
6. Schug, Z. T., and Gottlieb, E. (2009) Cardiolipin acts as a mitochondrial signalling platform to launch apoptosis, *Biochim. Biophys. Acta 1788*, 2022-2031.
7. Berghuis, A. M., and Brayer, G. D. (1992) Oxidation state-dependent conformational changes in cytochrome *c*, *J. Mol. Biol. 223*, 959-976.
8. Maity, H., Maity, M., and Englander, S. W. (2004) How cytochrome *c* folds, and why: submolecular foldon units and their stepwise sequential stabilization, *J. Mol. Biol. 343*, 223-233.
9. Rosell, F. I., Ferrer, J. C., and Mauk, A. G. (1998) Proton-linked protein conformational switching: definition of the alkaline conformational transition of yeast iso-1-ferricytochrome *c*, *J. Am. Chem. Soc. 120*, 11234-11245.
10. Ferrer, J. C., Guillemette, J. G., Bogumil, R., Inglis, S. C., Smith, M., and Mauk, A. G. (1993) Identification of Lys79 as an iron ligand in one form of alkaline yeast iso-1-ferricytochrome *c*, *J. Am. Chem. Soc. 115*, 7507-7508.
11. Sigma-Aldrich. (2015) Cytochrome c, www.sigmaaldrich.com/life-science/metabolomics/enzyme-explorer/learning-center/cytochrome-c.html.

12. Kagan, V. E., Tyurin, V. A., Jiang, J., Tyurina, Y. Y., Ritov, V. B., Amoscato, A. A., Osipov, A. N., Belikova, N. A., Kapralov, A. A., Kini, V., Vlasova, I. I., Zhao, Q., Zou, M., Di, P., Svistunenko, D. A., Kurnikov, I. V., and Borisenko, G. G. (2005) Cytochrome *c* acts as a cardiolipin oxygenase required for release of proapoptotic factors, *Nat. Chem. Biol. 1*, 223-232.
13. Assfalg, M., Bertini, I., Dolfi, A., Turano, P., Mauk, A. G., Rosell, F. I., and Gray, H. B. (2003) Structural model for an alkaline form of ferricytochrome *c*, *J. Am. Chem. Soc. 125*, 2913-2922.
14. Bandi, S., and Bowler, B. E. (2011) Probing the dynamics of a His73-heme alkaline conformer in a destabilized variant of yeast iso-1-cytochrome *c* with conformationally gated electron transfer methods, *Biochemistry 50*, 10027–10040.
15. Bandi, S., and Bowler, B. E. (2008) Probing the bottom of a folding funnel using conformationally gated electron transfer reactions, *J. Am. Chem. Soc. 130*, 7540-7541.
16. Bandi, S., Baddam, S., and Bowler, B. E. (2007) Alkaline conformational transition and gated electron transfer with a Lys 79 -> His variant of iso-1-cytochrome *c*, *Biochemistry 46*, 10643-10654.
17. Kristinsson, R., and Bowler, B. E. (2005) Communication of stabilizing energy between substructures of a protein, *Biochemistry 44*, 2349-2359.
18. Cherney, M. M., Junior, C., and Bowler, B. E. (2013) Mutation of trimethyllysine-72 to alanine enhances His79-heme mediated dynamics of iso-1-cytochrome *c*, *Biochemistry 52*, 837-846.
19. Cherney, M. M., Junior, C. C., Bergquist, B. B., and Bowler, B. E. (2013) Dynamics of the His79-heme alkaline transition of yeast iso-1-cytochrome *c* probed by conformationally gated electron transfer with Co(II)bis(terpyridine), *J. Am. Chem. Soc. 135*, 12772-12782.
20. Bandi, S., and Bowler, B. E. (2013) A cytochrome *c* electron transfer switch modulated by heme ligation and isomerization of a peptidyl-prolyl bond, *Biopolymers (Pept Sci) 100*, 114-124.
21. Martinez, R. E., and Bowler, B. E. (2004) Proton-mediated dynamics of the alkaline conformational transition of yeast iso-1-cytochrome *c*, *J. Am. Chem. Soc. 126*, 6751-6758.
22. Shoichet, B. K., Baase, W. A., Kuroki, R., and Matthews, B. W. (1995) A relationship between protein stability and protein function, *Proc. Natl. Acad. Sci. U.S.A. 92*, 452-456.
23. Goldstein, R. A. (2007) Amino-acid interactions in psychrophiles, mesophiles, thermophiles, and hyperthermophiles: insights form the quasi-chemical approximation, *Protein Sci. 16*, 1887-1895.
24. Feller, G. (2013) Psychrophilic Enzymes: From Folding to Function and Biotechnology, *Scientifica 2013*, 28.
25. Lonhienne, T., Gerday, C., and Feller, G. (2000) Psychrophilic enzymes: revisiting the thermodynamic parameters of activation may explain local flexibility, *Biochim. Biophys. Acta 1543*, 1-10.
26. Hammack, B. N., Smith, C. R., and Bowler, B. E. (2001) Denatured state thermodynamics: residual structure, chain stiffness and scaling factors, *J. Mol. Biol. 311*, 1091-1104.
27. Liggins, J. R., Lo, T. P., Brayer, G. D., and Nall, B. T. (1999) Thermal stability of hydrophobic heme pocket variants of oxidized cytochrome *c*, *Protein Sci. 8*, 2645-2654.

28. Nozaki, M. (1960) Studies on cytochrome *c*: IV. mode of existence of native and modified cytochrome *c*, *J. Biochem., Tokyo 47*, 592-599.
29. Margoliash, E., and Lustgarten, J. (1962) Interconversion of horse heart cytochrome *c* monomer and polymers, *J. Biol. Chem. 237*, 3397-3405.
30. Hirota, S., Hattori, Y., Nagao, S., Taketa, M., Komori, H., Kamikubo, H., Wang, Z., Takahashi, I., Negi, S., Sugiura, Y., Kataoka, M., and Higuchi, Y. (2010) Cytochrome *c* polymerization by successive domain swapping at the C-terminal helix, *Proc. Natl. Acad. Sci. U.S.A. 107*, 12854-12859.
31. Junedi, S., Yasuhara, K., Nagao, S., Kikuchi, J.-i., and Hirota, S. (2014) Morphological change of cell membrane by interaction with domain-swapped cytochrome *c* oligomers, *ChemBioChem 15*, 517-521.
32. Wang, Z., Matsuo, T., Nagao, S., and Hirota, S. (2011) Peroxidase activity enhancement of horse cytochrome *c* by dimerization, *Org. Biomol. Chem. 9*, 4766-4769.
33. Muenzner, J., and Pletneva, E. V. (2014) Structural transformations of cytochrome *c* upon interaction with cardiolipin, *Chem. Phys. Lipids 179*, 57-63.
34. Hanske, J., Toffey, J. R., Morenz, A. M., Bonilla, A. J., Schiavoni, K. H., and Pletneva, E. V. (2012) Conformational properties of cardiolipin-bound cytochrome *c*, *Proc. Natl. Acad. Sci. U.S.A. 109*, 125-130.
35. Henzler-Wildman, K., and Kern, D. (2007) Dynamic personalities of proteins, *Nature 450*, 964-972.
36. Cherney, M. M., and Bowler, B. E. (2011) Protein dynamics and function: making new strides with an old warhorse, the alkaline conformational transition of cytochrome *c*, *Coord. Chem. Rev. 255*, 664-677.
37. Ansari, A., Berendzen, J., Bowne, S. F., Frauenfelder, H., Iben, I. E. T., Sauke, T. B., Shyamsunder, E., and Young, R. D. (1985) Protein states and proteinquakes, *Proc. Natl. Acad. Sci. U.S.A. 82*, 5000-5004.
38. Banci, L., Bertini, I., Rosato, A., and Varani, G. (1999) Mitochondrial cytochromes *c*: a comparative analysis, *J. Biol. Inorg. Chem. 4*, 824-837.
39. Barker, P. D., and Mauk, A. G. (1992) pH-Linked conformational regulation of a metalloprotein oxidation-reduction equilibrium: electrochemical analysis of the alkaline form of cytochrome *c*, *J. Am. Chem. Soc. 114*, 3619-3624.
40. Döpner, S., Hildebrandt, P., Rosell, F. I., Mauk, A. G., von Walter, M., Buse, G., and Soulimane, T. (1999) The structural and functional role of lysine residues in the binding domain of cytochrome *c* in the electron transfer to cytochrome *c* oxidase, *Eur. J. Biochem. 261*, 379-391.
41. Döpner, S., Hildebrandt, P., Rosell, F. I., and Mauk, A. G. (1998) Alkaline conformational transitions of ferricytochrome *c* studied by resonance Raman spectroscopy, *J. Am. Chem. Soc. 120*, 11246-11255.
42. Krishna, M. M., Maity, H., Rumbley, J. N., Lin, Y., and Englander, S. W. (2006) Order of steps in the cytochrome *c* folding pathway: evidence for a sequential stabilization mechanism, *J. Mol. Biol. 359*, 1410-1419.
43. Krishna, M. M., Lin, Y., Rumbley, J. N., and Englander, S. W. (2003) Cooperative omega loops in cytochrome *c*: role in folding and function, *J. Mol. Biol. 331*, 29-36.
44. Bai, Y., Sosnick, T. R., Mayne, L., and Englander, S. W. (1995) Protein folding intermediates: native-state hydrogen exchange, *Science 269*, 192-197.

45. Laun, P., Buettner, S., Rinnerthaler, M., Burhans, W. C., and Breitenbach, M. (2012) Yeast Aging and Apoptosis, In *Subcellular Biochemistry: Aging Research in Yeast* (Breitenbach, M., Jazwinski, S. M., and Laun, P., Eds.), pp 207-232, Springer, Netherlands.
46. Blouin, C., Guillemette, J. G., and Wallace, C. J. A. (2001) Resolving the individual components of a pH induced conformational change, *Biophys. J. 81*, 2331-2338.
47. Nelson, C. J., and Bowler, B. E. (2000) pH dependence of formation of a partially unfolded state of a Lys 73 -> His variant of iso-1-cytochrome *c*: implications for the alkaline conformational transition of cytochrome *c*, *Biochemistry 39*, 13584-13594.
48. Pollock, W. B., Rosell, F. I., Twitchett, M. B., Dumont, M. E., and Mauk, A. G. (1998) Bacterial expression of a mitochondrial cytochrome *c*. Trimethylation of Lys72 in yeast iso-1-cytochrome *c* and the alkaline conformational transition, *Biochemistry 37*, 6124-6131.
49. McClelland, L. J., Mou, T.-C., Jeakins-Cooley, M. E., Sprang, S. R., and Bowler, B. E. (2014) Structure of a mitochondrial cytochrome *c* conformer competent for peroxidase activity, *Proc. Natl. Acad. Sci. U.S.A. 111*, 6648-6653.
50. Kostrzewa, A., Páli, T., Wojciech, F., and Marsh, D. (2000) Membrane location of spin-labeled cytochrome *c* determined by paramagnetic relaxation reagents, *Biochemistry 39*, 6066-6074.
51. Myers, J. K., Pace, C. N., and Scholtz, J. M. (1995) Denaturant *m* values and heat capacity changes: relation to changes in accessible surface areas of protein unfolding, *Protein Sci. 4*, 2138-2148.
52. Schellman, J. A. (1978) Solvent denaturation, *Biopolymers 17*, 1305-1322.
53. Godbole, S., Dong, A., Garbin, K., and Bowler, B. E. (1997) A lysine 73->histidine variant of yeast iso-1-cytochrome *c*: evidence for a native-like intermediate in the unfolding pathway and implications for *m* value effects, *Biochemistry 36*, 119-126.
54. Duncan, M. G., Williams, M. D., and Bowler, B. E. (2009) Compressing the free energy range of substructure stabilities in iso-1-cytochrome *c*, *Protein Sci. 18*, 1155-1164.
55. Rosell, F. I., and Mauk, A. G. (2002) Spectroscopic properties of a mitochondrial cytochrome *c* with a single thioether bond to the heme prosthetic group, *Biochemistry 41*, 7811-7818.
56. Rumbley, J. N., Hoang, L., and Englander, S. W. (2002) Recombinant equine cytochrome *c* in *Escherichia coli*: high-level expression, characterization, and folding and assembly mutants, *Biochemistry 41*, 13894-13901.
57. Deng, W. P., and Nickoloff, J. A. (1992) Site-directed mutagenesis of virtually any plasmid by eliminating a unique site, *Anal. Biochem. 200*, 81-88.
58. Redzic, J. S., and Bowler, B. E. (2005) Role of hydrogen bond networks and dynamics in positive and negative cooperative stabilization of a protein, *Biochemistry 44*, 2900-2908.
59. Wandschneider, E., Hammack, B. N., and Bowler, B. E. (2003) Evaluation of cooperative interactions between substructures of iso-1-cytochrome *c* using double mutant cycles, *Biochemistry 42*, 10659-10666.
60. Pace, C. N. (1986) Determination and analysis of urea and guanidine hydrochloride denaturation curves, *Methods Enzymol. 131*, 266-280.
61. Baddam, S., and Bowler, B. E. (2005) Thermodynamics and kinetics of formation of the alkaline state of a Lys 79->Ala/Lys 73->His variant of iso-1-cytochrome *c*, *Biochemistry 44*, 14956-14968.

62. Margoliash, E., and Frohwirt, N. (1959) Spectrum of horse-heart cytochrome *c*, *Biochem. J. 71*, 570-572.
63. Baddam, S., and Bowler, B. E. (2005) Conformationally gated electron transfer in iso-1-cytochrome *c*: engineering the rate of a conformational switch, *J. Am. Chem. Soc. 127*, 9702-9703.
64. Fergusson, J. E., and Love, J. L. (1972) Ruthenium ammines, *Inorganic Synthesis 13*, 208-213.
65. Allen, A. D., and Senoff, C. V. (1967) Preparation and infrared spectra of some ammine complexes of ruthenium (II) and ruthenium (III), *Can. J. Chem. 45*, 1337-1341.
66. Matsubara, T., and Ford, P. C. (1978) Photochemistry of ruthenium(II)-saturated amine complexes $Ru(NH_3)_6^{2+}$, $Ru(NH_3)_5H_2O^{2+}$, and $Ru(en)_3^{2+}$ in aqueous solution, *Inorg. Chem. 17*, 1747-1752.
67. Meyer, T. J., and Taube, H. (1968) Electron transfer reactions of ruthenium ammines, *Inorg. Chem. 7*, 2369-2370.
68. Godbole, S., Hammack, B., and Bowler, B. E. (2000) Measuring denatured state energetics: deviations from random coil behavior and implications for the folding of iso-1-cytochrome *c*, *J. Mol. Biol. 296*, 217-228.
69. Eaton, W. A., and Hochstrasser, R. M. (1967) Electronic spectrum of single crystals of ferricytochrome *c*, *J. Chem. Phys. 46*, 2533-2539.
70. Dragomir, I., Hagarman, A., Wallace, C., and Schweitzer-Stenner, R. (2007) Optical band splitting in cytochrome *c* at room temperature probed by visible electronic circular dichroism spectroscopy, *Biophys. J. 92*, 989-998.
71. Baddam, S., and Bowler, B. E. (2006) Tuning the rate and pH accessibility of a conformational electron transfer gate, *Inorg. Chem. 45*, 6338-6346.
72. Bortolotti, C. A., Paltrinieri, L., Monari, S., Ranieri, A., Borsari, M., Battistuzzi, G., and Sola, M. (2012) A surface-immobilized cytochrome *c* variant provides a pH-controlled molecular switch, *Chem Sci 3*, 807-810.
73. Sanchez, R., and Zhou, M.-M. (2011) The PHD finger: a versatile epigenomic reader, *Trends Biochem. Sci. 36*, 364-372.
74. Daze, K. D., and Hof, F. (2013) The cation-π interaction at protein-protein interaction interfaces: developing and learning from synthetic mimics of proteins that bind methylated lysines, *Acc. Chem. Res. 46*, 937-945.
75. Hartshorn, R. T., and Moore, G. R. (1989) A denaturation-induced proton-uptake study of horse ferricytochrome *c*, *Biochem. J. 258*, 595-598.
76. Moore, G. R. (1983) Control of redox properties of cytochrome *c* by special electrostatic interactions, *FEBS Lett. 161*, 171-175.
77. Cusanovich, M. A., and Tollin, G. (1996) Kinetics of electron transfer of *c*-type cytochromes with small reagents, In *Cytochrome c: A Multidisciplinary Approach* (Scott, R. A., and Mauk, A. G., Eds.), pp 489-513, University Science Books, Sausalito, CA.
78. Wijetunge, P., Kulatilleke, C. P., Dressel, L. T., Heeg, M. J., Ochrymowycz, L. A., and Rorabacher, D. B. (2000) Effect of conformational constraints on gated electron-transfer kinetics. 3. Copper(II/I) complexes with cis- and trans-cyclopentanediyl-1,4,8,11-tetrathiacyclotetradecane, *Inorg. Chem. 39*, 2897-2905.
79. Meagher, N. E., Juntunen, K. L., Salhi, C. A., Ochrymowycz, L. A., and Rorabacher, D. B. (1992) Gated electron-transfer behavior in copper(II/I) systems. Comparison of the kinetics for homogeneous cross reactions, NMR self-exchange relaxation, and

electrochemical data for a copper macrocyclic tetrathioether complex in aqueous solution, *J. Am. Chem. Soc. 114*, 10411-10420.
80. Rorabacher, D. B. (2004) Electron transfer by copper centers, *Chem. Rev. 104*, 651-697.
81. Godbole, S., and Bowler, B. E. (1999) Effect of pH on formation of a nativelike intermediate on the unfolding pathway of a Lys 73 -> His variant of yeast iso-1-cytochrome *c*, *Biochemistry 38*, 487-495.
82. Levinthal, C. (1969) How to fold graciously, In *DeBrunner JTP, Munck E, editors. Mossbauer spec*, pp 22-24, Allerton House, Monticello, Illinois: University of Illinois Press, Mossbauer spectroscopy in biological systems.
83. Leopold, P. E., Montal, M., and Onuchic, J. N. (1992) Protein folding funnels: a kinetic approach to the sequence-structure relationship, *Proc. Natl. Acad. Sci. U.S.A. 89*, 8721-8725.
84. Tang, K. E. S., and Dill, K. A. (1998) Native protein fluctuations: the conformational-motion temperature and the inverse correlation of protein flexibility with protein stability, *J. Biomol. Struct. Dyn. 16*, 397-411.
85. Ritco-Vonsovici, M., Mouratou, B., Minard, P., Desmadril, M., Yon, J. M., Andrieux, M., Leroy, E., and Guittet, E. (1995) Role of the C-terminal helix in the folding and stability of yeast phosphoglycerate kinase, *Biochemistry 34*, 833-841.
86. Arnold, S., Curtiss, A., Dean, D. H., and Alzate, O. (2001) The role of a proline-induced broken-helix motif in α-helix 2 of *Bacillus thuringiensis* δ-endotoxins, *FEBS Lett. 490*, 70-74.
87. Amacher, J. F., Zhong, F., Lisi, G. P., Zhu, M. Q., Alden, S. L., Hoke, K. R., Madden, D. R., and Pletneva, E. V. (2015) A compact structure of cytochrome *c* trapped in a lysine-ligated state: loop refolding and functional implications of a conformational switch, *J. Am. Chem. Soc. 137*, 8435-8449.
88. McClelland, L. J., Seagraves, S. M., Khan, M. K. A., Cherney, M. M., Bandi, S., Culbertson, J. E., and Bowler, B. E. (2015) The response of Ω-loop D dynamics to truncation of trimethyllysine 72 of yeast iso-1-cytochrome *c* depends on the nature of loop deformation, *J. Biol. Inorg. Chem. 20*, 805-819.
89. Nocek, J. M., Stemp, E. D. A., Finnegan, M. G., Koshy, T. I., Johnson, M. K., Margoliash, E., Mauk, A. G., Smith, M., and Hoffman, B. M. (1991) Low-temperature, cooperative conformational transition within [Zn-cytochrome *c* peroxidase, cytochrome *c*] complexes: variation with cytochrome, *Journal of American Chemical Society 113*, 6822-6831.
90. Parrish, J. C., Guillemette, J. G., and Wallace, C. J. A. (2001) Contribution of leucine 85 to the structure and function of *Saccharomyces cerevisiae* iso-1 cytochrome *c*, *Biochem. Cell Biol. 79*, 517-524.
91. Lo, T. P., Guillemette, J. G., Louie, G. V., Smith, M., and Brayer, G. D. (1995) Structural studies of the roles of residues 82 and 85 at the interactive face of cytochrome *c*, *Biochemistry 34*, 163-171.
92. Lo, T. P., Murphy, M. E. P., Guillemette, J. G., Smith, M., and Brayer, G. D. (1995) Replacements in a conserved leucine cluster in the hydrophobic heme pocket of cytochrome *c*, *Protein Sci. 4*, 198-208.
93. Guillemette, J. G., Barker, P. D., Eltis, L. D., Lo, T. P., Smith, M., Brayer, G. D., and Mauk, A. G. (1994) Analysis of the bimolecular reduction of ferricytochrome c by

ferrocytochrome b5 through mutagenesis and molecular modelling, *Biochimie 76*, 592-604.
94. Stanbury, D. M., and Lednicky, L. A. (1984) Outer-Sphere Electron-Transfer Reactions Involving the Chlorite Chlorine Dioxide Couple - Activation Barriers for Bent Triatomic Species, *J. Am. Chem. Soc. 106*, 2847-2853.
95. Hoang, L., Bedard, S., Krishna, M. M., Lin, Y., and Englander, S. W. (2002) Cytochrome *c* folding pathway: kinetic native-state hydrogen exchange, *Proc. Natl. Acad. Sci. U.S.A. 99*, 12173-12178.
96. Davis, L. A., Schejter, A., and Hess, G. P. (1974) Alkaline isomerization of oxidized cytochrome *c*. Equilibrium and kinetic measurements, *J. Biol. Chem. 249*, 2624-2632.
97. Weinkam, P., Zimmermann, J., Sagle, L. B., Matsuda, S., Dawson, P. E., Wolynes, P. G., and Romesberg, F. E. (2008) Characterization of alkaline transitions in ferricytochrome *c* using carbon-deuterium infrared probes, *Biochemistry 47*, 13470-13480.
98. Verbaro, D., Hagarman, A., Soffer, J., and Schweitzer-Stenner, R. (2009) The pH dependence of the 695 nm charge transfer band reveals the population of an intermediate state of the alkaline transition of ferricytochrome *c* at low ion concentrations, *Biochemistry 48*, 2990-2996.
99. Hobbs, J. K., Jiao, W., Easter, A. D., Parker, E. J., Schipper, L. A., and Arcus, V. L. (2013) Change in heat capacity for enzyme catalysis determines temperature dependence of enzyme catalyzed rates, *ACS Chemical Biology 8*, 2388-2393.
100. Winge, D. R. (2012) Sealing the mitochondrial respirasome, *Mol. Cell. Biol. 32*, 2647-2652.
101. Yu, T., Wang, X., Purring-Koch, C., Wei, Y., and McLendon, G. L. (2001) A mutational epitope for cytochrome *c* binding to the apoptosis protease activation factor-1, *J. Biol. Chem. 276*, 13034-13038.
102. Olteanu, A., Patel, C. N., Dedmon, M. M., Kennedy, S., Linhoff, M. W., Minder, C. M., Potts, P. R., Deshmukh, M., and Pielak, G. J. (2003) Stability and apoptotic activity of recombinant human cytochrome *c*, *Biochem. Biophys. Res. Commun. 312*, 733-740.
103. Brayer, G. D., and Murphy, M. E. P. (1996) Structural studies of eukaryotic cytochromes *c*, In *Cytochrome c. A Multidisciplinary Approach* (Scott, R. A., and Mauk, A. G., Eds.), pp 103-166, University Science Books, Sausalito, California.
104. Kapetanaki, S. M., Silkstone, G., Husu, I., Liebl, U., Wilson, M. T., and Vos, M. H. (2009) Interaction of carbon monoxide with the apoptosis-inducing cytochrome *c*-cardiolipin complex, *Biochemistry 48*, 1613-1619.
105. Muenzner, J., Toffey, J. R., Hong, Y., and Pletneva, E. V. (2013) Becoming a peroxidase: cardiolipin-induced unfolding of cytochrome *c*, *J. Phys. Chem. B 112*, 12878-12886.
106. Hong, Y., Muenzner, J., Grimm, S. K., and Pletneva, E. V. (2012) Origin of the conformational heterogeneity of cardiolipin-bound cytochrome *c*, *J. Am. Chem. Soc. 134*, 18713-18723.
107. Belikova, N. A., Vladimirov, Y. A., Osipov, A. N., Kapralov, A. A., Tyurin, V. A., Potapovich, M. V., Basova, L. V., Peterson, J., Kurnikov, I. V., and Kagan, V. E. (2006) Peroxidase activity and structural transitions of cytochrome *c* bound to cardiolipin-containing membranes, *Biochemistry 45*, 4998-5009.
108. Bortolotti, C. A., Amadei, A., Aschi, M., Borsari, M., Corni, S., Sola, M., and Daidone, I. (2012) The reversible opening of water channels in cytochrome *c* modulates the heme iron reduction potential, *J. Am. Chem. Soc. 134*, 13670-13768.

109. Faye, G., Leung, D. W., Tatchell, K., Hall, B. D., and Smith, M. (1981) Deletion mapping of sequences essential for *in vivo* transcription of the iso-1-cytochrome *c* gene, *Proc. Natl. Acad. Sci. U.S.A. 78*, 2258-2262.
110. Herrmann, L. M., Flatt, P., and Bowler, B. E. (1996) Site-directed replacement of the invariant lysine 73 of *Saccharomyces cerevisiae* iso-1-cytochrome *c* with all ribosomally encoded amino acids, *Inorg. Chim. Acta 242*, 97-103.
111. Cutler, R. L., Pielak, G. J., Mauk, A. G., and Smith, M. (1987) Replacement of cysteine-107 of *Saccharomyces cerevisiae* iso-1-cytochrome *c* with threonine: improved stability of the mutant protein, *Protein Eng. 1*, 95-99.
112. Sherwood, C., and Brayer, G. D. (1985) Crystallization and preliminary diffraction data for iso-1-cytochrome *c* from yeast, *J. Mol. Biol. 185*, 209-210.
113. Otwinowski, Z., and Minor, W. (1997) Processing of X-ray diffraction data collected in oscillation mode, *Methods Enzymol. 276A*, 307-326.
114. Adams, P. D., Afonine, P. V., Bunkóczi, G., Chen, V. B., Davis, I. W., Echols, N., Headd, J. J., Hung, L.-W., Kapral, G. J., Grosse-Kunstleve, R. W., McCoy, A. J., Moriarty, N. W., Oeffner, R., Read, R. J., Richardson, D. C., Richardson, J. S., Terwilliger, T. C., and Zwart, P. H. (2010) PHENIX: a comprehensive Python-based system for macromolecular structure solution, *Acta Crystallogr., Sect. D: Biol. Crystallogr. 66*, 213-221.
115. Emsley, P., Lohkamp, B., Scott, W. G., and Cowtan, K. (2010) Features and development of Coot, *Acta Crystallogr., Sect. D: Biol. Crystallogr. 66*, 486-501.
116. DeLano, W. L. (2002) The PyMOL molecular graphics system, *DeLano Scientific, San Carlos, CA, USA*.
117. Berman, H. M., Westbrook, J., Feng, Z., Gilliland, G., Bhat, T. N., Weissig, H., Shindyalov, I. N., and Bourne, P. E. (2000) The protein data bank, *Nucleic Acids Res. 28*, 235-242.
118. Nelson, D. P., and Kiesow, L. A. (1972) Enthalpy of decomposition of hydrogen peroxide by catalase at 25 °C (with molar extinction coefficients of H_2O_2 solutions in the UV), *Anal. Biochem. 49*, 474-478.
119. Noble, R. W., and Gibson, Q. H. (1970) The reaction of ferrous horseradish peroxidase with hydrogen peroxide, *J. Biol. Chem. 245*, 2409-2413.
120. Goldschmid, O. (1953) The effect of alkali and strong acid on the ultraviolet absorption spectrum of lignin and related compounds, *J. Am. Chem. Soc. 75*, 3780-3783.
121. Diederix, R. E. M., Ubbink, M., and Canters, G. W. (2001) The peroxidase activity of cytochrome *c*-550 from *Paracoccus versutus*, *Eur. J. Biochem. 268*, 4207-4216.
122. DePillis, G. D., Sishta, B. P., Mauk, A. G., and Ortiz de Montellano, P. R. (1991) Small substrates and cytochrome *c* are oxidized at different sites of cytochrome *c* peroxidase, *J. Biol. Chem. 266*, 19334-19341.
123. Can, M., Krucinska, J., Zoppellaro, G., Andersen, N. H., Wedekind, J. E., Hersleth, H.-P., Andersson, K. K., and Bren, K. L. (2013) Structural characterization of *Nitrosomonas europaea* cytochrome *c*-552 variants with marked differences in electronic structure, *ChemBioChem 14*, 1828-1838.
124. Banci, L., Bertini, I., Bren, K. L., Gray, H. B., Sompornpisut, P., and Turano, P. (1995) Three-dimensional solution structure of the cyanide adduct of a Met80Ala variant of *Saccharomyces cerevisiae* iso-1-cytochrome *c*. Identification of ligand-residue interactions in the distal heme cavity, *Biochemistry 34*, 11385-11398.

125. Banci, L., Bertini, I., Liu, G., Lu, J., Reddig, T., Tang, W., Wu, Y., Yao, Y., and Zhu, D. (2001) Effects of extrinsic imidazole ligation on the molecular and electronic structure of cytochrome *c*, *J. Biol. Inorg. Chem. 6*, 628-637.
126. Yao, Y., Qian, C., Ye, K., Wang, J., Bai, Z., and Tang, W. (2002) Solution structure of cyanoferricytochrome *c*: ligand-controlled conformational flexibility and electronic structure of the heme moiety, *J. Biol. Inorg. Chem. 7*, 539-547.
127. Pokkuluri, P. R., Pessanha, M., Londer, Y. Y., Wood, S. J., Duke, N. E. C., Wilton, R., Catarino, T., Salgueiro, C. A., and Schiffer, M. (2008) Structures and solution properties of two novel periplasmic sensor domains with *c*-type heme from chemotaxis proteins of *Geobacter sulfurreducens*: implications for signal transduction, *J. Mol. Biol. 377*, 1498-1517.
128. Bren, K. L., Kellogg, J. A., Kaur, R., and Wen, X. (2004) Folding, conformational changes, and dynamics of cytochromes *c* probed by NMR spectroscopy, *Inorg. Chem. 43*, 7934-7944.
129. Louie, G. V., and Brayer, G. D. (1990) High-resolution refinement of yeast iso-1-cytochrome *c* and comparisons with other eukaryotic cytochromes *c*, *J. Mol. Biol. 214*, 527-555.
130. Lo, T. P., Komar-Panucci, S., Sherman, F., McLendon, G., and Brayer, G. D. (1995) Structural and functional effects of multiple mutations at distal sites in cytochrome *c*, *Biochemistry 34*, 5259-5268.
131. Cutler, R. L., Davies, A. M., Creighton, S., Warshel, A., Moore, G. R., Smith, M., and Mauk, A. G. (1989) Role of arginine-38 in regulation of the cytochrome *c* oxidation-reduction equilibrium, *Biochemistry 28*, 3188-3197.
132. Bushnell, G. W., Louie, G. V., and Brayer, G. D. (1990) High-resolution three-dimensional structure of horse heart cytochrome *c*, *J. Mol. Biol. 214*, 585-595.
133. Fitch, W. M. (1976) The molecular evolution of cytochrome *c* in eukaryotes, *J. Mol. Evol. 8*, 13-40.
134. Diederix, R. E. M., Ubbink, M., and Canters, G. W. (2002) Peroxidase activity as a tool for studying the folding of *c*-type cytochromes, *Biochemistry 41*, 13067-13077.
135. Diederix, R. E. M., Ubbink, M., and Canters, G. W. (2002) Effect of the protein matrix of cytochrome *c* in suppressing the inherent peroxidase activity of its heme prosthetic group, *ChemBioChem 3*, 110-112.
136. Kalanxhi, E., and Wallace, C. J. A. (2007) Cytochrome *c* impaled: investigation of the extended lipid anchorage of a soluble protein to mitochondrial membrane models, *Biochem. J. 407*, 179-187.
137. Sinibaldi, F., Howes, B. D., Piro, M. C., Polticelli, F., Bombelli, C., Ferri, T., Coletta, M., Smulevich, G., and Santucci, R. (2010) Extended cardiolipin anchorage to cytochrome *c*: a model for protein-mitochondrial membrane binding, *J. Biol. Inorg. Chem. 15*, 689-700.
138. Firsov, A. M., Kotova, E. A., Korepanova, E. A., Osipov, A. N., and Antonenko, Y. N. (2015) Peroxidative permeabilization of liposomes induced by cytochrome *c*/cardiolipin complex, *Biochim. Biophys. Acta 1848*, 767-774.
139. Kapralov, A. A., Kurnikov, I. V., Vlasova, I. I., Belikova, N. A., Tyurin, V. A., Basova, L. V., Zhao, Q., Tyurina, Y. Y., Jiang, J., Bayir, H., Vladimirov, Y. A., and Kagan, V. E. (2007) The hierarchy of structural transitions induced in cytochrome *c* by anionic phospholipids determines its peroxidase activation and selective peroxidation during apoptosis in cells, *Biochemistry 46*, 14232-14244.

140. Vladimirov, Y. A., Proskurnina, E. V., Izmailov, D. Y., Novikov, A. A., Brusnichkin, A. V., Osipov, A. N., and Kagan, V. E. (2006) Mechanism of activation of cytochrome *c* peroxidase activity by cardiolipin, *Biochemistry (Moscow) 71*, 989-997.
141. Yanamala, N., Kapralov, A. A., Djukic, M., Peterson, J., Mao, G., Klein-Seetharaman, J., Stoyanovsky, D. A., Stursa, J., Neuzil, J., and Kagan, V. E. (2014) Structural re-arrangement and peroxidase activation of cytochrome *c* by anionic analogues of vitamin E, tocopherol succinate and tocopherol phosphate, *J. Biol. Chem. 289*, 32488-32498.
142. Diederix, R. E. M., Busson, S., Ubbink, M., and Canters, G. W. (2004) Increase of the peroxidase activity of cytochrome *c*-550 by the interaction with detergents, *J. Mol. Catal. B: Enzym. 27*, 75-82.
143. Rytömaa, M., and Kinnunen, P. K. J. (1994) Evidence for two distinct acidic phospholipid-binding sites in cytochrome *c*, *J. Biol. Chem. 269*, 1770-1774.
144. Rytömaa, M., and Kinnunen, P. K. J. (1995) Reversibility of the binding of cytochrome *c* to liposomes, *J. Biol. Chem. 270*, 3197-3202.
145. Stewart, J. M., Blakely, J. A., and Johnson, M. D. (2000) The interaction of ferrocytochrome *c* with long-chain fatty acids and their CoA and carnitine esters, *Biochem. Cell Biol. 78*, 675-681.
146. Dickerson, R. E., Takano, T., Eisenberg, D., Kallai, O. B., Samson, L., Cooper, A., and Margoliash, E. (1971) Ferricytochrome *c*: I. general features of the horse and bonito proteins at 2.8 A resolution, *J. Biol. Chem. 246*, 1511-1535.
147. Tuominen, A. K. J., Wallace, C. J. A., and Kinnunen, P. K. J. (2002) Phospholipid-cytochrome *c* interaction: evidence for the extended lipid anchorage, *J. Biol. Chem. 277*, 8822-8826.
148. Kawai, C., Prado, F. M., Nunes, G. L. C., Di Mascio, P., Carmona-Ribeiro, A. M., and Nantes, I. L. (2005) pH-dependent interaction of cytochrome *c* with mitochondrial mimetic membranes: the role of an array of positively charges amino acids, *J. Biol. Chem. 280*, 34709-34717.
149. Kinnunen, P. K. J., Koiv, A., Lehtonen, J. Y. A., Rytömaa, M., and Mustonen, P. (1994) Lipid dynamics and peripheral interactions of proteins with membrane surfaces, *Chem. Phys. Lipids 73*, 181-207.
150. Pandiscia, L. A., and Schweitzer-Stenner, R. (2014) Salt as a catalyst in the mitochondria: returning cytochrome *c* to its native state after it misfolds on the surface of cardiolipin containing membranes, *Chem. Commun. 50*, 3674-3676.
151. Pandiscia, L. A., and Schweitzer-Stenner, R. (2015) Coexistence of native-like and non-native partially unfolded ferricytochrome *c* on the surface of cardiolipin-containing liposomes, *J. Phys. Chem. B 119*, 1334-1349.
152. Hayashi, Y., Nagao, S., Osuka, H., Komori, H., Higuchi, Y., and Hirota, S. (2012) Domain swapping of the heme and N-terminal α-helix in *Hydrogenobacter thermophilus* cytochrome c_{552} dimer, *Biochemistry 51*, 8608-8616.
153. Yamanaka, M., Nagao, S., Komori, H., Higuchi, Y., and Hirota, S. (2015) Change in structure and ligand binding properties of hyperstable cytochrome c_{555} from *Aquifex aeolicus* by domain swapping, *Protein Sci. 24*, 366-375.
154. Nagao, S., Ueda, M., Osuka, H., Komori, H., Kamikubo, H., Kataoka, M., Higuchi, Y., and Hirota, S. (2015) Domain-swapped dimer of *Pseudomonas aeruginosa* cytochrome c_{551}: structural insights into domain swapping of cytochrome *c* family proteins, In *PLoS ONE*.

155. Deshpande, M. S., Parui, P. P., Kamikubo, H., Yamanaka, M., Nagao, S., Komori, H., Kataoka, M., Higuchi, Y., and Hirota, S. (2014) Formation of domain-swapped oligomer of cytochrome *c* from its molten globule state oligomer, *Biochemistry 53*, 4696-4703.
156. Parui, P. P., Deshpande, M. S., Nagao, S., Kamikubo, H., Komori, H., Higuchi, Y., Kataoka, M., and Hirota, S. (2013) Formation of oligomeric cytochrome *c* during folding by intermolecular hydrophobic interaction between N- and C-terminal α-helices, *Biochemistry 52*, 8732-8744.
157. Schejter, A., Glauser, S. C., George, P., and Margoliash, E. (1963) Spectra of cytochrome *c* monomer and polymers, *Biochim. Biophys. Acta 73*, 641-643.
158. Kapralov, A. A., Yanamala, N., Tyurina, Y. Y., Castro, L., Arias, A. S., Vladimirov, Y. A., Maeda, A., Weitz, A. A., Peterson, J., Mylnikov, D., Demicheli, V., Tortora, V., Klein-Seetharaman, J., Radi, R., and Kagan, V. E. (2011) Topography of tyrosine residues and their involvement in peroxidation of polyunsaturated cardiolipin in cytochrome *c*/cardiolipin peroxidase complexes, *Biochim. Biophys. Acta 1808*, 2147-2155.
159. Vlasova, I. I., Tyurin, V. A., Kapralov, A. A., Kurnikov, I. V., Osipov, A. N., Potapovich, M. V., Stoyanovsky, D. A., and Kagan, V. E. (2006) Nitric oxide inhibits peroxidase activity of cytochrome *c*-cardiolipin complex and blocks cardiolipin oxidation, *J. Biol. Chem. 281*, 14554-14562.
160. Rajagopal, B. S., Edzuma, A. N., Hough, M. A., Blundell, K. L. I. M., Kagan, V. E., Kapralov, A. A., Fraser, L. A., Butt, J. N., Silkstone, G. G., Wilson, M. T., Svistunenko, D. A., and Worrall, J. A. R. (2013) The hydrogen-peroxide-induced radical behaviour in human cytochrome *c*–phospholipid complexes: implications for the enhanced pro-apoptotic activity of the G41S mutant, *Biochem. J. 456*, 441-452.
161. Herrmann, L. M., and Bowler, B. E. (1997) Thermal denaturation of iso-1-cytochrome *c* variants: comparison with solvent denaturation, *Protein Sci. 6*, 657-665.
162. Cohen, D. S., and Pielak, G. J. (1994) Stability of yeast iso-1-cytochrome *c* as a function of pH and temperature *Protein Sci. 3*, 1253-1260.
163. Betz, S. F., and Pielak, G. J. (1992) Introduction of a disulfide bond into cytochrome *c* stabilizes a compact denatured state, *Biochemistry 31*, 12337-12344.
164. Krishna, M. M., Lin, Y., Mayne, L., and Englander, S. W. (2003) Intimate view of a kinetic protein folding intermediate: residue-resolved structure, interactions, stability, folding and unfolding rates, homogeneity, *J. Mol. Biol. 334*, 501-513.

Appendix A

Table A.1. Oligonucleotide primers used for site-directed mutagenesis.[a]

Primer	Primer Sequence 5'-3'
$EcoRV^{-}AatII^{+}$	d(GTGCCACCTGA**CG**TCTAAGAAACC)[b]
K72A	d(CAGGAATATATTT**GGC**TGGGTTAGT)
N26H	d(GTGGAAAAGGGTGGCCCA**CAT**AAGGTTGGTCCAAACTTG)
N26H-r	d(CAAGTTTGGACCAACCTT**ATG**TGGGCCACCCTTTTCCAC)
N33H	d(ATAAGGTTGGTCCAAACTTG**CAT**GGTATCTTTGGCAGACACTC)
N33H-r	d(GAGTGTCTGCCAAAGATACC**ATG**CAAGTTTGGACCAACCTTAT)
Q39H	d(TTGAACGGTATCTTTGGCAGA**CAC**TCTGGTCAAGCT)
Q39H-r	d(AGCTTGACCAGA**GTG**TCTGCCAAAGATACCGTTCAA)
K73H	d(CATGTCAGAGTACTTGACTAACCCAGCC**CAT**TATATTCCTGGTACC)
K73H-r	d(GGTACCAGGAATATA**ATG**GGCTGGGTTAGTCAAGTACTCTGACATG)

[a] Mutation sites are underlined and bolded. [b] Converts the GATATC recognition site for EcoRV to the GACGTC site for AatII.

Table A.2. Fast phase rate observed constant, $k_{obs,1}$, and amplitude, A_1, data for the alkaline transition of the WT*/K73H variant obtained from stopped-flow upward pH jump measurements at 25 °C in 10 mM buffer, 0.1 M NaCl[a]

pH	A_1	$k_{obs,1}$ (s^{-1})	pH	A_1	$k_{obs,1}$ (s^{-1})
6.09	0.0075 ± 0.0007	11 ± 1	**8.33**	0.036 ± 0.004	12 ± 1
6.35	0.013 ± 0.001	11 ± 1	**8.52**	0.038 ± 0.001	12.7 ± 0.4
6.56	0.016 ± 0.002	10 ± 1	**8.81**	0.041 ± 0.001	13.0 ± 0.8
6.85	0.022 ± 0.002	10.1 ± 0.3	**9.05**	0.043 ± 0.002	13.9 ± 0.7
7.10	0.0263 ± 0.0009	10.5 ± 0.9	**9.29**	0.048 ± 0.001	14.2 ± 0.5
7.35	0.0305 ± 0.0007	10.4 ± 0.4	**9.52**	0.052 ± 0.002	16 ± 1
7.58	0.0328 ± 0.0009	10.2 ± 0.4	**9.67**	0.0633 ± 0.0009	16.2 ± 0.2
7.89	0.036 ± 0.001	10.8 ± 0.4	**9.77**	0.069 ± 0.002	17.8 ± 0.3
8.12	0.0364 ± 0.0009	11.8 ± 0.4	**10.12**	0.078 ± 0.001	19.2 ± 0.5

[a] Parameters are the average and standard deviation of a minimum of five pH jump (from pH 5, 0.1 M NaCl) kinetic traces (1 s time scale) fit to a double exponential equation. The kinetics were followed at 406 nm over the course of 1 second using pressure hold

Table A.3. Intermediate phase observed rate constant, $k_{obs,2}$, and amplitude, A_2, data for the alkaline transition of the WT*/K73H variant obtained from stopped-flow upward pH jump measurements at 25 °C in 10 mM buffer, 0.1 M NaCl[a]

pH	A_2	$k_{obs,2}$ (s^{-1})	pH	A_2	$k_{obs,2}$ (s^{-1})
7.89	0.0014 ± 0.0001	1.2 ± 0.5	**9.29**	0.005 ± 0.001	0.8 ± 10.2
8.12	0.007 ± 0.004	5 ± 2	**9.52**	0.0039 ± 0.0006	1.3± 0.4
8.33	0.0013 ± 0.0004	1.1 ± 0.5	**9.67**	0.007 ± 0.002	1 ± 1
8.52	0.0019 ± 0.0004	1.9 ± 0.8	**9.77**	0.0055 ± 0.0005	1.3 ± 0.3
8.81	0.0020 ± 0.0004	1.3 ± 0.4	**10.12**	0.006 ± 0.001	2.1 ± 0.9
9.05	0.0030 ± 0.0007	2 ± 1			

[a] Parameters are the average and standard deviation of a minimum of five pH jump (from pH 5, 0.1 M NaCl) kinetic traces fit to a quadruple exponential equation. The kinetics were followed at 406 nm over the course of 50 to 350 seconds.

Table A.4. First slow phase observed rate constant, $k_{obs,3}$, and amplitude, A_3, data for the alkaline conformational transition of the WT*/K73H variant obtained from stopped-flow upward pH jump measurements at 25 °C in 10 mM buffer, 0.1 M NaCl.[a]

pH	A_3	$k_{obs,3}$ (s^{-1})	pH	A_3	$k_{obs,3}$ (s^{-1})
6.56	0.002 ± 0.001	0.3 ± 0.3	**8.52**	0.010 ± 0.001	0.108 ± 0.007
6.85	0.004 ± 0.001	0.14 ± 0.09	**8.81**	0.010 ± 0.002	0.13 ± 0.01
7.10	0.0052 ± 0.0006	0.12 ± 0.01	**9.05**	0.012 ± 0.003	0.19 ± 0.04
7.35	0.0060 ± 0.0009	0.12 ± 0.03	**9.29**	0.04 ± 0.03	0.070 ± 0.009
7.58	0.007 ± 0.001	0.13 ± 0.02	**9.52**	0.020± 0.004	0.23 ± 0.06
7.89	0.008 ± 0.001	0.09 ± 0.01	**9.67**	0.014 ± 0.006	0.17 ± 0.08
8.12	0.009 ± 0.001	0.10 ± 0.02	**9.77**	0.0134 ± 0.0005	0.16 ± 0.01
8.33	0.009 ± 0.002	0.099 ± 0.005	**10.12**	0.010 ± 0.006	0.18 ± 0.07

[a] Parameters are the average and standard deviation of a minimum of five pH jump (from pH 5, 0.1 M NaCl) kinetic traces fit to a triple exponential equation from pH 6.56 to 7.58 and a quadruple exponential equation at pH ≥ 7.89. The kinetics were followed at 406 nm over the course of 50 to 350 seconds.

Table A.5. Second slow phase observed rate constant, $k_{obs,4}$, and amplitude, A_4, data for the alkaline conformational transition of the WT*/K73H variant obtained from stopped-flow upward pH jump measurements at 25 °C in 10 mM buffer, 0.1 M NaCl.[a]

pH	A_4	$k_{obs,4}$ (s^{-1})	pH	A_4	$k_{obs,4}$ (s^{-1})
6.09	0.0023 ± 0.0003	0.08 ± 0.02	**8.33**	0.0423 ± 0.0009	0.0287 ± 0.0009
6.35	0.0036 ± 0.0001	0.08 ± 0.01	**8.52**	0.060 ± 0.001	0.0358 ± 0.0004
6.56	0.004 ± 0.001	0.05 ± 0.01	**8.81**	0.080 ± 0.002	0.047 ± 0.002
6.85	0.004 ± 0.001	0.03 ± 0.01	**9.05**	0.095 ± 0.003	0.066 ± 0.001
7.10	0.0059 ± 0.0006	0.021 ± 0.002	**9.29**	0.08 ± 0.03	0.11 ± 0.02
7.35	0.008 ± 0.001	0.022 ± 0.003	**9.52**	0.097 ± 0.005	0.13 ± 0.01
7.58	0.013 ± 0.001	0.022 ± 0.003	**9.67**	0.093 ± 0.003	0.18 ± 0.01
7.89	0.020 ± 0.002	0.023 ± 0.001	**9.77**	0.0851 ± 0.0002	0.25 ± 0.003
8.12	0.030 ± 0.001	0.0250 ± 0.0007	**10.12**	0.083 ± 0.005	0.31 ± 0.02

[a] Parameters are the average and standard deviation of a minimum of five pH jump (from pH 5, 0.1 M NaCl) kinetic traces fit to a triple exponential equation from pH 6.56 to 7.58 and a quadruple exponential equation at pH ≥ 7.89. The kinetics were followed at 406 nm over the course of 50 to 350 seconds.

Table A.6. Kinetic parameters for the alkaline transition of the WT*/K73H variant obtained from stopped-flow downward pH jump measurements at 25 °C in 10 mM buffer, 0.1 M NaCl.[a]

pH	A_1	$k_{obs,1}(s^{-1})$	A_3	$k_{obs,3}(s^{-1})$	A_4	$k_{obs,4}(s^{-1})$
5.08	0.0236 ± 0.0008	10.3 ± 0.4	0.009 ± 0.001	0.032 ± 0.003	0.005 ± 0.002	0.012 ± 0.002
5.33	0.024 ± 0.007	11.6 ± 0.8	0.009 ± 0.001	0.042 ± 0.005	0.0116 ± 0.0008	0.010 ± 0.001
5.58	0.024 ± 0.001	10.3 ± 0.3	0.0084 ± 0.0008	0.042 ± 0.004	0.011 ± 0.001	0.010 ± 0.001
5.80	0.0184 ± 0.0009	9.1 ± 0.7	0.0078 ± 0.0007	0.062 ± 0.003	0.013 ± 0.001	0.010 ± 0.001
6.06	0.020 ± 0.001	9.3 ± 0.8	0.006 ± 0.002	0.06 ± 0.01	0.010 ± 0.001	0.011 ± 0.003
6.26	0.0168 ± 0.0008	8.9 ± 0.6	0.0045 ± 0.0003	0.11 ± 0.07	0.010 ± 0.002	0.0140 ± 0.0005
6.48	0.0129 ± 0.0008	8.3 ± 0.8	0.0038 ± 0.0008	0.068 ± 0.006	0.0079 ± 0.0005	0.013 ± 0.002

[a] Parameters are the average and standard deviation of a minimum of five pH jump (from pH 8.05, 0.1 M NaCl) kinetics traces. The fast phase parameters ($k_{obs,1}$ and A_1) are from single exponential fits to 1 second timescale data with pressure holds. The slow phase parameters ($k_{obs,3}$ and A_3; $k_{obs,4}$ and A_4) are from long timescale data fit to a triple exponential equation. Phase 2 observed in upward pH jump experiments is not observed in downward pH jump experiments.

Table A.7. Fast phase observed gated ET rate constants, $k_{gET,1}$, and amplitudes, $A_{gET,1}$, obtained by reducing oxidized WT*/K73H iso-1-Cyt*c* with hexaammineruthenium(II) chloride, a_6Ru^{2+}, at 25 °C in 10 mM buffer, 01. M NaCl.[a]

pH	$[a_6Ru^{2+}]$ (mM)	$A_{gET,1}$	$k_{gET,1}$ (s^{-1})
5[b]	13.0 ± 0.6	0.0472 ± 0.0010	560 ± 10
	6.6 ± 0.2	0.068 ± 0.001	236 ± 4
	2.8 ± 0.2	0.081 ± 0.001	109 ± 1
	1.2 ± 0.1	0.088 ± 0.004	41 ± 4
	0.8 ± 0.5	0.080 ± 0.009	17.6 ± 0.8
6[b]	12.8 ± 0.7	0.0367 ± 0.0010	590 ± 20
	5.8 ± 0.4	0.0543 ± 0.0007	248 ± 3
	3.0 ± 0.2	0.064 ± 0.001	125 ± 3
	1.6 ± 0.1	0.0687 ± 0.0006	72.4 ± 0.7
	0.74 ± 0.06	0.066 ± 0.001	30.0 ± 0.5
7[c]	16 ± 1	0.046 ± 0.002	700 ± 20
	8.0 ± 0.5	0.059 ± 0.001	330 ± 4
	3.7 ± 0.2	0.0658 ± 0.0007	149 ± 2
	2.0 ± 0.2	0.0687 ± 0.0005	83.9 ± 0.9
	0.94 ± 0.07	0.062 ± 0.001	40.1 ± 0.8
8[c]	16 ± 1	0.034 ± 0.001	540 ± 20
	8.2 ± 0.6	0.0421 ± 0.0009	270 ± 6
	3.9 ± 0.3	0.0465 ± 0.0003	120 ± 2
	1.7 ± 0.2	0.0432 ± 0.0008	48.3 ± 0.9
	1.00 ± 0.09	0.038 ± 0.001	36 ± 1
9[c]	13.6 ± 0.7	0.0105 ± 0.0008	440 ± 50
	6.6 ± 0.4	0.0158 ± 0.0008	220 ± 20
	2.8 ± 0.2	0.0183 ± 0.0004	101 ± 3
	1.4 ± 0.1	0.0169 ± 0.0009	52 ± 4
	0.81 ± 0.08	0.0136 ± 0.0009	35 ± 2

[a] Parameters are the average and standard deviation of a minimum of three kinetic traces followed by the increase in absorbance at 550 nm upon reduction of iso-1-Cyt*c*. pH 5 data were collected on a 5 second timescale and pH 6-9 data were collected on a one second timescale with pressure hold [b] Parameters are from fits to a double exponential equation. [c] Parameters are from fits to a triple exponential equation.

Table A.8. Intermediate phase observed gated ET rate constants, $k_{gET,2}$, and amplitudes, $A_{gET,2}$, obtained by reducing oxidized WT*/K73H iso-1-Cyt*c* with hexaammineruthenium(II) chloride, a_6Ru^{2+}, at 25 °C in 10 mM buffer, 01. M NaCl.[a]

pH	$[a_6Ru^{2+}]$ (mM)	$A_{gET,2}$	$k_{gET,2}$ (s^{-1})
5[b]	13.0 ± 0.6	0.0034 ± 0.0006	8 ± 2
	6.6 ± 0.2	0.0028 ± 0.0003	10 ± 2
	2.8 ± 0.2	0.0050 ± 0.0006	10 ± 2
	1.2 ± 0.1	0.009 ± 0.005	11 ± 4
	0.8 ± 0.5	0.019 ± 0.009	8 ± 2
6[b]	12.8 ± 0.7	0.0076 ± 0.0004	8.5 ± 0.8
	5.8 ± 0.4	0.0076 ± 0.0002	8.8 ± 0.3
	3.0 ± 0.2	0.0081 ± 0.0006	8.5 ± 0.7
	1.6 ± 0.1	0.0092 ± 0.0003	8.8 ± 0.6
	0.74 ± 0.06	0.016 ± 0.002	9.2 ± 0.7
7[c]	16 ± 1	0.0177 ± 0.0004	9.8 ± 0.6
	8.0 ± 0.5	0.0184 ± 0.0004	9.2 ± 0.3
	3.7 ± 0.2	0.0190 ± 0.0004	8.5 ± 0.4
	2.0 ± 0.2	0.0216 ± 0.0004	8.7 ± 0.4
	0.94 ± 0.07	0.0310 ± 0.0010	9.0 ± 0.4
8[c]	16 ± 1	0.0178 ± 0.0003	8.8 ± 0.3
	8.2 ± 0.6	0.0187 ± 0.0003	8.6 ± 0.3
	3.9 ± 0.3	0.0203 ± 0.0004	8.5 ± 0.4
	1.7 ± 0.2	0.0264 ± 0.0007	8.4 ± 0.4
	1.00 ± 0.09	0.0313 ± 0.0010	8.1 ± 0.4
9[c]	13.6 ± 0.7	0.0103 ± 0.0005	9.7 ± 0.6
	6.6 ± 0.4	0.0106 ± 0.0006	9.4 ± 0.8
	2.8 ± 0.2	0.0115 ± 0.0004	9.6 ± 0.6
	1.4 ± 0.1	0.0143 ± 0.0008	8.4 ± 0.8
	0.81 ± 0.08	0.018 ± 0.001	7.8 ± 0.4

[a] Parameters are the average and standard deviation of a minimum of three kinetic traces followed by the increase in absorbance at 550 nm upon reduction of iso-1-Cyt*c*. pH 5 data were collected on a 5 second timescale and pH 6-9 data were collected on a one second timescale with pressure hold. [b] Parameters are from fits to a double exponential equation. [c] Parameters are from fits to a triple exponential equation.

Table A.9. First slow phase observed gated ET rate constants, $k_{gET,3}$, and amplitudes, $A_{gET,3}$, obtained by reducing oxidized WT*/K73H iso-1-Cyt*c* with hexaammineruthenium(II) chloride, a_6Ru^{2+}, at 25 °C in 10 mM buffer, 01. M NaCl.[a]

pH	$[a_6Ru^{2+}]$ (mM)	$A_{gET,3}$	$k_{gET,3}$ (s^{-1})
7	19 ± 2	0.08 ± 0.2	0.3 ± 0.1
	8.3 ± 0.8	0.0031 ± 0.0004	0.4 ± 0.2
	4.0 ± 0.4	0.0037 ± 0.0004	0.30 ± 0.04
	1.9 ± 0.2	0.0031 ± 0.0004	0.16 ± 0.04
	0.7 ± 0.2	0.02 ± 0.05	0.11 ± 0.01
8	12.04 ± 0.08	0.0018 ± 0.0006	0.8 ± 0.4
	5.97 ± 0.07	0.003 ± 0.002	0.2 ± 0.1
	2.24 ± 0.06	0.004 ± 0.001	0.14 ± 0.08
	1.03 ± 0.02	0.0035 ± 0.0006	0.12 ± 0.02
	0.4 ± 0.3	0.0034 ± 0.0003	0.11 ± 0.02
9	10.2 ± 0.1	0.0020 ± 0.0002	0.5 ± 0.3
	4.160 ± 0.004	0.0020 ± 0.0006	0.3 ± 0.2
	1.78 ± 0.04	0.0018 ± 0.0006	0.18 ± 0.08
	1.205 ± 0.002	0.005 ± 0.008	0.2 ± 0.1
	0.5 ± 0.4	0.0013 ± 0.0002	0.20 ± 0.08

[a] Parameters are the average and standard deviation of a minimum of three kinetic traces followed by the increase in absorbance at 550 nm upon reduction of iso-1-Cyt*c*. Parameters are from fits of long time scale (up to 300 s) data to a quadruple exponential equation .

Table A.10. Second slow phase observed gated ET rate constants, $k_{gET,4}$, and amplitudes, $A_{gET,4}$, obtained by reducing oxidized WT*/K73H iso-1-Cyt*c* with hexaammineruthenium(II) chloride, a_6Ru^{2+}, at 25 °C in 10 mM buffer, 01. M NaCl.[a]

pH	$[a_6Ru^{2+}]$ (mM)	$A_{gET,4}$	$k_{gET,4}$ (s^{-1})
7	19 ± 2	0.02 ± 0.02	0.045 ± 0.007
	8.3 ± 0.8	0.0120 ± 0.0008	0.030 ± 0.002
	4.0 ± 0.4	0.0117 ± 0.0004	0.028 ± 0.002
	1.9 ± 0.2	0.0064 ± 0.0009	0.023 ± 0.002
	0.7 ± 0.2	0.009 ± 0.008	0.022 ± 0.002
8	12.04 ± 0.08	0.014 ± 0.001	0.0360 ± 0.0009
	5.97 ± 0.07	0.017 ± 0.002	0.029 ± 0.003
	2.24 ± 0.06	0.017 ± 0.002	0.023 ± 0.002
	1.03 ± 0.02	0.0175 ± 0.0006	0.022 ± 0.001
	0.4 ± 0.3	0.0165 ± 0.0005	0.0231 ± 0.0004
9	10.2 ± 0.1	0.062 ± 0.003	0.0256 ± 0.0004
	4.160 ± 0.004	0.066 ± 0.002	0.0229 ± 0.0004
	1.78 ± 0.04	0.063 ± 0.003	0.0223 ± 0.0003
	1.205 ± 0.002	0.05 ± 0.02	0.0221 ± 0.0002
	0.5 ± 0.4	0.0601 ± 0.0008	0.0221 ± 0.0001

[a] Parameters are the average and standard deviation of a minimum of three kinetic traces followed by the increase in absorbance at 550 nm upon reduction of iso-1-Cyt*c*. Parameters are from fits of long time scale (up to 300 s) data to a quadruple exponential equation.

Appendix B

Table B.11. Oligonucleotide primers used for L85A site-directed mutagenesis.[a]

primer	Primer sequence 5'-3'
L85A	caagatggcctttggtggg**gcg**aagaaggaaaaagacaga
L85A-r	tctgtctttttccttctt**cgc**cccaccaaaggccatcttg

[a] Mutation sites are shown in bold and underlined.

Table B.12. Kinetic parameters for the alkaline transition of the WT*/L85A variant obtained from upwards pH jump data monitored at 406 nm.[a]

pH	$A_{1,A85}$	$k_{obs,1,A85}$ (s^{-1})	$A_{2,A85}$	$k_{obs,2,A85}$ (s^{-1})	$A_{3,A85}$	$k_{obs,3,A85}$ (s^{-1})
6.83	0.0005 ± 0.0004	3 ± 2	0.0171 ± 0.0007	0.030 ± 0.003	0.002 ± 0.001	0.08 ± 0.01
7.08	0.0010 ± 0.0006	3 ± 3	0.029 ± 0.003	0.027 ± 0.002	0.008 ± 0.003	0.07 ± 0.01
7.32	0.003 ± 0.003	1.2 ± 0.9	0.04 ± 0.01	0.029 ± 0.002	0.018 ± 0.007	0.07 ± 0.02
7.62	0.002 ± 0.001	2 ± 2	0.056 ± 0.006	0.032 ± 0.002	0.034 ± 0.006	0.079 ± 0.007
7.93	0.004 ± 0.003	1.6 ± 0.9	0.067 ± 0.008	0.100 ± 0.005	0.064 ± 0.003	0.042 ± 0.001
8.09	0.007 ± 0.002	6 ± 5	0.10 ± 0.01	0.13 ± 0.01	0.06 ± 0.01	0.050 ± 0.004
8.30	0.006 ± 0.002	5 ± 5	0.144 ± 0.004	0.169 ± 0.006	0.040 ± 0.005	0.053 ± 0.004
8.53	0.010 ± 0.004	10 ± 6	0.171 ± 0.003	0.260 ± 0.008	0.031 ± 0.004	0.063 ± 0.004
8.80	0.010 ± 0.001	7 ± 3	0.1845 ± 0.0007	0.40 ± 0.01	0.023 ± 0.002	0.070 ± 0.007
9.00	0.016 ± 0.005	10 ± 6	0.190 ± 0.004	0.68 ± 0.02	0.017 ± 0.002	0.076 ± 0.008
9.22	0.019 ± 0.001	8 ± 3	0.189 ± 0.003	1.03 ± 0.02	0.0151 ± 0.0006	0.078 ± 0.006
9.42	0.033 ± 0.010	9 ± 4	0.17 ± 0.02	1.60 ± 0.08	0.015 ± 0.003	0.08 ± 0.02
9.54	0.038 ± 0.004	10 ± 3	0.163 ± 0.007	2.15 ± 0.07	0.0139 ± 0.0007	0.108 ± 0.009
9.70	0.076 ± 0.010	7.2 ± 0.8	0.10 ± 0.01	2.6 ± 0.1	0.0122 ± 0.0002	0.149 ± 0.004

[a] Parameters are the average and standard deviation of a minimum of five trials and are from 100-250 s timescale trials fit to a triple exponential equation.

Table B.13. Kinetic parameters for the alkaline transition of the WT*/L85A variant obtained from downwards pH jump data from pH 8.5 monitored at 406 nm.[a]

pH	$A_{1,A85}$	$k_{obs,1,A85}$ (s^{-1})	$A_{2,A85}$	$k_{obs,2,A85}$ (s^{-1})	$A_{3,A85}$	$k_{obs,3,A85}$ (s^{-1})
6.04	0.002 ± 0.001	4 ± 3	0.151 ± 0.002	0.0255 ± 0.0004	0.033 ± 0.003	0.070 ± 0.004
6.24	0.0022 ± 0.0009	2 ± 2	0.16 ± 0.01	0.0233 ± 0.0006	0.043 ± 0.008	0.059 ± 0.009
6.49	0.003 ± 0.002	5 ± 3	0.167 ± 0.005	0.0231 ± 0.0004	0.036 ± 0.004	0.066 ± 0.006
6.71	0.003 ± 0.001	4 ± 2	0.137 ± 0.005	0.0225 ± 0.0004	0.036 ± 0.005	0.061 ± 0.005
6.98	0.005 ± 0.003	2 ± 3	0.115 ± 0.008	0.025 ± 0.005	0.044 ± 0.010	0.05 ± 0.02
7.29	0.0015 ± 0.0003	0.9 ± 0.4	0.069 ± 0.004	0.0233 ± 0.0010	0.044 ± 0.005	0.057 ± 0.002
7.47	0.0017 ± 0.0009	0.5 ± 0.2	0.020 ± 0.007	0.021 ± 0.005	0.031 ± 0.007	0.055 ± 0.007

[a] Parameters are the average and standard deviation of a minimum of five trials and are from 200-400 s timescale data fit to a triple exponential equation. [b] Data are labeled so that each phase corresponds to the same phase from upward jumps.

Table B.14. Kinetic parameters for the alkaline transition of the WT*/L85A variant obtained from downward pH jump data from pH 9.5 monitored at 406 nm.[a]

pH	$A_{2,A85}$	$k_{obs,2,A85}$ (s^{-1})	$A_{3,A85}$	$k_{obs,3,A85}$ (s^{-1})
5.98	0.115 ± 0.005	0.028 ± 0.001	0.018 ± 0.006	0.10 ± 0.02
6.22	0.125 ± 0.004	0.0260 ± 0.0006	0.017 ± 0.003	0.09 ± 0.01
6.47	0.132 ± 0.003	0.0250 ± 0.0003	0.019 ± 0.002	0.087 ± 0.008
6.73	0.125 ± 0.006	0.024 ± 0.001	0.024 ± 0.008	0.07 ± 0.01
7.01	0.124 ± 0.002	0.0252 ± 0.0005	0.022 ± 0.003	0.080 ± 0.006
7.27	0.090 ± 0.005	0.028 ± 0.002	0.022 ± 0.007	0.084 ± 0.008
7.52	0.078 ± 0.008	0.034 ± 0.002	0.023 ± 0.006	0.10 ± 0.01

[a] Parameters are the average and standard deviation of a minimum of five trials and are from 250-350 s data timescale fit to a double exponential equation. [b] Data are labeled so that each phase corresponds to the same phase from upward jumps.

Table B.15. Kinetic parameters for the alkaline transition of the WT*/K73H/L85A variant obtained from upward pH jump data monitored at 406 nm.[a]

pH	$A_{1,H73A85}$	$k_{obs,1,H73A85}$ (s^{-1})	$A_{2,H73A85}$	$k_{obs,2,H73A85}$ (s^{-1})	$A_{3,H73A85}$	$k_{obs,3,H73A85}$ (s^{-1})
5.99	0.024 ± 0.001	6.8 ± 0.7	0.0024 ± 0.0002	0.004 ± 0.001	0.0007 ± 0.0001	0.17 ± 0.05
6.26	0.034 ± 0.002	7.2 ± 0.4	0.002 ± 0.002	0.006 ± 0.005	0.0009 ± 0.0001	0.11 ± 0.02
6.58	0.043 ± 0.001	7.7 ± 0.4	0.002 ± 0.001	0.02 ± 0.01	0.0007 ± 0.0001	0.20 ± 0.05
6.77	0.0482 ± 0.0008	8.3 ± 0.5	0.0007 ± 0.0004	0.011 ± 0.010	0.0009 ± 0.0002	0.18 ± 0.06
6.98	0.0522 ± 0.0006	8.9 ± 0.2	0.0011 ± 0.0003	0.019 ± 0.009	0.0007 ± 0.0003	0.21 ± 0.03
7.07	0.054 ± 0.002	9.4 ± 0.3	0.0010 ± 0.0002	0.011 ± 0.006	0.0009 ± 0.0002	0.17 ± 0.08
7.49	0.056 ± 0.001	10.2 ± 0.3	0.002 ± 0.002	0.01 ± 0.02	0.0012 ± 0.0003	0.15 ± 0.05
7.80	0.059 ± 0.001	11.3 ± 0.2	0.0011 ± 0.0003	0.03 ± 0.02	0.0014 ± 0.0005	0.25 ± 0.08
8.01	0.059 ± 0.004	11.4 ± 0.3	0.0015 ± 0.0008	0.02 ± 0.01	0.0021 ± 0.0002	0.18 ± 0.02
8.25	0.060 ± 0.003	12.2 ± 0.2	0.002 ± 0.001	0.10 ± 0.08	0.002 ± 0.001	0.1 ± 0.1
8.52	0.060 ± 0.001	12.8 ± 0.4	0.004 ± 0.002	0.3 ± 0.2	0.002 ± 0.001	0.05 ± 0.05
8.75	0.061 ± 0.001	13.4 ± 0.4	0.004 ± 0.001	0.33 ± 0.08	0.004 ± 0.001	0.11 ± 0.03
8.81	0.060 ± 0.001	13.9 ± 0.3	0.007 ± 0.001	0.31 ± 0.04	0.004 ± 0.001	0.12 ± 0.02
9.09	0.054 ± 0.001	16.0 ± 0.6	0.009 ± 0.002	0.51 ± 0.06	0.007 ± 0.002	0.20 ± 0.02
9.16	0.057 ± 0.001	14.7 ± 0.6	0.008 ± 0.002	0.41 ± 0.05	0.006 ± 0.002	0.15 ± 0.04
9.45	0.0499 ± 0.0009	17.4 ± 0.4	0.011 ± 0.002	0.66 ± 0.07	0.008 ± 0.002	0.25 ± 0.04
9.85	0.0447 ± 0.0009	19.8 ± 0.7	0.012 ± 0.004	1.0 ± 0.3	0.009 ± 0.004	0.36 ± 0.08

[a] Parameters are the average and standard deviation of a minimum of five trials. Amp_1 and $k_{obs,1}$ are from fits to 1 s trials with pressure holds using a bi-exponential equation. Amplitudes and rate constants for the second and third phase are from triple exponential fits to 50-350 s timescale trials.

Table B.16. Kinetic parameters for the alkaline transition of the WT*/K73H/L85A variant obtained from downward pH jump data from pH 7.5 monitored at 406 nm.[a]

pH	$A_{1,H73A85}$	$k_{obs,1,H73A85}$ (s^{-1})	$A_{2,H73A85}$	$k_{obs,2,H73A85}$ (s^{-1})	$A_{3,H73A85}$	$k_{obs,3H73A85}$ (s^{-1})
5.01	0.0398 ± 0.0005	6.5 ± 0.1	0.0034 ± 0.0005	0.015 ± 0.002	-	-
5.33	0.0322 ± 0.0005	6.04 ± 0.07	0.0031 ± 0.0007	0.020 ± 0.001	-	-
5.60	0.035 ± 0.002	5.9 ± 0.2	0.0015 ± 0.0005	0.025 ± 0.005	-	-
5.84	0.027 ± 0.002	5.9 ± 0.3	0.002 ± 0.001	0.007 ± 0.006	-	-
6.03	0.023 ± 0.002	6.1 ± 0.3	0.0013 ± 0.0007	0.014 ± 0.006	-	-
6.28	0.017 ± 0.001	6.4 ± 0.2	-	-	0.0008 ± 0.0001	0.1 ± 0.1
6.52	0.012 ± 0.001	6.5 ± 0.3	-	-	0.0011 ± 0.0002	0.09 ± 0.03

[a] Parameters are the average and standard deviation of a minimum of five trials. Amp_1 and $k_{obs,1}$ are from fits of 1 s trials with pressure holds to a single exponential equation. Amp_2 and $k_{obs,2}$ are from 200 s trials fit to a double exponential equation for pH 5.33-6.52 and a triple exponential equation at pH 5.01.

Table B.17. Fast phase gated ET rate constants, $k_{obs1,ET}$, and amplitudes, $Amp_{1,ET}$, obtained by reducing oxidized WT*/K73H/L85A iso-1-Cyt*c* with bis(2,2',2"-terpyridine)cobalt(II), $Co(terpy)_2^{2+}$ at 25 ºC in 10 mM buffer, 01. M NaCl.[a]

pH	$[Co(terpy)_2^{2+}]$ (mM)	$Amp_{1,ET}$	$k_{obs1,ET}$ (s^{-1})
5	0.53	0.0025 ± 0.0005	11 ± 4
	1.05	0.010 ± 0.001	7 ± 1
	2.20	0.018 ± 0.001	12 ± 2
	3.26	0.0243 ± 0.0006	14.8 ± 0.5
	4.16	0.0272 ± 0.0006	19.4 ± 0.8
	4.89	0.030 ± 0.002	22 ± 1
5.5	0.72	0.0019 ± 0.0004	10 ± 4
	1.08	0.007 ± 0.001	8 ± 2
	2.40	0.0144 ± 0.0007	10.3 ± 0.8
	3.17	0.0190 ± 0.0007	14.6 ± 0.4
	3.47	0.0213 ± 0.0007	19.2 ± 0.5
	4.84	0.0225 ± 0.0006	22.2 ± 0.8
6	0.50	0.0024 ± 0.0003	9 ± 3
	0.87	0.0050 ± 0.0005	8 ± 2
	1.77	0.0104 ± 0.0005	11 ± 2
	2.92	0.0151 ± 0.0008	15 ± 1
	4.22	0.0182 ± 0.0008	20.0 ± 0.9
	5.15	0.017 ± 0.002	21 ± 2
6.5	0.54	0.0010 ± 0.0006	9 ± 5
	1.04	0.0020 ± 0.0003	9 ± 5
	2.16	0.005 ± 0.001	17 ± 4
	3.05	0.0068 ± 0.0005	16 ± 2
	4.02	0.0077 ± 0.0006	18 ± 2
	5.11	0.009 ± 0.001	23 ± 2
7	0.50	0.0008 ± 0.0003	8 ± 2
	1.00	0.0019 ± 0.0007	12 ± 8
	2.07	0.0035 ± 0.0007	16 ± 6
	3.19	0.0037 ± 0.0003	20 ± 2
	4.07	0.0039 ± 0.0008	22 ± 2
	5.10	0.0044 ± 0.0008	23 ± 3

[a]Parameters are the average and standard deviation of a minimum of five kinetic traces followed by the increase in absorbance at 550 nm upon reduction of iso-1-Cyt*c*. Data were collected on a 5 second timescale with pressure hold.

Table B.18. Slower phase gated ET rate constants obtained by reducing oxidized WT*/K73H/L85A iso-1-Cyt*c* with bis(2,2',2"-terpyridine)cobalt(II), $Co(terpy)_2^{2+}$ at 25 °C in 10 mM buffer, 01. M NaCl.[a]

pH	$[Co(terpy)_2^{2+}]$ (mM)	$Amp_{2,ET}$	$k_{obs2,ET}$ (s^{-1})	$Amp_{3,ET}$	$k_{obs3,ET}$ (s^{-1})	$Amp_{4,ET}$	$k_{obs4,ET}$ (s^{-1})
5	**0.53**	0.072 ± 0.004	0.73 ± 0.04	0.0079 ± 0.0006	0.12 ± 0.03	0.0097 ± 0.0008	0.015 ± 0.002
	1.05	0.068 ± 0.003	1.4 ± 0.3	0.006 ± 0.001	0.15 ± 0.04	0.0091 ± 0.0008	0.03 ± 0.01
	2.20	0.065 ± 0.001	1.77 ± 0.04	0.0045 ± 0.0007	0.16 ± 0.04	0.008 ± 0.002	0.038 ± 0.004
	3.26	0.0610 ± 0.0005	2.00 ± 0.06	0.0059 ± 0.0007	0.16 ± 0.07	0.007 ± 0.001	0.031 ± 0.007
	4.16	0.0567 ± 0.0004	2.07 ± 0.03	0.006 ± 0.001	0.13 ± 0.03	0.006 ± 0.001	0.028 ± 0.006
	4.89	0.0539 ± 0.0009	2.08 ± 0.05	0.006 ± 0.001	0.12 ± 0.05	0.005 ± 0.001	0.027 ± 0.008
5.5	**0.72**	0.059 ± 0.003	0.61 ± 0.02	0.0082 ± 0.0008	0.11 ± 0.01	0.0046 ± 0.0003	0.015 ± 0.004
	1.08	0.057 ± 0.001	1.06 ± 0.01	0.006 ± 0.001	0.12 ± 0.05	0.0036 ± 0.0009	0.02 ± 0.01
	2.40	0.048 ± 0.001	1.43 ± 0.05	0.004 ± 0.001	0.15 ± 0.09	0.004 ± 0.001	0.04 ± 0.02
	3.17	0.048 ± 0.001	1.66 ± 0.05	0.005 ± 0.001	0.13 ± 0.03	0.004 ± 0.001	0.034 ± 0.008
	3.47	0.042 ± 0.002	1.82 ± 0.05	0.004 ± 0.001	0.4 ± 0.3	0.005 ± 0.001	0.07 ± 0.01
	4.84	0.042 ± 0.002	1.81 ± 0.04	0.002 ± 0.001	0.4 ± 0.3	0.0058 ± 0.0007	0.083 ± 0.009
6	**0.50**	0.0718 ± 0.0004	0.53 ± 0.02	0.0122 ± 0.0009	0.105 ± 0.009	0.0072 ± 0.0001	0.012 ± 0.001
	0.87	0.074 ± 0.001	0.730 ± 0.009	0.0112 ± 0.0003	0.102 ± 0.003	0.0063 ± 0.0002	0.013 ± 0.002
	1.77	0.0708 ± 0.0009	1.02 ± 0.01	0.0101 ± 0.0003	0.121 ± 0.007	0.0060 ± 0.0003	0.018 ± 0.001
	2.92	0.0625 ± 0.0009	1.22 ± 0.02	0.0099 ± 0.0007	0.10 ± 0.01	0.0054 ± 0.0009	0.010 ± 0.004
	4.22	0.058 ± 0.001	1.30 ± 0.01	0.0098 ± 0.0005	0.13 ± 0.01	0.0049 ± 0.0004	0.0162 ± 0.0010
	5.15	0.055 ± 0.001	1.33 ± 0.03	0.0085 ± 0.0006	0.126 ± 0.008	0.0041 ± 0.0003	0.022 ± 0.003
6.5	**0.54**	0.045 ± 0.003	0.29 ± 0.01	0.016 ± 0.003	0.10 ± 0.02	0.0041 ± 0.0006	0.016 ± 0.002
	1.04	0.052 ± 0.001	0.444 ± 0.005	0.0116 ± 0.0007	0.107 ± 0.007	0.0038 ± 0.0004	0.018 ± 0.001
	2.16	0.0513 ± 0.0008	0.65 ± 0.01	0.0091 ± 0.0003	0.13 ± 0.02	0.0036 ± 0.0008	0.028 ± 0.008
	3.05	0.0532 ± 0.0006	0.803 ± 0.0010	0.0098 ± 0.0002	0.110 ± 0.005	0.0035 ± 0.0002	0.015 ± 0.004
	4.02	0.051 ± 0.003	0.86 ± 0.01	0.0096 ± 0.0004	0.11 ± 0.01	0.0031 ± 0.0003	0.012 ± 0.002
	5.11	0.0495	0.92	0.008	0.126	0.0031	0.027

		± 0.0009	± 0.02	± 0.001	± 0.009	± 0.0008	± 0.009
7	**0.50**	0.02 ± 0.01	0.12 ± 0.02	0.02 ± 0.01	0.3 ± 0.1	0.006 ± 0.002	.059 ± 0.002
	1.00	0.012 ± 0.001	0.39 ± 0.08	0.035 ± 0.001	0.28 ± 0.02	0.0092 ± 0.0009	0.071 ± 0.006
	2.07	0.04 ± 0.01	0.55 ± 0.08	0.01 ± 0.01	0.2 ± 0.1	0.005 ± 0.002	0.05 ± 0.02
	3.19	0.041 ± 0.001	0.67 ± 0.01	0.006 ± 0.002	0.18 ± 0.08	0.004 ± 0.002	0.06 ± 0.02
	4.07	0.040 ± 0.001	0.73 ± 0.02	0.0060 ± 0.0009	0.16 ± 0.09	0.002 ± 0.002	0.04 ± 0.02
	5.10	0.0373 ± 0.0005	0.81 ± 0.02	0.0058 ± 0.0009	0.15 ± 0.04	0.002 ± 0.0009	0.04 ± 0.02

[a]Parameters are the average and standard deviation of a minimum of five kinetic traces followed by the increase in absorbance at 550 nm upon reduction of iso-1-Cyt*c*. Data were collected on a 100-400 second timescale.

Table B.19. Starting concentrations used for numerical fitting of stopped-flow ET in Pro-Kineticist.

pH	[$Co(terpy)_2^{2+}$] (mM)	*cis*-Pro His73-Fe(III)heme (s^{-1})	*trans*-Pro His73-Fe(III)heme (s^{-1})	Lys79-Fe(III)heme (s^{-1})	Met80-Fe(III)heme (s^{-1})
5	0.53	5.6e-7	2.7e-6	-	1.5e-6
	1.05	5.7e-7	2.8e-6	-	1.5e-6
	2.20	5.8e-7	2.8e-6	-	1.6e-6
5.5	0.72	4.1e-7	2.3e-6	-	1.2e-6
	1.08	4.1e-7	2.3e-6	-	1.2e-6
	2.40	4.0e-7	2.2e-6	-	1.2e-6
6	0.50	5.0e-7	3.0e-6	2.4e-7	9.9e-7
	0.87	5.1e-7	3.3e-6	2.4e-7	1.0e-6
	1.77	5.2e-7	3.3e-6	2.4e-7	1.0e-6
6.5	0.54	4.2e-7	2.5e-6	1.5e-7	4.5e-7
	1.04	4.4e-7	2.6e-6	1.6e-7	4.7e-7
	2.16	4.3e-7	2.6e-6	1.6e-7	4.7e-7
7	0.50	3.5e-7	2.2e-6	1.3e-7	2.6e-7
	1.00	3.6e-7	2.3e-6	1.3e-7	2.8e-7
	2.07	3.7e-7	2.4e-6	1.4e-7	2.8e-7

Table B.20. Parameters determined from numerical fitting of stopped-flow ET data in Pro-Kineticist.[a]

pH	[$Co(terpy)_2^{2+}$] (mM)	$k_{obs1,ET,PK}$ (s^{-1})[b]	$k_{f,His,PK}$ (s^{-1})[b]	$k_{obs3,ET,PK}$ (s^{-1})[c]	$k_{obs4,ET,PK}$ (s^{-1})[c]
5	0.53	2.7 ± 0.2	5.0 ± 0.4	0.026 ± 0.002	-
	1.05	5.8 ± 0.3	4.8 ± 0.3	0.039 ± 0.004	-
	2.20	12 ± 2	3.9 ± 0.6	0.06 ± 0.01	-
5.5	0.72	2.6 ± 0.3	6 ± 1	0.040 ± 0.003	-
	1.08	5.7 ± 0.6	6.1 ± 0.7	0.058 ± 0.007	-
	2.40	11 ± 1	5.5 ± 0.5	0.075 ± 0.008	-
6	0.50	3.3 ± 0.3	5.6 ± 0.6	0.058 ± 0.005	0.0104 ± 0.0008
	0.87	5.7 ± 0.5	5.8 ± 0.6	0.074 ± 0.006	0.012 ± 0.002
	1.77	12 ± 1	5.3 ± 0.5	0.10 ± 0.02	0.017 ± 0.002
6.5	0.54	3 ± 1	10 ± 3	0.067 ± 0.001	0.015 ± 0.002
	1.04	6 ± 2	10 ± 4	0.087 ± 0.009	0.018 ± 0.002
	2.16	14 ± 4	10 ± 3	0.126 ± 0.009	0.026 ± 0.003
7	0.50	3.5 ± 0.3	15 ± 2	0.12 ± 0.03	0.04 ± 0.02
	1.00	5.4 ± 0.4	12.0 ± 1.0	0.10 ± 0.02	0.04 ± 0.02
	2.07	8.6 ± 0.5	10 ± 2	0.14 ± 0.02	0.04 ± 0.02

[a] Parameters are the average and standard deviation of a minimum of five kinetic traces followed by the increase in absorbance at 550 nm upon reduction of iso-1-Cyt*c*. [b] Data were collected on a 5 second timescale with pressure hold. [c] Data were collected on a 100-400 second timescale.

Appendix C

Table C.21. X-ray crystallography and data collection and refinement statistics.

Wavelength (Å)	0.978
Resolution range (Å)	15 - 1.4 (1.43 - 1.4)*
Space group	$P6_322$
Unit cell dimensions	
a, b, c (Å)	93.62, 93.62, 155.01
α, β, γ (◦)	90, 90, 120
Total reflections	644192
Unique reflections	71415
Multiplicity	9.0 (6.6)*
Completeness (%)	99.89 (99.23)*
Mean I/σ(I)	14.16 (2.43)*
Wilson B-factor	15.42
R_{sym}	0.09 (0.843)*
Refinement	
Resolution range (Å)	8 - 1.45 (1.47 - 1.45)*
R_{work}	0.145 (0.256)*
R_{free}	0.156 (0.290)*
Number of atoms	3967
Number of atoms/protein molecule	1728
ligands	152
water	368
Protein residues (both molecules)	216
RMS (bonds, Å)	0.016
RMS (angles, ◦)	1.48
Ramachandran favored (%)	97
Ramachandran outliers (%)	0
Average B-factor	20.20
macromolecules	17.80
ligands	15.60
solvent	33.30

*Data for highest resolution shell are given in brackets

Table C.22. Residues and waters with two positions or partial occupancy.

Residue	Chain A		Chain B	
	Occupancy Position A	Occupancy Position B	Occupancy Position A	Occupancy Position B
Val20	0.75	0.25	0.67	0.33
Glu21	0.50	0.50	1.00	-
Arg38	1.00	-	-	0.6
Asn52	0.48	0.52	0.50	0.50
Met64	0.37	0.63	0.35	0.65
Leu85	0.82	0.18	0.74	0.26
Arg91	0.47	0.52	1.00	-
Water 111	0.75	0.25	0.60	0.40
Water 116	0.20	0.80	0.77	0.23
Water 126	-	-	0.48	-
Water 136	1.00	-	0.87	-
Water 149	1.00	-	0.74	-

Table C.23. Michaelis-Menten parameters from the guaiacol assay of peroxidase activity of Cyt*c* variants at 25 °C.[a]

Variant	pH	k_{cat}, s^{-1}	K_m, μM	k_{cat}/K_m, $M^{-1}s^{-1}$
K72ACyt*c*[*Sc*]	6.0	2.2 ± 0.1	12.4 ± 0.8	$1.8 \pm 0.1 \times 10^5$
	6.5	3.0 ± 0.1	12.9 ± 0.5	$2.30 \pm 0.09 \times 10^5$
	7.0	3.5 ± 0.2	16 ± 1	$2.2 \pm 0.1 \times 10^5$
	7.5	3.53 ± 0.07	20.8 ± 0.8	$1.70 \pm 0.07 \times 10^5$
	8.0	2.8 ± 0.2	25 ± 1	$1.12 \pm 0.06 \times 10^5$
tmK72Cyt*c*[*Sc*]	6.0	2.2 ± 0.1	14 ± 2	$1.6 \pm 0.2 \times 10^5$
	6.5	2.84 ± 0.06	15 ± 1	$1.9 \pm 0.1 \times 10^5$
	7.0	2.6 ± 0.3	14 ± 3	$1.9 \pm 0.3 \times 10^5$
	7.5	2.60 ± 0.03	20.3 ± 0.6	$1.28 \pm 0.04 \times 10^5$
	8.0	1.39 ± 0.08	19.0 ± 0.9	$0.73 \pm 0.03 \times 10^5$
Horse Cyt*c*[b]	7.0	0.13	11.0	0.12×10^5

[a] Experimental conditions were 1 μM Cyt*c* and 50 mM H_2O_2 in 50 mM potassium phosphate buffer. All k_{cat}, K_m and k_{cat}/K_m values reported are the average of three independent experiments. Error values are the larger value of either the standard deviation of the average or the average of the standard error reported by SigmaPlot for each independent experiment. [b]Data are from reference (*32*). Error in the horse heart Cyt*c* parameters is reported to be ±5%.

Appendix D

Table D.24. X-ray crystallography data collection and refinement statistics.

Data Collection	
Wavelength, Å	0.98
Resolution, Å	27.15-2.003 (2.075-2.003)
Space group	P1
Unit-cell dimensions	
a, b, c, Å	50.351, 56.122, 56.127
α, β, γ, °	75.65, 63.37, 63.36
Total reflections	140,733
Unique reflections	31,532
Multiplicity	1.7 (1.7)
Completeness, %	95.8 (89.1)
Mean I/σ(I)	11.90 (2.52)
Wilson B factor	30.42
R_{sym}	0.035 (0.304)
Refinement	
R_{work}	0.2011 (0.2872)
R_{free}	0.2477 (0.3409)
No. of atoms	3,893
No. of atoms/protein molecule	3,304
Ligands	269
Waters	320
Protein residues	428
Rms, bonds, Å	0.008
Rms, angles, °	1.23
Ramachandran, favored, %	95
Ramachandran, outliers, %	0.24
Average B factors	37.60
Macromolecules	37.20
Ligands	37.90
Solvent	41.30